



Compréhension du rôle des additifs du type glycol sur l'amélioration des performances des catalyseurs d'hydrotraitement

Victor Raul Costa

► To cite this version:

Victor Raul Costa. Compréhension du rôle des additifs du type glycol sur l'amélioration des performances des catalyseurs d'hydrotraitement. Catalyse. Université Claude Bernard - Lyon I, 2008. Français. NNT : 2008LYO10008 . tel-00527378

HAL Id: tel-00527378

<https://theses.hal.science/tel-00527378>

Submitted on 19 Oct 2010

HAL is a multi-disciplinary open access archive for the deposit and dissemination of scientific research documents, whether they are published or not. The documents may come from teaching and research institutions in France or abroad, or from public or private research centers.

L'archive ouverte pluridisciplinaire **HAL**, est destinée au dépôt et à la diffusion de documents scientifiques de niveau recherche, publiés ou non, émanant des établissements d'enseignement et de recherche français ou étrangers, des laboratoires publics ou privés.

THESE

présentée

devant l'UNIVERSITE CLAUDE BERNARD - LYON 1

pour l'obtention

du DIPLOME DE DOCTORAT

(arrêté du 7 août 2006)

présentée et soutenue publiquement le

10 janvier 2008

par

Victor COSTA

**COMPRÉHENSION DU RÔLE DES ADDITIFS DU TYPE GLYCOL SUR
L'AMÉLIORATION DES PERFORMANCES DES CATALYSEURS
D'HYDROTRAITEMENT**

Directeur de thèse : Christophe GEANTET

JURY : Édouard GARBOVSKY, *Président*

Edmond PAYEN, *Rapporteur*

Véronique PITCHON, *Rapporteur*

Karin MARCHAND

Mathieu DIGNE

Christophe GEANTET

ACKNOWLEDGMENTS

This document summarizes the work developed during the last 3 years. It was a fruitful period for my professional and personal development, and many are to be thanked.

I will start by thanking Karin Marchand and Mathieu Digne for their guidance, knowledge, support and fruitful discussions during 3 years. I could not imagine better promoters to become a researcher. Besides teaching me from a scientific point of view, they also made grow up as a person and as a professional. Most of all, I would like to thank them for their trust in me and their sincere friendship.

I would like to thank Christophe Geantet, my Ph.D. Director, for the analysis and questioning of my work, and for the scientific advices. The extraordinary human qualities of Christophe showed me that it is possible to be an outstanding researcher and a respected teacher at the same time! Our meetings were always very rich and pleasant!

Also, I would like to thank Tivadar Cseri, Gil Mabilon and Slavik Kasztelan for giving me the opportunity to work at IFP in the "Sulfures" group, the best group ever!

Thank you "sulfures" for these 3 years of good times! It was a pleasure to share labs with everybody. In particular, Marylin, Georges, Stephane Cremer, Stephane Rebours, Veronique and Sebastien. Also, for their wise advices, Dennis Uzio, Dennis Guillaume, Magalie and Elodie. I could not forget my office partner, Bertrand, for all the discussions, support and friendship throughout these years.

These acknowledgments wouldn't be complete without the "characterization" colleagues. Special thanks to Bernardette, Philippe, Mathieu, Laurent, Anne-Agathe, Anne-Lise, Christelle, Christophe, Tiziana, Loic, Florent, Alban and Jean.

All my other IFP colleagues are also to be thanked for the good moments we spent together, for the caffeine and nicotine breaks, the monday's football discussions, the lunches with philosophical discussions and seminars.

Finally, I would like to thank my family and friends for being there, believing in me and encouraging me to continue the pursuit of my objectives.

" ... it wasn't the beginning of happiness,
it was happiness!"

Michael Cunningham

GENERAL INDEX

GENERAL INTRODUCTION	1
-----------------------------	----------

CHAPTER I: BIBLIOGRAPHIC STUDY	3
---------------------------------------	----------

I.1. Introduction	5
I.2. Hydrotreatments and hydrotreating catalysts	5
I.2.1. Petroleum refining and hydrotreatments (HDT)	5
I.2.2. Middle distillates hydrotreatment catalysts	9
I.2.2.1. Standard preparation method of CoMo catalysts	9
I.2.2.2. Characterization of the CoMo catalysts active phase	10
I.2.3. Latest improvements in CoMo catalysts preparation	13
I.2.3.1. Improvements in HDT catalysts impregnation solution	14
I.2.3.2. Improvements in HDT catalysts activation step	20
I.2.4. Conclusions on hydrotreatments and hydrotreating catalysts	21
I.3. Glycol-type additives for hydrotreatment catalysts	22
I.3.1. Additive pre-impregnation of an alumina support	25
I.3.1.1. Alumina structure and properties	25
I.3.1.2. Additive-alumina interactions	26
I.3.2. Additive impregnation simultaneously with the active phase precursors	30
I.3.2.1. Modification of the impregnation solution by the additives	30
I.3.3. Additive impregnation of CoMo(P) catalysts	31
I.3.3.1. Impact of the nature of the additive	32
I.3.3.2. Impact of the additive loading	33
I.3.3.3. Modifications on the metal oxide phases due to additive	34
I.3.3.4. Interaction between the additive and phosphate in CoMoP calcined catalysts	35
I.3.4. Impact of additives on sulfidation	36
I.3.5. Conclusions on the impregnation of CoMo(P) catalysts by additives	38
I.4. Bibliographic study conclusions and thesis objectives	39
I.5. Bibliographic references	42

II.1. Catalysts preparation and additive impregnation.....	45
II.1.1. CoMo(P) catalysts preparation method.....	45
II.1.2. Additive impregnation of CoMo(P) catalysts.....	47
II.1.2.1. Additive impregnation prior to the metal precursors solution.....	47
II.1.2.2. Additive co-impregnation with the metal precursors solution.....	47
II.1.2.3. Additive impregnation of dried catalysts.....	47
II.1.2.4. Additive impregnation of calcined catalysts.....	48
II.1.3. Adsorption study.....	48
II.1.3.1. Impact of the ageing stage.....	50
II.1.3.2. Impact of the washing stage.....	50
II.1.3.3. Impact of the drying stage.....	51
II.2. Samples characterization.....	51
II.2.1. Elemental analysis methods.....	51
II.2.1.1. Lost on ignition (LOI).....	51
II.2.1.2. CHNS elemental analysis.....	51
II.2.1.3. X-ray Fluorescence (XRF).....	52
II.2.2. Physico-chemical analysis methods.....	52
II.2.2.1. Textural properties.....	52
II.2.2.2. Thermal analysis.....	52
II.2.2.3. Electronic Probe Microanalysis (EPMA).....	53
II.2.2.4. Transmission Electron Microscopy (TEM).....	53
II.2.3. Spectroscopic methods.....	53
II.2.3.1. Infrared spectroscopy.....	53
II.2.3.2. Raman spectroscopy.....	54
II.2.3.3. UV-Visible spectroscopy.....	55
II.2.3.4. Nuclear magnetic resonance (NMR).....	55
II.2.3.5. X-ray Diffraction spectroscopy (XRD).....	55
II.2.3.6. X-ray Photoelectron spectroscopy (XPS).....	55
II.2.3.7. X-ray Absorption spectroscopy (XAS).....	56
II.3. Catalysts activation.....	59
II.4. Catalytic tests.....	59
II.4.1. HSC test	59
II.4.2. Real feed HDS test.....	61
II.5. Bibliographic references.....	63

CHAPTER III: THE ROLE OF GLYCOL-TYPE ADDITIVES ON DRIED CoMo(P)

CATALYSTS

65

III.1. Introduction	67
III.2. Impact of the additive when impregnated on dried CoMo catalysts.....	67
III.2.1. Speciation of the precursor impregnation solutions.....	68
III.2.2. Speciation of the dried CoMo catalysts surface.....	69
<i>III.2.2.1. Influence of the additive on cobalt species.....</i>	<i>69</i>
<i>III.2.2.2. Influence of the additive on molybdenum species.....</i>	<i>74</i>
III.2.3. Thermal behavior.....	80
<i>III.2.3.1. Additive-free dried CoMo catalysts analysis.....</i>	<i>80</i>
<i>III.2.3.2. Additive-containing dried CoMo catalysts analysis.....</i>	<i>84</i>
III.2.4. Surface mechanism.....	87
III.3. Impact of the additive when impregnated on dried CoMoP catalysts.....	88
III.3.1. Speciation of the precursor impregnation solutions.....	88
III.3.2. Speciation of the dried CoMoP catalysts surface.....	92
<i>III.3.2.1. Influence of the additive on cobalt species.....</i>	<i>92</i>
<i>III.3.2.2. Influence of the additive on molybdenum species.....</i>	<i>94</i>
<i>III.3.2.3. Influence of the additive on phosphorus species.....</i>	<i>98</i>
III.3.3. Thermal behavior.....	104
<i>III.3.3.1. Additive-free dried CoMoP catalysts analysis.....</i>	<i>104</i>
<i>III.3.3.2. Additive-containing dried CoMoP catalysts analysis.....</i>	<i>106</i>
III.3.4. Surface mechanism.....	108
III.4. Chapter conclusion.....	109
III.5. Bibliographic references.....	109

CHAPTER IV: THE ROLE OF GLYCOL-TYPE ADDITIVES ON CALCINED CoMo(P)

CATALYSTS

113

IV.1. Introduction.....	115
IV.2. Impact of the additive when impregnated on calcined CoMo catalysts.....	115
IV.2.1. Textural properties of the calcined CoMo catalysts.....	116
IV.2.2. Speciation of the calcined CoMo catalysts.....	117
<i>IV.2.2.1. Influence of the additive on cobalt species.....</i>	<i>117</i>
<i>IV.2.2.2. Influence of the additive on molybdenum species.....</i>	<i>119</i>
IV.2.3. Metals distribution.....	121

IV.2.4. Thermal behavior.....	122
IV.2.4.1. Additive-free calcined CoMo catalysts analysis.....	122
IV.2.4.2. Additive-containing calcined CoMo catalysts analysis.....	123
IV.2.5. Surface mechanism.....	126
IV.3. Impact of the additive when impregnated on calcined CoMoP catalysts.....	126
IV.3.1. Textural properties of the calcined CoMoP catalysts.....	127
IV.3.2. Speciation of the calcined CoMoP catalysts.....	130
IV.3.2.1. Influence of the additive on cobalt species.....	130
IV.3.2.2. Influence of the additive on molybdenum species.....	132
IV.3.2.3. Influence of the additive on phosphorus species.....	134
IV.3.3. Metals and phosphorus distribution.....	140
IV.3.3.1. Phosphorus reaction with the additives.....	142
IV.3.4. Thermal behavior.....	145
IV.3.4.1. Additive-free calcined CoMoP catalysts analysis.....	145
IV.3.4.2. Additive-containing calcined CoMoP catalysts analysis.....	146
IV.3.4.3. Additives long-term stability.....	148
IV.3.5. Surface mechanism.....	149
IV.4. Chapter conclusion.....	150
IV.5. Bibliographic references.....	151

CHAPTER V: THE ROLE OF GLYCOL-TYPE ADDITIVES IN CoMo(P) CATALYSTS PREPARED FROM AN ADDITIVE-CONTAINING ALUMINA

153

V.1. Introduction.....	155
V.2. Characterization of the alumina support.....	155
V.2.1. Infrared analysis and surface acidity.....	156
V.2.2. Thermal behavior of the alumina support.....	157
V.3. Impact of the additive on the alumina support.....	158
V.3.1. Study of the additive structure after impregnation.....	158
V.3.2. Study of the additive-support interaction.....	159
V.3.3. Thermal behavior of the additive-impregnated alumina.....	161
V.3.4. Additive adsorption on alumina study.....	163
V.3.4.1. Excess impregnation.....	165
V.3.4.2. Incipient wetness impregnation.....	166
V.3.4.3. Additives adsorption mechanism on the alumina support.....	168

V.4. Impact of the additive on additive pre-impregnated CoMo(P) catalysts.....	169
V.4.1. Influence of the additive on the deposited cobalt species.....	169
V.4.2. Influence of the additive on the deposited molybdenum species.....	172
V.4.3. Metals and phosphorus distribution.....	174
V.4.4. Thermal behavior.....	175
V.5. Surface mechanism.....	176
V.6. Chapter conclusions.....	177
V.7. Bibliographic references.....	178

CHAPTER VI: THE ROLE OF GLYCOL-TYPE ADDITIVES ON CoMo(P) CATALYSTS PREPARED BY CO-IMPREGNATION 179

VI.1. Introduction.....	181
VI.2. Impact of the additive on the impregnation solutions.....	181
VI.2.1. Influence of the additive on the cobalt species in solution.....	182
VI.2.2. Influence of the additive on the molybdenum species in solution.....	183
VI.2.3. Influence of the additive on the phosphorus species in solution.....	184
VI.3. Impact of the additive on the catalysts prepared by co-impregnation.....	185
VI.3.1. Influence of the additive on the deposited cobalt and molybdenum species.....	185
VI.3.2. Metals and phosphorus distribution.....	187
VI.3.3. Thermal stability.....	188
VI.4. Surface mechanism.....	189
VI.5. Chapter conclusions.....	190
VI.6. Bibliographic references.....	191

CHAPTER VII: IMPACT OF THE ADDITIVE ON THE ACTIVATION STAGE AND EVALUATION OF CATALYTIC PERFORMANCES 193

VII.1. Introduction.....	195
VII.2. Impact of the additive on sulfided catalysts.....	195
VII.2.1. Influence of the additive on the final sulfided state (ex situ sulfidation).....	195
<i>VII.2.1.1. Influence of the additive on cobalt structure.....</i>	<i>196</i>
<i>VII.2.1.2. Influence of the additive on molybdenum structure.....</i>	<i>200</i>
<i>VII.2.1.3. Influence of the additive on the active phase morphology.....</i>	<i>208</i>

VII.2.2. Influence of the additive during the sulfidation stage (in situ sulfidation).....	210
VII.2.2.1. <i>Influence of the additive on cobalt structure</i>	210
VII.2.2.2. <i>Influence of the additive on molybdenum structure</i>	213
VII.2.3. Conclusion on the additive impact on the sulfidation stage.....	216
VII.3. Impact of the additive on catalytic performances.....	216
VII.3.1. Hydrogenation and isomerization reactions.....	217
VII.3.1.1. <i>Screening of additive-free dried and calcined CoMo(P) catalysts</i>	217
VII.3.1.2. <i>Influence of the additive on the hydrogenation and isomerization catalytic performances of dried and calcined catalysts</i>	218
VII.3.1.3. <i>Influence of the additive impregnation step location on the catalytic activity</i>	220
VII.3.1.4. <i>Influence of the additive loading on the catalytic activity</i>	222
VII.3.2. Hydrodesulfurization reaction.....	223
VII.3.3. Conclusion on the additive impact on the catalytic tests.....	224
VII.4. Chapter conclusion	225
VII.5. Bibliographic references.....	226

GENERAL CONCLUSION	227
---------------------------	------------

APPENDIX	229
-----------------	------------

APPENDIX A: Prepared catalysts properties.....	231
APPENDIX B: Additives liquid-gas equilibrium.....	235
APPENDIX C: Mathematical decomposition of experimental spectra.....	236
APPENDIX D: Tables Index.....	237
APPENDIX E: Figures Index.....	239

NOMENCLATURE AND ABBREVIATIONS

CATALYSTS, SAMPLES AND SOLUTIONS NOMENCLATURE

CoMo(P)	CoMo and CoMo(P) formulations
CoMo_AHM	CoMo prepared from ammonium heptamolybdate and cobalt nitrate
CoMo_HPA	CoMo prepared from cobalt molybdocobaltate salts
CoMoP(x)	CoMoP formulation, x refers to the P loading on the catalyst as wt% P_2O_5
Mo_AHM	Mo prepared from ammonium heptamolybdate
MoP(x)	MoP formulation, x refers to the P loading on the catalyst as wt% P_2O_5
P(x)	P sample, x refers to the P loading on the sample as wt% P_2O_5
name(d)	dried catalysts
name(c)	calcined catalysts
name(d)+TEG	TEG-containing catalyst prepared from a dried catalyst
name(c)+TEG	TEG-containing catalyst prepared from a calcined catalyst
name+TEG(PI)	TEG-containing catalyst prepared using the pre-impregnation method
name+TEG(CI)	TEG-containing catalyst prepared using the co-impregnation method

COMMON ABBREVIATIONS

AHM	Ammonium heptamolybdate
BET	Brunauer-Emmet-Teller
BJH	Brunauer-Jura-Harkins
CHNS	Carbon hydrogen nitrogen sulfur
DEGbe	Diethyleneglycol monobutyl ether
DMDS	Dimethyl disulfide
DRIFT	Diffuse reflectance infrared Fourier Transforms
DTG	Derivative thermogravimetry
EDS	Energy dispersive X-ray spectroscopy
EPMA	Electronic probe microanalysis
eV	Electron volt
EXAFS	Extend X-ray absorption fine structure
FT	Fourier Transforms
HDS	Hydrodesulfurization
HDT	Hydrotreatment
HYD	Hydrogenation
IFP	Institut Français du Pétrole
ISOM	Isomerization
LHSV	Liquid hourly space velocity
LOI	Lost on ignition
NMR	Nuclear magnetic resonance
TEG	Triethyleneglycol
TEM	Transmission electron microscopy
TGA	Thermo Gravimetric Analysis
wt%	Weight percentage
XANES	X-ray absorption near edge spectroscopy
XAS	X-ray absorption spectroscopy
XRD	X-ray diffraction
XRF	X-ray fluorescence
XPS	X-ray photoelectron spectroscopy

GENERAL INTRODUCTION

The growing public concern and future regulations regarding sulfur and nitrogen oxides emissions put a considerable pressure on the refining industry worldwide to produce cleaner fuels. The European Union is committed to reduce sulfur levels in diesel fuel down to 10 ppm in 2009, producing ultra-low-sulfur diesel (ULSD), instead of the 50 ppm set as target for 2005. At the same time, the European industry has to find more flexibility to face the growing demand for diesel against gasoline. Because of this, it becomes necessary to improve the hydrotreating (HDT) processes. It is actually the most important process of clean fuel production, allowing the elimination of heteroatoms (S, N, O and metals) from the petroleum charge and also adding hydrogen to unsaturated hydrocarbon molecules. Facing these challenges, several solutions may be adopted: to install new HDT reactors, to increase hydrogen pressure in reactors (which leads to technical problems and increases hydrogen consumption) or to improve catalysts performances by increasing their activity.

Heterogeneous catalysts have a growing importance in refining R&D since the introduction of catalysts in the industry. HDS catalysts performances have been regularly improving in the last 35 years allowing to achieve a 2.5 times increase in activity and a 6 times decrease in sulfur levels in fuels. The introduction of new catalyst formulations in general and the activation methods modifications have been responsible for this increase in performances. However, it is still necessary to keep researching in this area in order to achieve the 10 ppm sulfur level set for 2009.

Most common HDS catalysts nowadays are based on CoMoP or NiMoP formulations. Basically, they are sulfided metals from group VI.B (like Mo or W) promoted by Co or Ni, supported on a high specific surface area alumina. In the last 20 years, inorganic additives introduction, such as phosphorus, became quite usual in catalysts formulations, enhancing their performances.

A new development path in HDS is the use of organic additives. Those additives may be split into three categories: organosulfur molecules, chelating agents with the ability to complex the catalysts metal precursors and non chelating molecules, such as polyol or glycol ethers. The mechanisms lying behind organosulfur additives and chelating agents function are quite well described in academic literature. Why glycol-type additives have a positive effect on the catalytic activity has not been elucidated yet (chelating is very unlikely for glycols), but their use undoubtedly promotes the HDS activity of middle-distillate low pressure CoMo(P) catalysts. The aim of this thesis is thus to understand the role of glycol-type additives in the increase in catalytic performances they provide.

The bibliographic analysis reveals that gains in activity are observed independently of the additive introduction stage location: prior to, simultaneously, and sequentially to the metals precursor solution. Moreover, the sequential impregnation may be performed over dried or calcined catalysts. Although

catalytic improvements by additive impregnation are well established, contradictory explanations about the role of the additive are postulated. On the one hand, authors have concluded that glycol-type additives act as low temperature sulfidation inhibitors (below 200 °C). On the other hand, other studies reported increased low temperature sulfidation for the additive-containing catalysts. One possible origin of these discrepancies may arise from the nature of the oxide precursors used or to the additive impregnation stage location. The effect of the glycol-type additives may be different for each precursor, since different surface species are formed. For this reason, three types of alumina-supported catalysts are studied in the thesis: 1) a classic CoMo catalyst prepared from ammonium heptamolybdate and cobalt nitrate; 2) a CoMo catalyst prepared from cobalt molybdocobaltate heteropolycompounds; and 3) CoMoP catalysts with varying P/Mo molar ratios prepared from molybdenum trioxide, cobalt hydroxide and ortho-phosphoric acid. For the CoMoP catalysts, three P/Mo molar ratios are used: 1) 0.11, corresponding to the stoichiometry of the lacunary Keggin $\text{PMo}_9\text{O}_{34}\text{H}_6^{3-}$ heteropolyanions; 2) 0.40, corresponding to the stoichiometry of the $\text{P}_2\text{Mo}_5\text{O}_{23}^{6-}$ heteropolyanion; and 3) 0.57, where phosphorus is in excess with respects to the $\text{P}_2\text{Mo}_5\text{O}_{23}^{6-}$ heteropolyanion. The location of the additive introduction stage may also imply different phenomena since surface species may be different. This is the motivation to perform the additive impregnation directly on the alumina support, simultaneously with the metals precursor solution and sequentially on dried and calcined catalyst.

After the bibliographic study (Chapter I), the catalysts preparation and the experimental characterization methods and conditions are described in Chapter II.

Chapter III and IV are dedicated to study the additive impregnation of dried and calcined catalysts, respectively. More precisely, the objective is to determine if and how the additive modifies the surface species deposited on the catalysts surface.

Chapter V focuses on the impact of the additive when impregnated directly over the alumina support. This study comprises the effect of the additive on the properties and surface state of alumina, as well as the effect on the surface species after the impregnation of the metals precursor solution.

Chapter VI concerns the simultaneous impregnation of the additive and the impregnation of the metals precursor solution. The first part of the chapter studies the modifications induced by the additive on the impregnation solution. The second part focus on the surface species deposited on the catalysts surface after impregnation.

Finally, in Chapter VII, the impact of the additive during and after the sulfidation stage is studied, as well as the impact on the catalytic activities, as a function of the catalyst formulation and the location of the additive introduction stage.

CHAPTER I: BIBLIOGRAPHIC STUDY

I.1. Introduction.....	5
I.2. Hydrotreatments and hydrotreating catalysts	5
I.2.1. Petroleum refining and hydrotreatments (HDT).....	5
I.2.2. Middle distillates hydrotreatment catalysts.....	9
<i>I.2.2.1. Standard preparation method of CoMo catalysts.....</i>	<i>9</i>
<i>I.2.2.2. Characterization of the CoMo catalysts active phase</i>	<i>10</i>
I.2.3. Latest improvements in CoMo catalysts preparation.....	13
<i>I.2.3.1. Improvements in HDT catalysts impregnation solution</i>	<i>14</i>
<i>I.2.3.2. Improvements in HDT catalysts activation step</i>	<i>20</i>
I.2.4. Conclusions on hydrotreatments and hydrotreating catalysts.....	21
I.3. Glycol-type additives for hydrotreatment catalysts.....	22
I.3.1. Additive pre-impregnation of an alumina support.....	25
<i>I.3.1.1. Alumina structure and properties.....</i>	<i>25</i>
<i>I.3.1.2. Additive-alumina interactions</i>	<i>26</i>
I.3.2. Additive impregnation simultaneously with the active phase precursors	30
<i>I.3.2.1. Modification of the impregnation solution by glycol-type molecules.....</i>	<i>30</i>
I.3.3. Additive impregnation of CoMo(P) catalysts	31
<i>I.3.3.1. Impact of the nature of the additive</i>	<i>32</i>
<i>I.3.3.2. Impact of the additive loading</i>	<i>33</i>
<i>I.3.3.3. Modifications on the metal oxide phases due to additive</i>	<i>34</i>
<i>I.3.3.4. Interaction between the additive and phosphate in CoMoP calcined catalysts</i>	<i>35</i>
I.3.4. Impact of additives on sulfidation.....	36
I.3.5. Conclusions on the impregnation of CoMo(P) catalysts with glycol-type additives.....	38
I.4. Bibliographic study conclusions and thesis objectives	39
I.5. Bibliographic references.....	40

CHAPTER I: BIBLIOGRAPHIC STUDY

I.1. INTRODUCTION

In the first part of this bibliographic chapter, the general context of the present study is introduced, beginning by a brief description of a refinery, focusing on hydrotreatment in particular. Then the standard preparation of low-pressure middle-distillate hydrotreating CoMo catalysts is presented followed by a description of the different models proposed to describe CoMo catalysts active phase. Finally, recent breakthroughs regarding the chemistry involved in impregnation solutions as well as improvements in sulfidation treatments are described.

The second part of this chapter is dedicated to the additive impregnation of HDT catalysts by glycol-type additives. It is surprising to read in patents and academic literature that the additive impregnation promotes the HDS activity regardless of the step where the additive is introduced. Indeed, the additive introduction before or during the metals precursor solutions impregnation, after drying or calcination leads to improved performances. This study was therefore divided according to the different preparation steps where the additive is introduced: pre-impregnation of an alumina support, co-impregnation and impregnation over dried as well as post impregnation on calcined CoMo(P) catalysts. Finally, the presence of the additive on the catalyst during the activation step is studied.

In the end, the bibliographic chapter conclusions are followed by the objectives of this Ph.D. thesis.

I.2. HYDROTREATMENTS AND HYDROTREATING CATALYSTS

After describing the place of hydrotreatment in a refinery scheme, the various hydrotreatment processes are described, as well as the HDT catalysts going along with each product specifications.

I.2.1. PETROLEUM REFINING AND HYDROTREATMENTS (HDT)

Petroleum consists mainly in a mixture of hydrocarbons such as paraffins, aromatics and naphthenes (olefins and acetylenes are not present) and contains also small amounts of organic compounds with heteroatoms (like sulfur, nitrogen and oxygen) and metals (mostly nickel and vanadium). Crude oil also presents varied quantities of water, gas and inorganic compounds such as elemental sulfur and salts. Besides elemental composition, physical properties like density or viscosity may also be used to classify crude oils (d_4^{15} usually in the range 0.846 to 0.954 and viscosity from 10 up to 300 cSt) [1].

When crude oil arrives to a refinery, it is first processed to the atmospheric distillation, where compounds included in crude oil are separated according to their boiling points. Table I-1 presents the different fractions ordered by their boiling points.

Table I-1: Oil fractions classification.

Oil fractions	Range of ebullition temperatures (°C)
Gasoline	0 – 185
Kerosene	185 – 230
Diesel	230 – 370
Distillates	370 – 600
Residue	> 600

The aim of refining is to adapt raw fractions coming from the distillation tower to specifications required such as sulfur or nitrogen level as well as physical properties. Figure I-1 presents a very complete scheme of a modern refinery [2].

Hydrotreatment is by definition a catalytic treatment in presence of hydrogen that removes undesired compounds from a petroleum cut. The main impurities to remove are the sulfur-, nitrogen-, oxygen- and metal-containing compounds, as well as unsaturated hydrocarbon. The type and amount of those impurities varies with the boiling point of the raw fraction hydroprocessed. As may be seen from Table I-2, there are different hydrotreatment processes which may be characterized by the feedstocks they are processing and the product specifications that must be obtained. Process conditions and catalyst are thus chosen accordingly.

Depending on the desired compound to remove, the hydrotreatment procedure may consist in a hydrodesulfurization (HDS), hydrodenitrogenation (HDN), hydrodemetallization (HDM) and in some cases hidrodeoxygenation (HDO). If the desired compound is an unsaturated hydrocarbon, the hydrotreatment process involved is simply a hydrogenation (HYD). The choice of the catalyst formulation depends on the reaction one wants to promote, according to the stream feed composition and desired treatment. This choice is a function of the hydrogenation, acid properties of the catalyst. Table I-2 summarizes the different types of HDT applications in function of the feed stream.

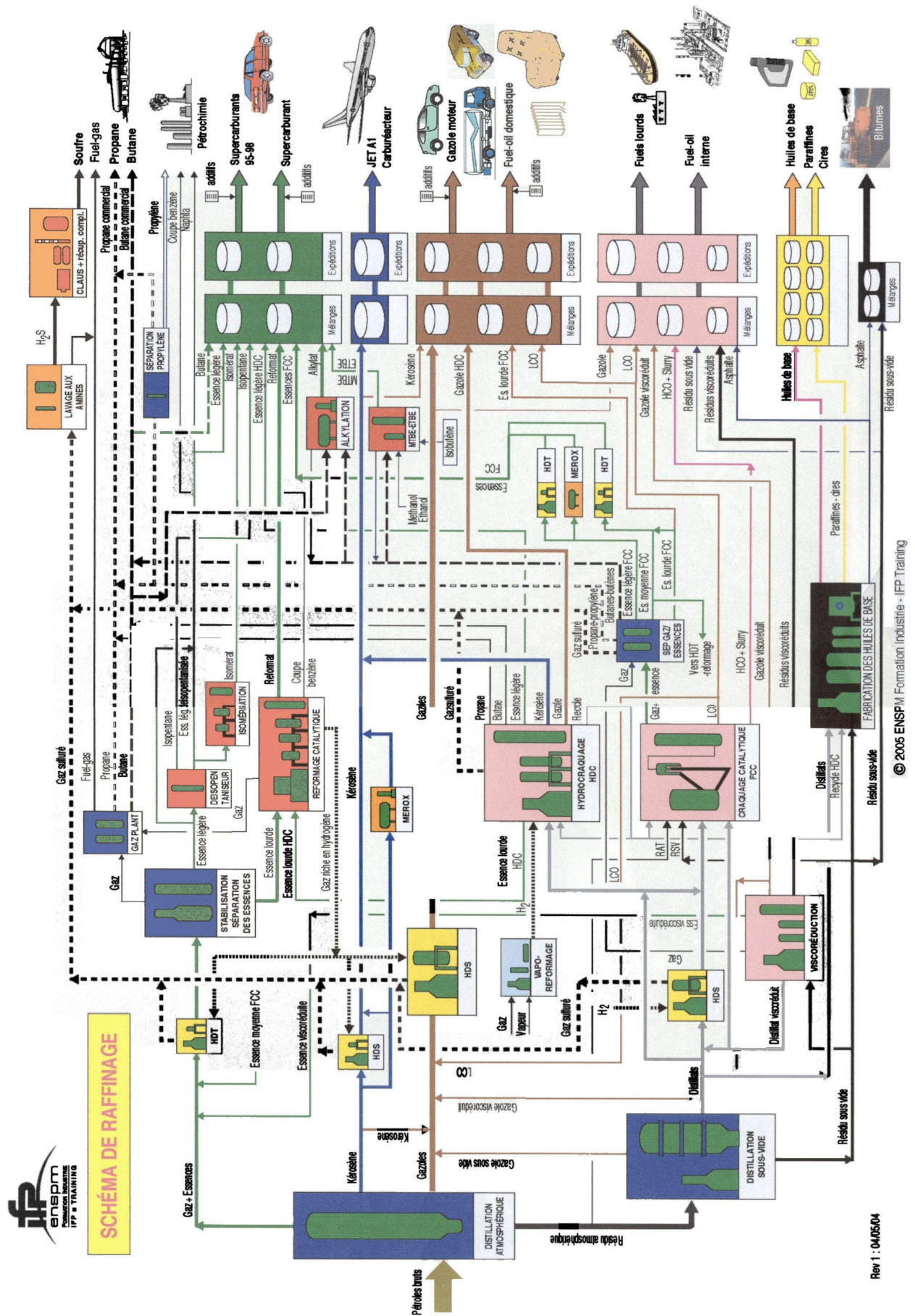


Figure I-1: Refinery scheme [2].

Table I-2: Most common HDT applications.

Operation	Stream	Purpose
HDT Naphtha	Light cut of AD	Desulfurization of LPG and Naphtha cut. Protection of reforming and isomerization catalysts.
HDS Kerosene	Kerosene cut from AD	Softening of kerosene cut in order to eliminate mercaptans from Jet A1 fuel.
HDS Diesel	Diesel cut from AD Diesel cut from FCC or Visbreaking VGO (vacuum gas oil)	Reducing sulfur levels from diesel fuel.
HDT of heavy cuts	AD residue and light VD cuts	Protection of conversion catalysts (HDM and HDS).
HDT gasoline FCC cut	Gasoline cut coming from FCC	Desulfurization while minimizing the loss in olefins.
HCK	VD distillates	Protection of hydroconversion catalysts (HDS, HDN and HYD).
	VD hydrotreated distillates	Decreasing molecular weight and increasing H/C ratio.

The decomposition of mercaptans, alcohols and aliphatic amines is quite easy. One of the most difficult molecules to desulfurize in middle distillates cuts is 4,6-dimethyldibenzothiophene (4,6-DMDBT) [3]. This compound is often used as a model reaction, as well as dimethyldibenzothiophene (DBT). The HDS mechanism of this sulfur-containing molecule is presented on Figure I-2. Two different pathways have been identified: the hydrogenation pathway (HYD) where hydrogenation comes before C-S bond breaking, and a direct desulfurization (DDS) pathway [3]. It is thus clear that the DDS/HYD selectivity of HDT catalysts will have a dramatic impact on their performances at ULSD (Ultra Low Sulfur Diesel, i.e. 10 ppm) level. Indeed, at that level, adsorption of refractory nitrogen species may inhibit the hydrogenation function. It is thus important to maintain an HDS activity via another route.

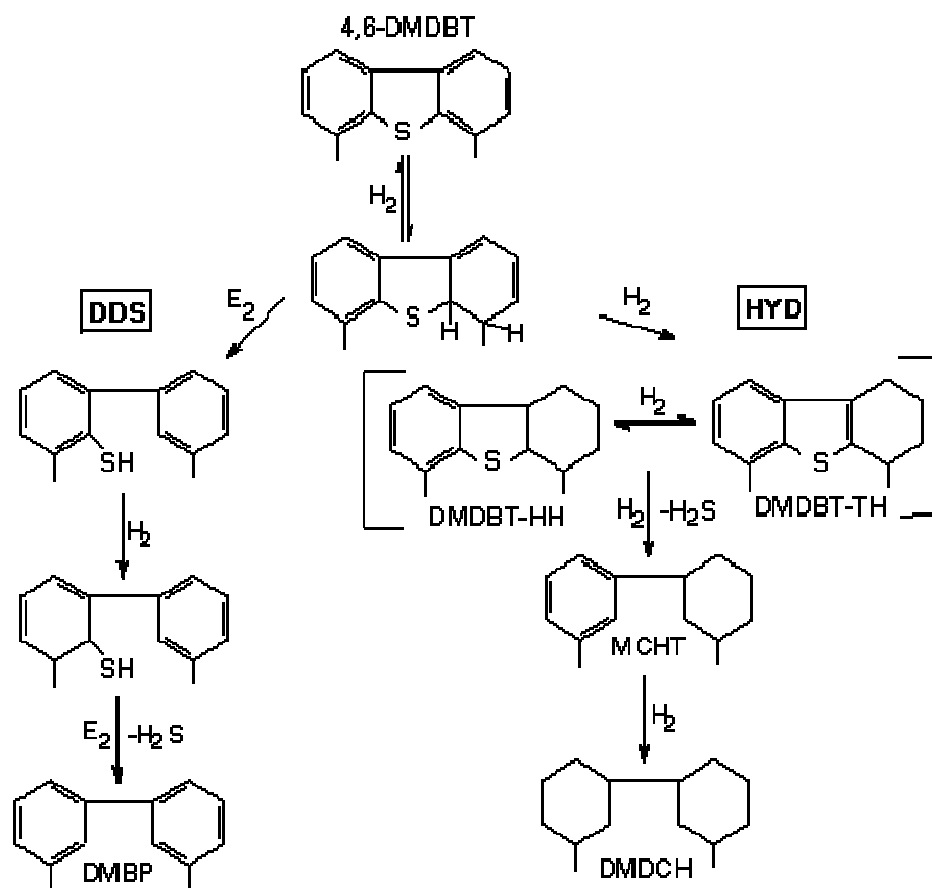


Figure I-2: Simplified reaction scheme of 4,6-DMDBT hydrodesulfurization (4,6 DMDBT stands for 4,6-dimethyldibenzothiophene; DMDBT-HH stands for 4-dimethylhexahydrodibenzothiophene; DMDBT-TH stands for 4-dimethyltetrahydrodibenzothiophene; DMBP for dimethylbiphenyl; MCHT for methylcyclohexyltoluene and DMDCH for dimethyldicyclohexane).

I.2.2. MIDDLE DISTILLATES HYDROTREATMENT CATALYSTS

Middle distillates hydrotreatment catalysts are CoMo or NiMo supported on a high surface alumina support. Due to their higher hydrogenation properties, NiMo catalysts are preferred for high-pressure processes (VGO hydrotreatment, HCK and FCC pretreatment). CoMo catalysts are favored at low pressure (30 to 40 bar). Since they are less active, CoMo catalysts were first successfully subjected to additive impregnation, which is why this part is dedicated to CoMo catalysts, their preparation and eventually the characterization and modeling of their active "CoMoS" phase.

I.2.2.1. Standard preparation method of CoMo catalysts

The classic common steps to prepare supported CoMo catalysts include the incipient wetness impregnation of a shaped support (extrudates) by a solution containing molybdenum and cobalt. The standard preparation method is historically based on solutions containing ammonium heptamolybdate (AHM) and cobalt nitrate. The impregnated solution volume is equal to the support pore volume to be impregnated. This impregnation step is followed by a maturation step, where the catalyst is stored at

room temperature in a water-saturated atmosphere for 24 hours. This step allows a good repartition of the precursors throughout the extrudates body. The next step consists in a drying step in order to remove the impregnation solvent and avoid steaming and thus sintering during the calcination step. The calcination step is subsequently carried out at temperatures ranging from 300 to 500 °C. A high temperature is indeed necessary to make sure that all counter ions, such as ammonium or nitrates are removed. Simultaneously, thermal treatments (drying and calcination) modify the structure of metal oxide precursors. The activation step may be carried out under gas phase ($\text{H}_2\text{S}/\text{H}_2$ mixture) or using spiked feeds containing a sulfiding agent such as for instance dimethyldisulfide.

I.2.2.2. Characterization of the CoMo catalysts active phase

Molybdenum-based HDT catalysts possess an active phase constituted by molybdenum disulfide. This phase is formed in the activation stage that transforms the initial oxide into a sulfide, MoS_2 . Molybdenum disulfide exhibits a layered structure: each sheet exhibit a chemically inert basal plane and two kinds of edge planes, Mo-edge and S-edge, exposing unsaturated Mo and S atoms. The cohesion between sheets is assured by Van de Waals forces. Several models have been developed to rationalize the description of supported MoS_2 nanoparticles (morphology, surface sites, location of promoter atoms, etc.) and their impact on the catalyst activity.

Rim-edge and geometric models

Daage and Chianelli [4] determined the HDS and HYD activities by changing the sheet size and stacking. They proposed a model in which only the base and top sheets are HYD actives (RIM crystallites). All sheets are active in HDS reactions. According to this model, when the stacking number increases, the HYD/HDS selectivity decreases. However, this model was developed based on results obtained for unpromoted bulk catalysts in dibenzothiophene (DBT) catalytic reaction, which limits its applicability.

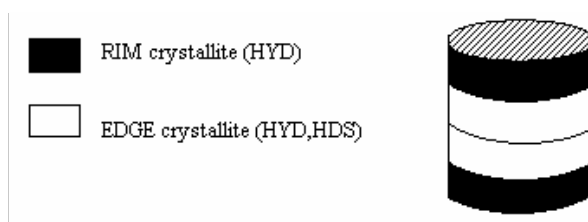


Figure I-3: RIM/EDGE model proposed by Daage and Chianelli [4].

The introduction of cobalt in conventional Mo catalysts has an intense effect on their activity: Mo and Co catalysts have a higher activity together than separately. Different models have been proposed to explain this synergetic effect: the monolayer model [5] in which cobalt is present in the alumina lattice and Mo-S species form a single-layer over the support; the contact synergy model [6,7]

proposing that CoS_x species are able to activate hydrogen that would create reduced centers on the neighboring MoS_2 ; or the intercalation model by Farragher and Cossee [8] assuming that cobalt atom is located between two MoS_2 sheets.

Nowadays, the "CoMoS" theory by Topsøe [9,10] is in general the admitted theory for the description of the HDS active phase in cobalt-promoted molybdenum catalysts. Topsøe used Mössbauer Emission Spectroscopy (MES) to find out that cobalt is present in several phases in a $\text{CoMo}/\text{Al}_2\text{O}_3$ catalyst and that their relative distribution depends on the preparation parameters and type of support. Three phases were identified using MES (Figure I-4). Cobalt atoms may be found in the alumina lattice, forming a CoAl_2O_4 phase. At high cobalt loadings, Co_9S_8 is detected in the alumina surface. Promoter atoms are located at the edges of a MoS_2 slab, forming a so-called "CoMoS" phase [11]. This decoration position was confirmed by NO adsorption studies [9]. Topsøe also observed a linear correlation between HDS activity and the amount of cobalt atoms present in the "CoMoS" phase [12], which suggests that this phase is the major responsible for the promotion effect in the catalytic activity.

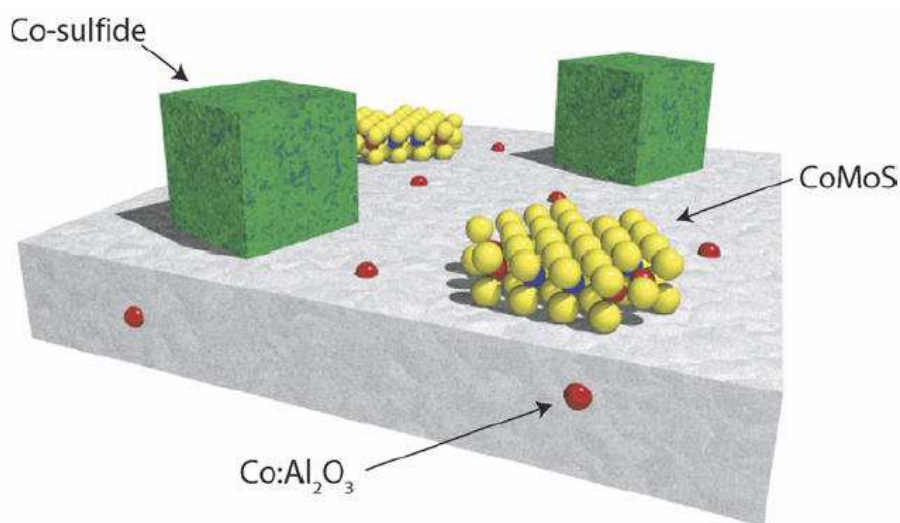


Figure I-4: Schematic representation of the different phases present in typical alumina-supported catalysts [10].

Kasztelan *et al.* [13] confronted several geometrical models with experimental data to elaborate a geometric model that describes the promoted crystallites structure according to the "CoMoS" phase theory (Figure I-5). In this model, promoter atoms substitute molybdenum atoms located on the edge planes.

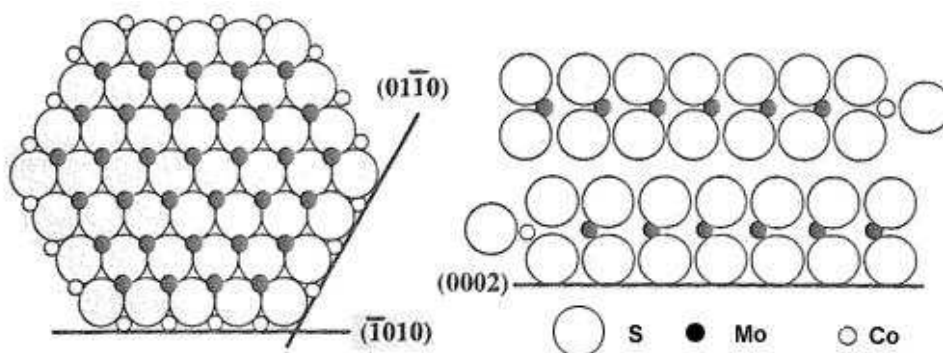


Figure I-5: Geometric Model for decorated MoS_2 proposed by Kasztelan *et al.* [13].

Towards a better understanding of the "CoMoS" mixed phase

Recently, modern techniques such as scanning tunneling microscopy (STM) and Density functional theory (DFT) have been applied to improve the description of "CoMoS" phase [14,15,16]. These works demonstrate that active phase morphology depends on the working conditions, namely, temperature and H_2S partial pressure. The morphology of MoS_2 nanoparticles is determined by the relative stability of two types of edge terminations, i.e., the S-edge and the Mo-edge. Using STM, for a gold (111) supported MoS_2 layer, Lauritsen *et al.* [14,15] observed dominant triangular crystallite morphology, which implies that one of the edges terminations is more stable than the other. Experimental and theoretical approaches conclude that the edge termination is a Mo-edge. Nevertheless, in HDS conditions, DFT calculations predict a hexagonal shape for the MoS_2 crystallite. The introduction of cobalt generates a hexagonal shape [16] even in STM analysis conditions (Figure I-6). Cobalt atoms have substituted molybdenum atoms at the S-edge. A tetrahedral environment of cobalt is produced if the outermost S atoms are assumed to be bridge-bonded monomer sulfur atoms in the Mo atoms plane. The proposed "CoMoS" model is thus seen to have intrinsic under-coordinated metal sites, which enable adsorption of the sulfur-containing reactants. For high sulfiding conditions, DFT calculations predicts that the promoter is found to be stable on both S- and Mo-edges.

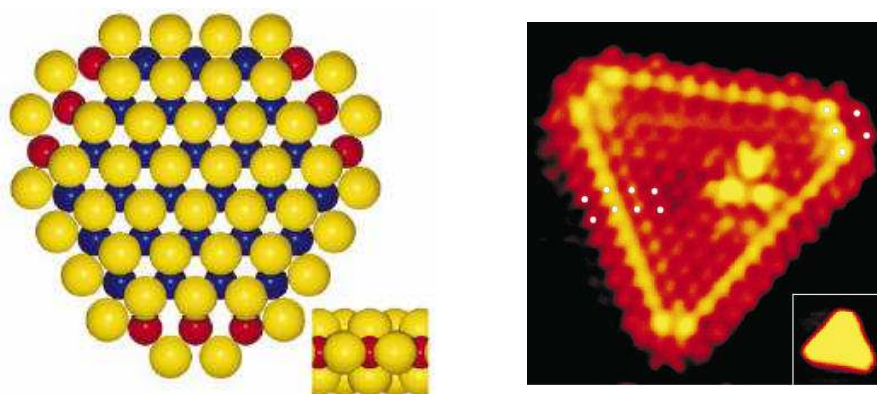


Figure I-6: MoS_2 crystallites decorated by cobalt - hexagonally truncated nanocluster. Left: schematic view. Right: STM image ($48\text{Å} \times 53\text{Å}$). Yellow: sulfur, blue: molybdenum; red: cobalt [14].

Type I and type II "CoMoS" phases

In the previous models, the presence of support is not explicitly taken into account. Topsøe *et al.* [11] described two different active phases in "CoMoS" structures, as a function of support-active phase interactions:

Type I "CoMoS" was historically defined by a low stacking (monolayer) and strong interactions with the support through Mo-O-Al bonds as well as poor coordination between Mo (and Co) and the sulfur atoms. This phase forms at lower sulfidation temperature.

Type II "CoMoS" was historically defined by high stacking and low interaction with the support (Van der Waals bonds). These sites are more active in thiophene HDS. This phase is obtained at high sulfidation temperatures or by using a complexing agent, like nitrotriacetic acid (NTA) [17]. The use of phosphates also promotes the formation of this type II phase.

A refinement on the notion of type I and II "CoMoS" phases was published by Hensen *et al.* [18]. A recent publication by Eijssbouts *et al.* [19] characterizes the MoS₂ morphology and promoter segregation in commercial type II CoMo HDT catalysts. Both articles agree that the preparation method defines the predominant active phase type. Hensen *et al.* concluded that type II phases could only be obtained by suppressing Mo-support interaction, which may be efficiently achieved by using an inert support material (like carbon) or a complexing agent. This support effect was studied by Bouwens *et al.* [20] that validated Hensen *et al.* hypothesis.

I.2.3. LATEST IMPROVEMENTS IN COMO CATALYSTS PREPARATION

The oxide state of the catalyst prior to sulfidation has been largely studied since the 60's [1]. Its morphology, structure and dispersion on the support have indeed a dramatic impact on the active phase characteristics and performances.

At low MoO₃ loadings, up to 6 wt% for an alumina with a specific surface area of 270 m²/g, molybdenum is mainly in monomolybdate form: MoO₄²⁻. In the 6 to 14 wt% range, heptamolybdates species Mo₇O₂₄⁶⁻ may be found. MoO₃ is formed when the alumina surface is saturated by polymolybdates species. These species adsorption is preferential because they strongly interact with alumina [1]. According to Bachelier *et al.* [21] the saturation of adsorbed Mo occurs at higher MoO₃ loadings and after this a higher amount of Mo will precipitate into large bulky islands (refractory to sulfidation), blocking to some extent the sulfidation of alumina-bonded Mo by steric hindrance. At high molybdenum loadings (MoO₃ ~ 18 wt%), sulfide CoMo catalysts may thus present bulky islands of unsulfided MoO_x (x = 2 or 3 depending of the extent of the reduction performed during the activation stage), as well as MoS₂ slabs. Therefore, all the introduced molybdenum is unfortunately not active for HDS. Limitations thus arise from molybdenum species solubility (precipitation) and poor dispersion of the active phase on the support, which may lead to sintering.

In terms of promoter loading, the ideal amount for HDS is a function of the VI.B group metal loading according to the promoter/metal atomic ratio. The ideal ratio is around 0.3 for the toluene hydrogenation case, which may be generalized for all HDS reactions. Figure I-7 shows that it is necessary to introduce excess cobalt to reach the Co/Mo atomic ratio of 0.3 on the active "CoMoS" phase. Indeed, other cobalt species may be found at the CoMo catalyst surface (Figure I-4), such as CoAl_2O_4 (dissolution/precipitation of alumina), CoMoO_4 (surface precipitation or sintering) at the oxide state and Co_9S_8 at the sulfide state (cobalt sulfidation occurs prior to molybdenum sulfidation).

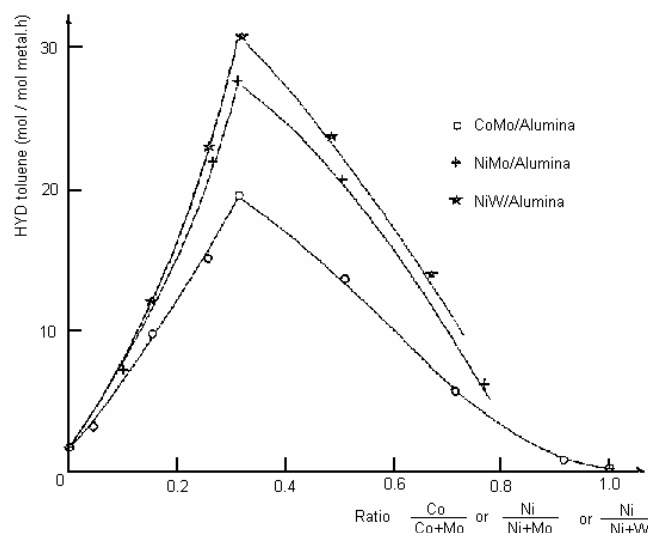


Figure I-7: Active phase composition influence in toluene HYD activity (60 bar, 350 °C, LHSV = 2 h⁻¹) [22].

Improvements have thus been made on each preparation step to reach more active catalysts with higher loadings. In order to increase dispersion and loading of the active phase, new impregnation solutions have been used. Improvements in activation procedures have also been made in order to efficiently sulfide ever more loaded catalysts.

I.2.3.1. Improvements in HDT catalysts impregnation solution

Heteropolyanions: definition and structure

Heteropolyanions (HPA) are inorganic anionic species: their structure is based on polyhedrons formed by a central atom surrounded by oxygen atoms. The central atom is usually a metal atom, but it also may be phosphorus or silicon. The most common polyhedrons contain four (tetrahedron) or six (octahedron) oxygen atoms. These MeO_4 and MeO_6 units share edges, corners or faces to form complex structures, called polyanions. When at least two types of metal are present (or one metal with P or Si), the term HPA is used. HPA may be found as a solid salt or dissolved in solution. In catalysis, such species may be observed in impregnation solution or deposited on support surface, as active phase precursors. For HDS catalyst, numerous molybdenum-based HPA are reported in literature and briefly described.

Keggin heteropolyanions - $\text{PMo}_{12}\text{O}_{40}^{3-}$

In the $\text{PMo}_{12}\text{O}_{40}^{3-}$ structure, the Mo/P ratio is equal to 12, where MoO_6 octahedrons are located around the central PO_4 tetrahedron (Figure I-8). Several isomers may exist. Other structures derived from the Keggin structure may be formed by removing one or three Mo octahedrons: $\text{PMo}_{11}\text{O}_{39}^{n-}$ and $\text{PMo}_9\text{O}_{34}^{n-}$. These two species exhibit vacancies and are called open-structure Keggin HPA. The vacancies may be filled with a second metal: for example, $\text{PMo}_{11}\text{O}_{39}^{11-}$ may interact with cobalt to give $\text{PCoMo}_{11}\text{O}_{40}^{7-}$.

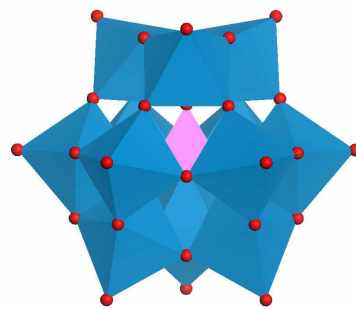


Figure I-8: Keggin heteropolyanion structure (isomer α).

Dawson Heteropolyanions – $\text{P}_2\text{Mo}_{18}\text{O}_{62}^{6-}$

The $\text{P}_2\text{Mo}_{18}\text{O}_{62}^{6-}$ structure corresponds to Mo/P ratio of 9. According to Pettersson *et al.* [23], the $\text{P}_2\text{Mo}_{18}\text{O}_{62}^{6-}$ anion is formed by dimerization of two $\text{PMo}_9\text{O}_{34}\text{H}_6^{3-}$ anions. In solution, this species is observed at acid pH and ^{31}P NMR showed that equilibrium exists between these mono- and dimeric forms [24].

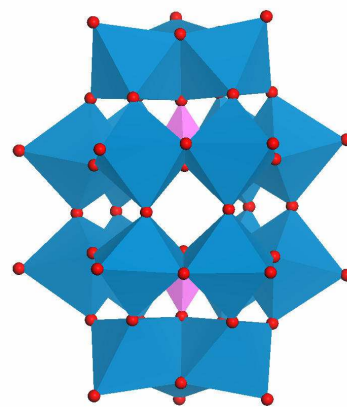


Figure I-9: Dawson heteropolyanion structure.

Diphosphopentamolybdate heteropolyanions – $\text{P}_2\text{Mo}_5\text{O}_{23}^{6-}$

This anion has a Mo/P ratio of 5/2. In this structure, 5 MoO_6 octahedrons form a ring bonded by the edges and 2 central PO_4 tetrahedrons (Figure I-10). The global structure is distorted. In solution, this heteropolycompound is the stable one when the molar ratio P/Mo is higher than 0.4.

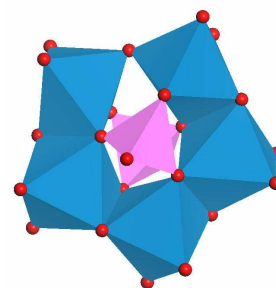


Figure I-10: Diphosphopentamolybdate heteropolyanion structure.

Anderson heteropolyanions – $\text{XMo}_6\text{O}_{24}\text{H}_6^{n-}$

In this anion, six MoO_6 octahedrons are organized in the same plane surrounding a central atom, X (Figure I-11), which may be trivalent (Co^{III} and Al^{III}) or bivalent (Ni^{II}). For instance, the $\text{CoMo}_6\text{O}_{24}\text{H}_6^{3-}$ structure, noted as CoMo_6 , may be synthesized in solution. Cobalt(II) may be used as counter ion position to form the $\text{Co}_{3/2}[\text{CoMo}_6\text{O}_{24}\text{H}_6]$ salt.

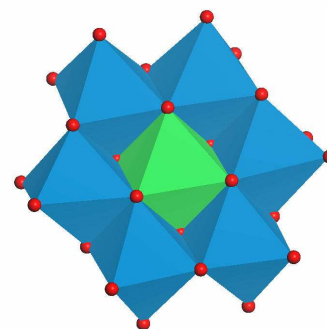


Figure I-11: Anderson heteropolyanion structure.

Dimeric molybdocobaltic species derived from the Anderson HPA exists when the element X is cobalt, $\text{Co}_2\text{Mo}_{10}\text{O}_{38}\text{H}_4^{6-}$ (Figure I-12), noted as $\text{Co}_2\text{Mo}_{10}$. Cobalt may also coordinate this dimeric HPA in a counter ion position to form the $\text{Co}_3[\text{Co}_2\text{Mo}_{10}\text{O}_{38}\text{H}_4]$ salt.

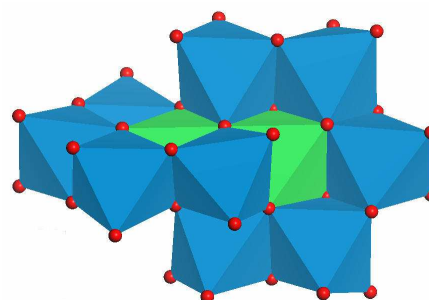


Figure I-12: $\text{Co}_2\text{Mo}_{10}\text{O}_{38}\text{H}_4^{6-}$ heteropolyanion structure.

Heteropolyanions characterization

The different types of HPA structures may be characterized by spectroscopic measurements. Reference data for pure HPA salt have been reported in literature: these data are used to detect the presence of HPA in impregnation solutions or on catalyst supports. For instance, a compilation of the IR and Raman spectra data for solid AlMo_6 , CoMo_6 and $\text{Co}_2\text{Mo}_{10}$ salts is presented in Table I-3.

Table I-3: IR and Raman data (cm^{-1}) of bulk Anderson salts [25].

Ammonium salts						Cobalt salts					
CoMo_6		$\text{Co}_2\text{Mo}_{10}$		AlMo_6		CoMo_6		$\text{Co}_2\text{Mo}_{10}$		AlMo_6	
Raman	IR	Raman	IR	Raman	IR	Raman	IR	Raman	IR	Raman	IR
949	941	954	944	947	947	952	946	957	940	947	1061
920	893	915	904	900	900	903	896	917	908	900	960
898	646	602	855	577	654	575	642	602	690	581	947
569	583	570	679	382	577	560	582	565	630	377	783
546	449	521	606	363	449	355	450	355	606	363	654

The different HPA containing phosphorus may be distinguished using IR, Raman spectroscopies or ^{31}P NMR (Table I-4).

Table I-4: ^{31}P NMR chemical shift data for reference compounds [30].

Assignment	Chemical shift [ppm]
$\text{PMo}_{12}\text{O}_{40}$	-3.9 to -4.5
$\text{P}_2\text{Mo}_{18}\text{O}_{62}$	-3.1
$\text{P}_2\text{Mo}_5\text{O}_{23}$	2.2
Hydrated AlPO_4	-19.2
AlPO_4	-25 to -30
Crystalline AlPO_4	-32
H_3PO_4	0

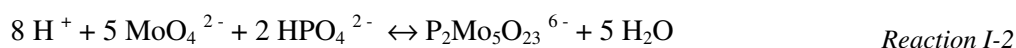
Uses of HPA in catalysts preparation

The presence of HPA on catalyst may result from chemical reaction during the impregnation stage. Carrier *et al.* [26] demonstrated by NMR and Raman spectroscopy that the Anderson anion $\text{Al}(\text{OH})_6\text{Mo}_6\text{O}_{18}^{3-}$, noted as AlMo_6 , is spontaneously formed when heptamolybdate solutions are contacted with alumina in the pH range 4-6, according to Reaction I-1. AlMo_6 structure is adsorbed on support surfaces and is destroyed during calcination around 240 °C [26].

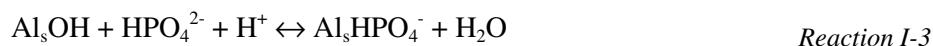


Phosphorus is one of the most widely used additives in alumina supported Mo-based HDT catalysts: patents [27] claim that this element improves the HDT catalyst performances. Several explanations have been proposed to explain the role of phosphorus [28]: the increase of the crystallites stacking due to phosphorus inclusion in alumina structure, decreasing the available surface for metal deposition, the strong interactions between phosphate anions strongly and alumina, leading to smaller interaction between oxide precursors and alumina and/or the formation of phosphorus-containing HPAs. Adding phosphorus in the impregnation solution, different HPA species, which have different Mo/P ratios, may be prepared. The nature of the predominant species depends on experimental conditions, like pH value, concentration of the different species and the solvent nature. The first advantage of these species is that they usually exhibit higher solubility than molybdate salts. The molybdenum loading of the catalyst may also be increased.

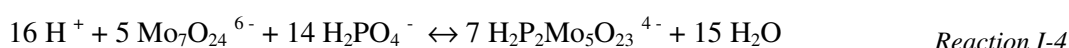
Several studies have been undertaken to analyze the behavior of the phosphorus-containing HPAs during the impregnation stage and their impact on the catalytic activity. The case of diphosphopentamolybdates solution is well documented. Cheng and Luthra [29] suggested the existence of an equilibrium between phosphate and molybdate while studying their competitive adsorption on alumina using NMR analysis.



When the solution arrives to the alumina pores, the hydroxyl groups from the alumina surface are progressively released upon absorption by ion exchange, causing the pH to rise. The equilibrium of Reaction I-2 is moved to the left and causes the diphosphopentamolybdate HPA decomposition. This decomposition is aided by the strong interaction between the phosphate ion and the alumina surface site:

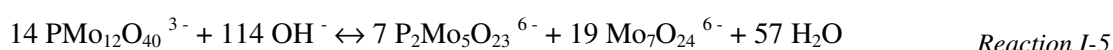


R. Iwamoto [30] proposed the Reaction I-4 in addition to Reaction I-2 to describe the decomposition of diphosphopentamolybdate ions:



At higher phosphate concentrations, the $\text{P}_2\text{Mo}_5\text{O}_{23}^{6-}$ anion adsorbs intact: the excess phosphate prevent the HPA decomposition. Griboval *et al.* [31] found that the optimum phosphorus loading was around 1.2 wt% P_2O_5 . This content corresponds to a P/Mo atomic ratio of diphosphopentamolybdate anion.

However, better activities were found with lower phosphorus content by using Keggin phosphomolybdates as starting material. Griboval *et al.* [32] suggested that the non-reduced cobalt HPA salt decomposes during impregnation because of the support tampon effect (high pH), but the reduced cobalt HPA salt stays unaltered. The non-reduced $\text{PMo}_{12}\text{O}_{40}^{3-}$ ion is stable up to pH 3 and the reduced $\text{PMo}_{12}\text{O}_{40}^{7-}$ up to pH 7. Iwamoto and Grimblot [30] proposed the $\text{PMo}_{12}\text{O}_{40}^{3-}$ decomposition at high pH as shown in Reaction I-5:



In opposition to the results described above, Cheng *et al.* [29] concluded by NMR observations that the non-reduced heteropolyanion keeps his structure unaltered until the drying stage because the phosphate group is enclosed by a shell of MoO_6 octahedra, avoiding this way phosphate interactions with alumina that would lead to the HPA destruction. Griboval *et al.* [33] obtained the same results and verified that the non-reduced HPA salt lead to more active catalysts. This increase in the catalytic performance is due to the oxomolybdates species deposition in close proximity to cobalt ions, which leads to a better decoration of MoS_2 crystallites during sulfidation. Besides, this close proximity decreases the cobalt atoms fraction involved in the formation of CoAl_2O_4 surface species [24]. In agreement with Pedro da Silva [34], Griboval *et al.* works also showed an increase in crystallites stacking.

Recently, de Jong group [35,36] conducted time and space-resolved Raman spectroscopic studies of CoMo/Al₂O₃ catalyst bodies. It was shown that, after impregnation with a solution containing H₂PMo₁₁CoO₄₀⁵⁻, the phosphate reaction with Al₂O₃ in acid pH forming an AlPO₄ phase, leads to the disintegration of this HPA complex inside the catalyst body. Hence, a decreasing phosphate concentration may be expected towards the pellet center. Heptamolybdate and hydrated Co(II) species are formed. The processes described above are summarized in Figure I-13, in which the different complexes distribution inside the alumina pellets after impregnation with the H₂PMo₁₁CoO₄₀⁵⁻ solution, is presented in a schematic manner. As a conclusion, the structure of deposited HPA is not homogeneous along the catalyst pellet.

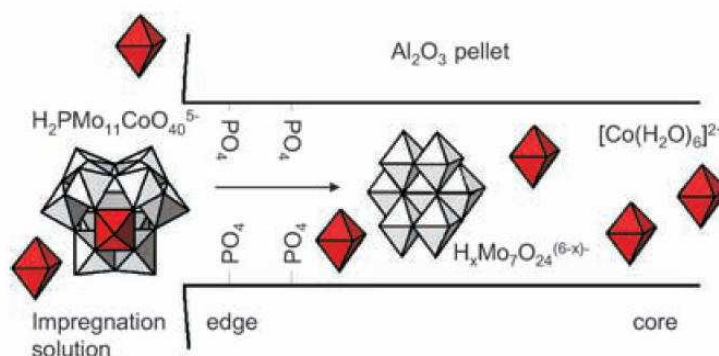


Figure I-13: Schematic representation of molybdenum and cobalt complexes distribution over an alumina after impregnation with an H₂PMo₁₁CoO₄₀⁵⁻ solution [35].

HPAs without phosphorous may be used as active phase precursors. Cabello *et al.* [37,38] prepared CoMo oxide precursors through equilibrium adsorption over alumina using ammonium salts of Anderson CoMo₆ heteropolyanions. The Co(III) species are not stable in solution but if they are in a HPA structure, they are kept preserved until the impregnation step. The activity for the thiophene HDS reaction conducted at 280 °C was similar to that of the traditional catalyst (9.3 wt% Mo and 1.8 wt% Co). Although the molybdenum content was equal in both catalysts, the cobalt content is lower in a HPA-route preparation (0.8 wt% Co) but the metallic dispersion over the support is comparatively higher. Cabello *et al.* [39] studied this dimeric compound, noted Co₂Mo₁₀, and found better thiophene HDS conversions than commercial CoMo and (NH₄)₃[CoMo₆O₂₄H₆] catalysts. DRIFT results showed that Co₂Mo₁₀ species are present in alumina surface. The authors suggested that the poor symmetry of Co₂Mo₁₀ causes a steric effect that enables the formation of small MoS₂ crystallites, favoring their stacking and decoration by Co atoms. These characteristics lead to a greater activity.

C. Martin [25] showed that catalysts using Co₃[Co₂Mo₁₀O₃₈H₄] salt as precursor are more active than conventional CoMo catalysts in thiophene HDS (+50%). The author suggests that the active phase dispersion is improved, due to the molybdenum and cobalt deposition on alumina surface in the same molecule. Moreover, the formation of the parasites crystalline phases is limited. The phosphoric acid introduction into a Co₃[Co₂Mo₁₀O₃₈H₄] solution lead to the initial HPA destruction to form diphosphopentamolybdate species.

Chelating agents

The first publications mentioning the use of chelating agents as additives in HDT catalysts date back to the 80's. For example, Shell Society patented in **EP0181035B1** [40] the use nitroacetic acid (NTA) for the improvement in catalytic performances of NiMo and CoMo catalysts supported on silica. The HYD, HDS and HDN activities were multiplied from 2 to 5 times.

In the academic literature, an important number of publications were written in the last two decades. Van Veen [41], Sun and Prins [42], Cattaneo [43], van Dillen [44] and Ohta [45] have worked on HDT catalysts made using chelating agents. The more usual chelating molecules are the NTA, diA-EDTA, 1,2-cyclohexanediamine-N,N,N',N'-tetraacetic (CyDTA) and ethylenediamine.

Mazoyer *et al.* [1] have demonstrated that diA-EDTA selectively form a stable complex with cobalt. These molecules also complex cobalt present in crystalline phases (CoMoO_4 , Co_3O_4) which are refractory to sulfiding. The "CoMoS" phase formation is thus improved. Cobalt complexation has another important consequence: it delays cobalt sulfidation to temperatures corresponding to molybdenum sulfidation temperatures, which results in cobalt and molybdenum cosulfidation and thus to more "CoMoS" phase.

Prins group [42] also described chelating agents as hard basic ligands that interact with coordinatively unsaturated Al^{3+} cations on the alumina surface: the strongest Lewis sites are no more available for metallic species absorption. Consequently, molybdenum is predominantly present as polyanions, which may be more easily sulfided than the MoO_4^{2-} anions into MoS_2 crystallites. Simultaneously, the Co^{2+} cations also interact more weakly with the alumina. They may be more efficiently sulfided and better distribute along the edges of the MoS_2 crystallites in the "CoMoS" phase. Finally, the smaller surface area and the weaker interaction of molybdenum with the support lead to a higher stacking of MoS_2 crystallites. The formation of the more active type II "CoMoS" phases is enhanced. Chelating agents have thus allowed an increase in catalytic activities by enhancing "CoMoS" phase formation.

I.2.3.2. Improvements in HDT catalysts activation step

The industrial HDT catalysts activation step is usually conducted in liquid phase. Sulfidation feedstocks, also called "spiked feeds", may include molecules such as dimethyldisulfide (DMDS), dimethylsulfide (DMS). These molecules decompose at low temperatures and quickly react with hydrogen to form H_2S on the catalyst surface. DMDS is nowadays widely used in refinery, mainly for safety reasons.

The introduction of highly loaded catalysts (>20 wt% MoO_3) and the use of different active phase precursors or chelating agents [46,47] have forced new paths for activation treatments such as a reduction of the sulfidation temperature or length, as well as variation in H_2S partial pressure. It may be clearly stated that the sulfidation procedure has a dramatic effect on the active phase morphology and consequently on the number of active sites formed. Indeed, Eijssbouts *et al.* [19] showed in a recent

study that the liquid-phase and gas-phase sulfiding procedures on various NiMoP and CoMoP alumina-supported commercial catalysts led to very different MoS₂ stacking numbers and lengths. Type I catalysts were obtained using H₂S/H₂ whereas type II catalysts were obtained from the same catalyst batch by using liquid-phase sulfidation. According to the authors, this must be related to the exothermicity of H₂S/H₂ sulfidation that is suppressed if a liquid is present and the heat of the sulfidation reaction is partly absorbed by the liquid phase. However, characterizations of spent HDT catalysts clearly evidenced the destruction of the mixed Co(Ni)MoS phase and an important segregation of NiS or Co₉S₈ when compared to the fresh sulfided catalyst.

T.S. Nguyen [48] studied the HDS catalytic performances of alumina-supported CoMo catalysts using liquid- and gas-phase sulfidations in presence of DMDS. The liquid-phase sulfidation lead to better performances in the HDS conversion of dibenzothiophene and 4,6-dibenzothiophene model molecules and in the real feed HDS conversion.

Various sulfidation organosulfur additives have also been used to improve the sulfidation rate as well as the mixed "CoMoS" yield. Organic compounds like alkylpolysulfurs (R-S_x-R) have thus been used in the activation of industrial catalysts. The decomposition products, which are formed at low temperature, lead to a better sulfidation and induce a higher active site density [49]. Chianelli *et al.* [50] even suggested that the active phase under working conditions could be a carbosulfide phase, CoMoS_{2-x}C_x.

More recently, Eijsbouts *et al.* also proposed a new process to obtain high performances for additive-containing HDT catalysts that may only be activated by using a gas phase sulfidation [46]. The catalyst is first impregnated with hydrotreated gas oil and then subjected to drying. Subsequently, the gas phase sulfidation is carried out using H₂S/H₂ mixture.

1.2.4. CONCLUSIONS ON HYDROTREATMENTS AND HYDROTREATING CATALYSTS

Hydrotreatment catalysts are designed according to feedstocks and required product specifications. For middle distilled hydrotreatment, the active phase consists in "CoMoS" phase dispersed on a high surface area alumina. Historically, CoMo catalysts were prepared using heptamolybdate and cobalt nitrate. Increasing active phase loading was difficult, due to the low solubility of these species, and the active phase dispersion was poor, which led to sintering and thus decreased the yield in active "CoMoS" phase. Many improvements have been carried out regarding impregnation solutions with the introduction of HPA species. These species have a high solubility and lead to high dispersion of the active phase. Higher active phase loading were thus reach and accordingly more efficient sulfidation procedures were implemented. By addition of a new preparation step, it was shown that further increases in activity were still possible. This new preparation step consists in catalysts impregnation by a glycol-type molecule and is described in the following section of this chapter.

I.3. GLYCOL-TYPE ADDITIVES FOR HYDROTREATMENT CATALYSTS

The use of glycol-type additives in HDT catalysts was first introduced by the Japanese Society Sumitomo Metal Mining in 1994. This society patented in the **EP0601722A1** [51] the use of typical HDS or HDN catalysts impregnated with organic molecules containing hydroxyl and ether functional groups. After this first patent, an important number of patents were taken by the Akzo Nobel [52,53,56], Albemarle Catalysts [47] and Sumitomo [54,55]. Differences between those patents arise from the preparation step where the additive is introduced. It is therefore interesting to decompose the present study according to the different additive impregnation stage locations as summarized on Figure I-14.

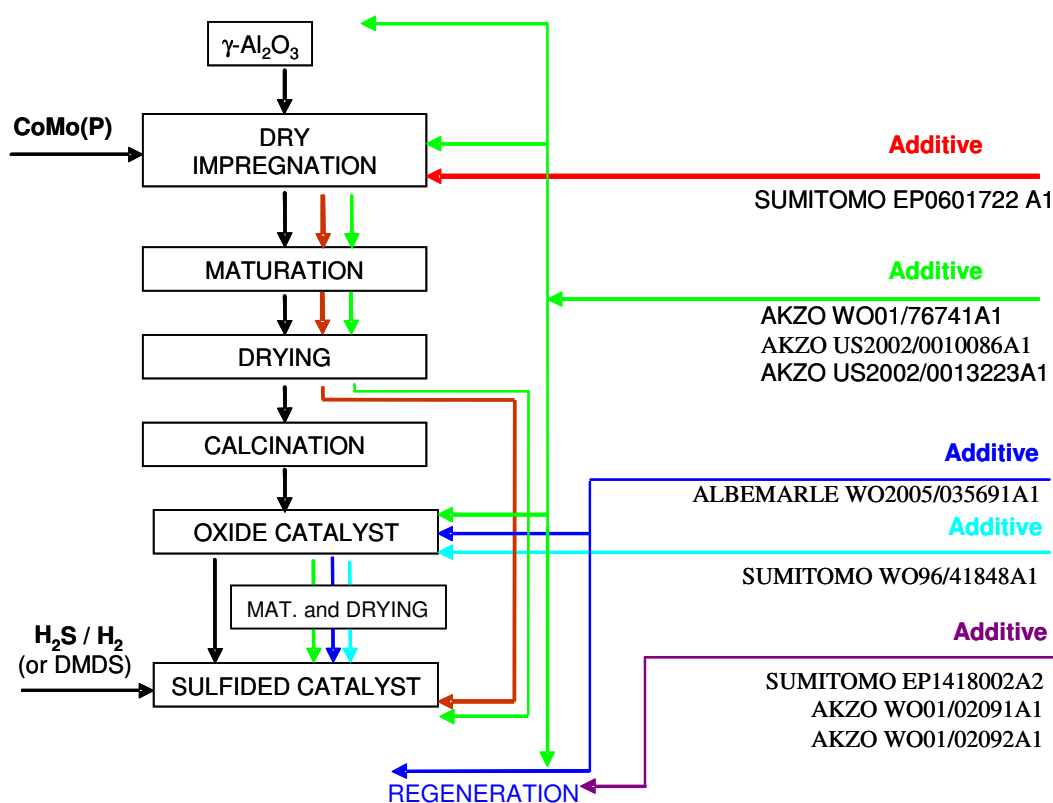


Figure I-14: Possible additive impregnation stage locations in the preparation method of CoMo(P) catalysts as described in patents: Sumitomo EP0601722A1 [51]; AKZO WO01/76741A1 [52]; AKZO US2002/0010086A1 [53]; Albemarle WO2005/035691A1 [47]; Sumitomo WO96/41848A1 [54]; Sumitomo EP141002A2 [55]; AKZO WO01/02091A1 [56].

Despite the important number of industrial patents deposited in the last decade, the academic literature concerning this subject is not as rich. Researchers like Nicosia and Prins [57,58,59,60], Mazoyer-Galliou [1] and R. Iwamoto [61] just recently began to study these type of HDT additives.

The glycol-type molecules suited for impregnation of HDT catalysts were first defined by Sumitomo in patents **EP0601722A1** [51] or **WO96/41848A1** [54]. This definition comprised molecules with 2 to 10 carbon atoms having at least two hydroxyl groups and ethers thereof. As claimed, suitable compounds include aliphatic alcohols, their ethers or polyethers. For polyethyleneglycol (PEG), a molecular weight between 200 and 600 is preferred [54]. Another family of compounds is composed of saccharides and polysaccharides.

The suggested alcohol or glycol additive amount in the above patents is preferably 0.05 to 3 fold of the total moles of the carried active metal elements and for the sugar groups 0.05 to 1 fold. If the loading exceeds the upper limits mentioned above, the impregnation solution viscosity becomes high enough to cause difficulty to this solution to penetrate into the alumina pores and a large quantity of organic compounds are present in the catalysts surface leading to detrimental coke formation when the catalyst is used. Recently, van Dillen *et al.* [44] proposed that the viscosity increase may have a beneficial effect on the active phase dispersion and, consequently on catalytic activity. According to the authors, since the solvent evaporation takes place at the exterior of the support particles, the capillary flow of the solution to its exterior surface may take place, thereby causing the production of eggshell catalysts, often with poor dispersion of the active phase. An increase in the impregnation solution viscosity suppresses the solution outward flow and leads to more uniform profiles over the support bodies.

The catalyst preparation method described in Sumitomo patents imposes that additive-containing catalysts should be dried at a temperature inferior to 200 °C without further calcination. This operation should remove the maximum amount of solvent (usually water) and at the same time prevent the evaporation or decomposition of the organic molecules adsorbed into the alumina pore surface. The drying step should be carried out under such conditions that at least 50% and more preferably 90% of the additive is still present in the catalyst after the drying step.

Table I-5: Glycol-type molecules suitable to be used as additives claimed in Sumitomo EP0601722A1 [51] and WO96/41848A1 [54].

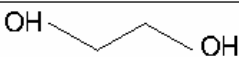
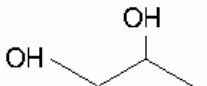
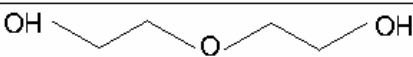
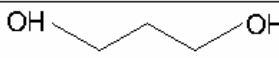

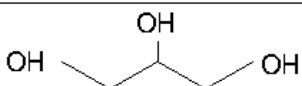

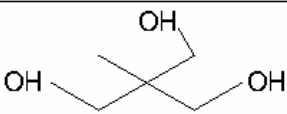
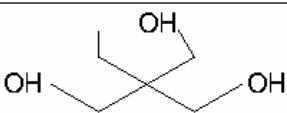
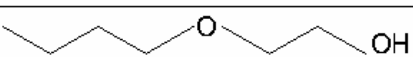
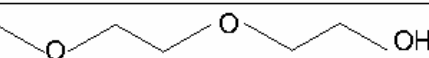
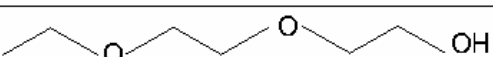
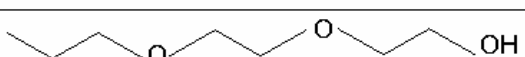
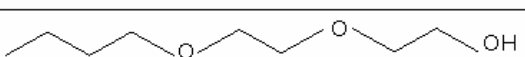
Type	Compound	Chemical structure
Alcohols and Ethers	Ethyleneglycol	
	Propyleneglycol	
	Diethyleneglycol	
	Trimethyleneglycol	
	Triethyleneglycol	
	Glycerin	
	Polyethyleneglycol	
	Trimethylolethane	
	Trimethylolpropane	
	Ethyleneglycol monobutyl ether	
	Diethyleneglycol monomethyl ether	
	Diethyleneglycol monoethyl ether	
	Diethyleneglycol monopropyl ether	
	Diethyleneglycol monobutyl ether	

Table I-6 provides information about the boiling point, melting point and decomposition temperature of the additives described in Table I-5 and their viscosities.

Table I-6: Additives normal boiling point (nbp), melting point (mp), decomposition temperatures (dec) and viscosities [51].

Type	Name	Boiling point (°C)	Viscosity at 20°C (cPs)
Alcohols and ethers	Ethyleneglycol	197	21
	Propyleneglycol	188-199	56
	Diethyleneglycol	245	38
	Trimethyleneglycol	210-211	56
	Triethyleneglycol	285	48
	Glycerin	290	1500
	Trimethylolethane	197 (mp)	solid
	Trimethylolpropane	295 (mp)	solid
	Ethyleneglycol monobutyl ether	171	3
	Diethyleneglycol monomethyl ether	193	4
	Diethyleneglycol monoethyl ether	203	4
	Diethyleneglycol monopropyl ether	213	5
	Diethyleneglycol monobutyl ether	231	6
	Polyethyleneglycol 200	200 (dec)	61
	Polyethyleneglycol 400	-	100
	Polyethyleneglycol 600	-	140

I.3.1. ADDITIVE PRE-IMPREGNATION OF AN ALUMINA SUPPORT

This form of additive introduction can be found in patents **WO01/76741A1** [52], **US2002/0010086A1** [53] and **US2002/0013223A1** deposited by Akzo Nobel. These patents are not exclusively dedicated to the additive impregnation directly over alumina but they comprise the impregnation prior to, subsequent to, or simultaneously to the incorporation of the metal components. In these patents, the subsequent additive impregnation is preferred. Because of it, the patent examples only refer to this type of additive impregnation, leaving the pre-impregnation case without any preparation or activity examples.

I.3.1.1. Alumina structure and properties

γ -alumina is a transition alumina, widely used as catalyst and catalyst support. The γ -alumina structure exhibits a centered cubic face sublattice of oxygen and the aluminum atom is located in the octahedral and tetrahedral interstices (about 25% of tetrahedral aluminum atoms). At the atomic level, the important point for catalytic applications is the nature and the termination of the exposed surfaces. Indeed, the surfaces sites are responsible of the acid-basic properties of γ -alumina, which govern the interaction between the support and the active phase precursors and/or the additives molecules. Different types of sites are usually distinguished:

- Coordinatively unsaturated (CUS) surface aluminum atoms, responsible of the Lewis acidity. Their acidic strength mainly depends on their coordination (Al^{III} , Al^{IV} and Al^{V}) and can be studied by absorption of basic probe molecules (carbon monoxide, pyridine, etc.).

- Coordinatively unsaturated (CUS) surface oxygen atoms that generate Lewis basicity. They are studied using acidic probe molecule absorption.

- Surface hydroxyl groups: as a function of their local environment, they may exhibit Lewis and Brønsted basicity ($\text{HO}-\mu_1$ groups) or Brønsted acidity ($\text{HO}-\mu_3$ groups). They may be monitored by probe molecule absorption or by their stretching frequencies (located between 3000 and 4000 cm^{-1} on IR spectrum). A recent assignment of the stretching frequency, based on DFT calculations, is given in Table I-7.

The nature and the surface concentration of these surface groups depend on experimental parameters, such as sample morphology and temperature pre-treatment.

Table I-7: IR attributions for alumina hydroxyl groups proposed by Digne [62].

Frequency interval (cm^{-1})	Attribution (cm^{-1})
3785-3800	$\text{Al}^{\text{IV}}-\mu_1\text{-OH}$ of (110)
3760-3780	$\text{Al}^{\text{VI}}-\mu_1\text{-OH}$ of (100)
3740-3745	$\text{Al}-\mu_1\text{-OH}$ of (111)
3730-3735	$\text{Al}^{\text{V}}-\mu_1\text{-OH}$ of (110)
3690-3710	$(\text{Al}^{\text{VI}})_2-\mu_2\text{-OH}$ of (110)
3590-3650	$(\text{Al}^{\text{VI}})_3-\mu_3\text{-OH}$ of (100)
below 3590	hydrogen bonded OH

I.3.1.2. Additive-alumina interactions

Textural properties of an additive-containing support

P. Mazoyer [1] looked for modifications in the textural properties of an additive-containing alumina by means of nitrogen physisorption. A γ -alumina was impregnated with an amount of DEGbe corresponding to a DEGbe/Mo molar ratio of 1 if using a CoMo catalyst with 15 wt% MoO_3 . The obtained BET surface area and pore volume are presented in Table I-8.

Table I-8: BET surface area and pore volume of an additive-free and additive-containing alumina [1].

Sample	BET Surface area [m^2/g]	Pore volume [cm^3/g]
$\gamma\text{-Al}_2\text{O}_3$	290	0.72
$\gamma\text{-Al}_2\text{O}_3 + \text{DEGbe}$	278	0.70

No significant modifications are observed in the textural properties after additive impregnation. Nevertheless, no information about the analysis pretreatment is provided and if the temperature chosen was higher than the additive boiling point, the additive might not be present on the support.

Additive-support interactions during impregnation

Tunius *et al.* [63] stated while studying DEGbe as a cosolvent that its affinity for the alumina surface is very low and that the extensive use of hydrogen-bonding possibilities is necessary for DEGbe adsorption to occur. These hydrogen-bonding possibilities are presented in Figure I-15.

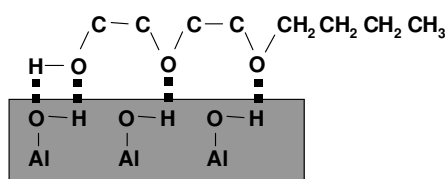
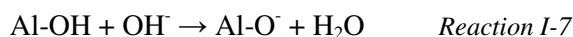


Figure I-15: Schematic representation of hydrogen-bonding possibilities for DEGbe adsorption over alumina [63].

Saravanan *et al.* [64] developed this reasoning by studying the equilibrium adsorption of polyethyleneglycol (PEG-10000) onto a α -alumina. It was observed that the adsorption density decreases as the pH increases. In the acidic pH region, the proton-donating capacity of the Al-OH groups is enhanced due to the addition of H^+ ions:



In this case, the surface of alumina will be charged more positively. Therefore, it is possible to expect higher interaction through hydrogen bonding between the surface aluminol groups and the ether oxygen atom from PEG. On the other hand, in the alkaline region, due to the addition of OH^- , the proton-donating capacity of Al-OH groups decreases, which may be represented as follows:



This increase in $Al-O^-$ species is unfavorable for hydrogen bonding. Further, in the alkaline region the positive surface of alumina decreases and becomes more negatively charged at high pH, resulting in electrostatic repulsion between alumina surface and PEG.

The authors refined Tunius conclusions upon glycol-type molecules adsorption over alumina and proposed 3 plausible interaction mechanisms (Figure I-16):

- 1) The interaction between the hydrogen of Al-OH groups and the ether oxygen of PEG through hydrogen-bonding (Brønsted acid-base interaction);

- 2) The coordination between Al^{3+} Lewis acidic sites and the basic ether oxygen of PEG (Lewis acid-base interaction);
- 3) Electrostatic interaction between positively charged alumina surface and feebly negatively charged ethoxy oxygen of PEG, below pH 9 (isoelectrical point of alumina, IEP).

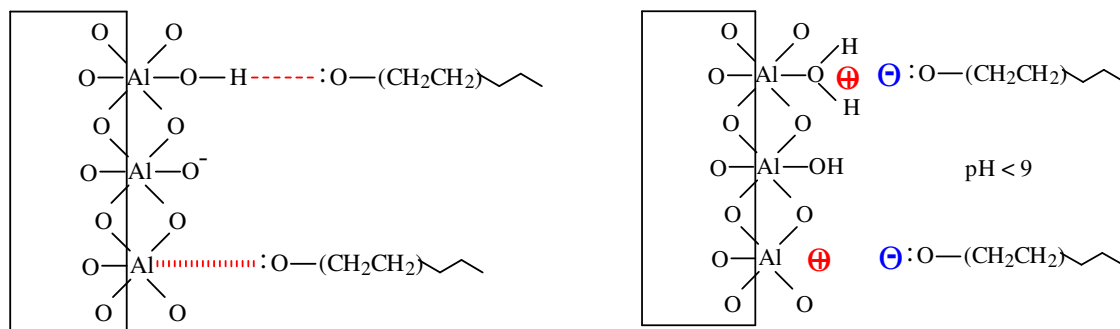


Figure I-16: Schematic representation of PEG adsorption mechanisms on alumina. Left: (---) Brønsted acid-base interaction, (||||) Lewis acid-base interaction; Right: Electrostatic interactions at $\text{pH} < 9$ [64].

P. Mazoyer [1] conducted adsorption studies by excess impregnation of alumina with DEGbe. The obtained suspension was stirred for 24 hours and the solid fraction was filtered, washed with water and dried. Different DEGbe concentrations were used (0.4 and 2.0 M) and the adsorbed quantity was measured by carbon analysis. The results showed low amounts of carbon (0.6 and 0.8 wt% C), which are very low compared to the geometric monolayer coverage of the support surface by DEGbe which was estimated at 22 wt%.

This study shows that DEGbe interactions may be weak interactions, involving hydrogen bonding and Lewis acid-base interaction. These interactions are greatly dependant of the solution pH and especially to its relative value compared to the IEP of alumina. This may be the reason why no adsorption isotherm has ever been reported.

Drying Impact on the additive-support interactions

Nicosia and Prins [57,58] conducted DRIFT studies on glycol-containing γ -alumina. The IR spectrum showed that TEG interacts with the basic alumina hydroxyl groups. During the drying step, dehydration occurs giving place to Al-O-C bonds at 1650 cm^{-1} (Figure I-17). In order to study the importance of OH groups in support-additive interactions, Prins decided to carry out the same experiment using triethyleneglycol dimethyl ether (TEG-DME) which does not have terminal hydroxyl groups to interact with alumina. The weak signal of this peak with TEG-DME confirms that TEG is interacting through OH terminal groups.

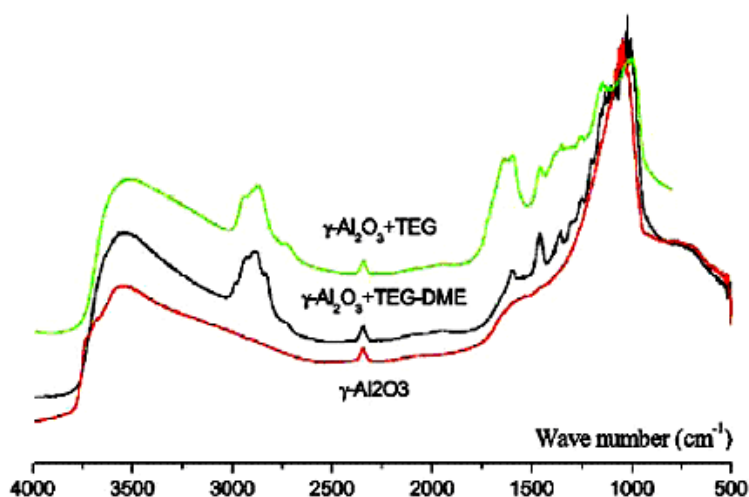


Figure I-17: DRIFT spectra of alumina impregnated with glycol-type additives [57].

Iwamoto *et al.* [61] studied the adsorption of PEG-400 onto γ -alumina. PEG400 was impregnated using incipient wetness impregnation. After impregnation, the catalysts were dried at 220°C in air for 3 hours. The XPS spectra of PEG/ Al_2O_3 showed that $I_{\text{C}}/I_{\text{Al}}$ increased linearly with increasing PEG addition up to 10 wt%. PEG probably occupies the alumina surface as a monolayer up to 10% but tends to aggregate above 10 wt% PEG addition. Iwamoto suggests that PEG addition blocks the aggregation of cobalt and molybdenum atoms and prevent sintering until the active metals interact with the alumina support during the calcination step.

Activity of catalysts prepared using an additive-containing support

Unfortunately, no example of such a catalyst could be found in patent literature. However, Nicosia and Prins [57,58] prepared, characterized and tested several additive-free and additive-containing CoMo(P)/ γ - Al_2O_3 catalysts. One of the studied catalysts (CoMoP/ γ - Al_2O_3 +TEG) was prepared by pre-impregnation of an alumina support with triethyleneglycol and two posterior impregnations with an impregnation solution containing MoO_3 , CoCO_3 and H_3PO_4 . The obtained catalytic activity in thiophene HDS at 350 °C for the pre-impregnated catalyst is lower than the CoMoP/ γ - Al_2O_3 catalyst prepared with the same precursor solution. However, due to the reduced total water pore volume of the additive-containing alumina, the double-impregnation method was used, possibly leading to a poorer dispersion of the molybdenum, cobalt and phosphorus atoms over the support. Moreover, the TEG pre-impregnated catalyst also presented a smaller BET surface area and a smaller pore volume than the CoMoP/ γ - Al_2O_3 catalyst (Table I-9). Notice that prior to textural analysis, the samples were outgassed at 200 °C at 10 Pa for one night, which possibly removed all the additive by evaporation.

Table I-9: BET surface area, pore volume, average pore diameter and thiophene HDS conversion for additive-free and TEG pre-impregnated CoMoP catalysts.

Catalyst	BET Surface area [m ² /g]	Pore volume [cm ³ /g]	Average pore diameter [nm]	Conversion/ (Mo+Co) (g ⁻¹)
CoMoP/ γ -Al ₂ O ₃	144	0.32	6.3	2.4
CoMoP/ γ -Al ₂ O ₃ +TEG	101	0.20	5.6	2.3

I.3.2. ADDITIVE IMPREGNATION SIMULTANEOUSLY WITH THE ACTIVE PHASE PRECURSORS

This section comprises the analysis of the industrial and academic literature concerning the impregnation of a support with a solution containing the glycol-type additive and the active phase precursors. In a first point, the obtained HDS catalytic activities are described and interpreted, followed by an analysis of the impregnation solution and finally, the interactions between the additive, the active phase precursor species and the support.

I.3.2.1. Modification of the impregnation solution by glycol-type molecules

Spectroscopic techniques have been used to study the interactions between molybdenum and cobalt aqueous species and the additive. UV-Visible spectroscopy (Figure I-18) [1] of an aqueous solution containing AHM, cobalt nitrate and diethyleneglycol monobutyl ether (DEGbe) showed no modifications in cobalt absorption band: no complex is formed between cobalt and DEGbe. In the triethyleneglycol (TEG) case, no modification in the UV-Visible bands was observed in presence or absence of the additive [48]. ¹³C NMR spectra directly showed that carbon was not in close proximity to cobalt [58], showing that TEG did not form chelates with Co²⁺ ions.

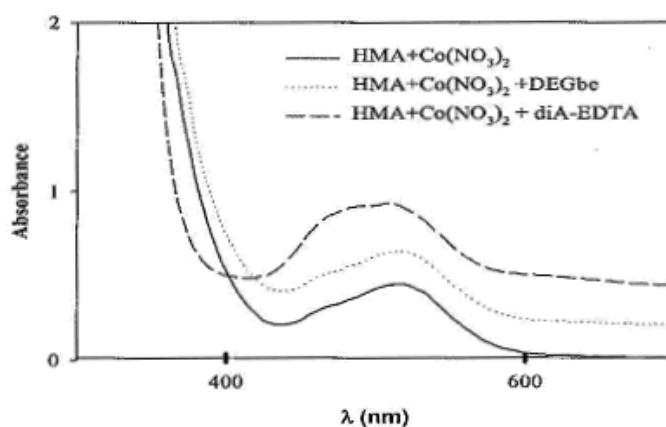


Figure I-18: UV-Visible spectra of AHM and cobalt nitrate aqueous solutions in presence of additives [1].

Laser Raman spectroscopy was used to characterize the impregnation solutions containing cobalt, molybdenum and phosphorus with and without TEG [57,58]. A common feature of the spectra (Figure I-19) are the bands arising at about 940 and 890 cm⁻¹: in both cases, P₂Mo₅O₂₃⁶⁻ is the predominant species. The peaks occurring at about 2978, 2886 and 1466 cm⁻¹ are due to the additives (CH

stretching, CH₂ scissoring and CH₂ twisting, respectively). The small shoulder observed at 830 cm⁻¹ for the solutions containing TEG is reported in the literature as a TEG C-O stretching vibration. Moreover, Mo K-edge EXAFS showed that the distances and coordination numbers of Mo-Mo and Mo-P shells correspond to the HP₂Mo₅O₂₃⁵⁻ anion, which is in agreement with their stoichiometry and loadings. Combining these results together with ³¹P NMR analysis, the authors concluded that the presence of TEG did not affect the HP₂Mo₅O₂₃⁵⁻ stability. Nevertheless, for AHM, cobalt nitrate and DEGbe solutions, a slight band shift for molybdenum UV absorption bands towards lower wavelengths was observed [1].

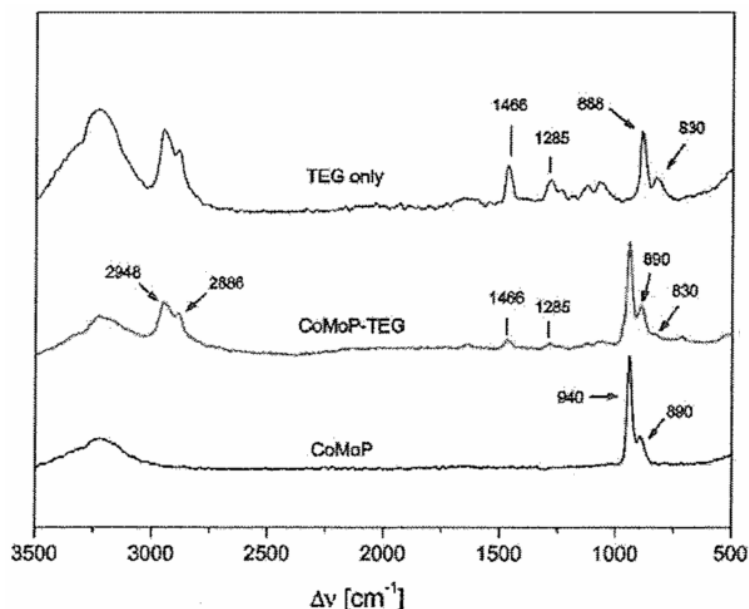


Figure I-19: Laser Raman spectra of CoMoP, CoMoP-TEG and TEG solutions [57].

As a conclusion, no clear evidence of interactions between molybdenum and/or cobalt species and additive molecules have been demonstrated in literature.

I.3.3. ADDITIVE IMPREGNATION OF CoMo(P) CATALYSTS

Patents EP0601722A1 [51] and WO96/41848A1 [54] are very rich in examples. All catalysts tested for HDS activity were presulfided using a Kuwait straight-run light gas oil (LGO) containing 1.15 wt% of sulfur and 68 ppm of nitrogen after adding 3 wt% butanethiol as a sulfiding agent. The presulfidation treatment and testing conditions for all the catalysts in this patent were carried out according to data reported in Table I-10.

These examples were analyzed in order to find out if there was a general trend in activity improvements as a function of the quantity or type of additive used.

Table I-10: Conditions for presulfidation and test reactions used in WO96/41848A1 [54] patent examples.

Sulfiding conditions		Test conditions	
Reaction temperature (°C)	316	Reaction temperature (°C)	330
Hydrogen pressure (kg/cm ²)	20	Hydrogen pressure (kg/cm ²)	30
LHSV (h ⁻¹)	1	LHSV (h ⁻¹)	2
Hydrogen / feed ratio (NI/I)	200	Hydrogen / feed ratio (NI/I)	300
Flowing time of oil (h)	18	Flowing time of oil (h)	168

I.3.3.1. Impact of the nature of the additive

Sumitomo patent WO96/41848A1 [54] that claims the additive impregnation over a calcined catalyst, presents a wide variety of additives. The active phase precursors are the same used in Sumitomo patent EP0601722A1 [51] and the reference catalyst has a Co/Mo/P loading of 3/22/4 wt%, respectively (expressed as oxides). This reference catalyst was used as a starting material for the additive impregnation in the HDS catalytic tests. The catalysts were dried for 16 hours at 100 °C and calcined for 3 hours at 400 °C in air. To be tested, 15 ml of each catalyst was brought into a continuous reactor and tested using two kinds of feeds: (A) Kuwait straight-run LGO containing 1.15 wt% S and 68 ppm N; (B) Feed A to which 3 wt% butanediol has been added.

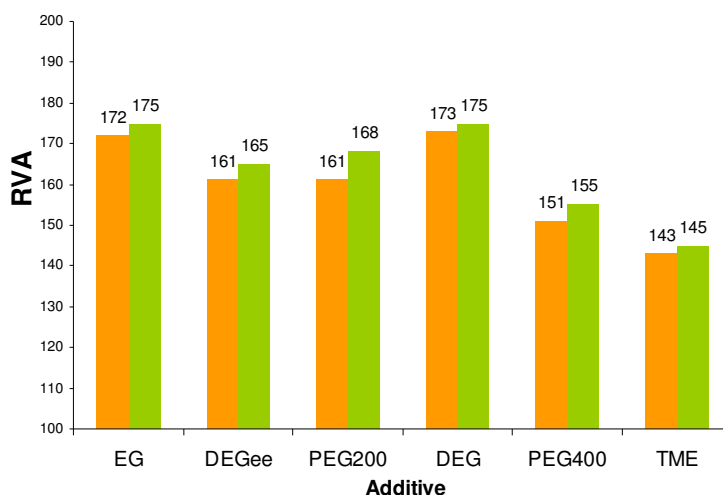


Figure I-20: HDS activities for additive-containing CoMoP catalysts (4/22/3 wt% reported to their oxides and using a γ -alumina) presented in Sumitomo WO96/41848A1 [54] examples. The first column (orange) refers to Feed A and the second column (green) to Feed B.

RVA stands for relative value of rate constant; EG for ethyleneglycol; DEGe for diethyleneglycol monoethyl ether; PEG200 for polyethyleneglycol (MW200); DEG for diethyleneglycol; PEG400 for polyethyleneglycol (MW400) and TME for trimethylol ethane.

The first conclusion that comes out from Figure I-20 is that the butanediol introduction in the oil feed slightly increases the HDS activity. For the catalysts impregnated with PEG400 and TME, their lower activities are probably related to a chemical steric effect occurring during the adsorption into the support or to the reduced accessibility to the microporosity due to the fact that these molecules are the biggest among all additives (PEG400 molecule is a polymer and therefore has a considerable length and TME molecule is too ramified, occupying a considerable volume). However, it is hard to draw a conclusion on the relation between the nature of the additive and the increase in activity observed.

I.3.3.2. Impact of the additive loading

In Sumitomo patent WO96/41848A1 [54], several catalysts were prepared varying the additive to metals molar ratio and the preparation method. Looking at the diethyleneglycol example in the patent, it is possible to plot Figure I-21.

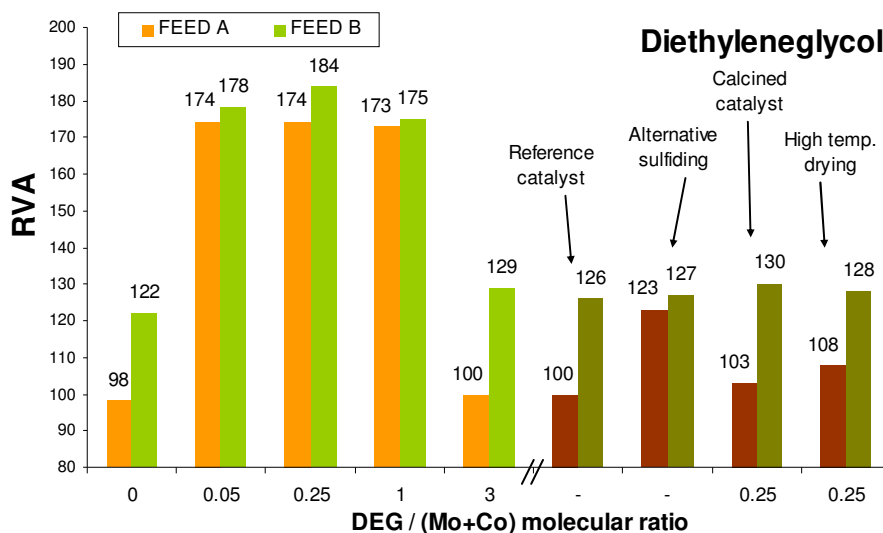


Figure I-21: HDS activities for DEG-impregnated CoMoP catalysts (4/22/3 wt% reported to their oxides and using a γ -alumina) presented in Sumitomo WO96/41848A1 [54] patent examples.

The catalyst prepared with no additive was only contacted with water. Its activity is much lower than that of catalysts impregnated with glycol ethers. This means that the increase in activity observed is specific to the chemical compound introduced and not to the catalyst water content. The alternative sulfiding was conducted using TNPS as described in Japanese patent publication No. H-479701. The calcined catalyst was submitted to a treatment at 400 °C for 3 hours. The first column of each catalyst (orange and brown) refers to Feed A and the second column (green and dark green) to Feed B.

Figure I-21 also shows that the additive loading effect on HDS activity is negligible for Feed B. Contrary to Sumitomo patent EP0601722A1 [51] (co-impregnation), this maximum changes for each additive and at the same time changes with the feed used. It may also be seen from all the catalysts examples that the butanediol presence (Feed B) increases the activity up to 30%. This improvement may be due to the presence of an organic compound during the sulfidation stage or to the alcohol functions in that molecule. In the catalysts with a DEG/(Mo+Co) molar ratio between 0.05 and 1.00, the catalytic enhancement due to butanediol presence is comprised in the enhancement induced by the glycol-type additive.

I.3.3.3. Modifications on the metal oxide phases due to additive

According to Nicosia and Prins [57,58,59], the main role of TEG is achieved during the support impregnation. By reacting with the basic Al-OH surface sites of the alumina support, glycol hinders the interaction between the active phase precursors and the alumina support. In this way, glycol favors the formation of oxidic clusters with a very high Co/Mo atomic ratio. Therefore, more cobalt atoms are available to promote the MoS₂ crystallites formed upon sulfidation. This hypothesis is valid when speaking about co-impregnation but fails to explain the role of the additives in the HDS catalytic performances if the additive impregnation is conducted on the calcined catalysts, where the metal phase is already deposited over the alumina.

Concerning the Mo speciation, using UV-Visible diffuse reflectance spectroscopy, Nicosia *et al.* [57,58] found in all samples containing phosphorus a broad band centered at 225 nm that is common to both tetrahedral and octahedral coordinated molybdenum atoms. A much broader signal centered at 325 nm was observed for CoMoP/SiO₂, CoMoP-TEG/Al₂O₃, CoMoP_std-TEG/Al₂O₃ and CoMoP/Al₂O₃+TEG catalysts. This signal is typical for octahedrally coordinated molybdenum species. However, in the CoMoP-TEG-DME/Al₂O₃ spectrum, this signal is weak and in CoMoP/Al₂O₃ and CoMoP_std/Al₂O₃ spectra, it is absent. This suggests that the absence of glycols leads to tetrahedral geometry for molybdenum species. In the same study, Mo X-ray absorption of CoMoP-TEG/Al₂O₃ and CoMoP/Al₂O₃+TEG catalysts showed that the diphosphopentamolybdate structure formed in solution was retained in the support and that a tetrahedral geometry is observed for molybdenum species. Therefore, both UV-Visible reflectance and Mo X-ray absorption suggest the existence of tetrahedral and octahedral coordination for molybdenum in presence of glycol.

In a more recent study, Nicosia and Prins [60] used a ZnMoP/Al₂O₃ catalyst to conduct ³¹P NMR analysis because the paramagnetic cobalt is known to shift and broaden the NMR signal. The use of diamagnetic zinc avoids this paramagnetic effect, thus allowing a better spectrum interpretation. These catalysts were prepared without any final calcination. The main result that came out of the NMR spectrum of the TEG-impregnated ZnMoP/Al₂O₃ catalyst was the existence of more than 80% molybdenum diphosphate and about 15% of PMo₁₂O₄₀³⁻ species, also confirmed by Raman analysis. In this way, the ³¹P NMR results on Zn-containing samples showed that TEG not only favors the phosphate group polymerization and as the P/Mo ratio decreases, leads to Keggin PMo₁₂O₄₀³⁻ HPAs formation.

It is possible to establish a relation between the increase of the DDS selectivity and the amount of "CoMoS" phase. In fact, the DDS mechanism is favored by the presence of "CoMoS" sites [3]. This result suggests that the additive-containing CoMo catalyst, due to the additives, has a superior number of promoted sites than the reference CoMo catalyst, and consequently, has a beneficial effect upon the overall HDS activity.

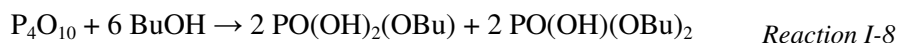
Thermal analyses were carried out by Mazoyer on calcined catalysts impregnated with DEGbe [1]. It was found out that desorption occurs at lower temperatures for the additive-containing calcined

catalyst (180 °C) than for the additive-containing support (260 °C). On the other hand, the thermal decomposition begins at the same temperature for both systems but it ends later in the support case. These results suggest that the additive is not fixed in the same way in the presence of an oxide phase than into the support. The presence of metals or their oxide phase decrease the strength of the interaction between DEGbe and alumina or DEGbe is preferentially fixed over the active phase precursor.

No significant modifications in molybdenum and cobalt oxidation degree were shown by XPS analysis in the study conducted by P. Mazoyer [1] using impregnation on oxide commercial catalysts.

I.3.3.4. Interaction between the additive and phosphate in CoMoP calcined catalysts

A reaction between alcohols and phosphates was reported in several studies [65,66]. Livage *et al.* [65] described a reaction between solid P_4O_{10} and alcohols to form phosphate esters:



The reaction products were identified by the ^{31}P NMR spectrum of the resulting solution. At room temperature, the mixture shows a complex signal (coming from the dimeric species) but it becomes simpler after heating for 24 hours under reflux, making possible to identify $PO(OH)_2(OBu)$, $PO(OH)(OBu)_2$ and $PO(OH)_3$ – phosphoric acid (Figure I-22). According to the author, adding water to the P_2O_5 -ROH mixture displaces the reaction towards the formation of more hydrolyzed species, the more hydrolyzed one being phosphoric acid.

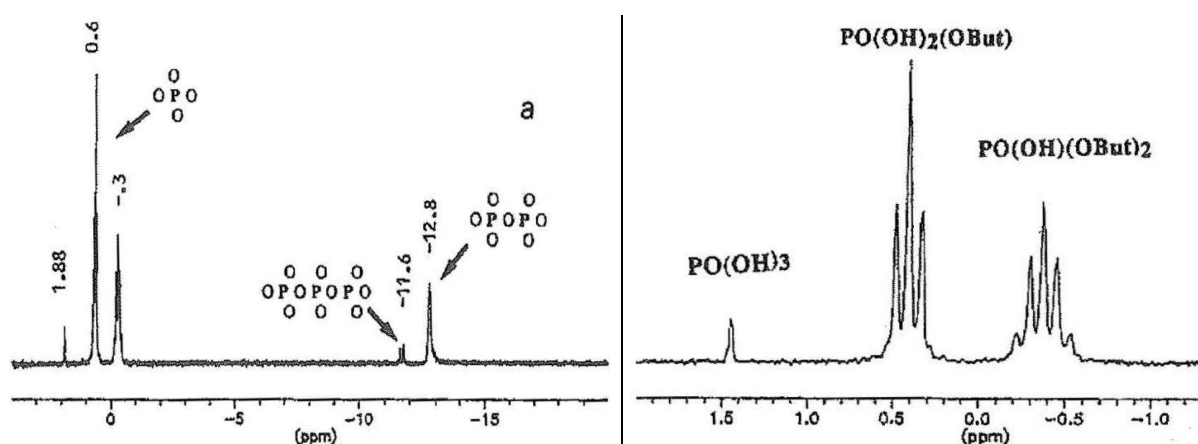


Figure I-22: Liquid State ^{31}P NMR spectra of P_2O_5 dissolved in *n*-butanol: (a) after 24 h at room temperature; (b) after 24 h under reflux [65].

The (a) spectrum shows two groups of peaks. The first one is made of three signals: a singlet ($\delta=1.88$ ppm), a triplet ($\delta=0.63$ ppm) and a quintet ($\delta=-0.28$ ppm). They may be assigned to monomeric $PO(OH)_{3-x}(OR)_x$ species with $x=0, 1$ and 2 respectively. The second group of peaks around

$\delta = -12$ ppm should correspond to dimeric ($\delta = -12.8$ ppm) and trimeric ($\delta = -11.6$ ppm) phosphate species. For CoMoP catalysts, a possible reactivity between phosphorus surface species (Al-PO₄ groups, P₂O₅ crystallites, etc.) and alcoholic additives have to be explored.

I.3.4. IMPACT OF ADDITIVES ON SULFIDATION

EXAFS and XPS characterization have been used in academic studies to determine the role of glycol-type additives during the sulfidation step. Results obtained are not always consistent and are confronted below.

Geantet and Mazoyer have studied the sulfidation of industrial calcined CoMo and CoMoP catalysts post-impregnated with DEGbe [1,67]. They have shown, by elemental analysis on bare and DEGbe-impregnated CoMo/alumina catalysts that the global sulfidation is delayed at temperatures inferior to 150 °C (Figure I-23).

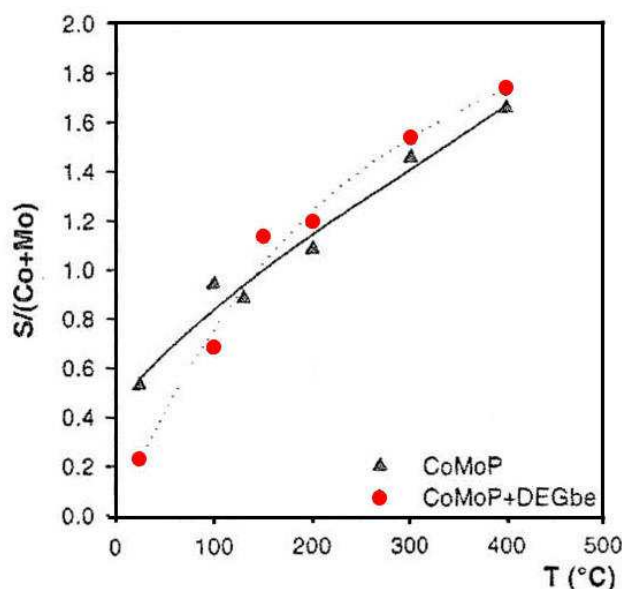


Figure I-23: Sulfidation degree of additive-free and additive-containing calcined CoMoP catalysts [1].

To this extent, the effect obtained is similar to that of chelating agents, as described in section I.2.3.1. Indeed, in catalysts impregnated with chelating agents, molybdenum sulfidation is found unchanged whereas cobalt sulfidation is delayed. A smaller temperature gap between cobalt and molybdenum sulfidations leads to smaller amounts of Co₉S₈ and thus higher yields in "CoMoS". Geantet and Mazoyer thus studied by EXAFS the sulfidation of molybdenum and cobalt at their K-edge. They found out that both metals sulfidation were delayed at temperatures inferior to 150 °C [67]. XPS analyses were performed after sulfidation at 100 °C and 400 °C, using the same CoMo and DEGbe-CoMo catalysts. Identical spectra were obtained at 400 °C, whereas at 100 °C, the amount of Mo⁶⁺ assigned to molybdenum oxide was higher in the additive-containing catalyst. No interpretation

was given by Geantet and Mazoyer for the sulfidation delay they observed at low temperature for additive-containing catalysts.

Similar results were obtained by T.S. Nguyen while using a calcined CoMo catalyst post-impregnated with TEG [48]: elemental analysis revealed that the global sulfidation is delayed at temperatures below 150 °C and the XAS study showed that the sulfidation of both metals is slowed down. The author proposed that TEG acted as a low temperature sulfidation inhibitor (below 150 °C).

On the other hand, Prins and Nicosia studied CoMo and CoMoP catalysts prepared by co-impregnation of the metal salts and TEG, drying without any further calcination or thermal treatment except during sulfidation [58]. They concluded from their EXAFS study that sulfidation at low temperatures was faster for additive-containing dried CoMo and CoMoP catalysts. Results are reported on Figure I-24 and clearly show that uncalcined CoMo catalysts prepared using cobalt nitrate have much higher sulfidation temperatures than the corresponding additive-containing catalysts as well as the CoMoP catalysts.

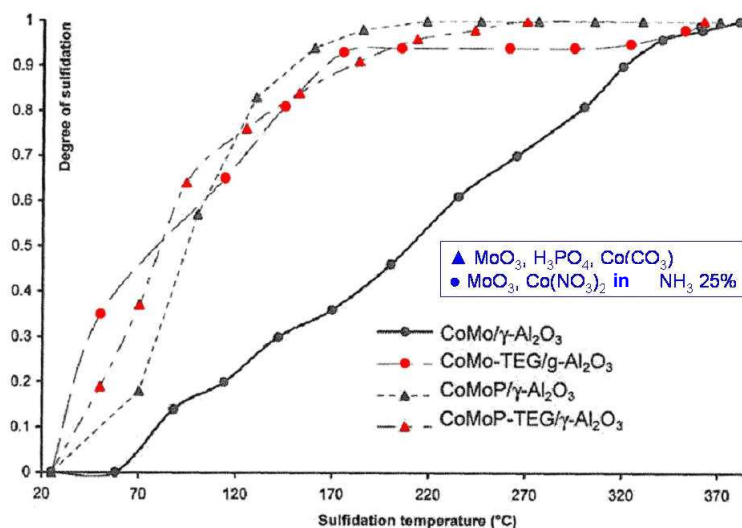


Figure I-24: Sulfidation degree for additive-free and additive-containing CoMo(P) catalysts [59].

According to Nicosia and Prins, TEG-support interactions may decrease cobalt-alumina and molybdenum heteropolyanions-support interactions and thus favor the precipitation of large cobalt-diphosphopentamolybdate islands over the support, resulting in the formation of more "CoMoS" phase. Although the sulfidation degrees measured (Figure I-24) demonstrate that the additive-containing catalysts are sulfided at lower temperatures, the assumption of a higher "CoMoS" yield is unfortunately not supported by XPS results.

Results obtained by those teams stress the importance of the preparation method used to prepare catalysts with or without the additive, as well as the respective order of the additive impregnation and the different preparation steps. In fact, by impregnating calcined catalysts, P. Mazoyer and T.S. Nguyen made sure that ammonium and nitrate were nicely removed and did not delay sulfidation. On the contrary, Prins and Nicosia introduced the additive in the impregnation solution (MoO_3 and

Co(NO₃)₂ for the CoMo catalyst) and subsequently could not do any thermal treatment without removing the additive and losing its beneficial effect. This may account for the late sulfidation of the reference CoMo catalyst used by Prins and Nicosia for which nitrates must be decomposed prior to sulfiding. The difference between additive-containing catalysts and reference catalysts becomes smaller towards the end of the sulfidation. It is noteworthy also to note that Prins and Nicosia explanation of the role of TEG in the increase in catalytic activity may not apply to calcined catalysts, where the interaction between metal oxides and the support are already strong. Since both additive impregnation methods lead to improved catalytic performances, several effects may combine to explain glycol ether effect in the improvement of catalytic performances of CoMo(P) catalysts.

I.3.5. CONCLUSIONS ON THE IMPREGNATION OF CoMo(P) CATALYSTS WITH GLYCOL-TYPE ADDITIVES

All academic studies and industrial patents described show an increase in catalytic activity regardless of the stage where the glycol-type agent is added. This fact suggests that the role of these molecules may be the sum of several combined effects.

Regarding support additive impregnation prior to introduction of molybdenum and cobalt precursors, Prins *et al.* have explained that additive may prevent cobalt-alumina interaction, and thus increase the "CoMoS" phase content. However, this does not account for additive post-impregnation of calcined CoMoP catalysts, since strong interactions already exist between oxide phases and alumina. However, Mazoyer and Nguyen did observe better performances for additive-containing calcined CoMo(P) catalysts. This means that another phenomenon may also be implied in the obtained performances.

The academic literature clearly shows that the additives do not form chelates with the metal active phase precursor components, neither induce changes in the metals oxidation degree in solution or upon impregnation. The study of monometallic systems conducted by P. Mazoyer showed that the additives have no beneficial effect in the performances of the catalysts. This result suggests that the action of the additive is probably related to cobalt promotion of MoS₂ slabs, thus acting upon the nature or the number of the promoted sites. TEM analysis of additive-free and additive-containing CoMo/Al₂O₃ sulfided samples showed that additive does not change the MoS₂ crystallites length or stacking, which suggests that the role of the additives is finally related to the quantity and dispersion of these crystallites over the support.

On a different issue, the phosphorus eggshell profile described by de Jong group [35] becomes more uniform when an additive is introduced due to a solubilization effect. The diffraction peak that appears in all additive-containing samples at about 6 and 8°, regardless of the additive impregnation step location, assigned by Mazoyer to an Anderson HPA suggests that Mo- and Co-containing phases are redissolved to form these species.

The most visible effect of the additive occurs during sulfidation. Mazoyer and Nguyen works showed that the additives slow down the sulfidation below 150 °C, leading to better sulfidation rates and consequently better HDS activities. The results from Nicosia and Prins show exactly the opposite, suggesting that the sulfidation is indeed faster and occurs at lower temperatures. However, the active phase precursors used for the reference CoMo catalyst do not allow a valid comparison.

I.4. BIBLIOGRAPHIC STUDY CONCLUSIONS AND THESIS

OBJECTIVES

The study conducted by P. Mazoyer on monometallic systems suggested that the role of the additive is possibly related to the cobalt promotion effect. From the study of bimetallic calcined CoMo systems, the same author finally concluded that the increase of activity comes from an increase of the quality (better promoted) and quantity (more crystallites and better dispersed) of the MoS₂ active phase, resulting from a slow down in the sulfidation step induced by the additive. On the other hand, Nicosia and Prins studied additive-containing catalysts prepared by co-impregnation. They showed that the additive may prevent HPA decomposition. They explained this phenomenon by the formation of an additive layer between the active phase precursors and the support. This leads to the deposition of cobalt and molybdenum in close proximity, improving the "CoMoS" yield. However, this hypothesis fails to explain the HYD activity enhancement verified for calcined catalysts, where the active phase precursors are in strong interaction with alumina. The XRD peak claimed in Sumitomo additive patents around 6 and 8°, regardless of the additive impregnation step location, assigned by Mazoyer to an Anderson HPA suggests that Mo- and Co-containing phases are redissolved to form these species. This hypothesis was not explored in the bibliography and could be one of the key-points behind the enhanced observed HDS activity.

The objective of this thesis is therefore to understand the mechanisms that may explain the activity increase in additive-containing catalysts. For this purpose, a correlation must be established between physico-chemical characteristics of CoMo and CoMoP catalysts at the different preparation steps and their performances. This work has thus been divided according to the place where additive impregnation is performed and the last chapter is dedicated to study the additive impact on the sulfidation stage and on catalytic performances.

Key-points

1. *Mazoyer proposed that the additive impregnation of calcined catalysts leads to an increase of the promotion and dispersion of the "CoMoS" phase, as a consequence of the sulfidation inhibition at low temperatures induced by the additive.*
2. *Prins group proposed while using co-impregnation, that the additive prevents HPA decomposition by the formation of an additive layer between the active phase precursors and the support.*

I.5. BIBLIOGRAPHIC REFERENCES

- 1 P. Mazoyer-Galliou, Ph.D. thesis Université Claude Bernard - Lyon 1, **1998**.
- 2 Formation *Bruts-Raffinage-Produits-Schemas de Fabrication*, ENSPM Formation Industrie, **2005**.
- 3 F. Bataille, J.L. Lemberton, P. Michaud, G. Pérot, M. Vrinat, M. Lemaire, E. Schulz, M. Breysse and S. Kasztelan, J. Catal. 191, 409, **2000**.
- 4 M. Daage and R. Chianelli, J. Catal. 149, 414, **1994**.
- 5 F. Massoth, J. Catal. 36, 164, **1975**.
- 6 B. Delmon, Bull. Soc. Chim. Belg. 88, 979, **1979**.
- 7 P. Grange and X. Vanhaeren, Catal. Today 36, 375, **1997**.
- 8 A.L. Farragher, P. Cossee, in: J.W. Hightower (Ed.), *Proceedings of the Fifth International Congress on Catalysis*, Amsterdam, 1301, **1973**.
- 9 H. Topsøe and N.Y. Topsøe, J. Catal. 84, 386, **1983**.
- 10 H. Topsøe, Appl. Catal. A: General 322, 8, **2008**.
- 11 H. Topsøe, B. Clausen and F.E. Massoth, *Catalysis: Science and Technology* vol. 11, Springer-Verlag, Berlin, **1996**.
- 12 H. Topsøe and B. Clausen, Appl. Catal. 25, 273, **1986**.
- 13 S. Kasztelan, H. Toulhoat, J. Grimblot and J.P. Bonnelle, Appl. Catal. 13, 127, **1984**.
- 14 J.V. Lauritsen, S. Helveg; E. Lægsgaard, I. Stensgaard, B.S. Clausen, H. Topsøe and F. Besenbacher, J. Catal. 197, 1, **2001**.
- 15 J.V. Lauritsen, M. Bollinger, E. Lægsgaard, K. Jacobsen, J. Nørskov, B. Clausen, H. Topsøe and F. Besenbacher, J. Catal. 221, 510, **2004**.
- 16 H. Schweiger, P. Raybaud, G. Kresse and H. Toulhoat, J. Catal. 207, 76, **2002**.
- 17 J.A.R. van Veen, E. Gerkema, A. van der Kraan and A. Knoester, J. Chem. Soc. Chem. Commun. 1684, **1987**.
- 18 E.J.M. Hensen, V.H.J. de Beer, J.A.R. van Veen and R.A. van Santen, Catal. Lett. 84, 1, 59, **2002**.
- 19 S. Eijsbouts, L.C.A. van den Oetelaar and R.R. van Puijenbroek, J. Catal. 229, 352, **2005**.
- 20 S. Bouwens, F. van Zon, M. Dijk, A. van der Kraan, V. de Beer, J. van Veen and D. Koningsberger, J. Catal. 146, 375, **1994**.
- 21 J. Bachelier, M. Tilliette, J. Duchet and D. Cornet, J. Catal. 76, 300, **1982**.
- 22 P. Leprince, *Le Raffinage du Pétrole: Procédés de Transformation - IFP*, Éditions Technip, Paris, **1998**.
- 23 L. Patterson, I. Anderson and L.O. Öhman, Inorg. Chem. 25, 4726, **1986**.
- 24 A. Griboval, P. Blanchard; E. Payen, M. Fournier and J.L. Dubois, Cat. Today 45, 277, **1998**.
- 25 C. Martin, Ph.D. thesis Université des Sciences et Technologies de Lille, **2003**.
- 26 X. Carrier, J. Lambert and M. Che, J. Am. Chem. Soc. 119, 10137, **1997**.
- 27 EP0469675B1, **1996**.

-
- 28 S.K. Maity, J. Ancheyta, L. Soberanis and R. Alonso, Appl. Catal. A: General 253, 125, **2003**.
- 29 W. Cheng and N. Luthra, J. Catal. 109, 163, **1988**.
- 30 R. Iwamoto and J. Grimblot, *Advances in Catalysis*, vol. 44, 417, **2000**.
- 31 A. Griboval, P. Blanchard; E. Payen, M. Fournier, J.L. Dubois and J.R. Bernard, App. Catal. A 217, 173, **2001**.
- 32 A. Griboval, P. Blanchard, E. Payen, M. Fournier and J.L. Dubois, Chem. Lett. 12, 1259, **1997**.
- 33 A. Griboval, P. Blanchard; L. Gengembre, E. Payen, M. Fournier, J.L. Dubois and J.R. Bernard, J. Catal. 188, 102, **1999**.
- 34 P. da Silva, Ph.D. thesis Université Pierre et Marie Curie, **1998**.
- 35 J. Bergwerff, L. de Water, T. Visser, P. Peinder, B. Leliveld, K. de Jong and B. Weckhuysen, Chem. Eur. J. 11, 4591, **2005**.
- 36 L. de Water, J. Bergwerff, B. Leliveld, B. Weckhuysen and K. de Jong, J. Phys. Chem. B 109, 14513, **2005**.
- 37 C. Cabello, I. Botto, F. Cabrerizo, M. González and H. Thomas, Ads. Sc. Tech. 18, 7, 591, **2000**.
- 38 C. Cabello, I. Botto and H. Thomas, Appl. Catal. A 197, 79, **2000**.
- 39 C. Cabello, F. Cabrerizo, A. Alvarez and H. Thomas, J. Mol. Catal. 186, 1-2, 89, **2002**.
- 40 EP0181035B1, **1990**.
- 41 G. Kishan, J.A.R. van Veen and J.W. Niemantsverdriet, Topics in Catalysis 29, 3, **2004**.
- 42 M. Sun, D. Nicosia and R. Prins, Cat. Today 86, 173, **2003**.
- 43 R. Cattaneo, F. Rota and R. Prins, J. Catal. 199, 318, **2001**.
- 44 A. van Dillen, R. Teröde, D. Lensveld, J. Geus and K. de Jong, J. Catal. 216, 257, **2003**.
- 45 Y. Ohta, T. Shimizu, T. Honma and M. Yamada, *Hydrotreatment and Hydrocracking of Oil Fractions*, Elsevier Science B.V., **1999**.
- 46 EP1043069B1, **2005** and US6,540,908B1, **2003**.
- 47 WO2005/035691A1, **2005**.
- 48 T.S. Nguyen, Ph.D. thesis Université Claude Bernard - Lyon 1, **2005**.
- 49 F. Labruyère, P. Dufresne, M. Lacroix and M. Breyse, Catal. Today 43, 11, **1998**.
- 50 R. Chianelli and G. Berhault, Catal. Today 53, 357, **1999**.
- 51 EP0601722A1, **1994**.
- 52 WO01/76741A1, **2001** and US2002/0013223A1, **2002**.
- 53 US2002/0010086A1, **2002**.
- 54 WO96/41848A1, **1996**.
- 55 EP1418002A2, **2004**.
- 56 WO01/02091A1, **2001** and WO01/02092A1, **2001**.
- 57 D. Nicosia, Ph.D. thesis Swiss Federal Institute of Technology Zurich, **2005**.
- 58 D. Nicosia and R. Prins, J. Catal. 229, 424, **2005**.

- 59 D. Nicosia and R. Prins, J. Catal. 231, 258, **2005**.
- 60 D. Nicosia and R. Prins, J. Catal. 234, 414, **2005**.
- 61 R. Iwamoto, N. Kagami and A. Iino, J. Jpn. Petrol. Inst. 48, (4), 237, **2005**.
- 62 M. Digne, Ph.D. thesis, École Normale Supérieure de Lyon, **2003**.
- 63 M. Tunius and Rolf Sköld, Colloids and Surfaces 46, 297, **1990**.
- 64 L. Saravanan and S. Subramaniam, J. Colloid Interface Science 284, 363, **2005**.
- 65 J. Livage, P. Barboux, M. Vandenborre, C. Schmutz and F. Taulelle, J. Non-Cryst. Sol. 147, 18, **1992**.
- 66 W. Weng and J. Baptista, J. Sol-Gel Sci. Tech. 8, 654, **1997**.
- 67 P. Mazoyer, C. Geantet, F. Diehl, C. Pichon, T.S. Nguyen and M. Lacroix, Oil&Gas Sci. Tech. – Rev. IFP, Vol. 60, 5, 791, **2005**.

CHAPTER II: EXPERIMENTAL

II.1. Catalysts preparation and additive impregnation.....	45
II.1.1. CoMo(P) catalysts preparation method.....	45
II.1.2. Additive impregnation of CoMo(P) catalysts.....	47
II.1.2.1. Additive impregnation prior to the metal precursors solution.....	47
II.1.2.2. Additive co-impregnation with the metal precursors solution.....	47
II.1.2.3. Additive impregnation of dried catalysts.....	47
II.1.2.4. Additive impregnation of calcined catalysts.....	48
II.1.3. Adsorption study.....	48
II.1.3.1. Impact of the ageing stage.....	50
II.1.3.2. Impact of the washing stage.....	50
II.1.3.3. Impact of the drying stage.....	51
II.2. Samples characterization	51
II.2.1. Elemental analysis methods.....	51
II.2.1.1. Lost on ignition (LOI).....	51
II.2.1.2. CHNS elemental analysis.....	51
II.2.1.3. X-ray Fluorescence (XRF).....	52
II.2.2. Physico-chemical analysis methods.....	52
II.2.2.1. Textural properties.....	52
II.2.2.2. Thermal analysis.....	52
II.2.2.3. Electronic Probe Microanalysis (EPMA).....	53
II.2.2.4. Transmission Electron Microscopy (TEM).....	53
II.2.3. Spectroscopic methods.....	53
II.2.3.1. Infrared spectroscopy.....	53
II.2.3.2. Raman spectroscopy.....	54
II.2.3.3. UV-Visible spectroscopy.....	55
II.2.3.4. Nuclear magnetic resonance (NMR).....	55
II.2.3.5. X-ray Diffraction spectroscopy (XRD).....	55
II.2.3.6. X-ray Photoelectron spectroscopy (XPS).....	55
II.2.3.7. X-ray Absorption spectroscopy (XAS).....	56
II.3. Catalysts activation.....	59

II.4. Catalytic tests	59
II.4.1. HSC test.....	59
II.4.2. Real feed HDS test	61
II.5. Bibliographic references.....	63

CHAPTER II: EXPERIMENTAL

II.1. CATALYSTS PREPARATION AND ADDITIVE IMPREGNATION

This section describes the experimental techniques used for the alumina-supported CoMo(P) catalysts preparation and their impregnation with the additive, as well as the additive impregnation directly over the support. All catalysts and supports referred in the next chapters are prepared according to the preparation method described in this section, except if specified otherwise.

II.1.1. CoMo(P) CATALYSTS PREPARATION METHOD

All catalysts were prepared by pore volume impregnation of a commercial γ -alumina shaped trilobes (BET surface area of 300 m²/g).

A reference CoMo alumina-supported catalyst (18 wt% MoO₃) was prepared according to the classical route using ammonium heptamolybdate and cobalt nitrate, referred to as CoMo_AHM (Figure II-1). The Co/Mo molar ratio was fixed to 0.39, which corresponds to a Co loading of 3.7 wt% CoO. Due to the low solubility of the molybdenum salt (1.74 mol Mo/l [1]), a double-impregnation method was used. In the first step, an amount of (NH₄)₆Mo₇O₂₄·4H₂O (powder 99%, Merck) and Co(NO₃)₂·6H₂O (powder 99%, VWR) were dissolved in water at room temperature. This solution was used to impregnate the support. After one night of ageing in a water-saturated atmosphere at room temperature, the catalyst was dried at 120 °C for 2 hours. At this point, part of the dried catalyst mass was stored and the remaining catalyst was calcined for 2 hours at 450 °C using a 5 °C/min ramp. The dried and calcined catalysts were then re-impregnated to obtain the desired molybdenum and cobalt loadings. To perform the second impregnation, the total water pore volume of the catalyst prepared in the first step was determined for the calcined (0.768 ml/g) and dried (0.339 ml/g) catalysts. After the second ageing step, both catalysts were dried. The catalyst that was submitted to calcination was re-calcined after the drying stage. In terms of nomenclature, the letter "c" or "d" stands for calcined or only dried catalysts.

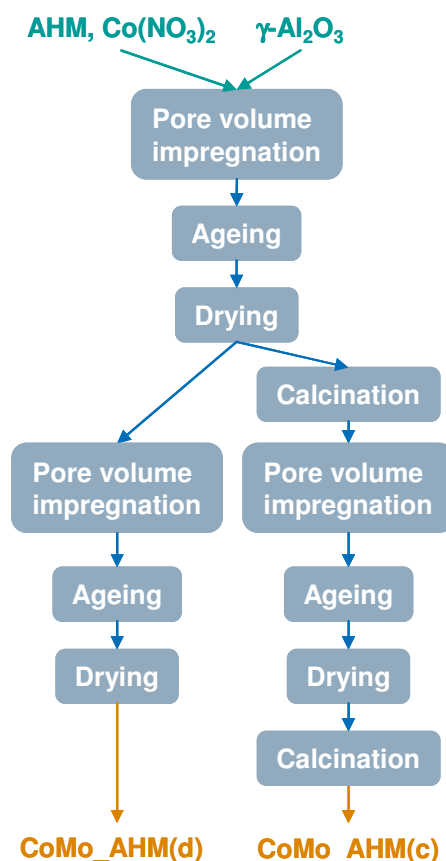


Figure II-1: Schematic representation of the CoMo_AHM catalysts preparation.

A second CoMo alumina-supported catalyst was prepared using a heteropolyanion route, referred to as CoMo_HPA. The Co/Mo molar ratio was fixed to 0.50 (4.7 wt% CoO). The impregnation solution was prepared by following the method described by C. Martin [1] to obtain the $\text{Co}_3[\text{Co}_2\text{Mo}_{10}\text{O}_{38}\text{H}_4]$ salt. This solution was then impregnated on the support, followed by an ageing period of one night. The drying stage was conducted at 120 °C for 2 hours. Part of the catalysts was stored and the other part was calcined at 450 °C for 2 hours using a 5 °C/min ramp (Figure II-2).

Phosphorus-containing catalysts were prepared with 3 different P/Mo molar ratios: 0.11, 0.40 and 0.57 (1.0, 3.6 and 5.1 wt% P_2O_5 , respectively). The first ratio corresponds to the lacunary Keggin $\text{PMo}_9\text{O}_{34}\text{H}_6^{3-}$ heteropolyanion stoichiometry, the second ratio corresponds to the $\text{P}_2\text{Mo}_5\text{O}_{23}^{6-}$ HPA stoichiometry and the third ratio leads to an excess of phosphorus when compared to the diphosphopentamolybdate HPA. The Co/Mo molar ratio was fixed to 0.39. To prepare these catalysts, an amount of MoO_3 (powder, Axens) and $\text{Co}(\text{OH})_2$ (powder, Axens) were dissolved in water. Afterwards, orthophosphoric (85 wt%, SDS) was added to the aqueous CoMo solution to obtain the desired ratio. These solutions were then stirred and refluxed at 90 °C for 2 hours in order to fully dissolve the CoMoP precursors and allow the formation of the heteropolyanionic compounds. The impregnation of the support was made at room temperature, followed by one night of ageing. All catalysts were then dried at 120 °C for 2 hours. For each catalyst, part of the dried catalyst mass was stored and another part was calcined at 450 °C for 2 hours using a 5 °C/min ramp (Figure II-2). The notation CoMoP(*x*) was adopted, where *x* is the catalyst loading in phosphorus expressed as P_2O_5 . Besides this, the suffix "c" or "d" stands for calcined or dried catalyst. For example, CoMoP(5c) refers to a calcined CoMoP catalyst with a 3.7/18/5.1 wt% loading expressed as oxides (P/Mo=0.57).

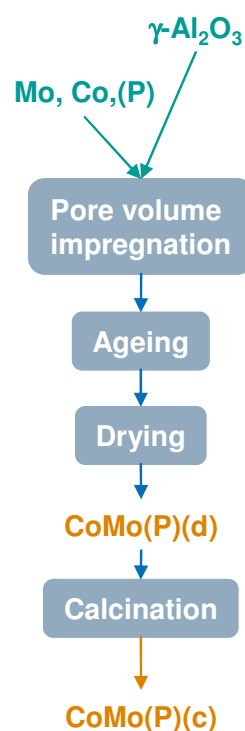


Figure II-2: Schematic representation of the CoMo(P) catalysts preparation.

Mo(P) catalysts were also prepared according to the same methodology, except that no cobalt precursor was used. In the case of phosphorus-containing catalysts, a MoP(2) sample (P/Mo molar ratio of 0.22) was prepared because this was the minimal amount of phosphorus that allowed the solutions precursors to dissolve. Besides these catalysts, samples were also prepared by impregnation of phosphorus directly into alumina, referred to as P(*xy*)/ Al_2O_3 , where *x* corresponds to the wt% P_2O_5 and *y* to either dried or calcined samples. Their detailed composition is reported to Appendix A.

Table II-1 summarizes the molar target ratios and precursors of the prepared CoMo(P) catalysts.

Table II-1: P/Mo, Co/Mo molar ratios and precursors used in the preparation of the CoMo(P) catalysts.

Catalyst	Target Co/Mo	Target P/Mo	Mo precursor	Co precursor	P precursor
CoMo_AHM	0.39	-	$(\text{NH}_4)_6\text{Mo}_7\text{O}_{24} \cdot 4\text{H}_2\text{O}$	$\text{Co}(\text{NO}_3)_2 \cdot 6\text{H}_2\text{O}$	-
CoMo_HPA	0.50	-	$\text{Co}_3[\text{Co}_2\text{Mo}_{10}\text{O}_{38}\text{H}_4]$		-
CoMoP(1)		0.11			
CoMoP(3)	0.39	0.40	MoO_3	$\text{Co}(\text{OH})_2$	H_3PO_4
CoMoP(5)		0.57			

II.1.2. ADDITIVE IMPREGNATION OF CoMo(P) CATALYSTS

As shown in the previous chapter, the additive may be introduced in the CoMo(P) catalyst prior to, simultaneously and sequentially to the metal precursors solution impregnation. In addition, the sequential impregnation may be performed on dried or calcined catalysts. All catalysts were prepared by pore volume impregnation and no further calcination was applied once the additive is introduced. The additive/Mo molar ratio is fixed to 0.75 and the additive is triethyleneglycol (TEG), except if specified otherwise. The additive-containing catalysts properties are reported to Appendix A.

II.1.2.1. Additive impregnation prior to the metal precursors solution

The first step consisted in impregnating the support with a 1.06 mol/l TEG aqueous solution, corresponding to 11.8 wt% of TEG in alumina. This loading was calculated in order to obtain a final TEG/Mo molar ratio of about 0.75. The additive-containing support was aged for one night, followed by a drying stage of 6 hours at 70 °C and 50 mbar. The next step involved the determination of the new water pore volume. To do so, part of the additive-containing support was impregnated only with water until the pore volume was completely filled. The new pore volume was 0.650 cm³/g. Then, the metal precursor solution was impregnated on the support previously impregnated with TEG. The final step consisted on a drying stage of 6 hours at 70 °C and 50 mbar.

The catalysts thus prepared are noted (PI), which stands for pre-impregnation.

II.1.2.2. Additive co-impregnation with the metal precursors solution

In this case, TEG was introduced in the metal precursor impregnation solution. The TEG/Mo ratio was fixed in the solution. The resulting solution was impregnated on the supported, followed by the ageing stage (one night) and the drying stage (70 °C and 50 mbar).

The catalysts thus prepared are noted (CI), which stands for co-impregnation.

II.1.2.3. Additive impregnation of dried catalysts

The additive impregnation of dried catalysts requires the previous determination of the catalyst water pore volume. To do this, part of the catalysts were impregnated only with water. The

determined water volumes are reported to Table II-2. These water-impregnated catalysts were dried for 2 hours at 120 °C and stored for further analysis and tests. The samples thus prepared are noted 'H₂O'. For example, CoMo_AHM(d)+H₂O refers to a dried CoMo_AHM catalyst only impregnated with water. Once the water pore volume is determined, the additive aqueous solution is impregnated on the fresh catalysts. The catalysts are then aged for one night and dried for 6 hours at 70 °C and 50 mbar. These catalysts are noted 'TEG'. Besides dried CoMo(P) catalysts, dried Mo(P) and P/Al₂O₃ samples were also impregnated with the additive.

Table II-2: Water pore volume (WPV) of dried CoMo(P), Mo(P) and P/Al₂O₃ samples.

Sample	WPV (cm ³ /g)	Sample	WPV (cm ³ /g)	Sample	WPV (cm ³ /g)
CoMo_AHM(d)	0.349	Mo_AHM(d)	0.542	P(1d)/Al ₂ O ₃	0.549
CoMo_HPA(d)	0.359	MoP(2d)	0.613	P(3d)/Al ₂ O ₃	0.510
CoMoP(1d)	0.346	MoP(3d)	0.387	P(5d)/Al ₂ O ₃	0.491
CoMoP(3d)	0.451	MoP(5d)	0.445		
CoMoP(5d)	0.429				

II.1.2.4. Additive impregnation of calcined catalysts

The same methodology and experimental conditions than the dried catalysts case were used for the impregnation of calcined catalysts: part of the calcined catalysts was only impregnated with water in order to determine the water pore volume (Table II-3) and then the calcined catalysts were impregnated with TEG. No further calcination was applied in additive-containing catalysts.

Table II-3: Water pore volume (WPV) of calcined CoMo(P), Mo(P) and P/Al₂O₃ samples.

Sample	WPV (cm ³ /g)	Sample	WPV (cm ³ /g)	Sample	WPV (cm ³ /g)
CoMo_AHM(c)	0.683	Mo_AHM(c)	0.731	P(1c)/Al ₂ O ₃	0.853
CoMo_HPA(c)	0.815	MoP(2c)	0.833	P(3c)/Al ₂ O ₃	0.961
CoMoP(1c)	0.831	MoP(3c)	0.761	P(5c)/Al ₂ O ₃	0.798
CoMoP(3c)	0.767	MoP(5c)	0.780		
CoMoP(5c)	0.798				

II.1.3. ADSORPTION STUDY

The adsorption study consisted in the impregnation of alumina by different additive solutions and posterior washing to remove the physisorbed or weakly bonded additive. A preliminary additive excess impregnation study was conducted on alumina. Afterwards, pore volume impregnations were carried out on alumina using DEGbe and TEG.

The excess impregnation method was used to impregnate alumina with diethyleneglycol monobutyl ether (DEGbe). This impregnation technique is used to obtain the adsorption equilibrium between additives and alumina. The ratio between the solution volume and the support weight was

10 ml/g. The amount of DEGbe in solution (3.0 mol/l) was 5 times superior to the amount of OH groups in alumina (12 OH/nm²). The solution and alumina were introduced in a closed vessel and were slowly stirred (100 translations per minute) for 96 hours at room temperature. After that period, the solution was stored to be analyzed and part of the sample was washed with water (3x 50 ml). The washing solutions were also stored to be analyzed. The washed and unwashed samples were then dried at 50 mbar and 70 °C.

The pore volume impregnation method was used to impregnate alumina with aqueous DEGbe solutions at room temperature. The ageing stage was conducted on a water saturated atmosphere under different experimental conditions. Then, the DEGbe-containing support was dried for 6 hours at 70 °C and 50 mbar. These drying conditions were used in order to minimize the additive evaporation. No further calcination was applied.

The amount of deposited DEGbe was determined by CHNS elemental analysis, before and after the washing stage, as shown in the in Figure II-3.

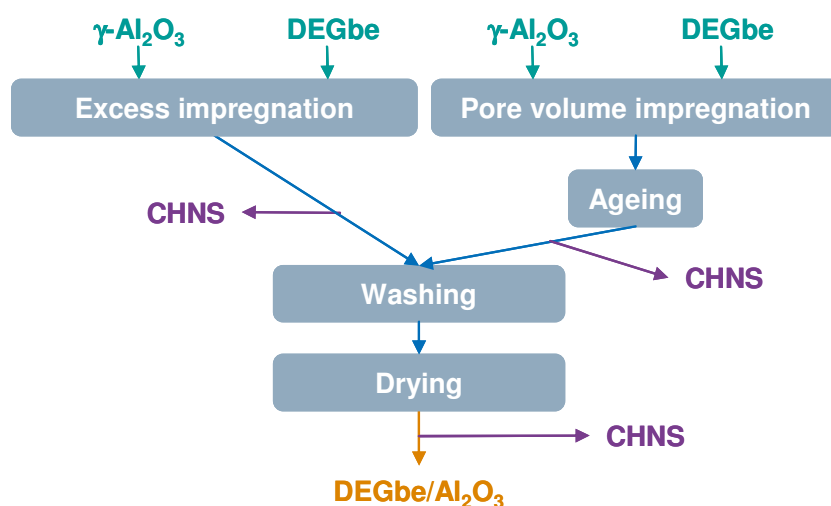


Figure II-3: Experimental procedure used in the adsorption study.

A second method was developed using pore volume impregnations and including an intermediary drying stage (6 hours at 70 °C and 50 mbar) before the washing stage with the purpose of eliminating the additive weakly bonded to the alumina surface. DEGbe and TEG were used as additives with a target loading of 20.0 wt% in relation to alumina (3.09 DEGbe/nm² and 3.34 TEG/nm²). The ageing stage was conducted at room temperature in a water-saturated atmosphere for 2 nights. The experimental procedure is represented in Figure II-4.

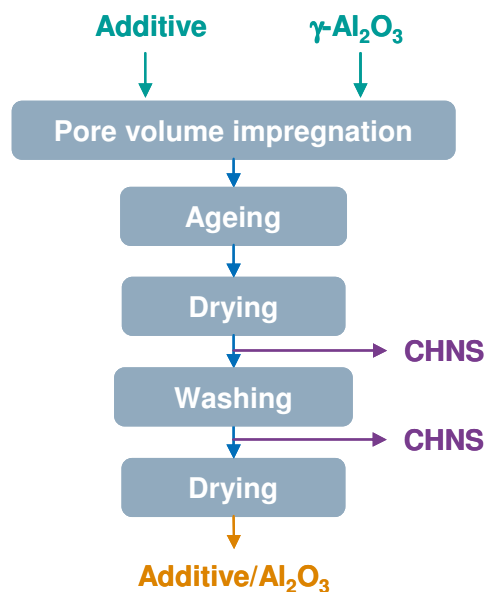


Figure II-4: Experimental procedure used in the adsorption study with an intermediary drying step.

The additives adsorption study involves several techniques that need to be optimized in order to achieve reliable and reproducible results, as described in the following paragraphs.

II.1.3.1. Impact of the ageing stage

The different viscosities and solubilities of additives may limit the diffusion into the alumina pores, preventing the additive to access the extrudate core. Based on this, several ageing times and temperatures were tested in the pore volume impregnations using DEGbe. The objective was to determine what ageing conditions are necessary to reach a maximum of adsorption, by changing the diffusion time and the additive viscosity (temperature effect). The experimental conditions are summarized in Table II-4.

Table II-4: Experimental conditions for DEGbe pore volume impregnation on alumina.

Notation	Target loading (DEGbe/nm ²)	T (°C)	Ageing period (days)
D0.2-ms	0.22	RT	1
D3.6-ms	3.60	RT	1
D3.6-m2		RT	2
D3.6-m7		RT	7
D3.6-m2-80		80	2
D3.6-m7-80		80	7

Note: RT stands for room temperature

II.1.3.2. Impact of the washing stage

The purpose of this operation is to remove the additive molecules that do not belong to the adsorption monolayer. In the washing operation, the amount of additive removed by the solvent is a

function of the contact time between the two phases, the quantity of solvent used and the additive solubility in the solvent. The choice of solvent plays an important role: it should have a good solubility or miscibility towards the additive and should have a relatively low boiling point that allows the easy removal of the solvent from the support during the drying stage without removing the additive. Water was used because they satisfy these restrictions. For each preparation, the number of washing operations and the used amount of solvent are identical. This allows the comparison of the different additives minimizing the different mass transferences and the evaluation of the strength of the interaction with alumina.

The carbon concentration in the washing solutions may be used as an indicator of the washing performance. This concentration was determined by liquid CHNS elemental analysis.

II.1.3.3. Impact of the drying stage

The drying operation was conducted at 50 mbar for 6 hours. The temperature was chosen in order to remove the maximum of solvent while removing as little additive as possible. This temperature must thus be higher than the solvent boiling point at this pressure and smaller than the boiling point of the additive. It becomes then necessary to estimate the boiling point at different pressures. For this purpose, Antoine's Equation was used with the parameters found in the literature [2] (Appendix B). Diethyleneglycol monobutyl ether and triethyleneglycol samples were dried at 70 °C because they have similar boiling points at atmospheric pressure.

II.2. SAMPLES CHARACTERIZATION

This section presents a brief description of the experimental techniques used to characterize the prepared solid samples, as well as the impregnation solutions.

II.2.1. ELEMENTAL ANALYSIS METHODS

II.2.1.1. Lost on ignition (LOI)

This analysis consists on a simple heating of the solid for 4 hours at high temperature. The most common temperatures used are 550 and 1000 °C, depending on the sample type. Under these conditions all the water contained in the solid vaporizes and so do the organic compounds (if any), decomposing to CO and CO₂. The weight loss allows quantifying the amount of water (and organic compounds). This analysis is systematic for all samples because the catalysts compositions are normally expressed in dried weight percent.

II.2.1.2. CHNS elemental analysis

This analysis was made using a *CE Instruments*TM EA1110 CHNS operating at 1000 °C. This equipment is used for the simultaneous quantification of carbon, hydrogen, nitrogen and sulfur of

organic or inorganic samples in solid, liquid or gaseous state. The average error is 5% for solids and gases and 10% for liquids. The analysis is divided in 3 stages:

1. 1 to 3 mg of sample, which are introduced in a tin (Sn) carrier, are precisely weighted and suddenly exposed to a temperature superior to 1000 °C (flash) in presence of oxygen diluted in helium;
2. The combustion gases (CO, CO₂, H₂O, NO, NO₂, SO₂ and SO₃) are then transported by the vector gas onto an oxidation and reduction catalyst. The obtained gases (N₂, CO₂, H₂O and SO₂) are afterwards separated in a chromatographic column;
3. The gases that leave the column are analyzed by a TCD (thermal conductivity detector) previously calibrated. The TCD signal is converted by software to the CHNS elemental composition.

This analysis was used to measure the amount of organic molecules in the samples.

II.2.1.3. X-ray Fluorescence (XRF)

XRF analyses were made using a *Philips*TM spectrometer PW2404 providing quantitative results with an incertitude around 2% for cobalt, molybdenum, phosphorus and aluminum.

In this method, high energy X-ray radiation excites an inner electron of the analyzed element. The excited electron is ejected and the vacancy is quickly filled by an upper-level electron. The energy involved in this relaxation process is then evacuated as an X-photon. Each element possesses a characteristic emission wavelength and its intensity is proportional to the element concentration in the sample.

II.2.2. PHYSICO-CHEMICAL ANALYSIS METHODS

II.2.2.1. Textural properties

The Brunauer-Emmet-Teller (BET) and Brunauer-Jura-Harkins (BJH) methods were used for the determination of the samples textural properties. These methods are based on the nitrogen adsorption-desorption isotherm at 77 K. The BET method uses simply the adsorbed nitrogen volume to measure the specific available surface. The BJH method uses the N₂ desorption curve to calculate the sample pore distribution and the adsorption is used to measure the N₂ specific surface area. The nitrogen adsorption requires a pre-treatment under vacuum and 300 °C to remove the adsorbed water and gases.

II.2.2.2. Thermal analysis

The thermogravimetric analysis (TGA) was made using a TGA 851 *Mettler*TM providing quantitative results with an incertitude around 1%. The gaseous effluents were characterized using a *Pfeiffer*TM Thermostar quadripolar mass spectrometer.

TGA follows the mass variations at different temperatures. These mass variations may be related to the progressive decomposition of the compounds present in the sample or to the departure of adsorbed species. A mass spectrometer may be coupled to the TGA for characterization of the gaseous effluents. This association allows the identification and measurement of the products evolution on temperature. In this study, all samples were submitted to a 10 °C/min ramp up to 600 °C in oxidic atmosphere (air).

II.2.2.3. Electronic Probe Microanalysis (EPMA)

The distribution profiles over alumina trilobe extrudates were obtained by Electronic Probe Microanalysis using a *JEOL*TM 8800R analyzer. It is a local elemental analyzer technique, currently used for the distribution profile determination of the elements impregnated over an alumina extrudate. This technique is based on the sample X-ray emission under the influence of a focalized electron beam that induces the sample electronic excitation and simultaneous X-photon emission. The spatial displacement of the incident beam allows measuring the element distribution profile over the extrudate. The profile is characterized by a distribution factor (R) which is the ratio between the average concentration and the square of the local concentration. The final R is the average R value obtained for 5 different extrudates (25 measurements along the section of the extrudate). The distribution is homogeneous if $R=1$. An egg-shell distribution occurs if $R<1$ (edge distribution) and a dome distribution if $R>1$ (centric distribution).

II.2.2.4. Transmission Electron Microscopy (TEM)

TEM analyses were made using a *JEOL*TM 2010-200 kV microscope equipped with a LaB₆ source (point-per-point resolution of 0.196 nm). This experimental technique allows visualizing the morphology of the deposited phases on the sulfided catalyst, like the MoS₂ crystallites or bulk structures. In particular, MoS₂ crystallites size and stacking histograms are determined after the observation of a minimum of 250 slabs.

TEM is an imaging technique whereby a beam of electrons is transmitted through the sample. A high-contrast image is formed by blocking electrons deflected away from the optical axis of the microscope by placing the aperture to allow only unscattered electrons through (Bright Field technique).

II.2.3. SPECTROSCOPIC METHODS

II.2.3.1. Infrared spectroscopy

Transmission mode

In this case, the sample is crossed by an incident IR beam of known intensity (I_0) and the resulting beam intensity is measured (I). The characteristic frequencies of the sample are collected. The Beer-

Lambert law may be used to relate the I_0/I ratio with the sample concentration and obtain quantitative results.

Diffuse reflectance

Diffuse Reflectance IR Fourier Transform (DRIFT) spectroscopy evolved in the last years due to its great potential performing *in situ* analysis under reactive environments and over IR non-transparent materials. The most common application in catalysis is the monitoring of adsorbed surface species at variable temperature.

Any radiation focused on a surface may be absorbed, directly reflected, internally reflected or diffused in all directions. The latter effect is analyzed by this method. The Beer-Lambert law is no longer applicable. However, a similar expression called the Kabelka-Munk equation [3] may be derived. Nevertheless, quantitative results remain difficult to obtain. DRIFT measurements were performed on a *Nexus* spectrometer in argon atmosphere. For each measurement, 128 scans were collected. The temperature program is presented in Figure II-5.

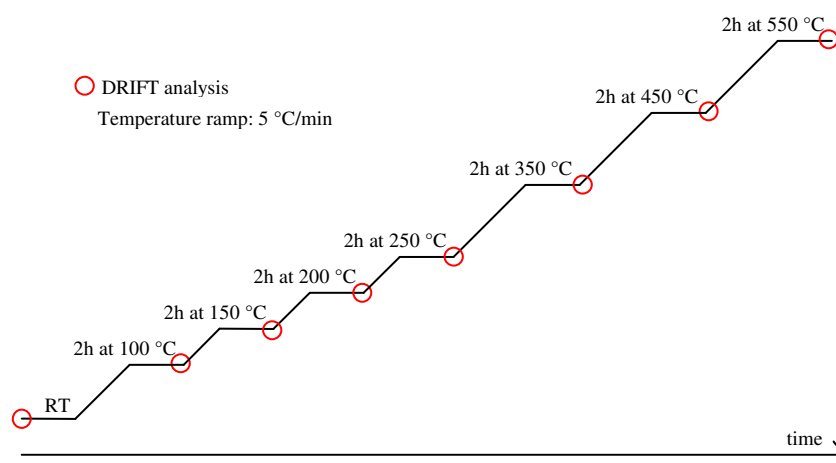


Figure II-5: Temperature program used in DRIFT spectroscopy.

II.2.3.2. Raman spectroscopy

Raman spectroscopy analyses were made at IRCE Lyon. (Institut de Recherches sur la Catalyse et l'Environnement de Lyon) using a *JobinYvon*TM LabRam HR.

Raman spectroscopy probes the sample vibration states. This analysis may be considered complementary to IR analysis because the transition selection rules are different. One advantage in using Raman spectroscopy is that alumina strongly adsorbs in IR under 1000 cm^{-1} and in Raman, the diffusion signal is weak. Another advantage is that water, which is responsible for strong IR adsorption peaks, is less visible in Raman. So, Raman spectroscopy is a technique that allows structural analysis about the catalyst adsorbed species and the impregnation solutions, identifying the different species present in the sample.

II.2.3.3. UV-Visible spectroscopy

The UV-Visible spectra were acquired using a *Varian*TM Cary 4G spectrometer equipped with a praying Mantis (*Harrick*TM) for solid analysis. The acquisition domain was 900-190 nm with an acquisition step of 1 nm. The liquid samples were acquired in absorbance mode and the solid samples in diffuse reflection mode (DRS).

UV-Visible spectroscopy is routinely used in the quantitative or qualitative determination transition metal ions solutions. These solutions are usually colored because d electrons within the metal atoms can be excited from one electronic state to another. Moreover, the color of metal ion solutions is strongly affected by the presence of other species, such as certain anions or ligands

II.2.3.4. Nuclear magnetic resonance (NMR)

This technique was used to characterize the molecular structure of different elements in liquid and solid samples. ³¹P NMR analyses were made using an *Avance300* spectrometer using a 4 mm probe-head employing a spinning frequency between 12 kHz. The chemical shift was referenced to an 85% phosphoric acid solution. Proton and ¹³C NMR spectroscopies were also acquired using the same equipment. When a paramagnetic atom or ion is in close proximity to an atom, broadening and shifting of the NMR signals of this atom are typically observed. Since cobalt and nickel ions are paramagnetic, NMR is difficult to use for Ni- and Co-promoted HDT catalysts.

II.2.3.5. X-ray Diffraction spectroscopy (XRD)

The diffraction patterns were acquired by a *PANanalytical*TM X'Pert Pro spectrometer equipped with a theta-theta goniometer using a copper cube ($\lambda=0.15402$ nm). The analysis range is from $2\theta = 2$ to 72° with a step of 0.05° . The counting time is 12 seconds per step.

XRD is a versatile, non-destructive technique that reveals detailed information about the chemical composition and crystallographic structure of different materials. When a monochromatic X-ray beam with wavelength λ is projected onto a crystalline material at an angle θ , diffraction occurs only when the distance traveled by the rays reflected from successive planes differs by a complete number n of wavelengths. Plotting the angular positions and intensities of the resultant diffracted peaks of radiation produces a pattern, which is characteristic of the sample. Where a mixture of different phases is present, the resultant diffractogram is formed by addition of the individual patterns.

II.2.3.6. X-ray Photoelectron spectroscopy (XPS)

The spectra were acquired using an XPS *Kratos*TM Axis Ultra spectrometer equipped with an aluminium monochromator (K_α X-rays, 1.486.6 eV) and a hemispheric analyzer working at a constant energy of 40 eV. The analyses were carried out at room temperature in ultra-high vacuum conditions (pressure inferior to 10^{-9} torr). The acquisition step was 0.05 eV for cobalt and 0.10 eV for the other

analyzed elements. For each sample, the final result is the average of two acquisitions. The binding energies were calibrated using the C1s level of the contamination carbon at 284.60 eV.

XPS is a quantitative spectroscopic technique that measures the elemental composition, chemical state and/or electronic state of the elements that exist within a sample surface. XPS spectra are obtained by irradiating a material with a beam of X-rays while simultaneously measuring the kinetic energy and number of electrons that escape from the surface (maximum depth of about 10 nm) of the sample being analyzed.

II.2.3.7. X-ray Absorption spectroscopy (XAS)

X-ray absorption spectroscopy is an element-specific probe of the local structure (short range) of elements in a sample. Since the local structure does not depend on long-range crystalline order, it is possible to study the structure of amorphous phases.

XAS principle

This spectroscopy results from the absorption of a high energy X-ray by an atom in the sample. XAS is commonly divided into two spectral regions. The first is the X-ray absorption near edge structure (XANES) spectral region. XANES spectra are unique to the oxidation state and speciation of the element of interest. Thus, this method is capable of discriminating species of similar formal oxidation state but different coordination. For example, octahedral Mo(VI) can be differentiated from tetrahedral Mo(VI). The more distant region of the X-ray absorption spectrum is the extended X-ray absorption fine structure (EXAFS) region. EXAFS spectra are best described as a series of periodic sine waves that decay in intensity as the incident energy increases from the absorption edge. These sine waves result from the interaction of the ejected photoelectron with the surrounding atomic environment. As such, their amplitude and phase depend on the local structure of excited atom. Since this interaction is well understood, theory is sufficiently advanced that the local structure of the excited atom can be determined by matching a theoretical spectrum to the experimental spectrum. This fitting yields many types of information, including the identity of neighboring atoms, their distance from the excited atom, the number of atoms in the shell and the degree of disorder in the particular atomic shell (as expressed by the Debye-Waller factor) [4].

XAS acquisition

The spectra were acquired at the X1 beam line at HASYLAB (Hamburg, Germany). The absorption K-edges of molybdenum (20000 eV) and cobalt (7709 eV) were studied. The oxidic and sulfided samples were diluted in boron nitride. Two alumina-supported CoMoP samples were also sulfided *in situ* using a 15% H₂S/H₂ gas mixture and with a dedicated cell to perform *in situ* analysis [5]. The samples were sulfided during the heating ramp (6 °C/min) and for an additional 15 minutes

period once the desired temperature was reached. Then, the cell was purged with argon for 15 minutes and only then the spectra were acquired.

For molybdenum, 3 spectra were acquired per sample. A Si(311) crystal was used in the line monochromator and a metallic molybdenum foil (20 μm) was placed after the sample to be used as reference. The ionization chambers, used as transmission detectors, are located before the sample, between the sample and the reference cell and after the reference cell. These chambers were filled with 200, 600 and 950 torr of krypton, respectively. For cobalt, five spectra were acquired per sample. A Si(111) crystal was used in the line monochromator and a metallic cobalt foil was used as a reference (5 μm). The ionization chambers were filled with krypton at 100, 300 and 950 torr. The acquisition step, range and time used for both analyses are summarized in Table II-5.

Table II-5: Acquisition parameters used for the molybdenum and cobalt K-edges.

Element	Acquisition range (eV)	Acquisition step (eV)	Acquisition time (s)
Molybdenum	19750-19950	4	2
	19950-20050	2	2
	20050-21000	3	2
Cobalt	7459-7659	4	2
	7659-7759	2	2
	7759-8709	2	2

The spectra were firstly calibrated using the first derivative maximum of the reference foil absorption spectrum. Then, the spectra thus acquired were normalized using cubic spline routines. The normalized spectra of the same sample are merged. As an example, in Figure II-6 is plotted the molybdenum K-edge absorption spectra before and after normalization.

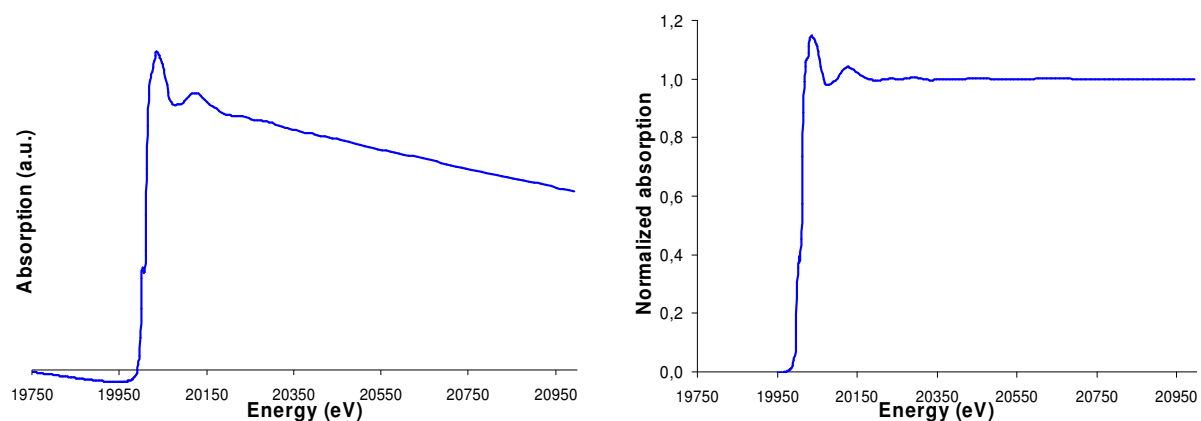


Figure II-6: Mo K-edge absorption (left) and normalized spectra (right) of the CoMoP(5d) catalyst.

EXAFS extraction

The first step consists in converting the normalized signal in a function of the wave vector (k). The interference function, $\chi(k)$ is then calculated by subtraction of the extracted signal with the absorption of the isolated atom (modulation ignoring the oscillations). To compensate the oscillations attenuation when k increases, $\chi(k)$ is multiplied by k^n . For molybdenum and cobalt atoms, n is usually 3. An example of the interference function is shown in Figure II-7.

The next step involves the determination of the radial distribution function. To do so, Fourier Transforms (FT) are applied to the interference function, leading to a radial distribution of the different atoms around the absorber atom. The FT requires a weighting window characterized by k_{\min} and k_{\max} values, where the function is non null. In our case, a Hanning window was always used ($\tau=2.50$). For simplicity, only the FT modulus is represented. An example is given in Figure II-7.

All operations described in this section were done using the ATHENA (v0.8.046) software [6].

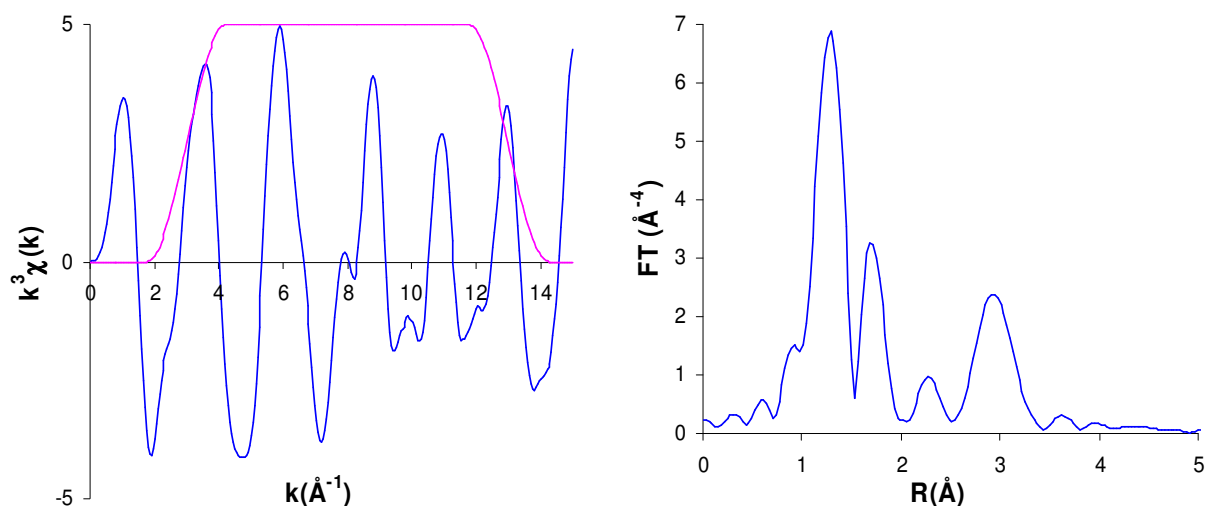


Figure II-7: Mo K-edge k^3 -weighted Interference function(left) and FT modulus (right) of the CoMoP(5d) sample. FT Hanning window from 3 to 13 \AA^{-1} , $\tau=2.5$.

EXAFS fitting

Only the sulfided samples were fitted. The Fourier transformation of the normalized k^3 -weighted EXAFS signal was performed with Hanning window functions as well as the backward FT. The curve fitting procedure was performed in R-space. Coordination numbers (N), interatomic distances (R), Debye-Waller parameters (σ^2), and energy shifts (ΔE_0) were used as variables in the fitting procedure. The ARTEMIS (v0.8.003) software [6] was used to simulate the experimental curves.

II.3. CATALYSTS ACTIVATION

For analysis purposes, the catalysts were activated by means of an *ex situ* gas-phase sulfidation at atmospheric pressure. To do so, about 2 grams of the catalyst extrudates were introduced in a glass reactor and heated from room temperature to 400 °C followed by 2 hours at this temperature under a 15% H₂S/H₂ gas mixture flow. The heating ramp was 5 °C/min and the gas flow was 2 liters per gram of catalyst per hour. This gas flow insures at least a 5-fold excess sulfur in relation to MoS₂ stoichiometry. At the end of the sulfidation, the H₂S/H₂ flow was interrupted and the cell was cooled down to room temperature under argon flow. Afterwards, vacuum was applied and the reactor was sealed to prevent the sample reoxidation. The reactor cell was then divided into 3 subcells each containing approximately 1/3 of the sulfided catalyst.

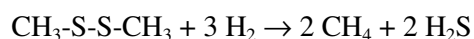
II.4. CATALYTIC TESTS

The catalytic performances of the prepared alumina-supported CoMo(P) catalysts were tested in toluene hydrogenation in presence of hydrogen and a constant sulfur rate (HSC test) and in real feed hydrodesulfurization.

II.4.1. HSC TEST

The HSC test allows evaluating the catalysts performances in toluene hydrogenation (HYD) and cyclohexane isomerization (ISOM). Sulfidation and reaction are conducted on a fixed bed reactor (T32) using 2 cm³ of catalyst. The catalysts were previously crushed and the fraction 315-1000 µm was diluted in 6 cm³ of solid SiC.

Sulfidation as well as the catalytic test itself are conducted at 350 °C and 60 bar. The liquid feed ($d=0.795 \text{ g.cm}^{-3}$) contained 74.1 wt% cyclohexane, 20.0 wt% toluene and 5.9 wt% dimethyldisulfide (DMDS), used as sulfiding agent. DMDS ensures that the catalyst remains in the sulfided state throughout the test. It decomposes in presence of hydrogen at about 200 °C to produce H₂S [7]:



Reaction II-1

The H₂/feed ratio was constant and equal to 450 N l/l. The liquid feed flow was 8 cm³.h⁻¹ during the sulfidation stage, corresponding to a liquid hourly space velocity (LHSV) of 4 h⁻¹. The sulfidation stage consists on a heating ramp from room temperature to 350 °C (2 °C.min⁻¹) followed by 1 hour at this temperature. After sulfidation, the liquid feed flow was modified to 4 cm³.h⁻¹ (LHSV of 2 h⁻¹) and the effluents are analyzed each hour by on-line gas chromatography. The test is 6 hours long. Table II-6 summarizes the operating conditions used in both stages.

Table II-6: Operating conditions for the sulfidation and test stages of the HSC catalytic test.

	Sulfidation stage	Test stage
Temperature	350 °C	350 °C
Heating ramp	2 °C.min ⁻¹	-
Pressure	60 bar	60 bar
Catalyst volume	2 cm ³	2 cm ³
Liquid feed flow	8 cm ³ .h ⁻¹	4 cm ³ .h ⁻¹
LHSV	4 h ⁻¹	2 h ⁻¹
H ₂ gas flow	3.6 NL.h ⁻¹	3.6 NL.h ⁻¹
H ₂ /feed ratio	450 NL.l ⁻¹	450 NL.l ⁻¹

During the HSC test, toluene hydrogenation and cyclohexane isomerization reactions are evaluated. The main reaction products are presented in Figure II-8.

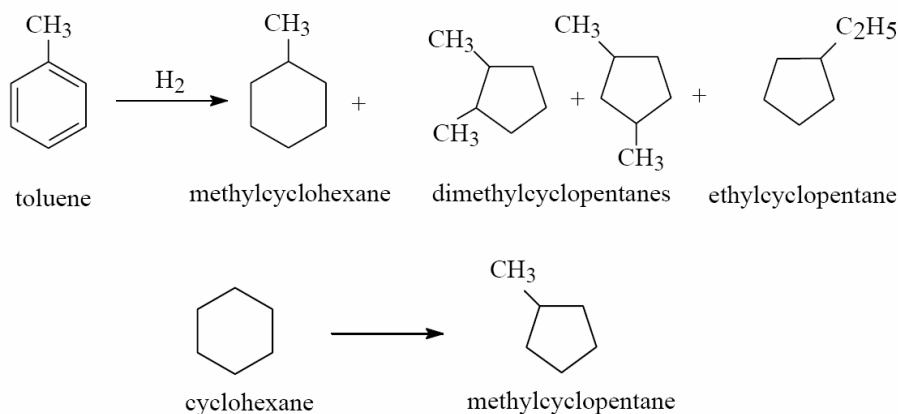


Figure II-8: Main reaction products of toluene hydrogenation and cyclohexane isomerization.

Results are expressed in terms of hydrogenating activity (A_{HYD}), calculated from the measured toluene conversion (X_{toluene}) considering a reaction order of 1 with respect to toluene (Equation II-1), and cyclohexane isomerization conversion (ISOM), which is used to infer about the catalyst acidity.

$$A_{\text{HYD}} = \ln \left(\frac{1}{1 - X_{\text{toluene}}} \right) \quad \text{Equation II-1}$$

The hydrogenating activity and the cyclohexane conversion correspond to the average of the individual measurements once the hydrogenating activity has stabilized. Normally, the three last points were used. As an example, the hydrogenating activity and the cyclohexane conversion evolution in time of the CoMoP(5d) catalyst are represented in Figure II-9.

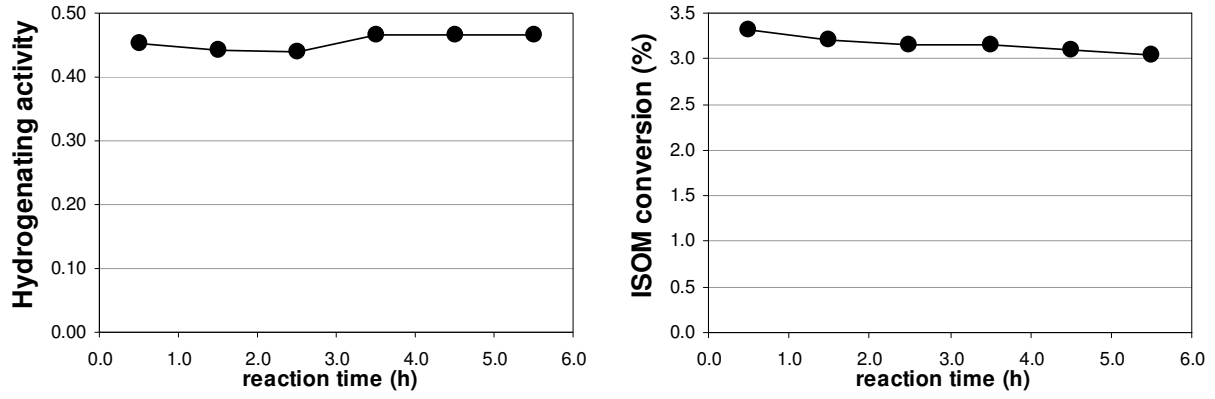


Figure II-9: Hydrogenation activity and isomerization conversion of the CoMoP(5d) catalyst.

In order to compare the performances of the different catalysts, toluene hydrogenation reaction rates (r_{HYD}) were calculated and expressed in converted toluene per molybdenum per hour, as shown in Equation II-2.

$$r_{\text{HYD}} = \frac{F_{\text{feed}} \cdot x_{\text{toluene}}}{d_{\text{feed}} \cdot \text{MW}_{\text{toluene}}} \cdot X_{\text{toluene}} \cdot \frac{m_{\text{catalyst}} \cdot x_{\text{molybdenum}}}{\text{MW}_{\text{molybdenum}}} \quad \text{Equation II-2}$$

r_{HYD} corresponds to the toluene hydrogenation reaction rate, in $\text{mol} \cdot \text{mol}^{-1} \cdot \text{h}^{-1}$; F_{feed} is the liquid feed flow, in $\text{cm}^3 \cdot \text{h}^{-1}$; x_{toluene} is the toluene mass fraction in the liquid feed; d_{feed} is the liquid feed density, in $\text{g} \cdot \text{cm}^{-3}$; X_{toluene} is the toluene conversion; m_{catalyst} is catalyst mass in the reactor, in g; $x_{\text{molybdenum}}$ is the molybdenum mass fraction in the catalyst and MW is the molecular weight, in $\text{g} \cdot \text{mol}^{-1}$.

The cyclohexane isomerization reaction rates (r_{ISOM}) were also determined but expressed in converted cyclohexane per catalyst mass per hour, as show in Equation II-3. In this case, the reaction rates are function of the catalyst mass because this reaction is more dependent of the support than the active phase.

$$r_{\text{ISOM}} = \frac{F_{\text{feed}} \cdot x_{\text{CC6}}}{d_{\text{feed}} \cdot \text{MW}_{\text{CC6}}} \cdot X_{\text{ISOM}} \cdot \frac{1}{m_{\text{catalyst}}} \quad \text{Equation II-3}$$

r_{ISOM} corresponds to the cyclohexane hydrogenation reaction rate, in $\text{mol} \cdot \text{g}^{-1} \cdot \text{h}^{-1}$ and CC6 corresponds to cyclohexane.

II.4.2. REAL FEED HDS TEST

The real feed test allows evaluating the catalysts performances in HDS in similar conditions to those used in the industry. Sulfidation and reaction are conducted on a fixed bed reactor (U39) using 4 cm^3 of catalyst. The catalysts were previously sorted by length and only the fraction 2-4 mm was kept and diluted in 4 cm^3 of solid SiC.

The sulfidation stage and the catalytic test itself were conducted at 30 bar. The sulfidation was carried out at 350 °C and the test at 335, 345 and 355 °C. The feed was a straight run gas oil (IFP reference S7273) with a density of 0.8484 g.cm⁻³ that contained 0.9134 wt% sulfur and 100 ppm of nitrogen. The sulfidation feed was basically the same except it contained 2 wt% of DMDS.

The H₂/feed ratio was constant and equal to 250 N l/l. The liquid feed flow was 4 cm³.h⁻¹ during sulfidation and test stage, corresponding to a liquid hourly space velocity (LHSV) of 1 h⁻¹. After sulfidation, DMDS is removed from the feed and the effluents are analyzed for sulfur and nitrogen contents each 2 hours. Table II-7 summarizes the operating conditions used in both stages.

Table II-7: Operating conditions for the sulfidation and test stages of the real feed HDS catalytic test.

	Sulfidation stage	Test stage
Temperature	350 °C	335, 345 and 355 °C
Pressure	30 bar	30 bar
Catalyst volume	4 cm ³	4 cm ³
Liquid feed flow	4 cm ³ .h ⁻¹	4 cm ³ .h ⁻¹
LHSV	1 h ⁻¹	1 h ⁻¹
H ₂ gas flow	1.0 Nl.h ⁻¹	1.0 Nl.h ⁻¹
H ₂ /feed ratio	250 Nl.l ⁻¹	250 Nl.l ⁻¹

For instance, the effluent sulfur concentration evolution with time and different test temperatures is presented in Figure II-10 for the CoMoP(5d)+TEG catalyst.

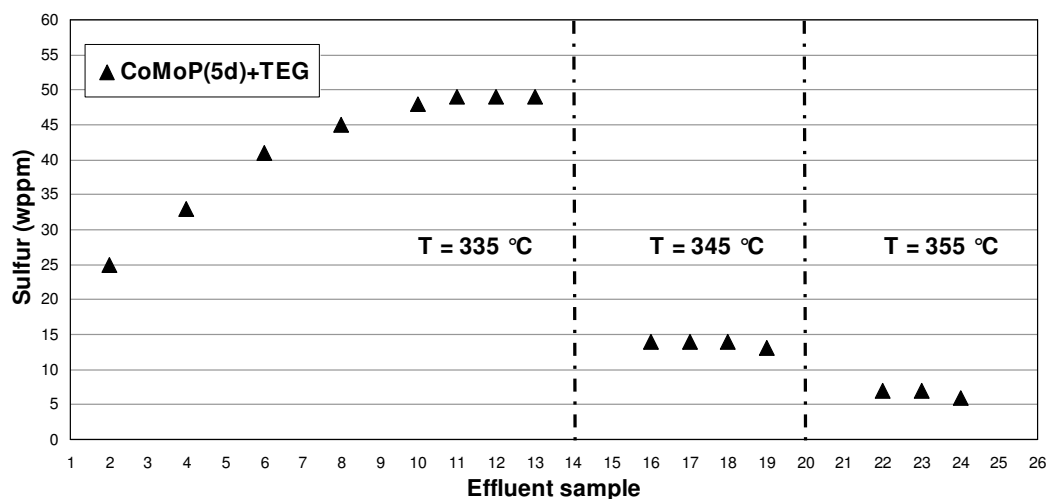


Figure II-10: Sulfur concentration evolution in the HDS test of the CoMoP(5d)+TEG catalyst.

The average sulfur concentration at each temperature was then used to calculate the total sulfur conversion (Equation II-4) and the HDS activity (Equation II-5) considering a reaction order of 1.2. Since measurements were made at different temperatures, it becomes possible to simulate the impact of each catalyst on the sulfur concentration of a specific feed as a temperature function. For this purpose, the Arrhenius equation was used (Equation II-6). As an example, the relation between sulfur content in the feed and the reactor temperature is shown in Figure II-11.

$$\text{conversion}(HDS) = \frac{C_0 - C}{C_0} \quad \text{Equation II-4}$$

$$\text{HDS activity} = \frac{1}{(n-1) \cdot C_0^{n-1}} \cdot \left[(1 - \text{conversion}(HDS))^{1-n} - 1 \right] \quad \text{Equation II-5}$$

$$\text{HDS activity} = A \cdot e^{-E_a/RT} \quad \text{Equation II-6}$$

C_0 and C are the sulfur concentration in the feed and in the effluent, respectively, in g.g^{-1} ; n is the reaction order ($n=1.2$); A is the pre-exponential factor of the Arrhenius equation, E_a is the activation energy, in cal.mol^{-1} , R is the ideal gas constant and T is the temperature, in K.

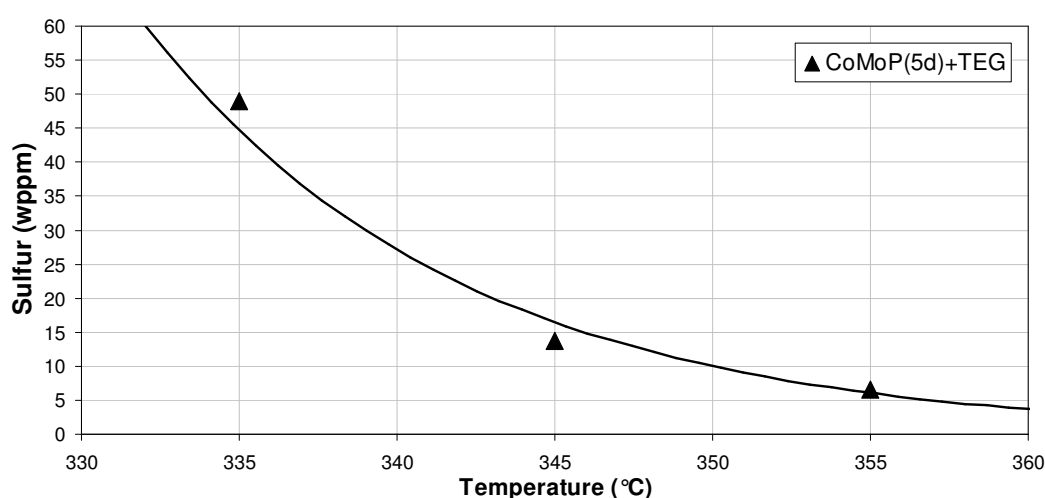


Figure II-11: Sulfur content after HDS reaction at different temperatures for the CoMoP(5d)+TEG catalyst.

II.5. BIBLIOGRAPHIC REFERENCES

- 1 C. Martin, Ph.D. thesis, Université des Sciences et Technologies de Lille, **2003**.
- 2 WebBook de Chimie NIST, <http://webbook.nist.gov/> in 8/11/**2005**.
- 3 T. Armaroli, T. Bécue and S. Gautier, Oil&Gas Sci. Tech. - Rev. IFP, Vol. 59, No. 2, 215 , **2004**.
- 4 E. Prouzet, *Cours Initiation à l'absorption des rayons X*, Montpellier mai **2006**.
- 5 D. Bazin, H. Dexpert and J. Lynch, *In Situ XAFS Measurements of Catalysts in X-ray Absorption Fine Structure for Catalysts and Surfaces*, Y. Iwasawa ed., World Scientific, London, 113-129, **1996**.
- 6 B. Ravel, M. Newville, Journal of Synchrotron Radiation, 12, 537, **2005**.
- 7 H. Topsøe, B. Clausen and F.E. Massoth, *Catalysis: Science and Technology* vol. 11, Springer-Verlag, Berlin **1996**.

CHAPTER III: THE ROLE OF GLYCOL-TYPE ADDITIVES ON DRIED CoMo(P) CATALYSTS

III.1. Introduction	67
III.2. Impact of the additive when impregnated on dried CoMo catalysts	67
III.2.1. Speciation of the precursor impregnation solutions	68
III.2.2. Speciation of the dried CoMo catalysts surface	69
<i>III.2.2.1. Influence of the additive on cobalt species</i>	<i>69</i>
<i>III.2.2.2. Influence of the additive on molybdenum species.....</i>	<i>75</i>
III.2.3. Thermal behavior	80
<i>III.2.3.1. Additive-free dried CoMo catalysts analysis</i>	<i>80</i>
<i>III.2.3.2. Additive-containing dried CoMo catalysts analysis</i>	<i>84</i>
III.2.4. Surface mechanism	87
III.3. Impact of the additive when impregnated on dried CoMoP catalysts.....	88
III.3.1. Speciation of the precursor impregnation solutions	88
III.3.2. Speciation of the dried CoMoP catalysts surface	92
<i>III.3.2.1. Influence of the additive on cobalt species</i>	<i>92</i>
<i>III.3.2.2. Influence of the additive on molybdenum species.....</i>	<i>94</i>
<i>III.3.2.3. Influence of the additive on phosphorus species.....</i>	<i>98</i>
III.3.3. Thermal Behavior.....	104
<i>III.3.3.1. Additive-free dried CoMoP catalysts analysis.....</i>	<i>104</i>
<i>III.3.3.2. Additive-containing dried CoMoP catalysts analysis</i>	<i>106</i>
III.3.4. Surface mechanism	108
III.4. Chapter conclusion	109
III.5. Bibliographic references	109

III.1. INTRODUCTION

Starting from different polyoxomolybdate precursors, the catalysts surface state will be studied prior to and after TEG impregnation to determine if the additive modifies the active phase precursors structure. Moreover, to determine if the phosphorus-additives synergy on HDS activity is established before the activation stage, phosphorus-containing catalysts are also prepared and studied.



The objective of this section is to determine if and how the CoMo-based catalysts surface species are modified after the additive impregnation. To do so, catalysts were prepared using different solution precursors: 1) AHM and $\text{Co}(\text{NO}_3)_2$ and 2) $\text{Co}_3[\text{Co}_2\text{Mo}_{10}\text{O}_{38}\text{H}_4]$. In a first step, the solutions are characterized to establish a relation between the solution precursors and species in solution. Then, the surface species on the prepared dried CoMo catalysts are characterized prior to and after additive impregnation.

III.2.1. SPECIATION OF THE PRECURSOR IMPREGNATION SOLUTIONS

In order to study the nature of cobalt and molybdenum species during impregnation, the precursor solutions were analyzed. Even though this study does not account for the effect that alumina might have on the pH and the nature of the solution species inside the catalysts porosity, it allows to evidence some of the differences between the studied systems. For this purpose, cobalt species were studied by UV-Visible spectroscopy and molybdenum species by Raman spectroscopy.

The CoMo_AHM precursor solution (red) has a pH value near 5 and a molybdenum concentration of 0.8 M and 0.3 M for cobalt (Co/Mo=0.39). The CoMo_HPA precursor solution (green) has a pH value near 4 and a molybdenum concentration of 1.9 M and 1.0 M for cobalt (Co/Mo=0.50).

The UV-Visible spectra (Figure III-2) reveal the same features for cobalt species obtained by dissolution of cobalt nitrate and cobalt species existing in CoMo_AHM (cobalt nitrate and ammonium heptamolybdate) aqueous solutions, exhibiting bands at 460, 513 and 615 nm. These bands are typical of the octahedral Co(II) d-d electronic transition in the hexaaquo complex $[\text{Co}(\text{H}_2\text{O})_6]^{2+}$ [1,2].

The CoMo_HPA aqueous solution shows a band at about 610 nm, assigned to the octahedral Co(III) d-d electronic transition [3,4], consistent with the presence of a molybdocobaltate HPA. Besides the Co(III) band, a shoulder at about 513 nm is also observed which arises from the Co(II) aquacomplex acting as a counter-ion.

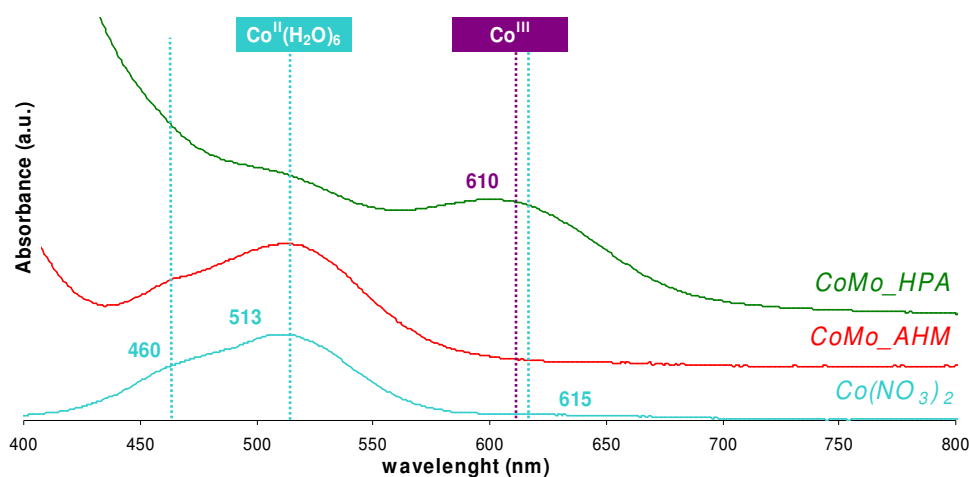


Figure III-2: UV-Visible spectra of the CoMo_AHM and CoMo_HPA impregnation solutions and the cobalt nitrate reference solution.

It has been shown in the literature [5,6] that the molybdocobaltate species $\text{Co}_{3/2}[\text{CoMo}_6\text{O}_{24}\text{H}_6]$ and its dimeric form $\text{Co}_3[\text{Co}_2\text{Mo}_{10}\text{O}_{38}\text{H}_4]$ have similar UV-Visible spectra but different Raman frequencies. To evaluate if the dimeric species has been well prepared, Raman analysis of CoMo_HPA impregnation solution was performed (Figure III-3). The strong Raman band at 956 cm^{-1} , the shoulder

at about 915 cm^{-1} and the weak bands at about 562 and 603 cm^{-1} show that the dimeric form of the molybdocobaltate is the main species in this solution. Nevertheless, a weak shoulder is observed at 950 cm^{-1} , indicating that the dimeric form is in equilibrium with the monomeric form.

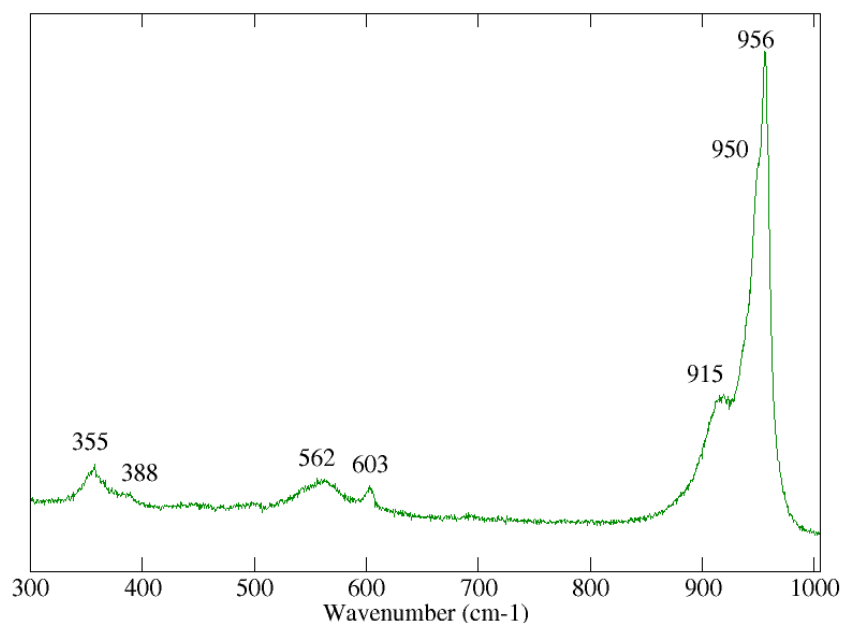


Figure III-3: Raman spectrum of the CoMo_HPA solution.

III.2.2. SPECIATION OF THE DRIED CoMo CATALYSTS SURFACE

To determine if the additive has an influence on dried CoMo-based catalysts surface species, the catalysts are characterized in absence and in presence of the additive. This allows interpreting the characterization results of the additive-containing samples based on the additive-free results. For this purpose, the description of cobalt-containing surface structures is firstly made. Then, molybdenum-containing species are described, which may or not contain cobalt, rendering a global vision about the surface state.

III.2.2.1. Influence of the additive on cobalt species

To obtain qualitative informations about the cobalt species and how they evolve after additive impregnation, UV-Visible spectroscopy is privileged. The description thus obtained is then complemented by XAS analyses, which allow determining the local environment for cobalt and how it is modified by the additive. Finally, to quantify the modifications in surface species (if any) XPS is used.

The UV-Visible diffuse reflectance spectroscopies conducted on dried CoMo_AHM and CoMo_HPA catalysts (Figure III-4) show the same features as those observed for the impregnation solutions. It reveals the presence of the Co(II) hexaaquo complex for the CoMo_AHM catalyst and the presence of Co(III) entities in the HPA-based catalyst.

After additive impregnation, no strong modification of UV-Visible spectra could be observed for the dried CoMo_AHM catalyst. This is not the case for the dried CoMo_HPA catalyst, where the spectral line slightly evolves: the Co(II) band increases whereas the Co(III) band decreases in the presence of the additive.

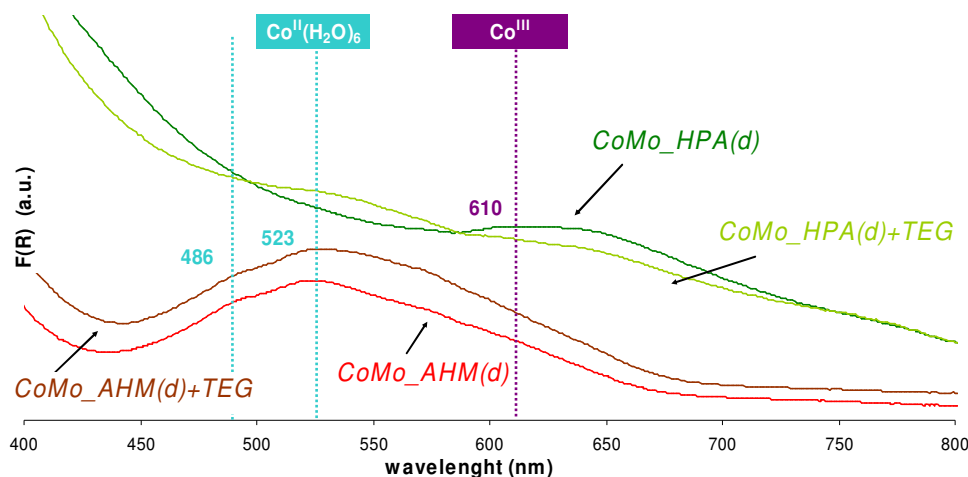
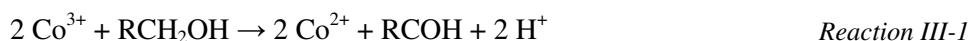


Figure III-4: UV-Visible diffuse reflectance spectra of CoMo_AHM(d), CoMo_HPA(d) and corresponding additive-containing catalysts.

The fact that no strong modification of UV-Visible spectra is observed after additive impregnation rules out cobalt complexation by the additive, contrarily to what was observed for chelating organic additives (containing carboxylic or amine functions) [7,8,9,10,11].

The evolution of the cobalt bands in the dried CoMo_HPA catalyst after additivation reflects a loss in Co(III) species while Co(II) species are formed. One possible explanation for this evolution is the redox properties of TEG, which is a primary alcohol. Indeed, TEG molecule can reduce Co(III), according to the following reactions:



As a consequence, the Co(III)/Co(II) ratio in the solution decreases and the molybdocobaltate HPAs partially decompose after the impregnation of the additive.

The previous results are confirmed by the Co K-edge X-ray absorption spectroscopy conducted on the same catalysts. The position and the shape of the cobalt K absorption edge (XANES) provide information about the charge and geometry of the cobalt atoms. Indeed, it is easy to distinguish Co^{2+} from Co^{3+} ions. The non-bonded and anti-bonded levels of Co^{3+} are less stabilized whereas the 1s level is more stabilized, leading to a higher transition energy [12]. According to reference data [4,6], the signal at 7725 eV is attributed to Co^{2+} whereas the signal at about 7733 eV is characteristic of Co^{3+} .

The absorption spectra in Figure III-5 show that the CoMo_AHM(d) catalyst only contains Co^{2+} containing species whereas the CoMo_HPA(d) catalysts contain both Co^{2+} and Co^{3+} ions. The spectra also show that the Co^{3+} contribution decreases after the additive impregnation, consistent with the UV-Visible spectroscopy observations.

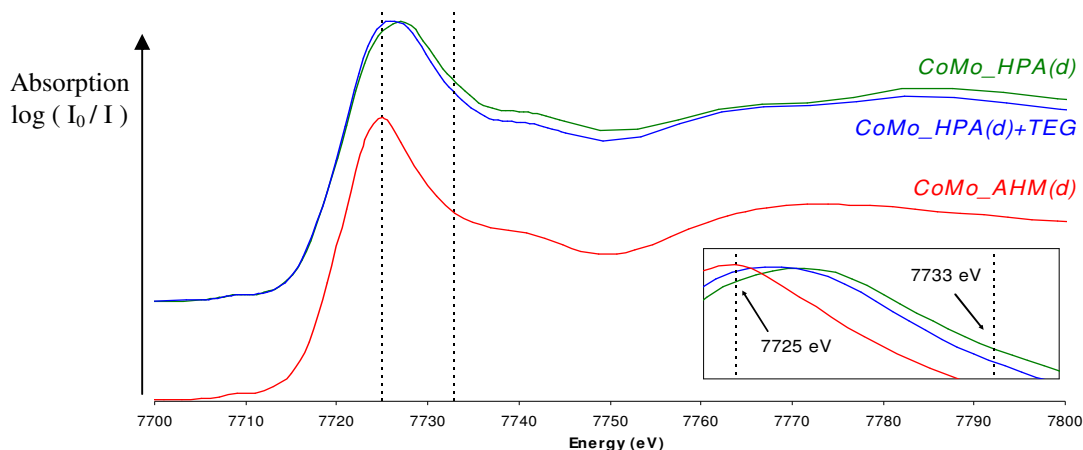


Figure III-5: Co K-edge XANES spectra of CoMo_AHM(d), CoMo_HPA(d) and CoMo_HPA(d)+TEG catalysts.

It is known that most of the polyoxoanions exhibit a wide range of Mo-O distances that make a thorough quantitative EXAFS analysis of the first Mo-O shell rather difficult [13]. As a matter of fact, many results obtained on supported oxidic Mo-based compounds lead to imperfect fits [14]. The same reasoning is also true for cobalt-containing compounds. Moreover, the existence of several Co phases on the catalyst surface, like both molybdocobaltates HPAs and oxide (Co_3O_4 , CoAl_2O_4 or CoMoO_4) make the fitting almost impossible, because EXAFS will provide average information of all these phases. For the above-mentioned reasons, the EXAFS analysis for the dried catalysts will focus only on qualitative aspects.

The Co K-edge EXAFS Fourier Transforms modulus (FT) in Figure III-6 show similar features for the additive-free and additive-containing dried CoMo_AHM catalysts, exhibiting the first Co-O shell at about 1.6 Å (not phase-corrected). In contrast, the dried CoMo_HPA catalysts show different FT features when compared to the AHM-based catalysts. Furthermore, the HPA-based catalysts spectra evolve after additive impregnation, exhibiting the first coordination shell at about 1.5 Å (not phase-corrected) whereas this distance was 1.4 Å before additive impregnation.

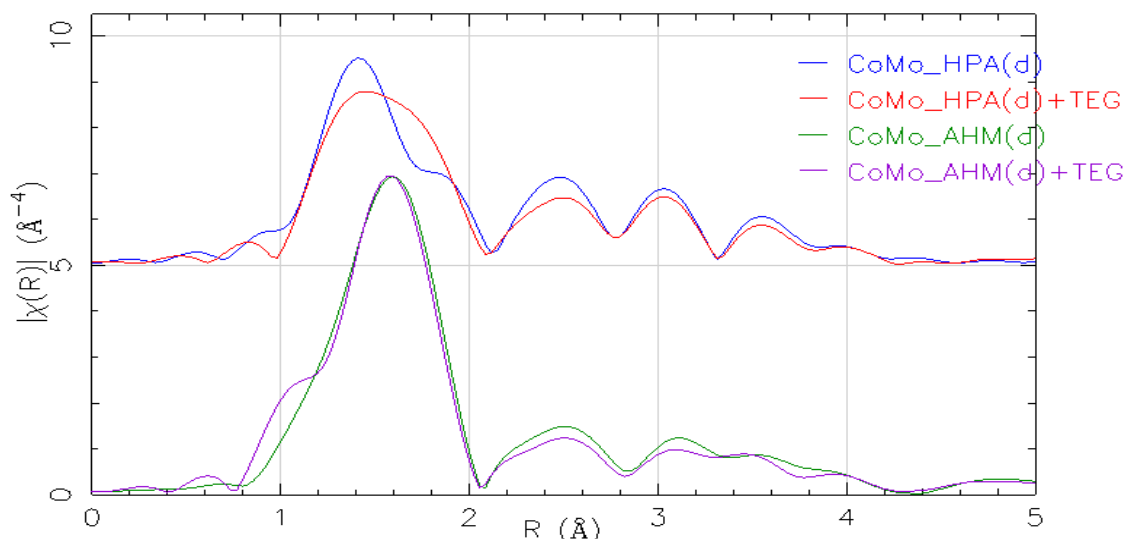


Figure III-6: Cobalt K-edge k^3 -weighted EXAFS Fourier Transforms (FT) of CoMo_AHM(d), CoMo_HPA(d) and corresponding additive-containing catalysts. FT Hanning window from 2 to 11; $\tau=2.5$.

The Co K-edge EXAFS of the CoMo_AHM(d) catalysts are in agreement with the UV-Visible and XANES results, confirming that the additive does not modify the local structure of cobalt. However, this is not the case for the CoMo_HPA(d) catalysts. Although no fitting was performed, the distance at about 1.4 Å (not phase-corrected) is assigned to a Co(III)-O contribution, which is in equilibrium with a Co(II)-O contribution that according to the AHM-based EXAFS occurs at about 1.6 Å. These observations are consistent with the existence of molybdocobaltate HPAs. Indeed, results published in the literature for the $\text{Co}_3[\text{Co}_2\text{Mo}_{10}\text{O}_{38}\text{H}_4]$ salt [6] report a Co(III)-O distance of 1.94 Å and 2.15 Å for the Co(II)-O bond (phase corrected).

When the additive is introduced, the Co(III)-O contribution decreases while the Co(II)-O increases, which is in agreement with the partial conversion of Co(III) species shown by UV-Visible and XANES spectroscopies.

XPS analysis was used to evaluate the loss of Co^{3+} ions after the additive impregnation. In the case of cobalt, the different 2p spectral contributions may be determined by mathematical decomposition combined with the use of non-supported solids as reference. For each detected species, the spectral envelope was composed of Co 2p_{1/2} and Co 2p_{3/2} core levels and several satellite peaks which are related to the former by binding energy and relative peak area.

For this purpose, a non-supported CoMoP (P/Mo=0.57, Co/Mo=0.39) reference solid was analyzed (not reported here) and the spectral envelope was successfully fitted (Co 2p_{3/2} binding energy of 781.3 eV for the main signal). It was verified by other analytical techniques (Co K-edge XANES and UV-Visible spectroscopy) that only Co^{2+} species were present in this sample. Afterwards, a non-supported $\text{Co}_3[\text{Co}_2\text{Mo}_{10}\text{O}_{38}\text{H}_4]$ solid was analyzed (not reported here) and the spectral envelope was first fitted only with Co^{2+} contributions obtained from the CoMoP reference solid. To complete the fit,

a main contribution at about 780.5 eV with satellite peaks was needed, which was assumed to be characteristic of Co^{3+} . However, the above-mentioned binding energies did not allowed to fully decompose the alumina-supported CoMoP(5d) catalyst, possibly due to specific alumina-cobalt interactions that induce modifications to cobalt energetic levels. Consequently, the same number of decomposition peaks (satellites) as well as their relative displacements on binding energy was kept but their relative intensity and the main peak absolute position were adjusted in order to fully simulate the experimental spectrum. This operation leads to a Co^{2+} main binding energy of 780.8 eV for alumina-supported samples (Figure III-8). Like in the non-supported catalysts, the supported CoMo_HPA(d) catalysts spectra were decomposed using the Co^{2+} peak position observed for the supported CoMoP(5d) sample and the remaining spectrum was completed with a new main contribution at 780.3 eV and associated satellite peaks, assumed to be characteristic of Co^{3+} (Figure III-9).

This method is quite different than that described by C. Martin [4], where a weak satellite at about 791 eV indicates the presence of Co^{3+} whereas an intense satellite at about 787 eV is assigned to Co^{2+} . This method was not used because this Co^{3+} satellite is already weak in non-supported samples and in supported catalysts it almost disappears, rendering the fit almost impossible. This is why our $\text{Co}^{2+}/\text{Co}^{3+}$ differentiation was based in the relative proportion between the main $\text{Co } 2p_{3/2}$ peak and the satellite at about 787 eV which is less important in presence of Co^{3+} than Co^{2+} (Figure III-7).

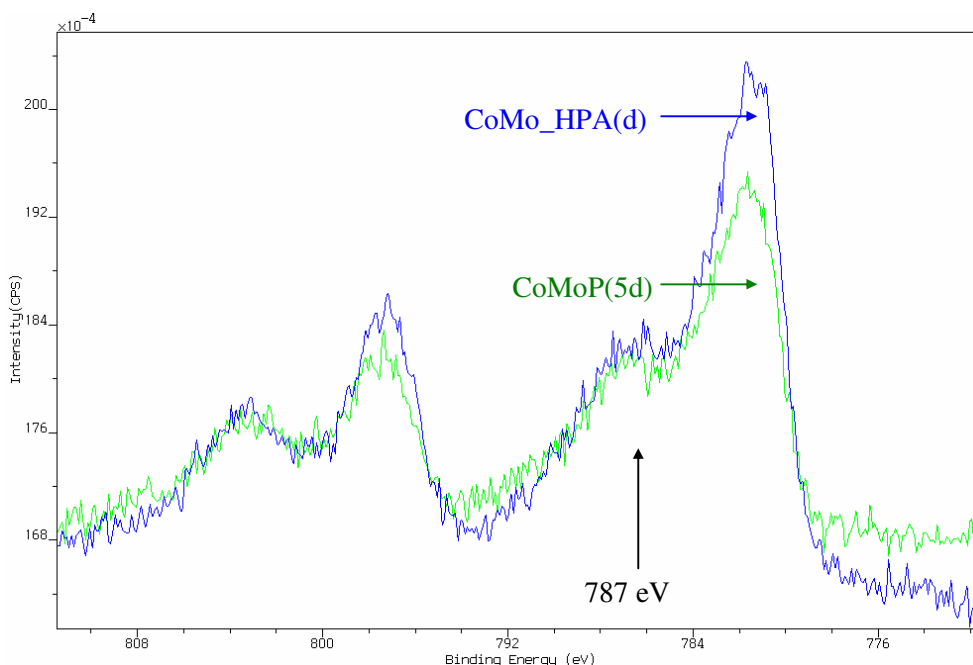


Figure III-7: Cobalt 2p XPS spectra of the CoMo_HPA(d) and CoMoP(5d) catalysts.

The decomposition thus obtained described satisfactorily the CoMo_HPA(d) and CoMo_HPA(d)+TEG catalysts spectra and no evidence of other phases like CoAl_2O_4 or CoMoO_4 was found at the catalysts surface (confirmed using XRD spectroscopy).

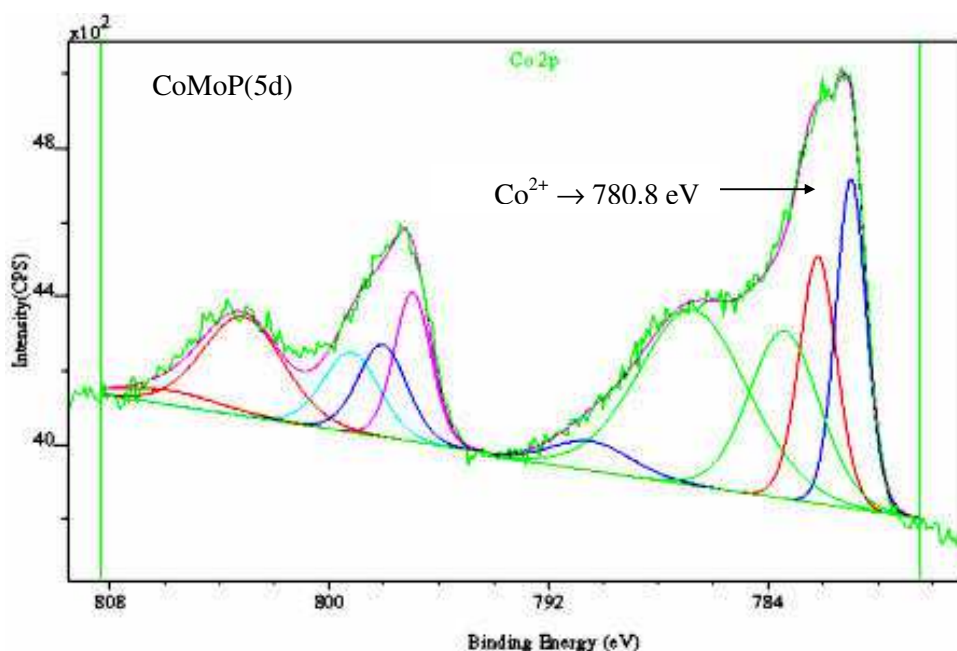


Figure III-8: Cobalt 2p XPS spectrum decomposition of the CoMoP(5d) catalyst. The upper green line corresponds to the experimental data and the red line corresponds to the fit.

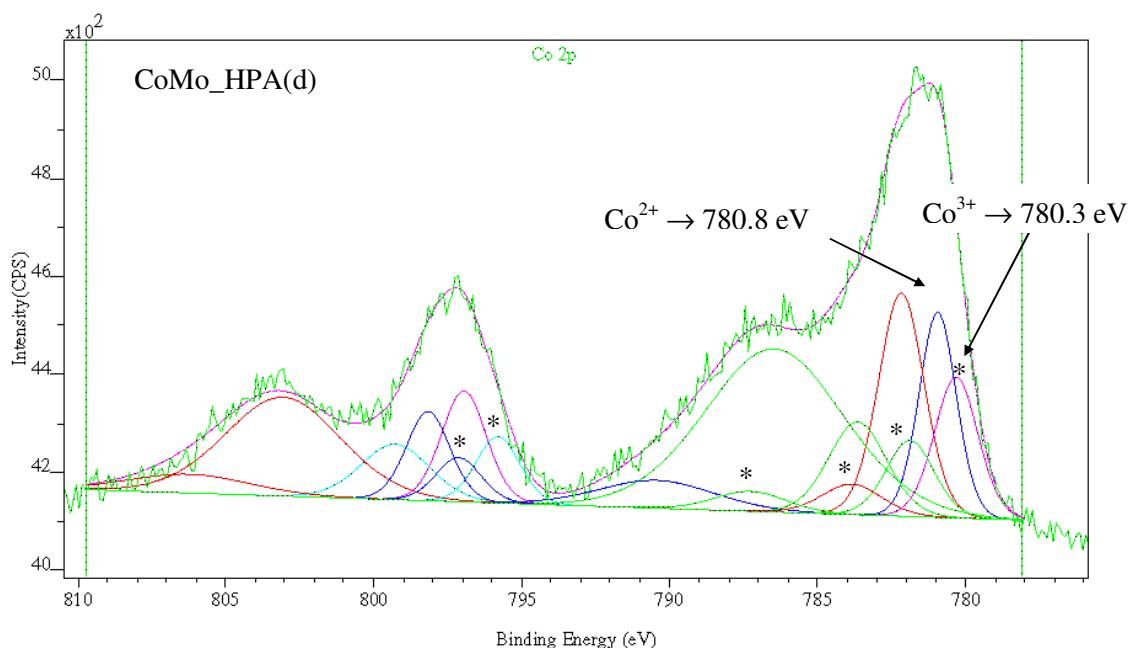


Figure III-9: Cobalt 2p XPS spectrum decomposition of the CoMo_HPA(d) catalyst. The upper green line corresponds to the experimental data and the red line corresponds to the fit. The Co^{3+} peaks are noted with *.

Using the XPS spectra decomposition, it is possible to calculate the $\text{Co}^{2+}/\text{Co}^{3+}$ ratio based on the relative areas of each contribution. The additive-free CoMo_HPA(d) catalyst reveals a 76/24 ratio. The additive-containing catalyst exhibits a slight decrease of the Co^{3+} amount ($\text{Co}^{2+}/\text{Co}^{3+}=79/21$). According to the molybdocobaltate HPA stoichiometry, the $\text{Co}^{2+}/\text{Co}^{3+}$ ratio is 60/40. The excess of Co^{2+} might be related to the HPA yield or to the ultra-vacuum used in the experimental facilities which may lead to the HPA decomposition.

In summary, no modification is observed in cobalt surface species after impregnation in the dried CoMo_AHM catalyst. For the dried CoMo_HPA catalysts, both UV-Visible and XANES spectroscopies show the presence of Co^{3+} entities, showing that the molybdocobaltate HPAs are partially preserved after the impregnation stage and that the additive leads to a slight increase of the $\text{Co}^{2+}/\text{Co}^{3+}$ proportion. Moreover, EXAFS spectroscopy shows that the additive impregnation leads to an increase of the Co(II)-O contribution on the first coordination shell, while the Co(III)-O contribution decreases. Finally, the XPS spectroscopy provides semi-quantitative information about the Co^{3+} loss due to additive impregnation, which is negligible.

III.2.2.2. Influence of the additive on molybdenum species

Raman spectroscopy was the privileged experimental method used to obtain qualitative informations about the molybdenum species in the catalysts surface. Combined with other experimental methods, like ^{27}Al NMR, XRD and X-ray Absorption spectroscopies, it is possible to extensively characterize the surface state of the catalysts in order to determine how the additive impacts on the active phase precursor structure of dried CoMo-based catalysts.

The Raman spectra of dried CoMo_AHM and CoMo_HPA catalysts are similar (Figure III-10): they exhibit bands at about 952 (intense), 900 (shoulder), 565, 355 and 220 cm^{-1} . These bands correspond to an Anderson heteropolyanion $\text{XMo}_6\text{O}_{24}\text{H}_6^{3-}$. In addition, the CoMo_AHM(d) catalyst also exhibits a band at about 1048 cm^{-1} , assigned to nitrate ions. For the HPA-based catalysts, the Raman spectra (Figure III-10) exhibits an additional shoulder at about 605 cm^{-1} attributed to $\text{Co}_3[\text{Co}_2\text{Mo}_{10}\text{O}_{38}\text{H}_4]$ [4].

After TEG impregnation, the Raman bands of the Anderson hexamolybdoaluminate species are observed in all CoMo catalysts. Besides that, a new shoulder at 830-835 cm^{-1} appears, arising from the C-O stretching vibration of TEG [15]. For the particular case of the CoMo_HPA(d) catalysts, the shoulder at 605 cm^{-1} is still visible, showing that the $\text{Co}_2\text{Mo}_{10}\text{O}_{38}\text{H}_4^{6-}$ HPA is preserved on the catalyst surface.

Table III-1: Raman shift of dried CoMo-based catalysts and reference data.

Catalysts	Main band (cm^{-1})	Other bands (cm^{-1})
CoMo_AHM(d)	952	1048, 900, 565, 355, 220
CoMo_HPA(d)	952	900, 605, 565, 355, 220
Bulk compounds [4]	Main band (cm^{-1})	Other bands (cm^{-1})
$(\text{NH}_4)_3\text{AlMo}_6\text{O}_{24}\text{H}_6$	947	900, 577, 382, 363
$\text{Co}_{3/2}\text{AlMo}_6\text{O}_{24}\text{H}_6$	947	900, 577, 382, 363
$\text{Co}_{3/2}\text{CoMo}_6\text{O}_{24}\text{H}_6$	952	920, 903, 575, 560, 355, 222
$\text{Co}_3\text{Co}_2\text{Mo}_{10}\text{O}_{38}\text{H}_4$	957	917, 602, 565, 355, 245

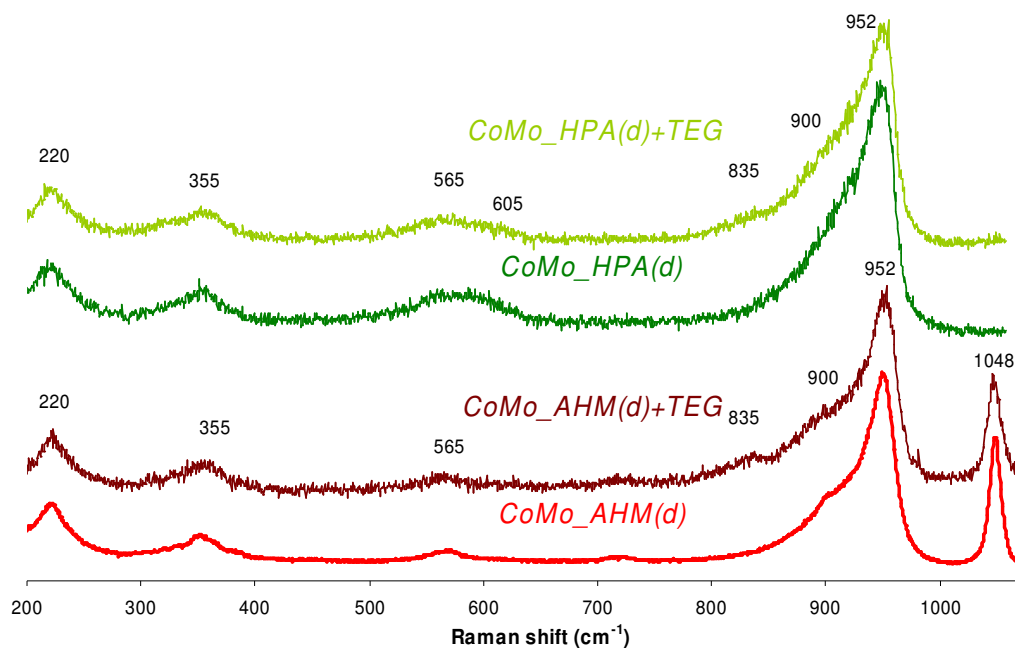


Figure III-10: Raman spectra of CoMo_AHM(d), CoMo_HPA(d) and corresponding TEG-containing catalysts.

In the case of dried CoMo_AHM(d) catalysts, Raman spectra reveal $\text{AlMo}_6\text{O}_{24}\text{H}_6^{3-}$ species. The formation of hexamolybdoaluminate [13,16] involves molybdenum-assisted dissolution of the alumina support: aluminum cations in solution react with molybdate to form $\text{AlMo}_6\text{O}_{24}\text{H}_6^{3-}$ [13]. Since hexamolybdoaluminate cobalt and ammonium salts have low solubilities (0.18 and 0.12 Mo mol/l, respectively [3,17]), they precipitate on the support surface, displacing the hexamolybdoaluminate formation equilibrium towards support dissolution, even at non-aggressive pH. As a consequence, the initial species in the impregnation solution ($\text{Mo}_7\text{O}_{24}^{6-}$) are mainly decomposed during the impregnation stage.

The Raman spectra of dried CoMo_HPA(d) catalysts is consistent with the UV-Visible, XANES and XPS data that showed the presence of Co^{3+} ions. The spectral features show the presence of both forms of the molybdocobaltate salt with Co^{2+} acting as counter-ion. Therefore, the initial species of the impregnation solutions ($\text{Co}_{3/2}[\text{CoMo}_6\text{O}_{24}\text{H}_6]$ and $\text{Co}_3[\text{Co}_2\text{Mo}_{10}\text{O}_{38}\text{H}_4]$) have been at least preserved after the impregnation and drying stages. The same bands are observed for the additive-containing sample. However, cobalt speciation showed a decrease of the Co^{3+} proportion after the additive introduction. Since the $\text{Co}_2\text{Mo}_{10}\text{O}_{38}\text{H}_4^{6-}$ Raman band arising at about 605 cm^{-1} is preserved, it is plausible to assume that $\text{CoMo}_6\text{O}_{24}\text{H}_6^{3-}$ partially decomposes to form $\text{AlMo}_6\text{O}_{24}\text{H}_6^{3-}$.

Since the Anderson HPAs $\text{CoMo}_6\text{O}_{24}\text{H}_6^{3-}$ and $\text{AlMo}_6\text{O}_{24}\text{H}_6^{3-}$ give rise to same Raman features, this experimental technique does not distinguish between these two species. For this reason, NMR analyses were conducted to evidence the presence of hexamolybdoaluminate species on the support surface.

The ^{27}Al MAS NMR spectra for alumina and AHM-based catalysts (Figure III-11, left) show the same proportion of 80/20 between hexacoordinated (resonance between 20 and -20 ppm) and tetraordinated aluminium atoms (resonance between 90 and 50 ppm). The additive-free and additive-containing spectra are quite similar, exhibiting the same features. These inconclusive results were the motivation to conduct $^{27}\text{Al}/^1\text{H}$ Cross-Polarization MAS NMR analyses. In this case, only aluminium atoms in dipolar contact with hydrogen atoms will be detected. Basically, they correspond to the surface aluminium atoms. The CP spectra (Figure III-11, right) reveal a strong broad resonance in between -20 and 20 ppm and a weaker broad resonance between 40 and 80 ppm. However, the signal to noise ratio is too important to draw further conclusions.

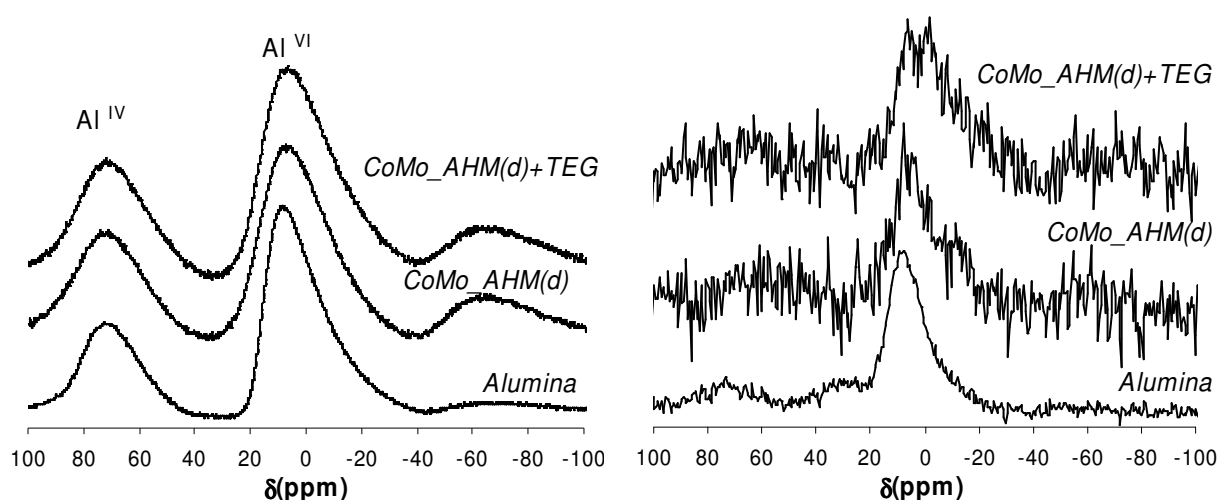


Figure III-11: ^{27}Al MAS NMR spectra (left) and $^{27}\text{Al}/^1\text{H}$ CP MAS NMR spectra of alumina, CoMo_AHM(d) and corresponding additive-containing catalyst.

The detection of hexamolybdoaluminates species on alumina-supported samples using ^{27}Al MAS NMR is a difficult task because the signal that arises from the central aluminum in $\text{AlMo}_6\text{O}_{24}\text{H}_6^{3-}$ species is weak in comparison to the strong signal of the aluminium atoms of alumina support [18]. For this reason, all the acquired spectra are quite identical.

With respect to the $^{27}\text{Al}/^1\text{H}$ CP MAS NMR, Carrier *et al.* [18,19] showed that this analysis is particularly suited for hexamolybdoaluminate HPA detection, because the central Al atom is bonded to 6 hydroxyl groups. The subtraction CP spectrum of an alumina impregnated with AHM at pH 4 and bare alumina showed a narrow peak at about 15.6 ppm [18]. This peak was attributed to the Anderson HPA. As mentioned above, this feature could not be observed in our samples.

Another approach was then used to detect the Anderson HPAs entities. Published studies used XRD measurements combined with transmission electron microscopy (TEM) to observe and identify hexamolybdoaluminates [7] and molybdocobaltates crystallites [20]. Such methods are suitable if the

HPA-based salts are precipitated onto the alumina surface and if the size of the salt crystallites is higher than few nanometers. In our case, TEM analysis on both the additive-free and additive-containing dried CoMo catalysts show a strong heterogeneity which clearly indicates that the analyzed catalysts have more than one phase. No evidence of $\text{AlMo}_6\text{O}_{24}\text{H}_6^{3-}$, $\text{CoMo}_6\text{O}_{24}\text{H}_6^{3-}$ or $\text{Co}_2\text{Mo}_{10}\text{O}_{38}\text{H}_4^{6-}$ crystallites was found.

However, XRD analysis for the CoMo_AHM(d) and CoMo_AHM(d)+TEG catalysts (Figure III-12) showed a strong and sharp diffraction peak at about 18° . Besides that feature, a peak at 8° is also observed which is described in the Sumitomo application patent [21] as a characteristic of the additive-containing catalysts. As shown in Figure III-12, this peak is also characteristic of hexamolybdoaluminate HPA, and was observed as well by Mazoyer-Galliou [7]. No evidence of oxide phases (CoMoO_4 , MoO_3 or CoAl_2O_4) is observed. The patterns also show that after the additive impregnation, a broad diffusion peak corresponding to an amorphous phase arises from 20 to 25° . A TEG-saturated catalyst (TEG/Mo molar ratio of about 2.5) was also analyzed to reveal the additive effect in the XRD pattern. In this case, all the crystallized phases disappeared and the signal from 20 to 25° increases drastically.

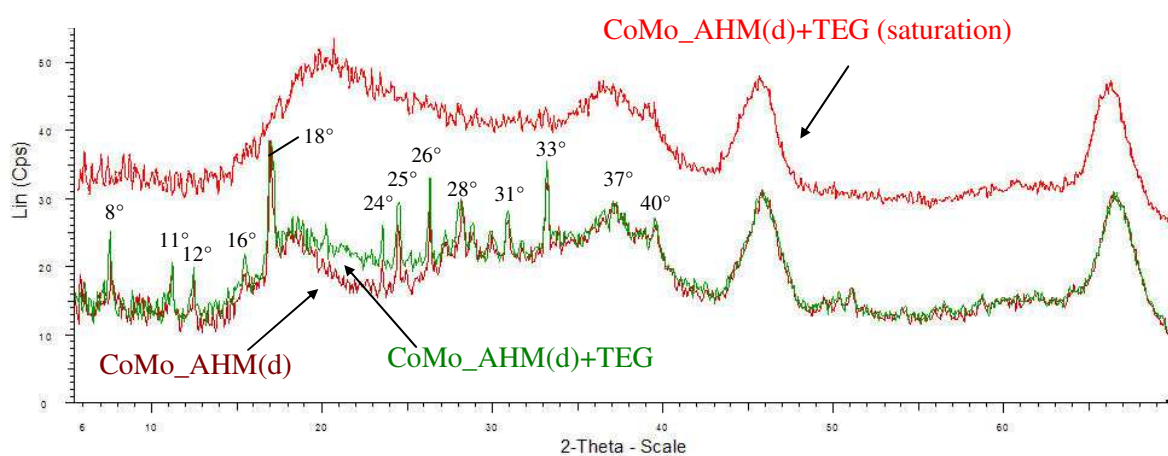


Figure III-12: X-ray Diffraction patterns for CoMo_AHM(d), CoMo_AHM(d)+TEG and CoMo_AHM(d) saturated with TEG.

The XRD patterns show that crystallites containing the hexamolybdoaluminate HPA are present in the alumina porosity. Indeed, it precipitates during the impregnation stage forming needle-shaped crystallites [7]. However, when an excess of TEG is impregnated on the catalyst, all crystallized phases disappear in the XRD pattern, meaning that the additive favors the formation of smaller HPA aggregates. As a consequence, TEG addition leads to an improved dispersion of molybdenum-containing species.

Molybdenum K-edge XAS analyses were also conducted on dried CoMo catalysts to determine if the additive modifies the nature of the molybdenum surface species. XANES was used to follow the evolution in the molybdenum oxidation state and geometry and EXAFS to characterize the local molybdenum environment.

The molybdenum K-edge XANES possesses the same pre-edge peak for all dried CoMo catalysts (Figure III-13, left) and corresponding additive-containing catalyst (not reported here).

As mentioned previously, the oxygen shells of the polyoxoanions are quite difficult to fit in EXAFS due to their spread Mo-O distance [13, 14]. For this reason, the Mo EXAFS will focus on qualitative aspects. The molybdenum K-edge k^3 -weighed EXAFS FT of dried CoMo catalysts (Figure III-13, right) show that both the first oxygen shell (0.5-2.5 Å, not phase corrected) and the second shell (2.5-3.5 Å, not phase corrected) around molybdenum are not affected by the additive. Furthermore, the FT functions of the CoMo AHM-based and HPA-based catalysts are identical.

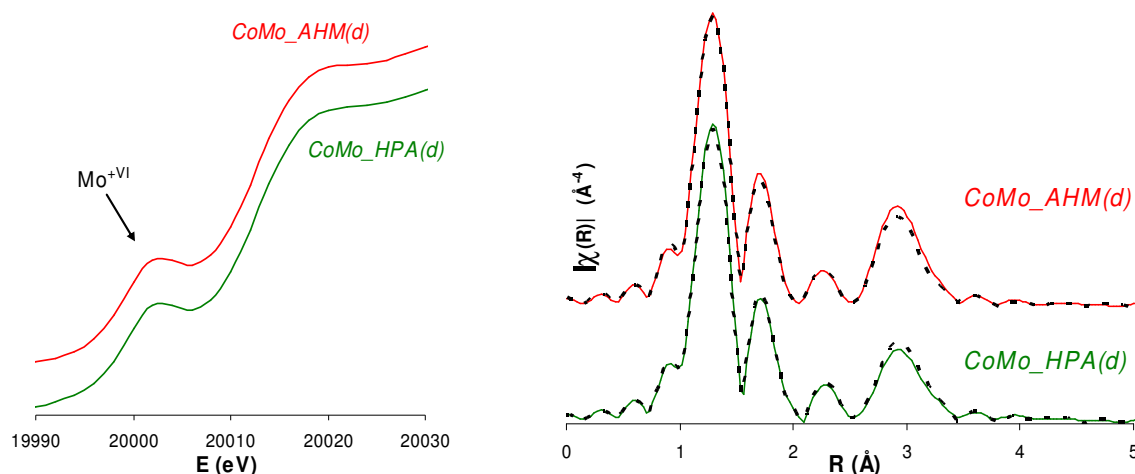


Figure III-13: Mo K-edge XANES (left) and k^3 -weighted EXAFS Fourier Transforms (FT) (right) of CoMo_AHM(d), CoMo_HPA(d) (— solid lines) and corresponding additive-containing catalysts (--- dashed lines). FT Hanning window from 3 to 13; $\tau=2.5$.

The observed pre-edge peak is associated to an octahedral symmetry and to 6+ oxidation state for molybdenum [12,22]. A direct interpretation is that this element does not change their oxidation state or local geometry after the additive impregnation. In terms of EXAFS, the FT of dried CoMo catalysts confirmed the Raman observations where the molybdenum structure is not affected by the additive. Moreover, the fact that all samples have similar spectra is not surprising since surface species are Anderson-like HPAs that have similar structures with respect to molybdenum.

Combining the molybdenum and the cobalt speciation, it is possible to establish the relation between impregnation solution species and the surfaces species nature prior to and after the additive impregnation (Table III-2).

Table III-2: Speciation results for CoMo precursor solutions and dried catalysts prior to and after TEG impregnation.

	Solution	Before TEG	After TEG
CoMo_AHM(d)	$[\text{Co}(\text{H}_2\text{O})_6]^{2+}$ NH_4^+ $\text{Mo}_7\text{O}_{24}^{6-}$ NO_3^-	$(\text{NH}_4, \text{Co})[\text{AlMo}_6\text{O}_{24}\text{H}_6]$ NH_4NO_3 $\text{Co}(\text{NO}_3)_2$	$(\text{NH}_4, \text{Co})[\text{AlMo}_6\text{O}_{24}\text{H}_6]$ NH_4NO_3 $\text{Co}(\text{NO}_3)_2$
CoMo_HPA(d)	$[\text{Co}(\text{H}_2\text{O})_6]^{2+}$ $[\text{CoMo}_6\text{O}_{24}\text{H}_6]^{3-}$ $[\text{Co}_2\text{Mo}_{10}\text{O}_{38}\text{H}_4]^{6-}$	$\text{Co}_{3/2}[\text{CoMo}_6\text{O}_{24}\text{H}_6]$ $\text{Co}_3[\text{Co}_2\text{Mo}_{10}\text{O}_{38}\text{H}_4]$	$\text{Co}_{3/2}[\text{AlMo}_6\text{O}_{24}\text{H}_6]$ $\text{Co}_{3/2}[\text{CoMo}_6\text{O}_{24}\text{H}_6]$ $\text{Co}_3[\text{Co}_2\text{Mo}_{10}\text{O}_{38}\text{H}_4]$

III.2.3. THERMAL BEHAVIOR

Thermogravimetric analysis (TGA) is carried out to study the temperature stability domain of the different surface species and how they are affected by the additive. In this sense, the additive-free catalysts are firstly analyzed and the collected data will then be used to interpret the analysis results for the additive-containing catalysts.

The derivative thermogravimetry (DTG) curves are calculated from the thermogravimetric analysis and then decomposed into linear combinations of Lorentz curves. Like in all the regression methods that comprise more than one inflexion, the decompositions should be interpreted as possible but not unique. A detailed description of the model is reported to Appendix C.

III.2.3.1. Additive-free dried CoMo catalysts analysis

An alumina that was only impregnated with ammonium heptamolybdate (18 wt% MoO_3), noted Mo_AHM(d), was first analyzed to be used as a reference. Then, the CoMo_AHM(d) catalysts was analyzed and finally the CoMo_HPA(d).

The reference Mo_AHM(d) sample revealed a total loss of 15.0 wt% with a DTG minimum at about 100 °C, corresponding to water removal, as shown by mass spectroscopy (Figure III-14).

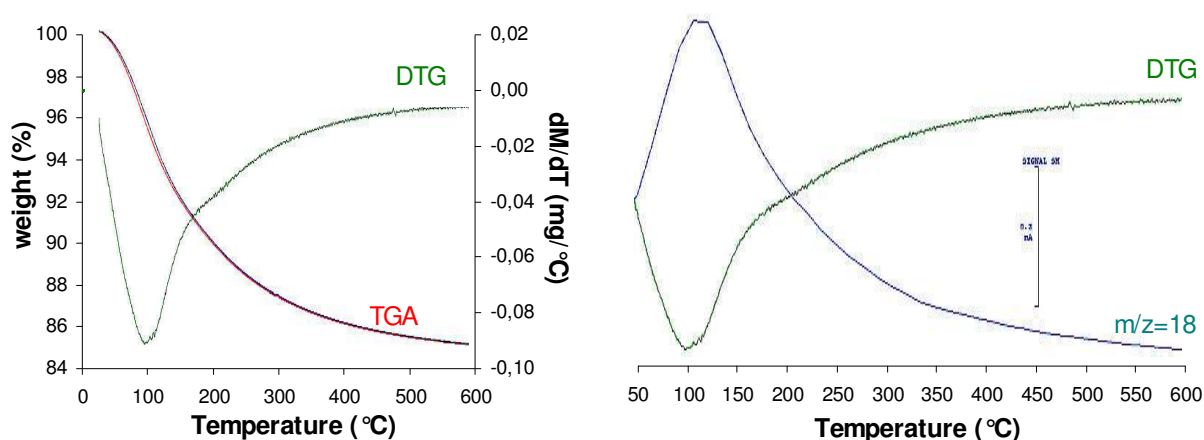


Figure III-14: Thermogravimetric analysis (TGA), derivative thermogravimetry (DTG) and mass spectroscopy results (right) of the Mo_AHM(d) sample.

Figure III-15 shows the TGA results of the CoMo_AHM(d) sample. It reveals a total loss of 18.6 wt% and the DTG shows two local minimums at about 100 and 250 °C and a shoulder at about 320 °C. The mass spectroscopy reveals continuous water removal, with a maximum at about 250 °C. An important N_2O depart ($m/z=44$) is also detected, starting at about 200 °C with a maximum at about 250 °C. A third mass fragment assigned to NO ($m/z=30$) is also detected with a maximum in the 350-400 °C region.

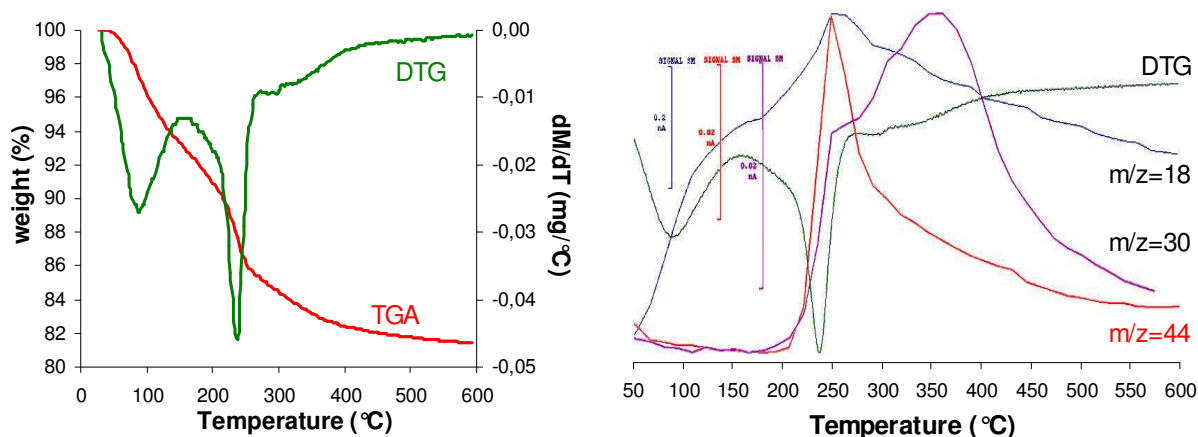


Figure III-15: Thermogravimetric analysis (TGA), derivative thermogravimetry (DTG) and mass spectroscopy results (right) of the CoMo_AHM(d) sample.

In order to obtain more precise qualitative and qualitative information about the thermal stability of the surface species on the catalysts, the DTGs are decomposed according to the above-mentioned method. For the sake of simplicity, the decomposition plots are inverted.

On the one hand, the dried Mo_AHM(d) sample DTG is decomposed into 3 contributions. They are centered at about 96, 207 and 308 °C that correspond to weight losses of 10.6, 3.3 and 0.9%, respectively (Figure III-16, left). On the other hand, the dried CoMo_AHM(d) sample shows 4 contributions centered at about 90, 202, 236 and 320 °C. They correspond to weight losses of 7.9, 4.0, 3.5 and 2.2%, respectively (Figure III-16, right).

The first curve in both samples DTG decompositions is assigned to physisorbed water. Based on the water removal shown in mass spectroscopy, the curve centered at about 205 °C is assigned to coordination water of the $\text{AlMo}_6\text{O}_{24}\text{H}_6^{3-}$ HPA [4]. According to the literature [18], the Anderson-type HPAs are fully destroyed between 230 and 250 °C giving rise to the so-called constitutional water. The curve centered at 236 °C in the CoMo_AHM(d) sample is assigned to the nitrate ions decomposition because this contribution is not observed in the reference dried Mo catalyst, which does not contain nitrate ions. Moreover, mass spectroscopy reveals mass fragments m/z 30 and 44 in this region, assigned to N_2O and NO, two possible decomposition products of nitrate ions. Finally, the curve centered at 320 °C results from the NH_4^+ decomposition, in agreement with the literature [4].

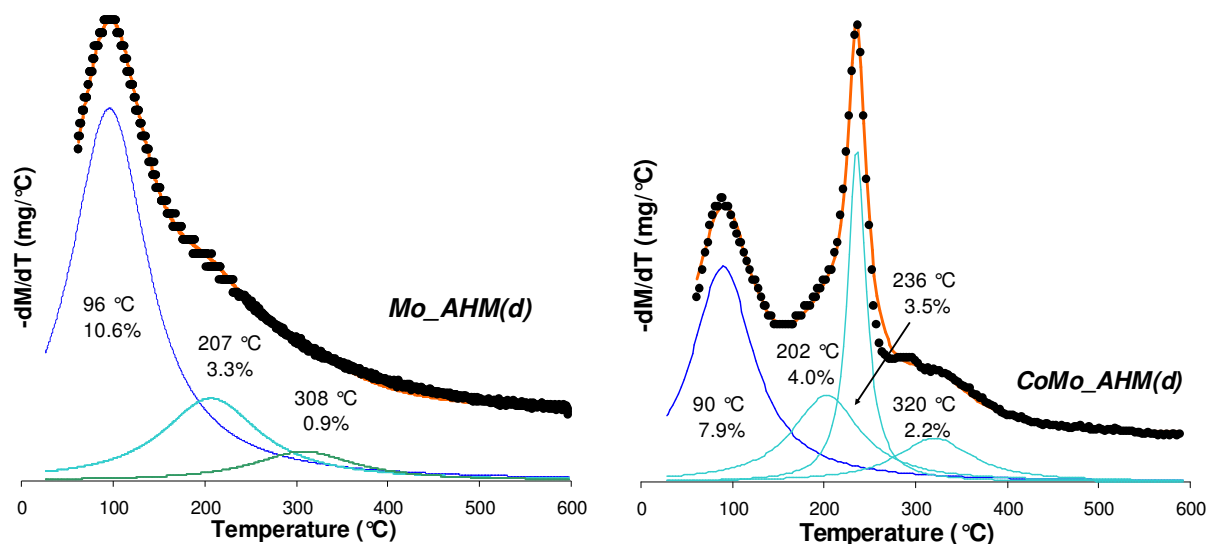


Figure III-16: *Mo_AHM(d)* (left) and *CoMo_AHM(d)* (right) samples DTG decompositions.

To verify the validity of DTG decompositions as well as the assignments made, the experimental data is compared to the expected weight losses assuming a 100% yield for HPA formation from molybdenum. According to the literature [4], the ammonium and cobalt hexamolybdoaluminate salts decompose in oxidic atmosphere according to the following reactions:

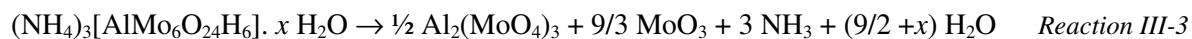


Table III-3 and Table III-4 presents the comparison between the experimental data and expected weight losses.

Table III-3: DTG decomposition assignments of the *Mo_AHM(d)* sample.

T (°C)	Experimental weight loss (%)	Assignment	Expected weight loss (%)
96	10.6	Physisorbed water	-
207	3.3	HPA coordination water	-
		HPA constitution water	1.4
308	0.9	NH ₃ (from ammonium ions)	1.6

Table III-4: DTG decomposition assignments of the *CoMo_AHM(d)* sample.

T (°C)	Experimental weight loss (%)	Assignment	Expected weight loss (%)
90	7.9	Physisorbed water	-
202	4.0	HPA coordination water	-
		HPA constitutional water	1.0
236	3.5	N ₂ O and NO (from nitrate ions)	4.5
320	2.2	NH ₃ (from ammonium ions)	1.4

The CoMo_HPA(d) sample revealed a total loss of 14.7 wt% with a DTG minimum at about 100 °C, corresponding to water depart as shown by the mass spectroscopy (Figure III-17). A shoulder in the DTG is also detected at about 215 °C.

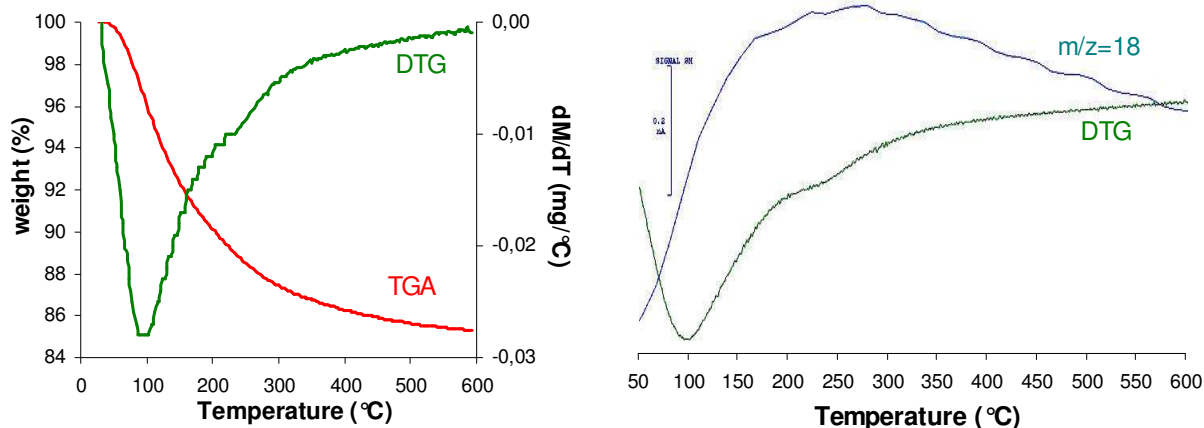


Figure III-17: Thermogravimetric analysis (TGA), derivative thermogravimetry (DTG) and mass spectroscopy results (right) of the CoMo_HPA(d) sample.

The DTG of the CoMo_HPA(d) is decomposed into 2 contributions (Figure III-18). The first contribution is centered at about 95 °C and corresponds to a weight loss of 11.6%. The second contribution is centered at about 215 °C and corresponds to 3.1 wt%. Based on the mass spectroscopy results, the first contribution is attributed to physisorbed water and the second contribution is assigned to the coordination water of the $\text{CoMo}_6\text{O}_{24}\text{H}_6^{3-}$ HPA.

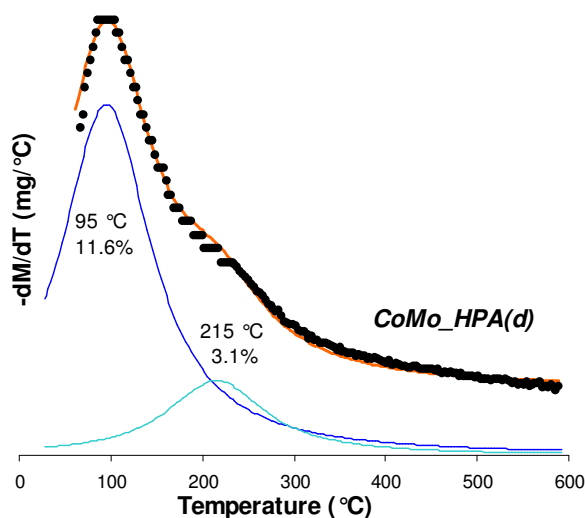


Figure III-18: DTG decomposition of the CoMo_HPA(d) catalyst.

According to the literature [4], cobalt HPA salts decompose according to the following reactions:

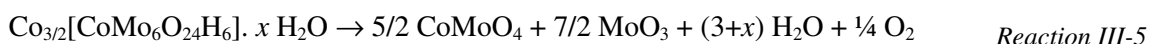


Table III-5 presents the comparison between the experimental data and expected weight losses. A 100% yield in the $\text{Co}_3[\text{Co}_2\text{Mo}_{10}\text{O}_{38}\text{H}_4]$ salt is considered.

Table III-5: DTG decomposition assignments of the CoMo_HPA(d) sample.

T (°C)	Experimental weight loss (%)	Assignment	Expected weight loss (%)
95	11.6	Physisorbed water	-
215	3.1	HPA coordination water	-
		HPA constitution water	0.4
		O ₂	0.1

III.2.3.2. Additive-containing dried CoMo catalysts analysis

To study if the additive modifies the temperature stability domain of the deposited surface species, the additive-containing Mo_AHM(d) and CoMo_HPA(d) catalysts are analyzed.

The Mo_AHM(d)+TEG sample revealed a total loss of 21.8 wt% with two local DTG minimums at about 75 and 220 °C (Figure III-19). Mass spectroscopy reveals a major water depart before 100 °C and two mass fragments centered at about 250 °C for the m/z 44 (CO₂) and 58 (ketone-type) (Figure III-19, right).

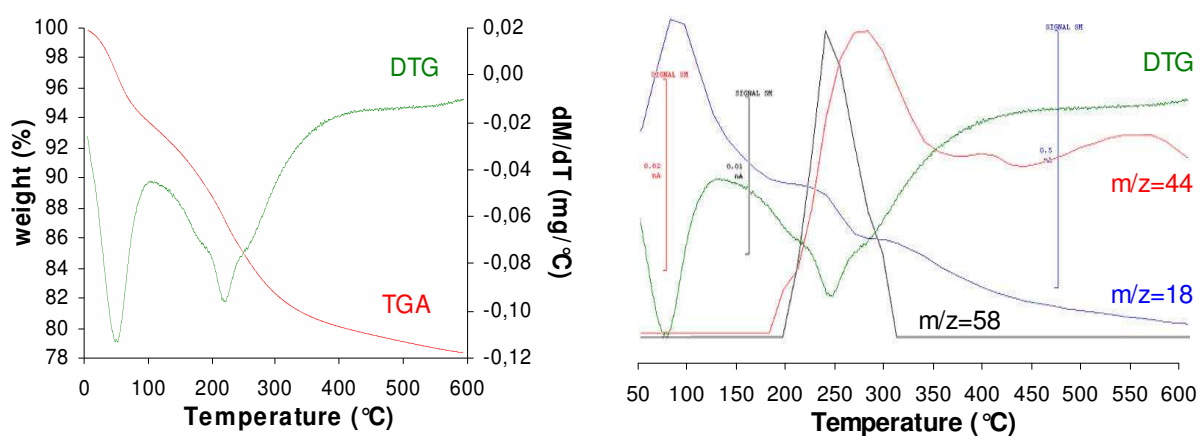


Figure III-19: Thermogravimetric analysis (TGA), derivative thermogravimetry (DTG) and mass spectroscopy results (right) of the Mo_AHM(d) sample.

The dried Mo_AHM(d)+TEG sample DTG is decomposed into 5 contributions. They are centered at about 74, 176, 220, 244 and 289 °C that correspond to weight losses of 7.2, 2.2, 4.3, 2.5 and 5.6%, respectively (Figure III-20).

Mass spectroscopy results suggest that the first two DTG decomposition curves correspond to water depart: the first assigned to physisorbed water and the second coordination water of the $\text{AlMo}_6\text{O}_{24}\text{H}_6^{3-}$ HPA. When compared to the additive-free catalyst, the water removal occurs at lower temperatures. The other three curves are assigned to the thermal decomposition products of TEG, as suggested by the mass fragments 44 and 58. Thus, the sum of the three contributions corresponds to 12.4 wt% whereas the amount of TEG measured by CHNS elemental analysis in the fresh catalyst is 11.5 wt%.

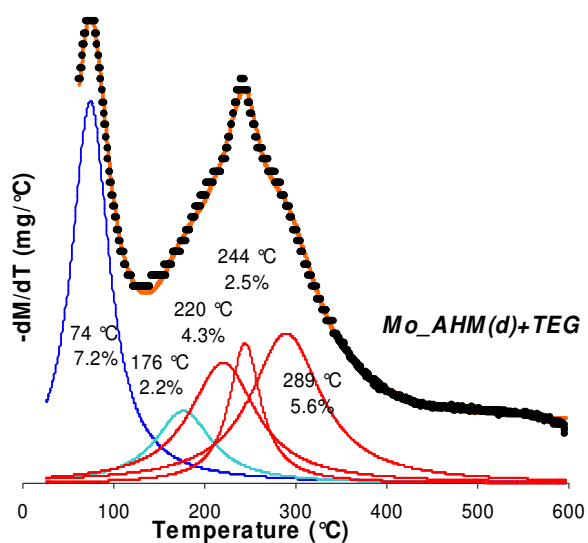


Figure III-20: DTG decomposition of the Mo_AHM(d)+TEG sample.

Using Reaction III-3 it is possible to establish a comparison between the experimental and the expected weight losses:

Table III-6: DTG decomposition assignments of the Mo_AHM(d)+TEG sample.

T (°C)	Experimental weight loss (%)	Assignment	Expected weight loss (%)
74	7.2	Physisorbed water	-
176	2.2	HPA coordination water	-
		HPA constitutional water	1.3
220	4.3	TEG (sum=12.4%)	11.5
244	2.5		
289	5.6		

The CoMo_HPA(d)+TEG sample revealed a total loss of 21.1 wt% with two DTG local minimums at about 80 and 250 °C (Figure III-21). The mass spectroscopy reveals a major water depart before 100 °C and four mass fragments centered at about 250 °C for the m/z 12 (carbon), 44 (CO_2), and 58 (ketone-type) (Figure III-21, right).

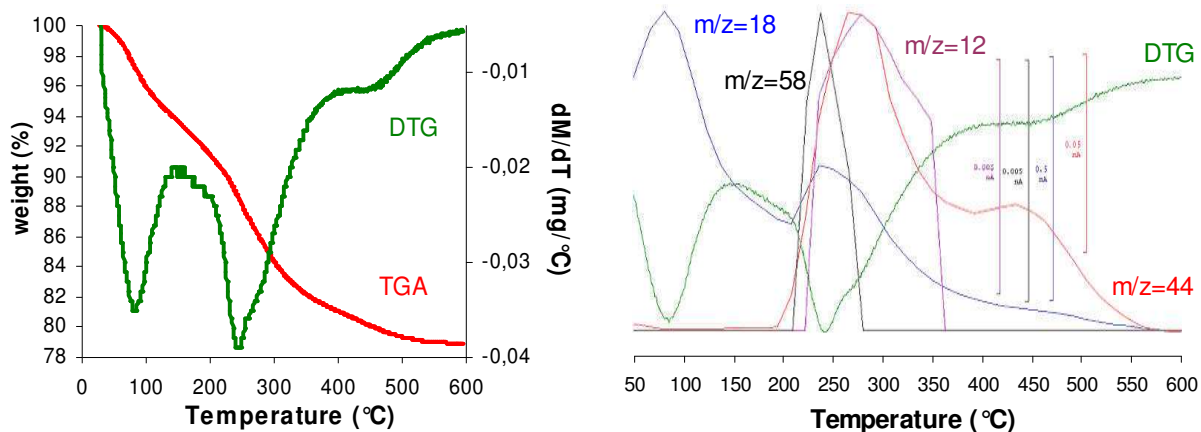


Figure III-21: Thermogravimetric analysis (TGA), derivative thermogravimetry (DTG) and mass spectroscopy results (right) of the CoMo_HPA(d)+TEG sample.

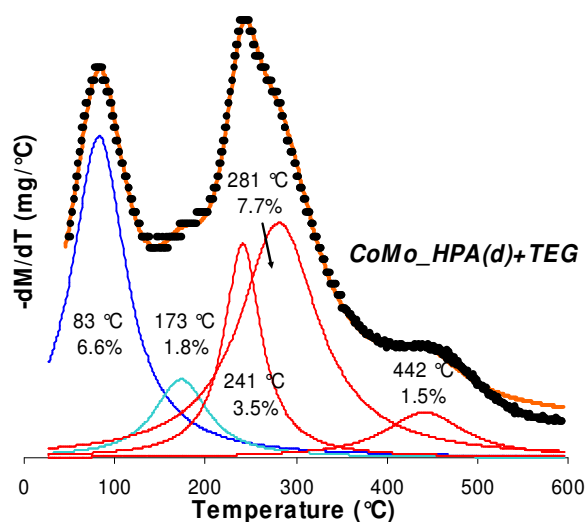


Figure III-22: DTG decomposition of the CoMo_HPA(d)+TEG catalyst.

Based on the mass spectroscopy results, the first contribution is attributed to physisorbed water and the second contribution is assigned to coordination water of the existing HPAs. The other three contributions are assigned to the decomposition products of TEG.

Table III-7 presents the comparison between the experimental data and expected weight losses. It was assumed that all molybdenum is in the $\text{Co}_3[\text{Co}_2\text{Mo}_{10}\text{O}_{38}\text{H}_4]$ salt and that the HPA decomposes according to Reaction III-6.

Table III-7: DTG decomposition assignments of the CoMo_HPA(d)+TEG sample.

T (°C)	Experimental weight loss (%)	Assignment	Expected weight loss (%)
83	6.6	Physisorbed water	-
173	1.8	HPA coordination water	-
		HPA constitution water	0.3
		O ₂	0.2
241	3.5		
281	7.7	TEG (sum=12.7%)	10.2
442	1.5		

III.2.4. SURFACE MECHANISM

Based on the speciation results and the additive physico-chemical properties, it becomes possible to suggest a mechanism for the additive effect on the active phase precursor structures.

Prior to additive impregnation, the surface species on the support for the dried CoMo_AHM catalyst are mainly hexamolybdoaluminates heteropolyanions. When the additive impregnation is performed, the surface species are redissolved and consequently transported throughout the catalyst body. Due to the low solubility of the $\text{Co}_{3/2}[\text{AlMo}_6\text{O}_{24}\text{H}_6]$ salt (0.18 mol Mo/l [4]), they precipitate even during the ageing stage and displace the alumina dissolution equilibrium towards the HPA formation. The proposed redispersion mechanism is in agreement with the literature [18], where the hexamolybdoaluminate formation was observed after rehydration of a calcined catalyst. The final preparation step for this catalyst, the drying stage, forces all species in solution to precipitate while the water solvent evaporates. Moreover, our XRD results showed that the additive favors the formation of smaller HPA aggregates and, as a consequence, leads to an improved dispersion of molybdenum-containing species. TEG mainly acts as a solvent: the redispersion of the surface species is favored by the additive physical properties. A schematic representation is shown in Figure III-23.

The mechanism for the dried CoMo_HPA catalyst is quite similar to the AHM-based catalysts. Raman characterization showed the presence of both forms of the molybdocobaltate HPA with the Co^{2+} acting as counter-ion. After the additive impregnation, $\text{CoMo}_6\text{O}_{24}\text{H}_6^{3-}$ partially decomposes to form polymolybdates and then after to form $\text{AlMo}_6\text{O}_{24}\text{H}_6^{3-}$ through support dissolution. Thus, the HPAs are redispersed and preserved after the final drying stage.

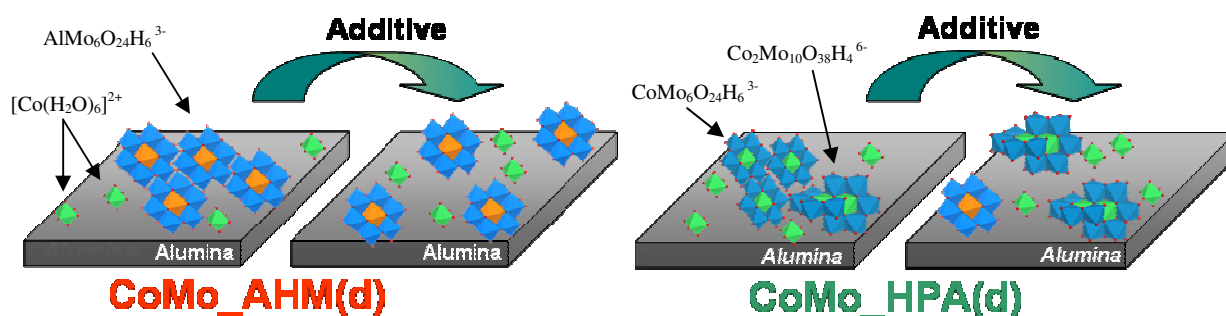


Figure III-23: Schematic representations of the redispersion mechanism induced by the additive for the dried CoMo_AHM(d) and CoMo_HPA(d) catalysts.

III.3. IMPACT OF THE ADDITIVE WHEN IMPREGNATED ON DRIED CoMoP CATALYSTS

The objective of this section is to determine if and how the CoMoP catalysts surface species are modified after the additive impregnation. To do so, catalysts were prepared with 3 different P/Mo ratios by aqueous dissolution of MoO_3 , $\text{Co}(\text{OH})_2$ and H_3PO_4 . In a first step, the solutions are characterized to establish a relation between the solution precursors and species in solution. Then, the surface species on the prepared dried CoMo catalysts are characterized prior to and after additive impregnation.

III.3.1. SPECIATION OF THE PRECURSOR IMPREGNATION SOLUTIONS

In order to study the nature of cobalt, molybdenum and phosphorus species during impregnation, the precursor solutions were analyzed. This study allows to evidence some of the differences between the studied systems. For this purpose, cobalt species were studied by UV-Visible spectroscopy, molybdenum species by Raman spectroscopy and phosphorus species by ^{31}P NMR.

The CoMoP(1) precursor solution (P/Mo=0.11, red) has a pH value near 4 and a molybdenum concentration of 1.9 M, 0.8 M for cobalt and 0.2 M for phosphorus. The CoMoP(3) precursor solution (P/Mo=0.40, green) has a pH value near 1 and a molybdenum concentration of 2.0 M, 0.8 M for cobalt and 0.8 M for phosphorus. The CoMoP(5) precursor solution (P/Mo=0.57, blue) also has a pH value near 1 and a molybdenum concentration of 2.0 M, 0.8 M for cobalt and 1.2 M for phosphorus.

The UV-Visible spectroscopies (Figure III-24) of all CoMoP precursor solutions reveal a shoulder at about 513 nm. Besides this band, the CoMoP(3) and CoMoP(5) solutions show a broad signal in the 600-900 nm region. For the particular case of the CoMoP(1) solution, a band is observed at about 564 nm.

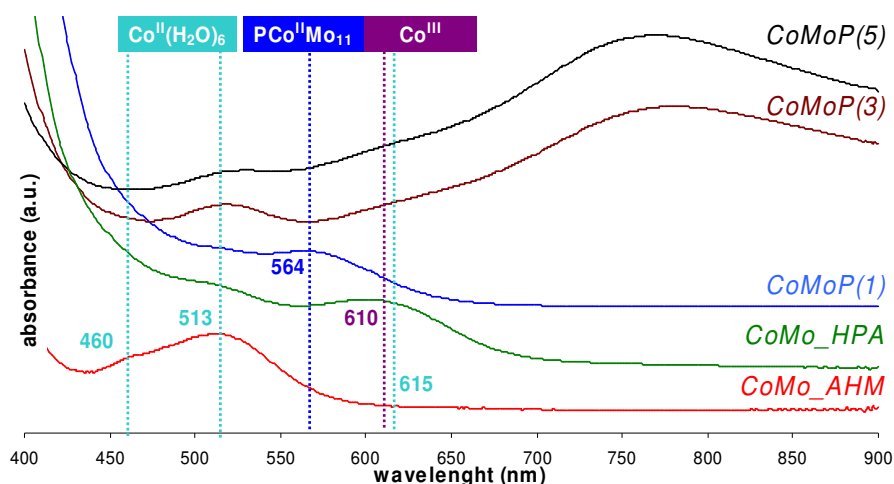


Figure III-24: UV-Visible spectra of: (a) CoMo_AHM, (b) CoMo_HPA, (c) CoMoP(1), (d) CoMoP(3) and (e) CoMoP(5) precursor solutions.

The band centered at 513 nm, as well as the shoulders at 460 and 615 nm, also observed in the CoMo-based solutions, is typical of a Co(II) d-d electronic transition in an octahedral environment [1,2]. This band is attributed to the Co(II) aquacomplex acting as counter-ion. The band observed at about 564 nm for the CoMoP(1) solutions is assigned to a Co(II) d-d electronic transition in a distorted octahedral environment [23], typical of the $\text{PCoMo}_{11}\text{O}_{40}^{7-}$ HPA.

The wide band in the 600-900 nm region, observed for the CoMoP solutions with a P/Mo molar ratio superior to 2/5 is assigned to a reduced compound. The same broad band was reported in the literature for the 4-electron reduced Keggin $\text{PMo}_{12}\text{O}_{40}^{3-}$ HPA [24]. It is well established that some HPAs may exchange electrons in multiple reversible steps and that reduced entities are stabilized by acidic pH [25]. In order to verify if the observed band arises from a reduced HPA form, solutions were prepared using different combinations of the solutions precursors. Therefore, Mo, MoP and CoP solutions were prepared and analyzed. The solutions spectra thus prepared are plotted in Figure III-25.

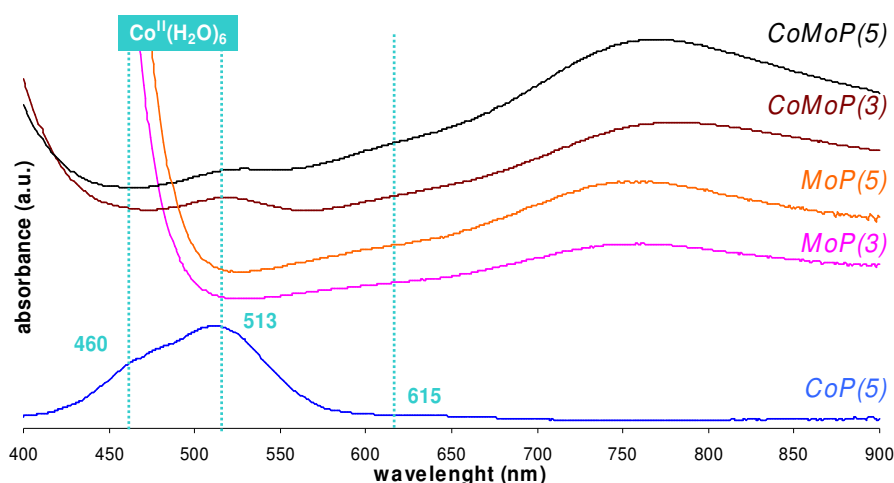


Figure III-25: UV-Visible spectra of: (a) CoP(5), (b) MoP(3), (c) MoP(5), (d) CoMoP(3) and (e) CoMoP(5) solutions.

The CoP(5) solution, in which Co and P concentrations are the same as in the CoMoP(5) solution and has a pH value near 0, does not exhibit the broad band in the 600-900 nm region. This means that molybdenum and phosphorus are necessarily involved in the reduced species responsible for this band. Thus, the MoP(3) and MoP(5) solutions exhibit this band, meaning that cobalt is not indispensable to form this reduced HPA. For these reasons, the band was assigned to the reduced Keggin $\text{PMo}_{12}\text{O}_{40}^{3-}$ HPA.

To obtain more precise information about molybdenum-containing entities, the CoMoP precursor solutions are analyzed by Raman spectroscopy. The Raman spectra of the CoMoP(5) and CoMoP(3) solutions (Figure III-26) show a weak sharp band at about 977 cm^{-1} and a weak broad band at about 720 cm^{-1} , corresponding to a Dawson $\text{P}_2\text{Mo}_{18}\text{O}_{62}^{6-}$ HPA [26,27]. However, the main species in solution

is the diphosphopentamolybdate HPA, revealed by an intense sharp band at about 944 cm^{-1} and smaller bands at 899 , 375 and 223 cm^{-1} [28]. The Raman spectrum of the CoMoP(1) solution is rather different than the previous, revealing an intense band at about 973 cm^{-1} and a broad bands at about 880 , 608 and 228 cm^{-1} , typical features of the $\text{PCoMo}_{11}\text{O}_{40}^{7-}$ HPA. The fact that this anion is not observed on the CoMoP(5) and CoMoP(3) solutions spectra is explained by the acidic pH of the solutions, well outside the pH stability range of this HPA, which is between 4 and 5 [25].

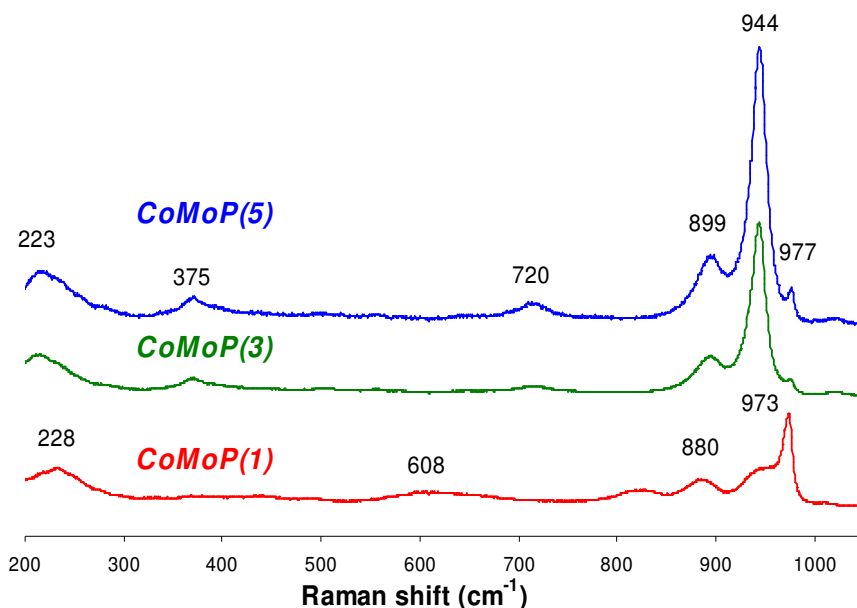


Figure III-26: Raman spectra of the CoMoP precursor solutions.

^{31}P NMR experiments were then conducted to infer about the phosphoric species in solution and thus refine the HPA species distribution, mainly because some of the Raman bands may be hidden by the strong $\text{P}_2\text{Mo}_5\text{O}_{23}^{6-}$ signal of the CoMoP(5) and CoMoP(3) solutions.

It is well known that when paramagnetic atoms, like cobalt, are in close proximity to the atom being studied, broadening and shifting of the NMR signal are typically observed. For this reason, NMR studies were conducted over unpromoted MoP solutions using the same molybdenum and phosphorus concentrations as for the CoMoP solutions. The ^{31}P NMR spectra of the MoP(5), MoP(3) and MoP(2) solutions are plotted in Figure III-27, left image. Spectra (a), (b) and (c) exhibit 3 signals at about 2.0, 0.5 and -1.0 ppm. However, these solutions are more acidic than the CoMoP solutions due to the absence of cobalt hydroxide. For this reason, dilutions to the MoP solutions were made until the original CoMoP solutions pH was reached. The spectra resonances on the diluted solutions (Figure III-27, right) are basically the same although the peak positions are shifted upfield. In addition, a new peak is observed at about -2.0 ppm.

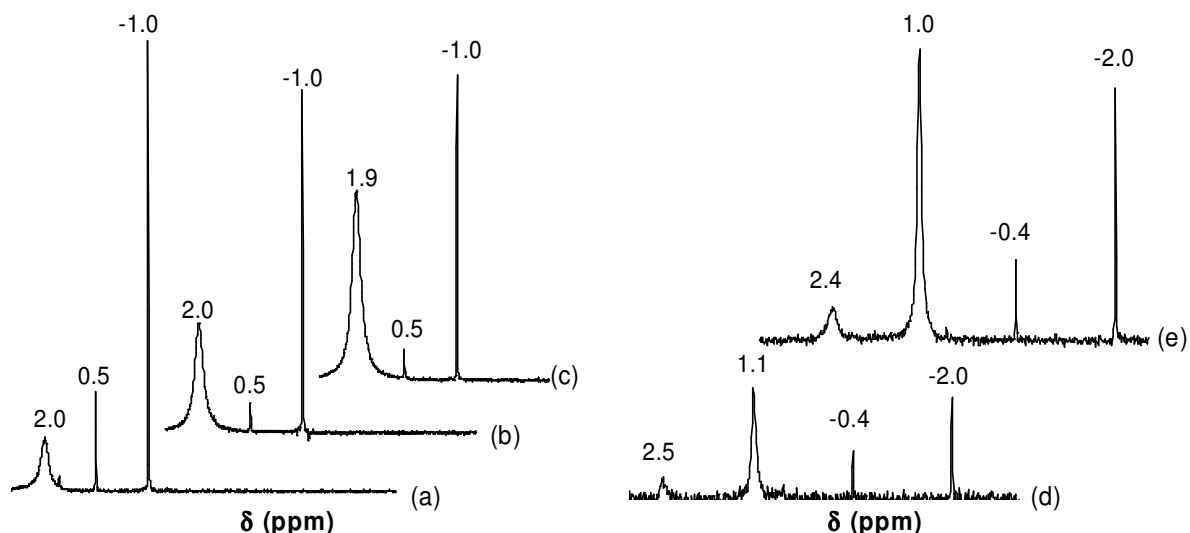
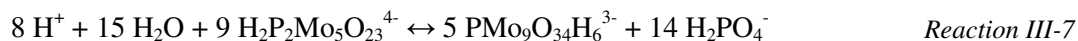


Figure III-27: ^{31}P NMR spectra of: (a) MoP(2), (b) MoP(3) and (c) MoP(5) precursor solutions. Spectra (d) and (e) correspond to dilutions of MoP(3) and MoP(5) precursor solutions, respectively.

The literature refers that the phosphorus species distribution in solution depends on the P/Mo ratio [25,29,30] and the solution pH [31]. Because these solutions have a similar pH (~ 0.3), the driving force behind the different spectral features is their P/Mo ratio.

The NMR resonance observed at about 2.0 ppm is assigned to the diphosphopentamolybdate HPA, which is formed even when the P/Mo ratio is inferior to the HPA stoichiometry (Figure III-27, left). The resonance at about 0.5 ppm is assigned to free phosphates more or less protonated and the signal at -1.0 ppm is assigned to the lacunary Keggin $\text{PMo}_9\text{O}_{34}\text{H}_6^{3-}$ HPA. These results are in agreement with the literature [25,29,31]. It is also possible to observe that the increasing P/Mo ratio leads to an increase in the $\text{P}_2\text{Mo}_5\text{O}_{23}^{6-}$ HPA signal and to a decrease in the lacunary Keggin HPA signal. Iwamoto *et al.* [32] proposed the existence of an equilibrium between these two HPAs in acidic media (Reaction III-7) that depends on the amount of phosphate groups in solution.



Concerning the diluted solutions, the resonances assigned to diphosphopentamolybdate, free phosphates and lacunary Keggin entities are also present but their position is shifted upfield, which is expected due to the higher solution pH [31]. The new peak observed at about -2.0 ppm is close to the value reported by Patterson *et al.* [29] for the Dawson HPA (-2.5 ppm).

The Raman analysis of the MoP(5) solution (Figure III-28) allows verifying the speciation results obtained by NMR. The spectrum reveals the presence of $\text{P}_2\text{Mo}_5\text{O}_{23}^{6-}$ (bands at 944, 890 and 370 cm^{-1}), $\text{P}_2\text{Mo}_{18}\text{O}_{62}^{6-}$ (bands at 976 and 716 cm^{-1}) and $\text{PMo}_9\text{O}_{34}\text{H}_4^{6-}$ (shoulder at 967 cm^{-1}).

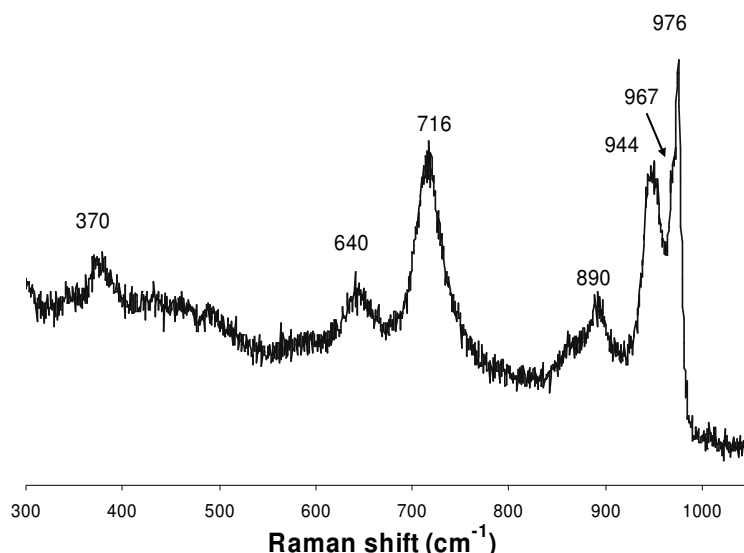


Figure III-28: Raman spectra of the MoP(5) precursor solution.

Based on the previous experimental methods, the CoMoP(5) and CoMoP(3) aqueous solutions mainly contain $[\text{Co}(\text{H}_2\text{O})_6]^{2+}$ and diphosphopentamolybdate HPAs. Besides these species, both $\text{PMo}_9\text{O}_{34}\text{H}_6^{3-}$ and $\text{P}_2\text{Mo}_{18}\text{O}_{62}^{6-}$ HPAs are present as well as traces of free phosphate groups. The CoMoP(1) solution contains, besides the cobalt hexaaquo complex, mainly $\text{PCoMo}_{11}\text{O}_{40}^{7-}$ and traces of $\text{P}_2\text{Mo}_5\text{O}_{23}^{6-}$ and free phosphate groups.

III.3.2. SPECIATION OF THE DRIED CoMoP CATALYSTS SURFACE

The influence of the additive on the dried CoMoP catalysts surface species is discussed in this section. To do so, the catalysts are characterized in absence and in presence of the additive. This allows interpreting the characterization results of the additive-containing samples based on the additive-free results. This section begins with the description of cobalt-containing surface structures, followed by the study of molybdenum-containing species. Finally the surface species containing phosphorus are characterized. These studies provide a global vision about the surface state and how they are affected by the additive.

III.3.2.1. Influence of the additive on cobalt species

To obtain qualitative informations about the cobalt species and how they evolve after additive impregnation, UV-Visible spectroscopy was privileged. The description thus obtained was then complemented by XAS analyses, which allow determining the local environment for cobalt and how it is modified by the additive.

The UV-Visible diffuse reflectance spectroscopies (DRS) conducted on dried CoMoP catalysts (Figure III-29) reveal the presence of the Co(II) aquacomplex in all catalysts (band at 513 nm). A contribution at 557 nm is also present in all samples, assigned to the $\text{PCoMo}_{11}\text{O}_{40}^{7-}$ HPA. This band is predominant in the CoMoP(1d) catalyst, which is not the case for catalysts with a higher P/Mo ratio. Indeed, the CoMoP(3d) and CoMoP(5d) catalysts show important contributions of the aquacomplex bands, revealing the existence of both species. Besides these bands, the CoMoP(5d) catalyst also shows a band in the 600-900 nm region.

No significant changes in the UV-Visible spectra are observed after TEG impregnation of the dried CoMoP(1d) catalyst. This is not the case for the CoMoP(3d) catalyst, where the contribution of the HPA band slightly increases in relation to the cobalt aquacomplex band after additive impregnation. The CoMoP(5d) spectrum is also modified after the additive impregnation: the broad band at high wavelengths disappears and the contribution coming from the aquacomplex increases.

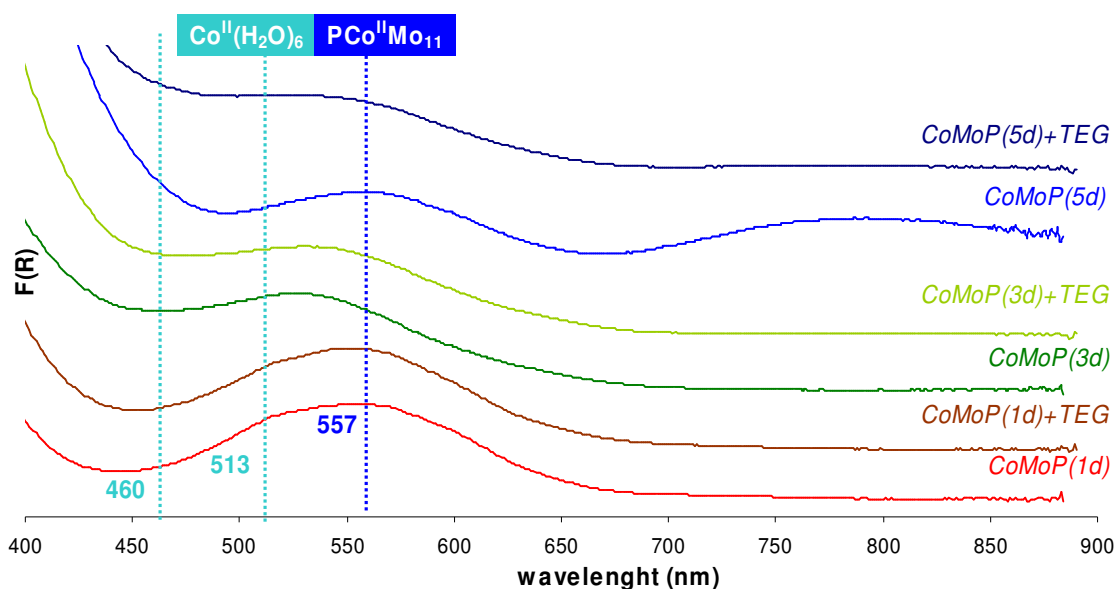


Figure III-29: UV-Visible DRS of dried CoMoP and corresponding additive-containing catalysts.

The UV-Visible DRS of the dried CoMoP(1d) catalyst shows that the $\text{PCoMo}_{11}\text{O}_{40}^{7-}$ HPA adsorbs intact, in agreement with the literature [23]. This species is also present in the CoMoP(3d) and CoMoP(5d) catalysts, although it was not formed in the impregnation solution. The presence of this HPA results from the partial decomposition of the cobalt diphosphopentamolybdate species after impregnation by reaction of the phosphate groups with alumina [23]. Concerning the wide band observed between 600 and 900 nm, which was previously assigned to a reduced HPA, it is still observed for the CoMoP(5d) catalyst but not for the CoMoP(3d) catalyst. This suggests that this compound is partially decomposed upon impregnation.

As for the CoMo-based catalysts, no metal complexation by the additives is showed in the dried catalysts. The spectral evolution observed after the additive impregnation of the CoMoP(3d) catalyst suggests that the additive favors the formation of more $\text{PCoMo}_{11}\text{O}_{40}^{7-}$ HPA species. However, the additive has a different effect on the CoMoP(5d) catalyst. On the one hand, the proportion of Co(II) aquacomplex increases. On the other hand, the disappearance of the band assigned to a reduced Keggin entity shows that this species is decomposed upon the additive impregnation. The CoMoP(3d) spectra already showed that this species was decomposed after impregnation. This suggests that the same phenomenon occurs in the CoMoP(5d) catalyst but since more $\text{PMo}_{12}\text{O}_{40}^{3-}$ is formed in the impregnation solution part of this species adsorbs intact. However, upon the second impregnation, the remaining reduced species are decomposed. Behind this decomposition may be either the increased pH of the solution upon contact with alumina, outside the pH stability range of this compound.

The previous results are confirmed by the Co K-edge X-ray absorption spectroscopy. The position and shape of the cobalt K-edge absorption (not reported here) is similar for the additive-free and additive-containing CoMoP catalysts, corresponding to Co^{2+} species. Moreover, the cobalt K-edge k^3 -weighted EXAFS Fourier Transforms (FT) (Figure III-30) show minor variations with respect to the first and second coordination shells (Co-O bonds), which are due to the quality of the raw XAS signal and corresponding FT extraction. However, the CoMoP(5d) EXAFS FT reveals a modification of Co coordination by Mo in presence of the additive, visible at about 3.5 Å (not phase corrected).

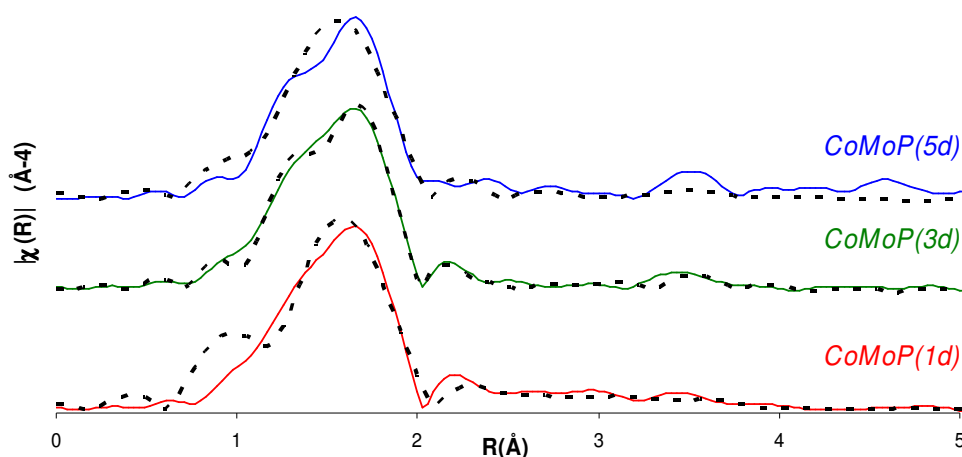


Figure III-30: Cobalt K-edge k^3 -weighted EXAFS FT of dried CoMoP (— solid lines) and corresponding additive-containing catalysts (--- dashed lines). FT Hanning window from 2 to 11; $\tau=2.5$.

III.3.2.2. Influence of the additive on molybdenum species

To determine how the additive impacts on the active phase precursors structure of dried CoMoP catalysts, the surface species that contain molybdenum are firstly characterized without TEG in samples with different P/Mo ratios. Then, the samples are characterized in presence of the additive. As previously, Raman spectroscopy was the most informative experimental method used to obtain

qualitative informations about the molybdenum species in the catalysts surface. This analysis is complemented by XAS at the molybdenum K-edge.

The Raman spectra of the CoMoP(1d) and CoMoP(3d) catalysts are similar (Figure III-30). Like in the dried CoMo_AHM catalysts case, the spectral features correspond to the Anderson $\text{AlMo}_6\text{O}_{24}\text{H}_6^{3-}$ HPA: a main band at 952 cm^{-1} and smaller bands at 900 (shoulder), 565 , 355 and 220 cm^{-1} . The CoMoP(5d) catalyst Raman spectrum (Figure III-32) shows the presence of $\text{P}_2\text{Mo}_5\text{O}_{23}^{6-}$ (main band at 944 cm^{-1}).

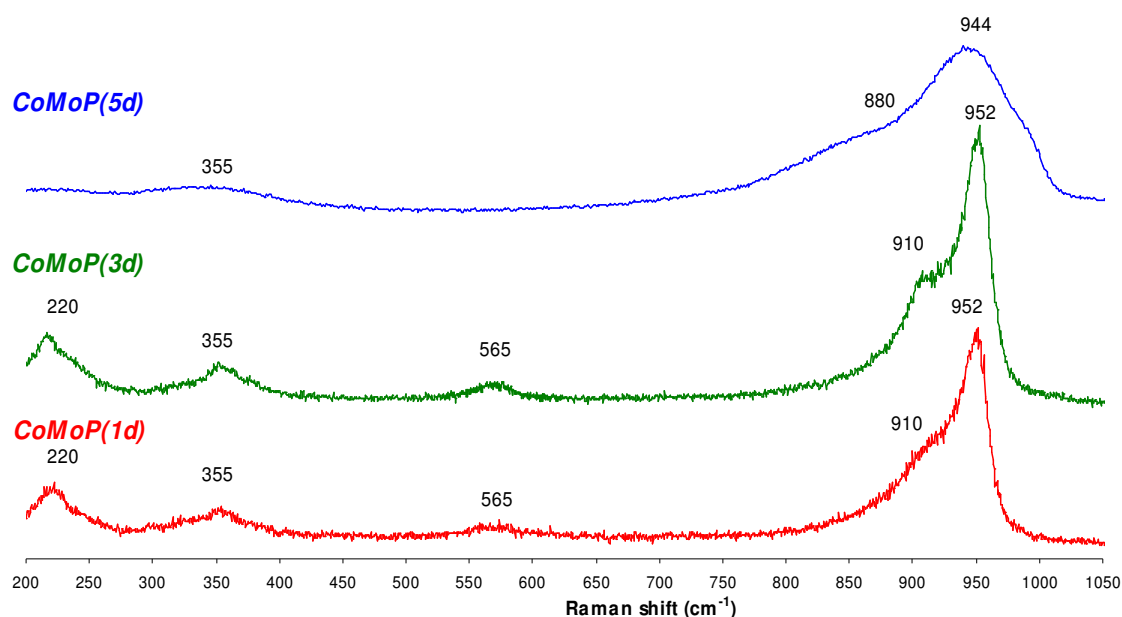


Figure III-31: Raman spectra of dried CoMoP catalysts.

Table III-8: Raman shift of dried CoMoP catalysts and reference data.

Catalysts	Main band (cm^{-1})	Other bands (cm^{-1})
CoMoP(1d)	952	910, 565, 355, 220
CoMoP(3d)	952	910, 565, 355, 220
CoMoP(5d)	944	880, 355
Reference compounds	Main band (cm^{-1})	Other bands (cm^{-1})
$(\text{Co})_{3/2}\text{AlMo}_6\text{O}_{24}\text{H}_6$ (bulk) [4]	947	900, 581, 377, 363, 222
$\text{H}_2\text{P}_2\text{Mo}_5\text{O}_{23}^{4-}$ (solution) [28]	942	893, 395, 370

The hexamolybdoaluminate species observed in the CoMoP(1d) and CoMoP(3d) catalysts result from the molybdenum-assisted dissolution of the alumina support [13,16]. As a consequence, the initial species that were present in the impregnation solutions ($\text{PCoMo}_{11}\text{O}_{40}^{7-}$ for the CoMoP(1) solution and $\text{P}_2\text{Mo}_5\text{O}_{23}^{6-}$ for the CoMoP(3) solution) are mainly decomposed during the impregnation stage. The phosphomolybdates adsorption on a support was described extensively by several authors. Some studies have observed the diphosphopentamolybdate HPA decomposition into AlPO_4 and polymolybdates upon adsorption [30,33] while others have reported that the $\text{P}_2\text{Mo}_5\text{O}_{23}^{6-}$ remains upon

adsorption [22]. These contradictions may be assigned to the different experimental conditions under which these studies were carried out. However, the CoMoP(5d) spectrum shows the adsorption of $P_2Mo_5O_{23}^{6-}$ without decomposition. Indeed, the phosphorus content of the impregnation solution ($P/Mo=0.54$), in excess compared to the diphosphopentamolybdate stoichiometry, limits the decomposition of this HPA. Their decomposition begins with the reaction between phosphate groups and alumina surface, which decreases the P/Mo molar ratio of the solutions within the alumina pores [23,34].

After TEG impregnation, the Raman bands of the Anderson hexamolybdoaluminate species are observed for all catalysts (Figure III-32) besides the shoulder at about $830-835\text{ cm}^{-1}$ arising from the C-O stretching vibration of TEG [22]. For the CoMoP(5d) catalyst, the additive leads to the disappearance of the $P_2Mo_5O_{23}^{6-}$ bands, replaced by those of $AlMo_6O_{24}H_6^{3-}$. Moreover, for phosphorus-containing catalysts with a P/Mo molar ratio equal or superior to 0.4, additive leads to the appearance of a band at about 971 cm^{-1} , whose intensity increases with the phosphorus content. This band corresponds to a Keggin-like HPA. The UV-Visible band observed at about 557 nm (Figure III-29) allows us to assign this Raman band to the substituted Keggin $PCoMo_{11}O_{40}^{7-}$ HPA, in agreement with the literature [25,28].

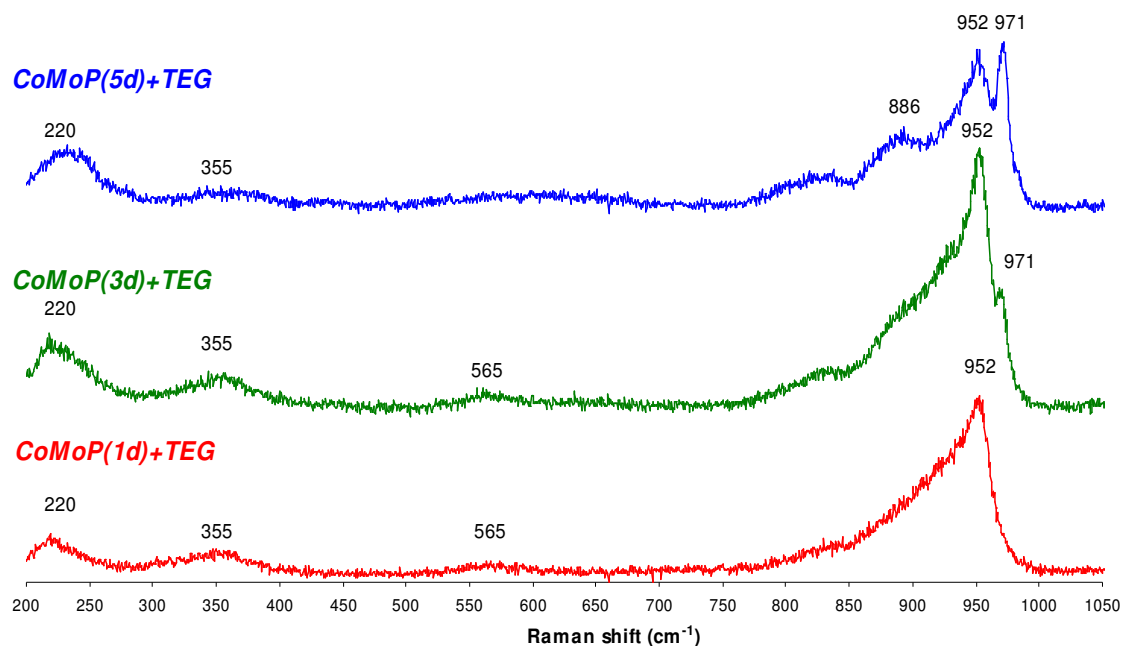


Figure III-32: Raman spectra of additive-containing dried CoMoP catalysts.

Table III-9: Raman shift of additive-containing dried CoMoP catalysts and reference data.

Catalysts	Main band (cm ⁻¹)	Other bands (cm ⁻¹)
CoMoP(1d)+TEG	952	835, 565, 355, 220
CoMoP(3d)+TEG	952	971, 835, 565, 355, 220
CoMoP(5d)+TEG	952	971, 886, 835, 355, 220
Reference compounds	Main band (cm ⁻¹)	Other bands (cm ⁻¹)
(Co) _{3/2} AlMo ₆ O ₂₄ H ₆ (bulk) [4]	947	900, 581, 377, 363, 222
H ₂ PCoMo ₁₁ O ₄₀ ⁵⁻ (solution) [35]	971	-

The additive effect on dried CoMoP catalysts was also studied using X-ray absorption spectroscopy at the molybdenum K-edge. The broad pre-edge molybdenum K-edge XANES (Figure III-33, left), associated to a 6+ state for molybdenum in octahedral geometry [12,22], is observed for all catalyst including those that contain the additive (not reported here).

The molybdenum K-edge k^3 -weighed EXAFS Fourier Transforms (FT) functions of dried CoMoP catalysts (Figure III-33, right) show the same FT for the additive-free and additive-containing CoMoP(1d) catalysts. The CoMoP(3d) and CoMoP(5d) catalysts FT functions show that both the first oxygen shell (1.0-1.5 Å, not phase corrected) and the second oxygen shell (1.5-2.0 Å, not phase corrected) around Mo are slightly affected by the additive impregnation, showing a decrease in intensity although the Mo-O distances remain constant. This effect becomes more pronounced as the phosphorus content of the catalysts increases. Furthermore, if the third shell (1.5-2.0 Å, not phase corrected) remains unaltered for all catalysts, this is not the case for the signal occurring between 2.5 and 3.5 Å.

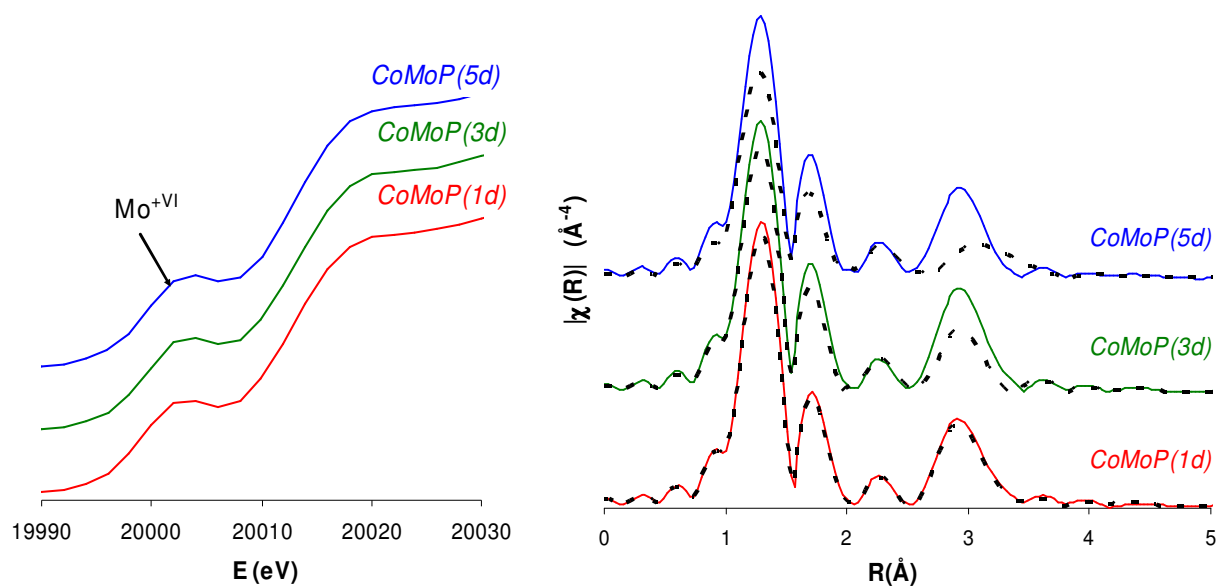


Figure III-33: Mo K-edge XANES (left) and k^3 -weighted EXAFS FT (right) of dried CoMoP (— solid lines) and corresponding additive-containing catalysts (--- dashed lines). FT Hanning window from 3 to 13; $\tau=2.5$.

The molybdenum K-edge EXAFS FT of the CoMoP(1d) sample prior to and after additive impregnation reveals that the surface species are the same. This result is consistent with the Raman and UV-Visible observations. However, in the CoMoP(3d) and CoMoP(5) samples, the two first coordination shells are less intense and the signal centered at about 3 Å is modified after additive impregnation. Some authors successfully fitted this signal with Mo-Mo and Mo-Al contributions [13,14,36] while others with Mo-Mo, Mo-P or even Mo-Co contributions [22]. Based on this, the spectra evolution observed in Figure III-33 (right image) is related to modifications on the HPAs deposited on the catalyst surface, which are in agreement with the observations made by Raman and UV-Visible spectroscopies.

III.3.2.3. Influence of the additive on phosphorus species

This section is dedicated to verify if the nature of the phosphorus-containing surface species is altered by the additive. The previous sections show that different molybdophosphoric HPAs may exist in the impregnation solution and at the catalyst surface depending on the P/Mo ratio. Thus, Raman spectroscopy showed that the additive leads to the formation of new molybdophosphoric species when the P/Mo molar ratio is equal or superior than 0.40. However, Raman spectroscopy is more suitable for the study of molybdenum-containing species. Therefore, to refine the characterization of phosphorus-containing species at the catalyst surface and to determine the impact of the additive on those species, a ^{31}P NMR study is conducted.

Initially, a series of dried phosphorus-impregnated aluminas with similar phosphorus loadings as the CoMoP catalysts is studied in absence and in presence of TEG. This allows collecting reference data about the different phases and also provides useful information about the additive effect on the deposited phosphorus species. These samples are noted as the previous P-containing catalysts. For example, P(5d) refers to a dried alumina-supported solid impregnated with a phosphorus amount that corresponds to 5 wt% P_2O_5 .

Then, the study of dried CoMoP catalysts is made. However, this study revealed to be inconclusive. It is well known that when paramagnetic atoms, like cobalt, are in close proximity to the atom being studied, broadening and shifting of the NMR signal are typically observed. For this reason, NMR studies are conducted in absence of cobalt. Therefore, a series of alumina-supported catalysts only impregnated with molybdenum trioxide and orthophosphoric acid were prepared and analyzed. The Mo loading of these catalysts is fixed at 18% MoO_3 and the P/Mo molar ratios are 0.57, 0.40 and 0.23. The latter ratio is superior to 0.11 used in the CoMoP catalysts due to dissolution limitations in solution at this pH (~0.3).

The spectra of the prepared dried P/Al_2O_3 solids (Figure III-34) show a non symmetrical broad band with maxima at about -7, -6 and -4 for the P(5d), P(3d) and P(1d) samples, respectively. After the additive impregnation, the bands are shifted towards the downfield to -10, -12 and -10, respectively.

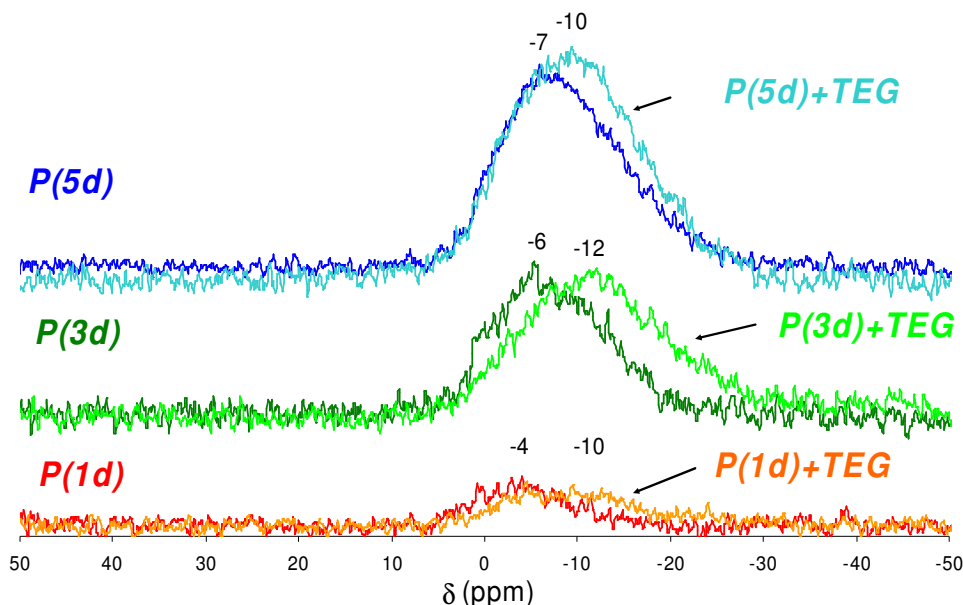


Figure III-34: ^{31}P MAS NMR spectra of dried P/Al_2O_3 and corresponding additive-containing samples.

In general, a shift towards the downfield means that the phosphorus-alumina interactions are increasing, either due to adsorbed phosphate polymers or due to the formation of stronger bonds with alumina [30,31,32].

To elucidate the nature of the different phosphorus species, a mathematical decomposition is made using Lorentz curves (Figure III-35). The samples spectra are fitted with curves centered at -14, -11, -5 and 0 ppm, in agreement with studies conducted on similar P/Al_2O_3 systems [30,33,37,38]. However, when the NMR spectrum shape suggests a signal overlap, multiple decompositions are possible. For this reason, the consequent interpretation should remain qualitative. A detailed description of the model is reported to in Appendix C.

The additive-free dried samples spectra are mainly composed of two contributions: -11 and -5 ppm. The decompositions also show that increased amounts of phosphorus lead to an increase of the resonance at -11 ppm. Similarly, the signal corresponding to the additive-containing samples is decomposed into 2 curves centered at -11 and -5 ppm. However, a new contribution at -14 ppm is necessary to fully describe the experimental data. The exception is the P(1d)+TEG sample that did not showed a contribution at -14 ppm.

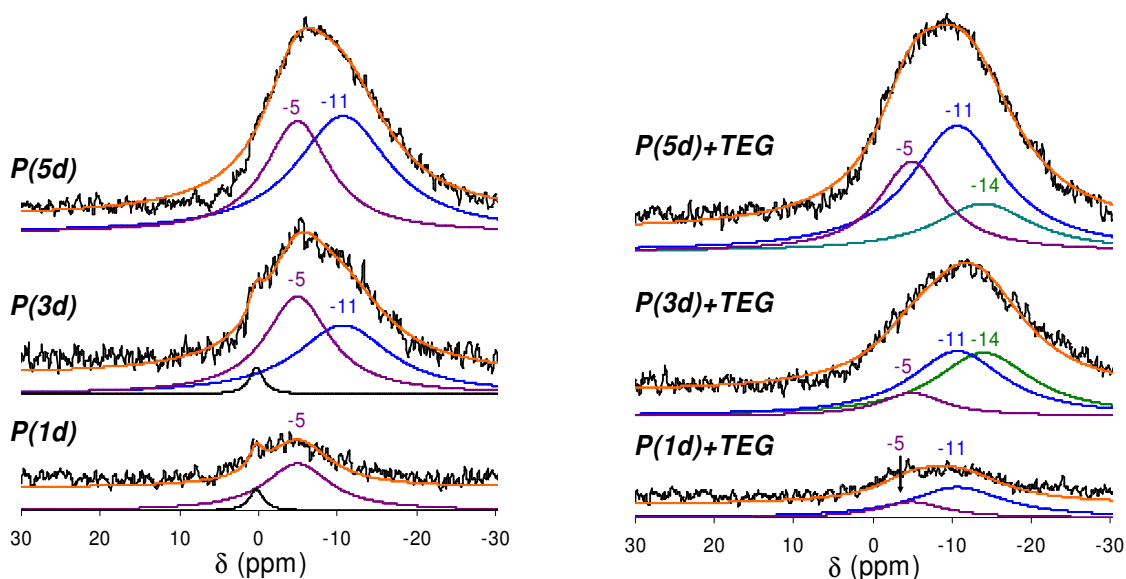


Figure III-35: ^{31}P MAS NMR spectra decomposition of dried $\text{P}/\text{Al}_2\text{O}_3$ (left) and corresponding additive-containing samples (right).

The signal at -11 ppm is assigned to disperse monophosphates adsorbed on the alumina surface [30,33]. The signal at -5 and 0 ppm is assigned to the phosphoric acid physisorption with different degrees of protonation. It was reported [33,38] that the proton loss induces a signal shift towards the downfield. The contribution at -14 ppm in the additive-containing samples arises from the adsorbed polyphosphates [32,38]. Most authors refer that two NMR resonances arise from these entities, one related to the terminal phosphate groups at about -14 ppm and a second signal at -26 ppm corresponding to the internal phosphate groups. The fact that the spectra decompositions only show the resonance of the terminal phosphate groups implies a low polymerization degree. Table III-10 summarizes the NMR resonances obtained from the experimental data decomposition.

Table III-10: ^{31}P MAS NMR data extracted from experimental data decompositions.

δ (ppm)	assignment
0	physisorbed phosphoric acid
-5	physisorbed phosphoric acid derivate
-11	monophosphates
-14	polyphosphates

In conclusion, the additive favors the polymerization of the phosphate groups. The same result was also observed by Nicosia *et al.* [15]. An extensive NMR study about the phosphates adsorption [37] showed that polymerization is favored when the support cannot accommodate phosphate as a monolayer.

Concerning the catalysts containing cobalt, molybdenum and phosphorus, the ^{31}P MAS NMR spectrum of the CoMoP(5d) sample shows a symmetrical broad band centered at about -8 ppm (Figure III-36).

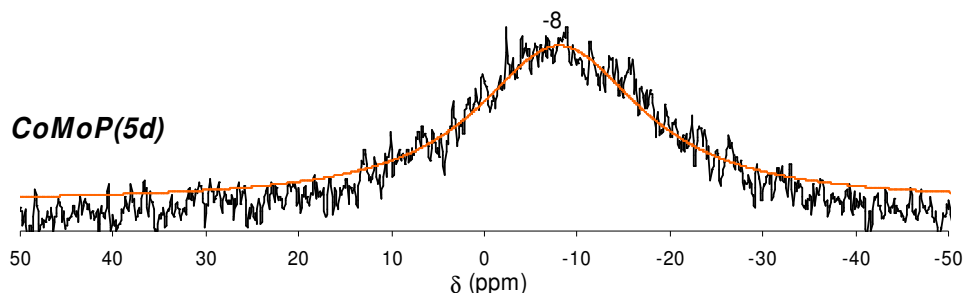


Figure III-36: ^{31}P MAS NMR spectrum of the CoMoP(5d) catalyst.

The sharp peaks that correspond to molybdenum-phosphorus HPA entities solutions are no longer observed despite the fact that Raman spectroscopy showed their presence on the catalyst surface. This result is not surprising due to the paramagnetic properties of cobalt that lead to the broadening of the NMR signal. For this reason, the ^{31}P MAS NMR studies were conducted over unpromoted MoP catalysts.

The dried MoP catalysts spectra (Figure III-37) show the same spectral features in all cases, exhibiting a single symmetrical broad band centered at about -11 ppm, assigned to dispersed monophosphate groups. Once the additive is introduced, the spectra are slightly shifted towards the downfield side and a sharp NMR peak appears at about -3.7 ppm.

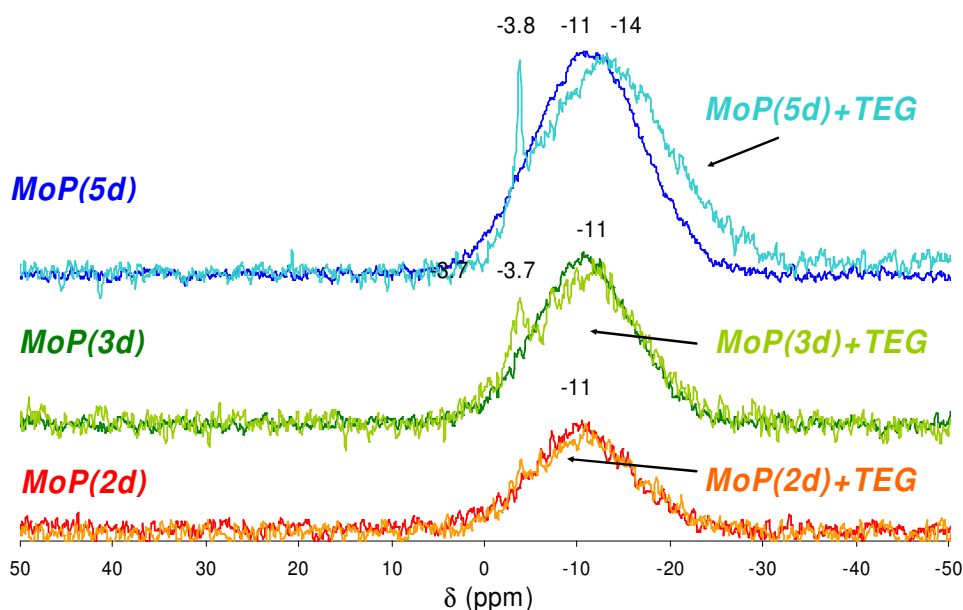


Figure III-37: ^{31}P MAS NMR spectra of dried MoP and corresponding additive-containing catalysts.

As for the P/Al₂O₃ samples, the spectra of the dried MoP catalysts are also decomposed (Figure III-38). The additive-free catalysts spectra is fitted with a single contribution at -11 ppm, previously assigned to dispersed monophosphate groups. Once the additive is impregnated, the spectra reveal a sharp peak at about -3.7 ppm that increases with the P/Mo ratio. Besides this peak, the decomposition of the MoP(5d) spectrum revealed two additional bands at -14 and -21 ppm.

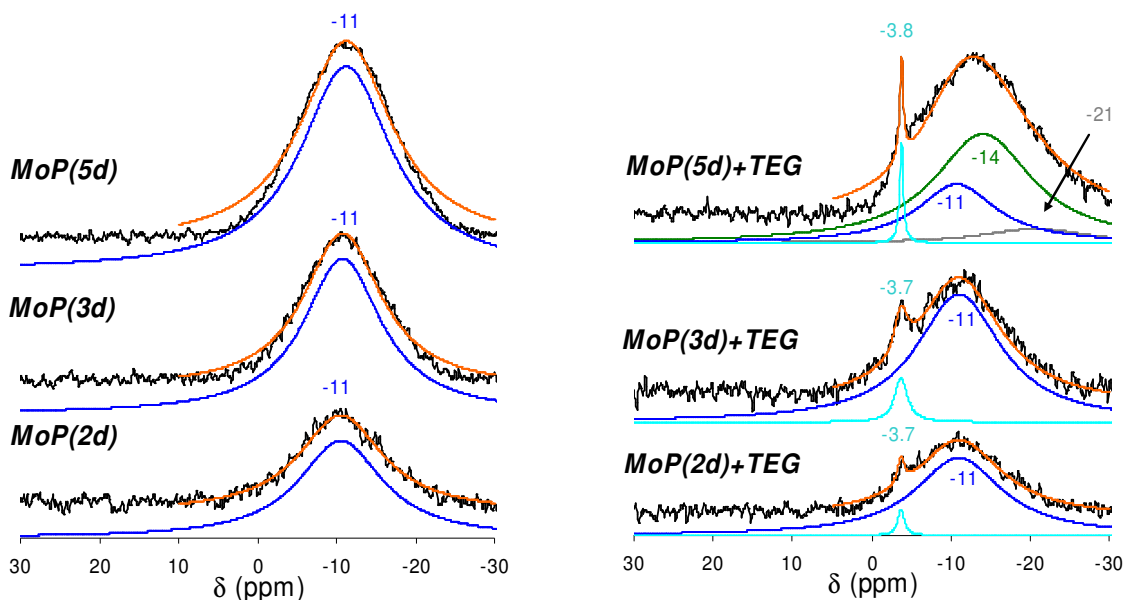


Figure III-38: ³¹P MAS NMR spectra decomposition of MoP (left) and corresponding additive-containing catalysts (right).

The exclusive existence of dispersed monophosphates in dried MoP catalysts is in agreement with the literature [18]: phosphate groups adsorb to alumina without polymerization in presence of molybdates. Thus, no evidence of Keggin-like or Dawson HPAs is revealed, which means that they are decomposed in alumina porosity after impregnation. However, the NMR resonance observed after additive impregnation at about -3.7 ppm is assigned to the Keggin PMo₁₂O₄₀³⁻ HPA [25,32], showing that this HPA adsorbs intact. In addition, when phosphorus is in excess in relation to the P₂Mo₅O₂₃⁶⁻ stoichiometry, besides phosphate polymerization (-14 ppm), Al-PO₄ bonds are formed (-21 ppm [28,32]).

Because these catalysts were prepared without cobalt, the impregnation solution pH is more acidic and the surface species prior and after additive impregnation may be different than those observed on CoMoP catalysts. For this reason and to complete the phosphorus speciation, Raman measurements were conducted to characterize the molybdenum species deposited on the dried MoP catalysts surface. The Raman spectra of the additive-free and additive-containing MoP(5d) catalysts (Figure III-39) exhibit an intense band at about 952 cm⁻¹ revealing the presence of the Anderson

hexamolybdoaluminate HPA. Moreover, after additive impregnation, besides the shoulder arising from TEG at about 830 cm^{-1} [22], two new peaks at about 973 and 988 cm^{-1} appear, assigned to the Keggin-like entities $\text{PMo}_{11}\text{O}_{39}\text{H}_4^{6-}$ and $\text{PMo}_{12}\text{O}_{40}^{3-}$ [25].

Contrarily to the CoMoP(5d) catalyst, the diphosphopentamolybdate HPA is not retained upon impregnation despite the fact that this species is present in the precursor solution, as shown by ^{31}P NMR (Figure III-37). The reason behind the HPA decomposition is related to the increased acidity of the impregnation solution, which favors the alumina dissolution upon impregnation and consequently leads to the $\text{AlMo}_6\text{O}_{24}\text{H}_6^{3-}$ formation. The bands observed at about 973 and 988 cm^{-1} reinforce the NMR observations, showing the formation of Keggin-like HPAs upon additive impregnation.

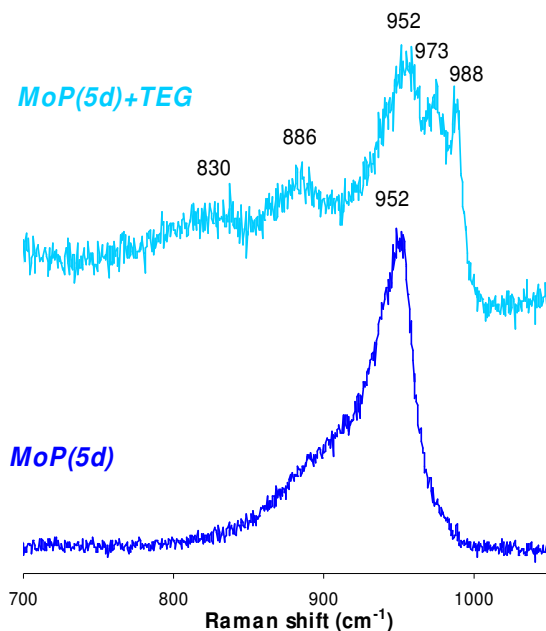


Figure III-39: Raman spectra of the MoP(5d) and corresponding additive-containing catalyst.

As a conclusion, in terms of phosphorus-containing species, the combined NMR and Raman study showed the formation of Keggin-like HPAs upon TEG impregnation. Besides the appearance of these HPAs, the structure of phosphorus-containing species (mainly isolated phosphate groups) is not affected by the additive, except when the P/Mo ratio is superior to 0.40. In this particular case, phosphate groups begin to polymerize and AlPO_4 is formed.

Combining the speciation results for dried CoMoP catalysts, it is possible to establish the relation between the impregnation solution species and the surfaces species nature prior to and after the additive impregnation. For the sake of simplicity, only the main components are resumed in Table III-11.

Table III-11: Speciation results for CoMoP precursor solutions and dried catalysts prior to and after TEG impregnation.

	Solution	Before TEG	After TEG
CoMoP(1d)	$[\text{Co}(\text{H}_2\text{O})_6]^{2+}$ $\text{PCoMo}_{11}\text{O}_{40}^{7-}$	$\text{Co}_{3/2}[\text{AlMo}_6\text{O}_{24}\text{H}_6]$ $\text{Co}_{7/2}[\text{PCoMo}_{11}\text{O}_{40}^{7-}]$ monophosphates	$\text{Co}_{3/2}[\text{AlMo}_6\text{O}_{24}\text{H}_6]$ $\text{Co}_{7/2}[\text{PCoMo}_{11}\text{O}_{40}^{7-}]$ monophosphates
CoMoP(3d)	$[\text{Co}(\text{H}_2\text{O})_6]^{2+}$ $\text{P}_2\text{Mo}_5\text{O}_{23}^{6-}$	$\text{Co}_{3/2}[\text{AlMo}_6\text{O}_{24}\text{H}_6]$ monophosphates	$\text{Co}_{3/2}[\text{AlMo}_6\text{O}_{24}\text{H}_6]$ $\text{Co}_{7/2}[\text{PCoMo}_{11}\text{O}_{40}^{7-}]$ monophosphates
CoMoP(5d)	$[\text{Co}(\text{H}_2\text{O})_6]^{2+}$ $\text{P}_2\text{Mo}_5\text{O}_{23}^{6-}$ $\text{P}_2\text{Mo}_{18}\text{O}_{62}^{6-}$	$\text{Co}_3[\text{P}_2\text{Mo}_5\text{O}_{23}]$ monophosphates	$\text{Co}_{3/2}[\text{AlMo}_6\text{O}_{24}\text{H}_6]$ $\text{Co}_{7/2}[\text{PCoMo}_{11}\text{O}_{40}^{7-}]$ monophosphates polyphosphates

III.3.3. THERMAL BEHAVIOR

The impact of the additive on the temperature stability domain of the different surface species was studied by thermogravimetric analysis (TGA). Like in the CoMo-based catalysts TGA study, the additive-free catalysts are firstly analyzed and the collected data will then be used to interpret the analysis results for the additive-containing catalysts. The experimental conditions and the methodology used is the same as described for the CoMo-based samples (§III.2.3).

III.3.3.1. Additive-free dried CoMoP catalysts analysis

This section is dedicated to the study of the CoMoP(1d) and CoMoP(5d) catalysts thermal decomposition in oxidic atmosphere.

The CoMoP(1d) sample revealed a total loss of 13.7 wt% with a DTG minimum at about 100 °C. Only water is detected by mass spectroscopy and the maximum of water removal occurs at about 200 °C (Figure III-40). The CoMoP(5) sample exhibits a similar behavior, with a total loss of 14.3 wt% during the thermal treatment. The DTG minimum also occurs at about 100 °C and only water is detected in the gaseous effluents with a maximum at about 150 °C (Figure III-41).

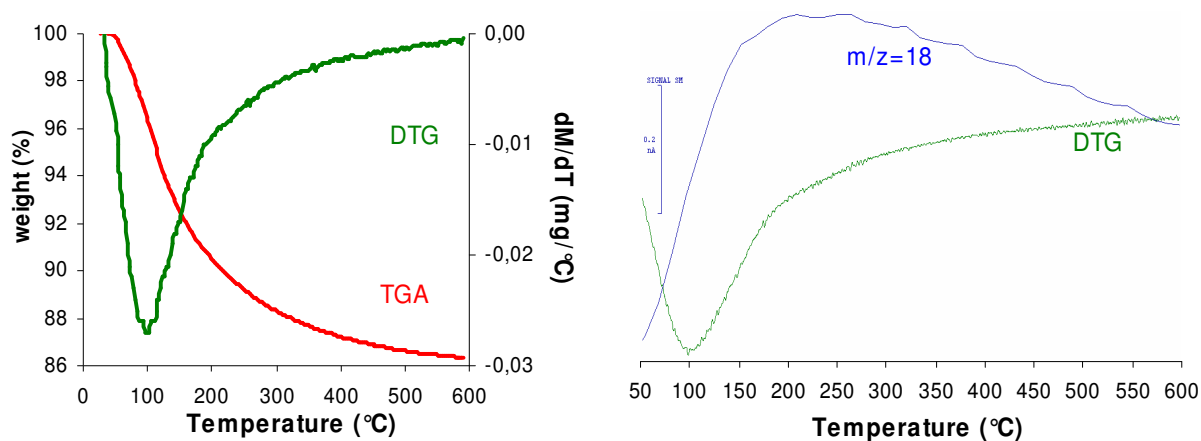


Figure III-40: Thermogravimetric analysis (TGA), derivative thermogravimetry (DTG) and mass spectroscopy results (right) of the CoMoP(1d) catalyst.

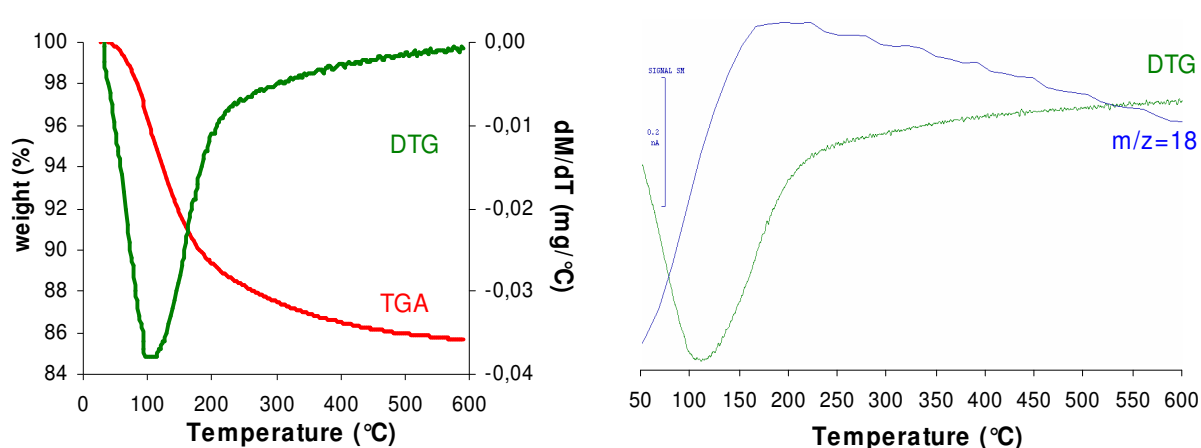


Figure III-41: Thermogravimetric analysis (TGA), derivative thermogravimetry (DTG) and mass spectroscopy results (right) of the CoMoP(5d) catalyst.

The CoMoP(1d) catalyst DTG is decomposed into 3 curves (Figure III-42, left). The curve centered at about 101 °C is assigned to physisorbed water. The curve centered at 225 is assigned to the coordination water of $\text{AlMo}_6\text{O}_{24}\text{H}_6^{3-}$ and $\text{PCoMo}_{11}\text{O}_{40}^{7-}$ and the curve centered at 350 °C is assigned to water resulting from the decomposition the same heteropolyanions (constitutional water). Similarly, the CoMoP(5d) catalyst DTG was decomposed into 3 curves (Figure III-42, right). The curve, centered at 103 °C is assigned to physisorbed water. According to Raman spectroscopy, the main species on the catalyst surface is the $\text{P}_2\text{Mo}_5\text{O}_{23}^{6-}$ anion. For this reason, the curve centered at about 149 °C is assigned to coordination water and the curve at about 295 °C is assigned to the constitutional water loss.

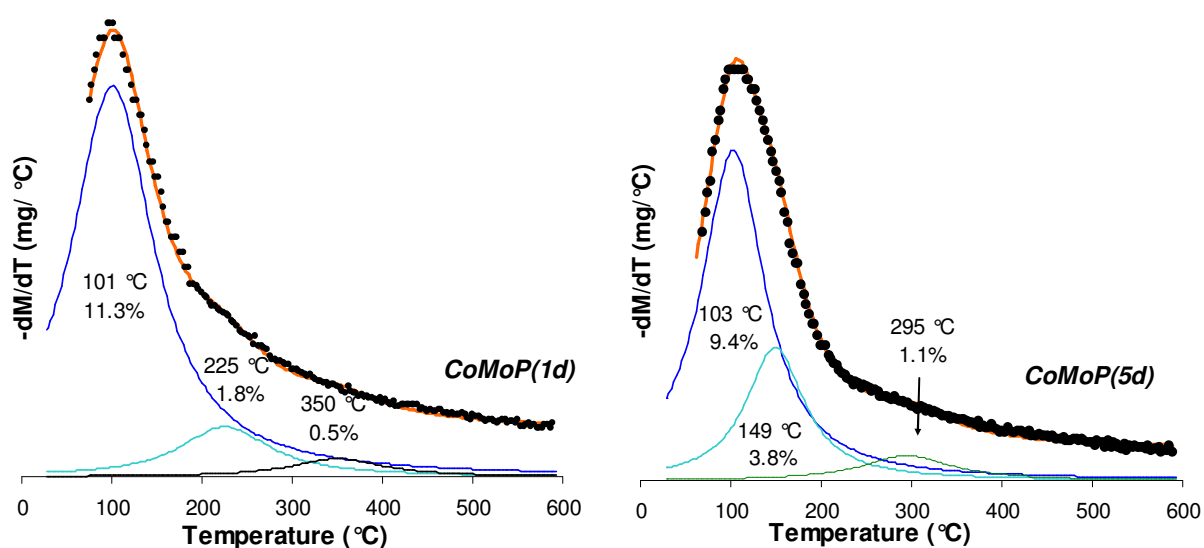


Figure III-42: CoMoP(1d) (left) and CoMoP(5d) (right) catalysts DTG decompositions.

Table III-12: DTG decomposition assignments of the CoMoP(1d) and CoMoP(5d) samples.

CoMoP(1d)			CoMoP(5d)		
T (°C)	Experimental weight loss (%)	Assignment	T (°C)	Experimental weight loss (%)	Assignment
101	11.3	Physisorbed water	103	9.4	Physisorbed water
225	1.8	AlMo ₆ O ₂₄ H ₆ ³⁻ and PCoMo ₁₁ O ₄₀ ⁷⁻ coordination water	149	3.8	P ₂ Mo ₅ O ₂₃ ⁶⁻ coordination water
350	0.5	AlMo ₆ O ₂₄ H ₆ ³⁻ and PCoMo ₁₁ O ₄₀ ⁷⁻ constitutional water	295	1.1	P ₂ Mo ₅ O ₂₃ ⁶⁻ constitution water

III.3.3.2. Additive-containing dried CoMoP catalysts analysis

To study if the additive modifies the temperature stability domain of the deposited surface species, the additive-containing CoMoP(1d) and CoMoP(5d) catalysts are analyzed.

The CoMoP(1d)+TEG sample revealed a total loss of 17.6 wt% with two local DTG minimums at about 100 and 250 °C and a shoulder at about 450 °C (Figure III-43, right). Mass spectroscopy reveals a maximum of water removal at about 280 °C and mass fragments starting at about 200 °C for the m/z 44 (CO₂) (Figure III-43, left). Traces of fragments 12, 22 (carbon-type) and 58 (ketone-type) are also found.

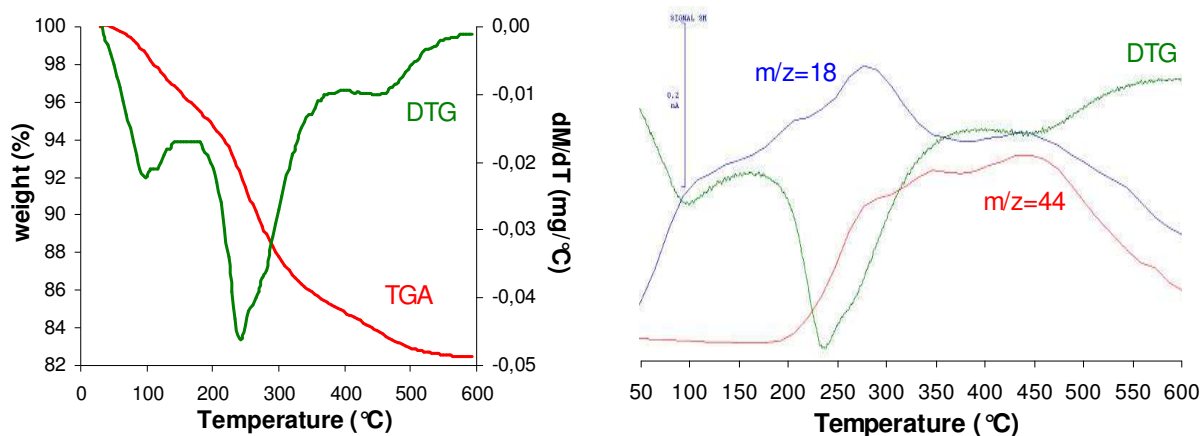


Figure III-43: Thermogravimetric analysis (TGA), derivative thermogravimetry (DTG) and mass spectroscopy results (right) of the CoMoP(1d)+TEG catalyst.

The CoMoP(5d)+TEG sample revealed a total loss of 20.3 wt% with two local DTG minimums at about 100 and 220 °C and a shoulder at about 400 °C (Figure III-44, right). Mass spectroscopy reveals a maximum of water removal at about 220 °C and mass fragments starting at about 200 °C for the m/z 44 (CO₂) (Figure III-44, left). Traces of fragments m/z 12, 22 (carbon-type) and 58 (ketone-type) are also detected.

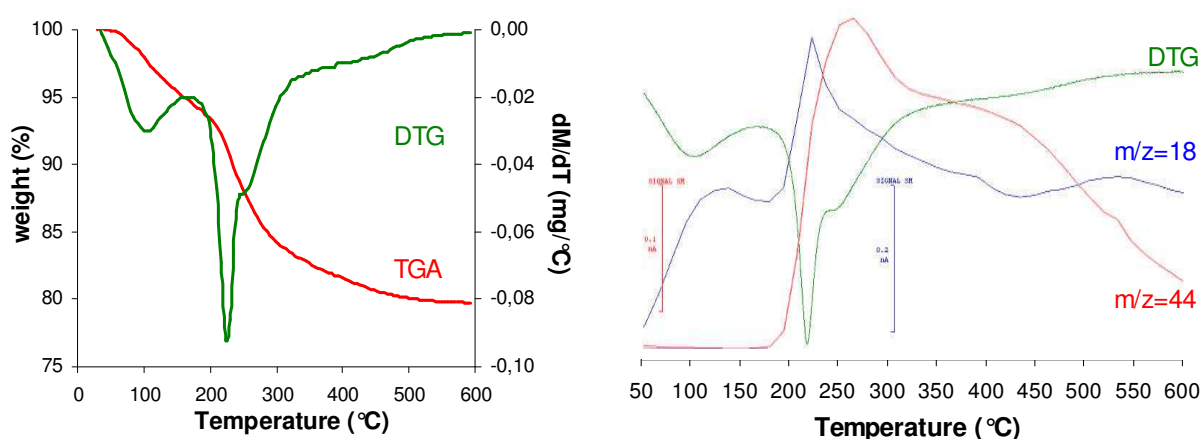


Figure III-44: Thermogravimetric analysis (TGA), derivative thermogravimetry (DTG) and mass spectroscopy results (right) of the CoMoP(5d)+TEG catalyst.

The CoMoP(1d)+TEG sample DTG is decomposed into 5 contributions. They are centered at about 101, 156, 241, 283 and 448 °C that correspond to weight losses of 3.3, 1.0, 5.6, 5.7 and 2.0%, respectively (Figure III-45, left). The CoMoP(5d)+TEG sample DTG is decomposed into 4 contributions. They are centered at about 103, 225, 253 and 407 °C that correspond to weight losses of 5.5, 3.5, 9.1 and 2.1%, respectively (Figure III-45, right).

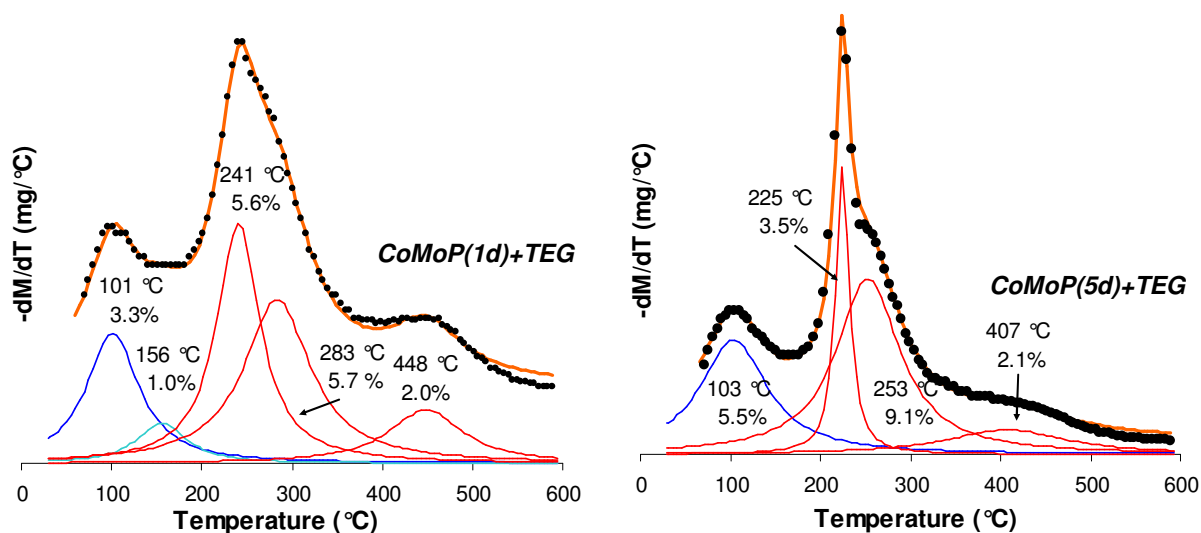


Figure III-45: CoMoP(1d)+TEG (left) and CoMoP(5d)+TEG (right) catalysts DTG decompositions.

The absence of carbon-containing fragments on mass spectroscopy before 200 °C suggest that the first two DTG decomposition curves of the CoMoP(1d)+TEG sample correspond to a water removal: the first assigned to physisorbed water and the second to constitutional water of the hexamolybdoaluminate HPA. As compared to the additive-free catalyst, the water removal occurs at

lower temperatures. The other three curves are assigned to the thermal decomposition products of TEG, accordingly to the mass fragment 44. The sum of these three contributions correspond to 13.2 wt% whereas the quantity measured by CHNS elemental analysis is 10.4 wt%. The difference may be assigned to the HPA constitutional water.

The additive-containing CoMoP(5d) catalyst DTG decomposition exhibited 3 contributions besides the physisorbed water loss. These curves are assigned to the TEG decomposition products. The sum of these three contributions correspond to 14.7 wt% whereas the quantity measured by CHNS elemental analysis is 12.3 wt%. The difference may be assigned to the HPA constitutional water.

Table III-13: DTG decomposition assignments of the CoMoP(1d)+TEG and CoMoP(5d)+TEG samples.

CoMoP(1d)			CoMoP(5d)		
T (°C)	Experimental weight loss (%)	Assignment	T (°C)	Experimental weight loss (%)	Assignment
101	3.3	Physisorbed water	103	5.5	Physisorbed water
156	1.0	AlMo ₆ O ₂₄ H ₆ ³⁻ coordination water	-	-	-
241	5.6	TEG (sum=13.2 wt%)	225	3.5	TEG (sum=14.7 wt%)
283	5.7		253	9.1	
448	2.0		407	2.1	

III.3.4. SURFACE MECHANISM

The transformations of the surface species nature are a function of the P/Mo molar ratio. When this ratio is smaller than 2/5, corresponding to the stoichiometry of the P₂Mo₅O₂₃⁶⁻ HPA, the mechanism is similar to the CoMo-based catalysts. Prior to the additive impregnation, the catalyst surface is mainly composed of AlMo₆O₂₄H₆³⁻, PCoMo₁₁O₄₀⁷⁻ HPAs and dispersed monophosphates. When the additive impregnation is performed, the surface species are redissolved and consequently transported throughout the catalyst body. On the one hand, due to the low solubility of the AlMo₆O₂₄H₆³⁻ salts [4], they precipitate even during the ageing stage and displace the alumina dissolution equilibrium towards the Anderson HPA formation. On the other hand, the Keggin-like HPAs are more soluble [25] and thus preserved upon adsorption, as shown by UV-Visible spectroscopy. The proposed redispersion mechanism is in agreement with the literature [18]. A schematic representation is shown in Figure III-46, left scheme.

The mechanism for the dried CoMoP catalysts with a P/Mo molar ratio superior to 2/5 involves the destruction of the P₂Mo₅O₂₃⁶⁻ HPA into molybdates and phosphates. The molybdenum-assisted support dissolution takes place and the Anderson hexamolybdoaluminate HPA is formed. Moreover, the free phosphate groups then react with molybdates to form PCoMo₁₁O₄₀⁷⁻ HPAs.

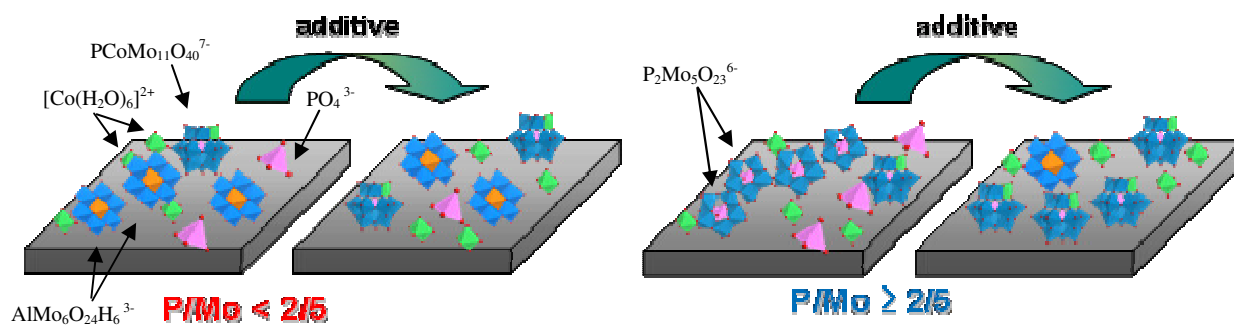


Figure III-46: Schematic representations of the redispersion mechanism induced by the additive for dried CoMoP catalysts.

III.4. CHAPTER CONCLUSION

The aim of this chapter is thus to verify if glycol-type additives have an influence on the active phase precursors structure in dried alumina-supported catalysts. Different impregnation solutions have been used containing ammonium heptamolybdate or decamolybdocobaltate heteropolyanions ($\text{Co}_2\text{Mo}_{10}\text{O}_{38}\text{H}_4^{6-}$) for CoMo catalysts and phosphomolybdate heteropolyanions with different P/Mo molar ratios (0.11, 0.40 and 0.57) for CoMoP catalysts. Surface species have been thoroughly characterized for all dried catalysts, prior to and after TEG impregnation. For all dried CoMo and CoMoP catalysts with a P/Mo molar ratio lower than 0.4, a redissolution phenomenon was shown after the additive impregnation stage, leading to the formation of the Anderson heteropolyanion $\text{AlMo}_6\text{O}_{24}\text{H}_6^{3-}$. This redissolution phenomenon is however limited by the low solubility of this Anderson HPA. For the CoMoP dried catalysts with a P/Mo molar ratio greater than 0.4, characterization of additive-containing catalysts showed $\text{PCoMo}_{11}\text{O}_{40}^{7-}$, on top of $\text{AlMo}_6\text{O}_{24}\text{H}_6^{3-}$ formation. Redissolution and redispersion due to the additive impregnation are thus enhanced.

Key points

1. The additive impregnation of dried CoMo and CoMoP catalysts with a P/Mo molar ratio inferior to 0.4 leads to species redispersion by formation of $\text{AlMo}_6\text{O}_{24}\text{H}_6^{3-}$ heteropolyanions.
2. The additive impregnation of CoMoP catalysts with a P/Mo molar ratio superior to 0.4 leads to enhanced redispersion due to $\text{PCoMo}_{11}\text{O}_{40}^{7-}$ formation, on top of the $\text{AlMo}_6\text{O}_{24}\text{H}_6^{3-}$ formation.

III.5. BIBLIOGRAPHIC REFERENCES

- 1 P. Blanchard, C. Mauchausse, E. Payen and J. Grimblot, J. Stud. Surf. Sci. Catal. 95, 1037, **1995**.
- 2 L.G. Roberts and F.H. Field, J. Am. Chem. Soc. 72,4232, **1950**.

- 3 C. Cabello, I. Botto and H. Thomas, *Appl. Catal. A* 197, 79, **2000**.
- 4 C. Martin, Ph.D. thesis, Université des Sciences et Technologies de Lille, **2003**.
- 5 C. Lamonier, C. Martin, J. Mazurelle, V. Harlé, D. Guillaume and E. Payen, *Appl. Catal. B* 70, 548, **2007**.
- 6 C. Martin, C. Lamonier, M. Fournier, O. Mentré, V. Harlé, D. Guillaume and E. Payen, *Chem. Mater.* 17, 4438, **2005**.
- 7 P. Mazoyer-Galliou, Ph.D. thesis, Université Claude Bernard - Lyon 1, **1998**.
- 8 G. Kishan, J.A.R. van Veen and J.W. Niemantsverdriet, *Topics in Catalysis*, 29, 3, **2004**.
- 9 M. Sun, D. Nicosia and R. Prins, *Cat. Today*, 86, 173, **2003**.
- 10 A. van Dillen, R. Teröde, D. Lensveld, J. Geus and K. de Jong, *J. Catal.*, 216, 257, **2003**.
- 11 Y. Ohta, T. Shimizu, T. Honma and M. Yamada, Elsevier Science B.V., **1999**.
- 12 C. Cartier dit Moulin, V. Briois and M. Vendaguer, *Cours Initiation à l'absorption des rayons X*, Chapitre III, Montpellier mai **2006**.
- 13 X. Carrier, E. Marceau and M. Che, *Pure Appl. Chem.*, Vol. 78, No. 5, 1039, **2006**.
- 14 R.G. Leliveld, A.J. Van Dillen, J.W. Geus and D.C. Koningsberger, *J. Catal.* 165, 184, **1997**.
- 15 D. Nicosia and R. Prins, *J. Catal.* 234, 414, **2005**.
- 16 L. Le Bihan, P. Blanchard, M. Fournier, J. Grimblot and E. Payen, *J. Chem. Soc., Faraday Trans.* 94, 937, **1998**.
- 17 C. Martin, C. Lamonier, M. Fournier, O. Mentré, V. Harlé, D. Guillaume and E. Payen, *Inorg. Chem.* 43, 4636, **2004**.
- 18 X. Carrier, J.F. Lambert and M. Che, *J. Am. Chem. Soc.* 119, 10137, **1997**.
- 19 X. Carrier, J.B. d'Espinose de la Caillerie, J.F. Lambert and M. Che, *J. Am. Chem. Soc.* 121, 3377, **1999**.
- 20 C. Cabello, F.M. Cabrerizo, A. Alvarez and H.J. Thomas, *J. Mol. Catal. A, Chem.* 186, 89, **2002**.
- 21 WO96/41848A1, Hydrotreating catalyst: composition, preparation, and use thereof, **1996**.
- 22 D. Nicosia and R. Prins, *J. Catal.* 229, 424, **2005**.
- 23 J.A. Bergwerff, L.G.A. van der Water, T. Visser, P. de Peinder B.R.G. Leliveld, K.P. de Jong and B.M. Weckhuysen, *Chem. Eur. J.* 11, 4591, **2005**.
- 24 A. Griboval, P. Blanchard, L. Gengembre, E. Payen, M. Fournier, J.L. Dubois and J.R. Bernard, *J. Catal.* 188, 102, **1999**.
- 25 A. Griboval, Ph.D. thesis, Université des Sciences et Technologies de Lille, **1998**.
- 26 A. Griboval, P. Blanchard, E. Payen, M. Fournier and J.L. Dubois, *Catal. Today* 45, 277, **1998**.
- 27 L.E. Briand, G.M. Valle and H.J. Thomas, *J. Mater. Chem.* 12, 299, **2002**.
- 28 J.A. Bergwerff, T. Visser, B.R.G. Leliveld, B.D. Rossenaar, K.P. de Jong and B.M. Weckhuysen, *J. Am. Chem. Soc.*, Vol. 126, No. 44, 14549, **2004**.
- 29 L. Pattersson, I. Andersson and L.O. Ohman, *Inorg. Chem.* 25, 4726, **1986**.

- 30 H. Kraus and R. Prins, *J. Catal.* 164, 251, **1996**.
- 31 J.A.R. van Veen, O. Sudmeijer, C.A. Emeis and H. de Wit, *J. Chem. Soc. Dalton Trans.* 1825, **1986**.
- 32 R. Iwamoto and J. Grimblot, *Adv. Catal.* 44, 417, **2000**.
- 33 J.A.R. van Veen, P.A.J.M. Hendricks, E.J.G.M. Romers and R.R. Andrea, *J. Phys. Chem.* 94, 5282, **1990**.
- 34 W.-C. Cheng and N.P. Luthra, *J. Catal.* 109, 163, **1988**.
- 35 J.A. Bergwerff, L.G.A. van de Water, T. Visser, P. de Peinder, B.R.G. Leliveld, K.P. de Jong and B.M. Weckhuysen, *Chem. Eur. J.* 11, 4591, **2005**.
- 36 G. Plazenet, E. Payen, J. Lynch and B. Rebours, *J. Phys. Chem. B* 106, 7013, **2002**.
- 37 E.R.H. van Eck, A.P.M. Kentgens, H. Kraus and R. Prins, *J. Phys. Chem.*, Vol. 99, No 43, 16085, **1995**.
- 38 T.R. Krawietz, P. Lin, K.E. Lotterhos, P.D. Torres, D.H. Barich, A. Clearfield and J.F. Haw, *J. Am. Chem. Soc.* 120, 8502, **1990**.

CHAPTER IV: THE ROLE OF GLYCOL-TYPE ADDITIVES ON CALCINED CoMo(P) CATALYSTS

IV.1. Introduction.....	115
IV.2. Impact of the additive when impregnated on calcined CoMo catalysts.....	115
IV.2.1. Textural properties of the calcined CoMo catalysts.....	116
IV.2.2. Speciation of the calcined CoMo catalysts	117
<i>IV.2.2.1. Influence of the additive on cobalt species.....</i>	<i>117</i>
<i>IV.2.2.2. Influence of the additive on molybdenum species</i>	<i>119</i>
IV.2.3. Metals distribution	121
IV.2.4. Thermal behavior	122
<i>IV.2.4.1. Additive-free calcined CoMo catalysts analysis</i>	<i>122</i>
<i>IV.2.4.2. Additive-containing calcined CoMo catalysts analysis.....</i>	<i>123</i>
IV.2.5. Surface mechanism	126
IV.3. Impact of the additive impregnated on calcined CoMoP catalysts	126
IV.3.1. Textural properties of the calcined CoMoP catalysts.....	127
IV.3.2. Speciation of the calcined CoMoP catalysts	130
<i>IV.3.2.1. Influence of the additive on cobalt species.....</i>	<i>130</i>
<i>IV.3.2.2. Influence of the additive on molybdenum species</i>	<i>132</i>
<i>IV.3.2.3. Influence of the additive on phosphorus species</i>	<i>134</i>
IV.3.3. Metals and phosphorus distribution	140
<i>IV.3.3.1. Phosphorus reaction with the additives</i>	<i>142</i>
IV.3.4. Thermal behavior	145
<i>IV.3.4.1. Additive-free calcined CoMoP catalysts analysis.....</i>	<i>145</i>
<i>IV.3.4.2. Additive-containing calcined CoMoP catalysts analysis</i>	<i>146</i>
<i>IV.3.4.3. Additives long-term stability</i>	<i>148</i>
IV.3.5. Surface mechanism	149
IV.4. Chapter conclusion	150
IV.5. Bibliographic references.....	151

CHAPTER IV: THE ROLE OF GLYCOL-TYPE ADDITIVES ON CALCINED CoMo(P) CATALYSTS

IV.1. INTRODUCTION

The previous chapter focused on the modifications made to the nature of the active phase precursors after additive introduction. A redissolution-reprecipitation mechanism was shown for dried catalysts in which the additive favored the redispersion of metals and phosphorus species. Thus, the industrial [1] and academic literature [2] report gains up to 30% in catalytic performances of calcined catalysts after additive introduction. It is known that calcination leads to the formation of structured oxide phases at the alumina surface by decomposition of the existing heteropolyanions, nitrates and ammonium ions. Therefore, the objective of this chapter is to provide answers to the following questions: 1) Does the additive modifies the surface species prior to the sulfidation stage? 2) Is the redispersion mechanism also valid for calcined catalysts?

Using the dried catalysts as starting material, calcined samples are prepared and the catalysts surface state will be studied to determine if the additive modifies the structure of the active phase precursors. To complete this analysis, the impact of the additive on the elements distribution in the catalyst body will be also studied.

As for the dried catalysts, to study the possible specific interactions between the additives and phosphorus, the chapter is divided in CoMo-based and CoMoP catalysts.

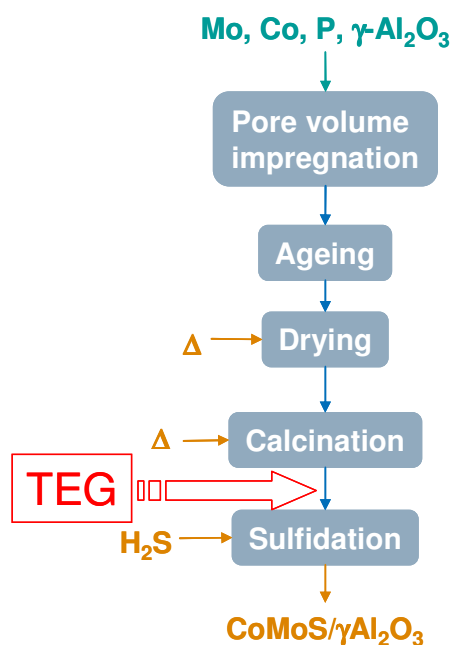


Figure IV-1: Preparation of additive-containing calcined CoMoP catalysts.

IV.2. IMPACT OF THE ADDITIVE IMPREGNATED ON CALCINED CoMo CATALYSTS

The objective of this section is to determine if the additive impregnation modifies the surface species or the elements distribution inside the calcined CoMo catalysts body. For this purpose, the dried CoMo_AHM and CoMo_HPA catalysts were calcined. In a first step, the textural properties of the calcined catalysts are characterized. Then, the surface species and the elements distribution inside the catalyst body are characterized prior to and after additive impregnation.

IV.2.1. TEXTURAL PROPERTIES OF THE CALCINED CoMo CATALYSTS

BET and BJH studies were carried out to determine how the porosity of the alumina support is affected by the impregnation of the precursor solution and by the different thermal treatments that the sample was submitted to. This will allow to show some of the differences between the studied systems.

Nitrogen adsorption measurements conducted on the calcined CoMo samples reveal similar surface areas and average pore diameters (Table IV-1). The samples exhibit losses of about 40 m²/g in BET surface when compared to the alumina support, which is mainly due to the deposition of the active phase precursors. Thus, the BET surface area (micro and mesoporosity) is always superior to the calculated BJH desorption surface area (mesoporosity), which indicates that the catalysts possess some microporosity.

Table IV-1: Surface area and average pore diameter of calcined CoMo-based catalysts and alumina.

Sample	BET surface area [m ² /g]	BJH adsorption surface area [m ² /g]	Average pore diameter (APD) (nm)*
CoMo_HPA(c)	264	228	9.1
CoMo_AHM(c)	255	239	9.7
γ -Alumina	300	299	10.0

* Calculated using the BJH adsorption surface area (APD=4V/S).

The porous distribution of the samples is plotted as a function of the pore volume derivative, calculated by the BJH method (Figure IV-2). It shows that alumina and calcined CoMo catalysts porous distribution is almost the same, with two population maxima at about 6 and 10 nm.

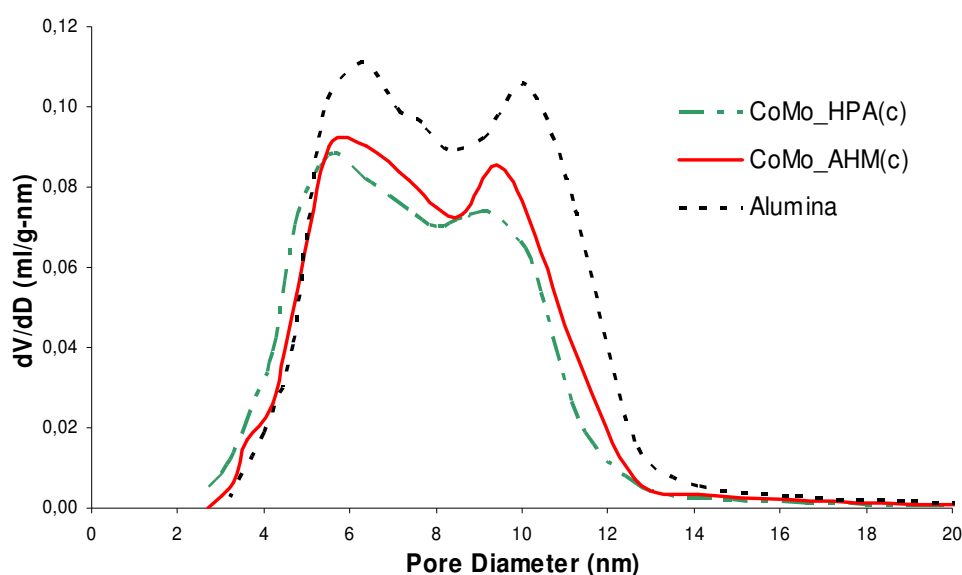


Figure IV-2: BJH porous distribution of alumina and calcined CoMo_AHM and CoMo_HPA catalysts.

With respect to the additive, a preliminary BET study showed that the impregnation of TEG leads to the same result as a calcined sample. Moreover, CHNS elemental analysis conducted on samples that were submitted to nitrogen adsorption measurements contained only residual carbon (<0.5 wt%), meaning that the additive decomposes during the outgassing pretreatment (vacuum at 300 °C). These results show that TEG does not modify the porosity of the alumina support.

IV.2.2. SPECIATION OF THE CALCINED CoMo CATALYSTS

The influence of the additive on the deposited surface species is studied by characterizing the calcined samples prior to and after TEG impregnation. For this purpose, cobalt and molybdenum species are determined.

IV.2.2.1. Influence of the additive on cobalt species

The qualitative analysis of cobalt species on the calcined catalysts is made by UV-Visible spectroscopy. In addition, the surface state description is complemented by XAS analyses, which allow determining the local environment of cobalt and how it is modified by the additive.

The UV-Visible diffuse reflectance spectra of all calcined CoMo catalysts exhibit bands at about 545, 580 and 650 nm (Figure IV-3) that correspond to cobalt aluminate, where cobalt is in tetrahedral symmetry (545, 580 and 630 nm) [3]. No significant modification of the spectra is observed after TEG impregnation.

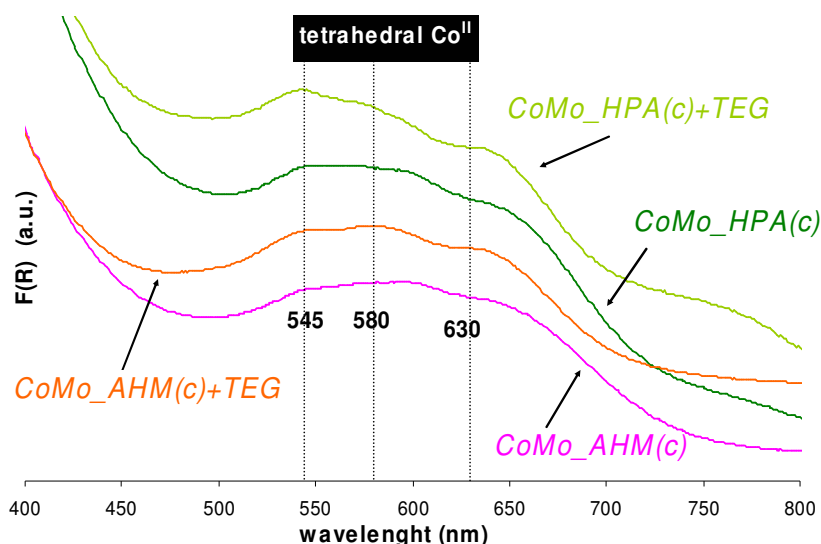
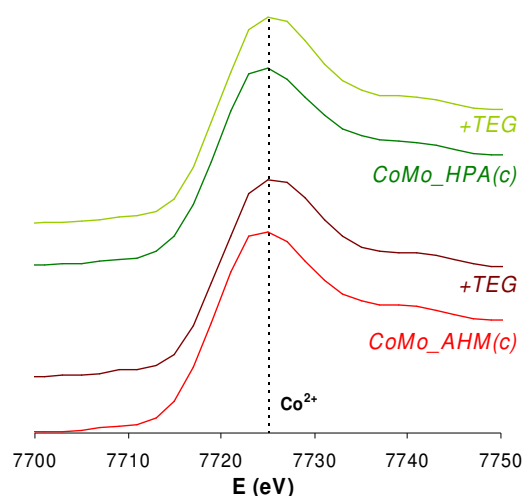


Figure IV-3: UV-Visible diffuse reflectance spectra of CoMo_AHM(c), CoMo_HPA(c) and corresponding additive-containing catalysts.

The fact that no strong modification on the spectra is observed after additive impregnation rules out cobalt complexation by the additives, in agreement with the UV-Visible observations of the dried catalysts. However, CoMoO₄ species (main bands at 525 and 587 nm) may be present on the catalysts,

besides CoAl_2O_4 -like species. Nevertheless, the amount of these species seems low since CoAl_2O_4 and CoMoO_4 phases are not detected in XRD. In the particular case of the calcined CoMo_HPA catalysts,

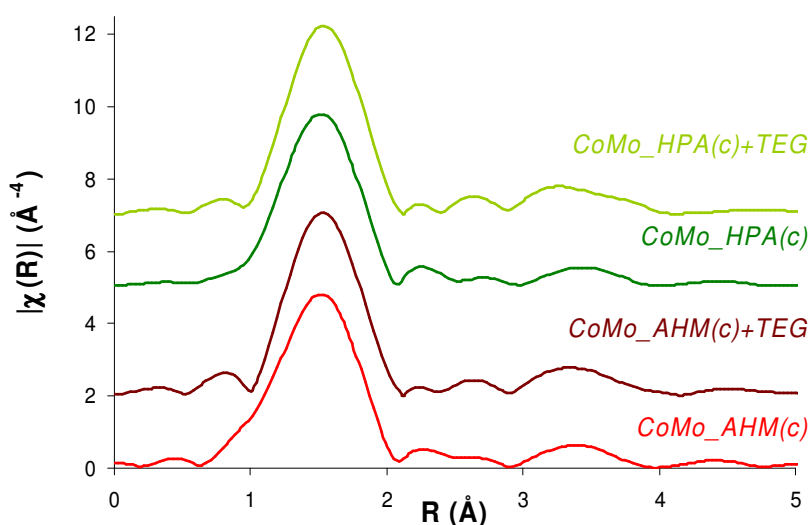


no band is observed at about 610 nm, typical of Co(III) entities [4,5]. This indicates that molybdocobaltate HPA entities are destroyed upon calcination and that they are not reconstructed after additive impregnation.

The absence of Co(III) species was confirmed by the cobalt K-edge XANES study. The maximum at about 7725 eV is typical of Co(II) species and no shoulder at about 7733 eV corresponding to Co(III) species [5,6] is visible (Figure IV-4).

Figure IV-4: Cobalt K-edge XANES spectra of CoMo_AHM(c), CoMo_HPA(c) and corresponding additive-containing catalysts.

The local environment for cobalt in calcined CoMo catalysts is studied using EXAFS spectroscopy (Figure IV-5). As mentioned in Chapter III, the EXAFS quantitative analysis is still rather difficult due to the different cobalt oxidic phases that constitute the catalysts. Besides that, despite all efforts to improve the quality of the EXAFS Fourier Transforms extraction, the size of the Hanning window used is rather small, which results in a loss of definition. From a qualitative point of view, the spectral features are similar to the additive-free catalysts in respect to the first Co-O shell (from 1 to 2 Å, not phase corrected) and the Co-metal shell (from 3 to 4 Å, not phase corrected). No significant



modifications are observed after the additive introduction, meaning that the average cobalt structure is maintained.

As a conclusion, the characterization methods reveal similar oxidic cobalt structures for all analyzed catalysts and the additive introduction does not have an impact in cobalt speciation.

Figure IV-5: Cobalt K-edge k^3 -weighted EXAFS Fourier Transforms (FT) of CoMo_AHM(c), CoMo_HPA(c) and corresponding additive-containing catalysts. FT Hanning window from 2 to 9; $\tau=2.5$.

IV.2.2.2. Influence of the additive on molybdenum species

To characterize the molybdenum-containing surface species prior to and after the additive impregnation, Raman analyses are conducted on the calcined CoMo catalysts. To complement the speciation, X-ray diffraction and X-ray absorption spectroscopy techniques are also used.

The Raman spectra of calcined catalysts exhibit similar features with a broad band centered at 955-950 cm^{-1} and a shoulder at about 860 cm^{-1} (Figure IV-6). These bands correspond to dispersed and ill-defined polyoxomolybdate structures. After TEG impregnation, a strong band at 952 cm^{-1} and a small band at 565 cm^{-1} appear in the spectra, assigned to Anderson heteropolyanions [5,7].

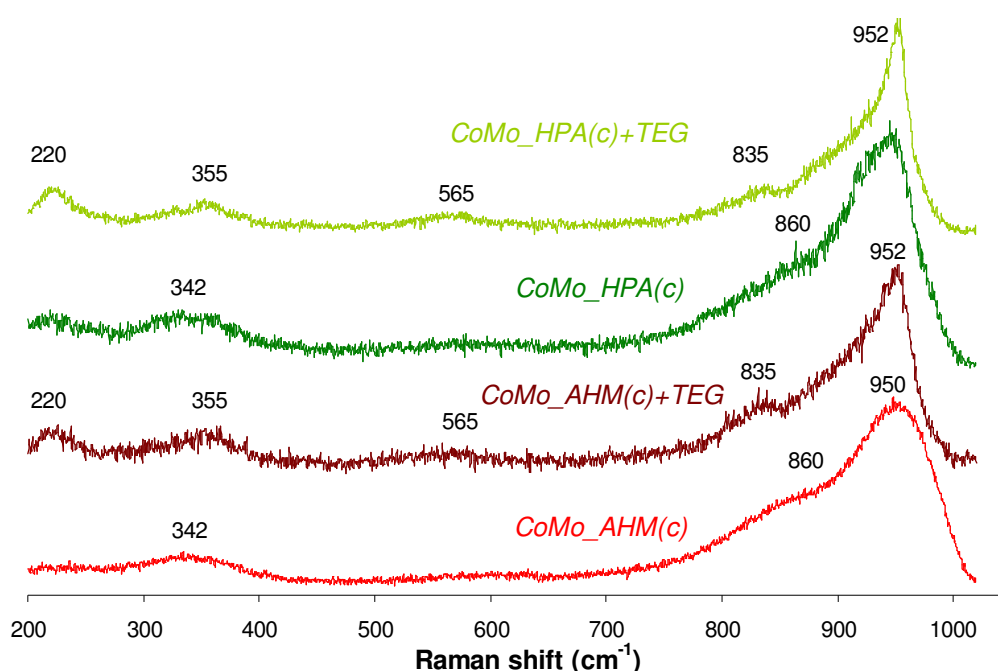


Figure IV-6: Raman spectra of calcined CoMo and corresponding additive-containing catalysts.

The absence of Raman bands in the 550-600 cm^{-1} region and the spectral line shape of the calcined CoMo catalysts show that the calcination stage at 450 °C leads to the destruction of all HPA structures observed in the dried catalysts. Moreover, the TEG impregnation of calcined catalysts induces a similar effect than in the case of dried catalysts: the Raman spectra show the hexamolybdoaluminate HPA formation. For the CoMo_HPA(c)+TEG catalyst, the surface species is now the $\text{AlMo}_6\text{O}_{24}\text{H}_6^{3-}$ HPA instead of the $\text{CoMo}_6\text{O}_{24}\text{H}_6^{3-}$ and $\text{Co}_2\text{Mo}_{10}\text{O}_{38}\text{H}_4^{6-}$ anions as observed in the corresponding dried catalyst. Indeed, the shoulder at 605 cm^{-1} assigned to the decamolybdodicobaltate HPA [4,5] is no longer observed (Figure IV-6) and no evidence of Co(III) species is found in UV-Visible and XANES spectroscopies.

As for the dried CoMo_AHM catalysts case, the XRD analysis is used to detect the Anderson hexamolybdoaluminate heteropolyanion as well as other possible crystalline phases. The diffraction spectra of the calcined CoMo_AHM catalysts (Figure IV-7) no longer exhibit the sharp spectral lines observed in the dried catalysts case (Figure III-9). Thus, all spectra show that a crystallized MoO_3 -like phase is formed. Other phases like CoMoO_4 and CoAl_2O_4 are not detected in this sample. In addition, a catalyst saturated with TEG is also characterized and confirmed that the massive arising in the 20° and 25° region is related to the additive, corresponding to an amorphous phase.

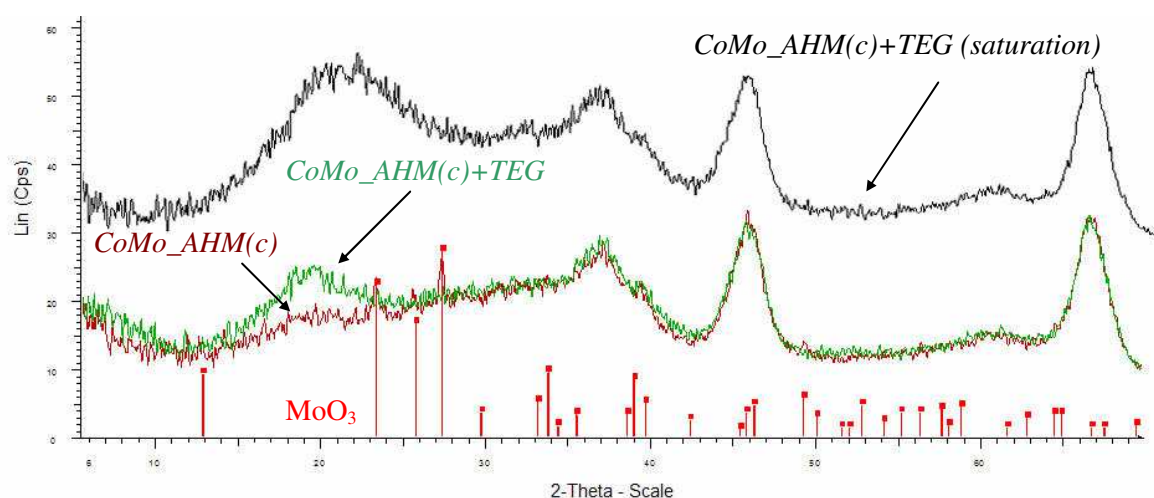


Figure IV-7: X-ray Diffraction spectra for CoMo_AHM(c), CoMo_AHM(c)+TEG and CoMo_AHM(c) saturated with TEG. For reference, the vertical lines in the bottom correspond to crystallized MoO_3 .

The absence of sharp lines in the XRD spectra show that the crystalline phase attributed to $\text{AlMo}_6\text{O}_{24}\text{H}_6^{3-}$ is decomposed upon calcination and gives rise to MoO_3 -like structures, consistent with the polyoxomolybdate structures observed in Raman spectroscopy.

Molybdenum K-edge XAS analyses are also conducted on the calcined CoMo catalysts to determine if modifications are made to the molybdenum local environment after additive impregnation.

The XANES spectra of the CoMo catalysts (Figure IV-8, left) is similar in all cases. Besides this, the k^3 -weighted EXAFS Fourier Transforms (Figure IV-8, right) show the same features for all additive-free catalysts. However, after additive impregnation, the Fourier Transforms reveal the same distances as the additive-free catalyst although the peak intensities are modified, especially the peak centered at about 3 \AA (not phase corrected).

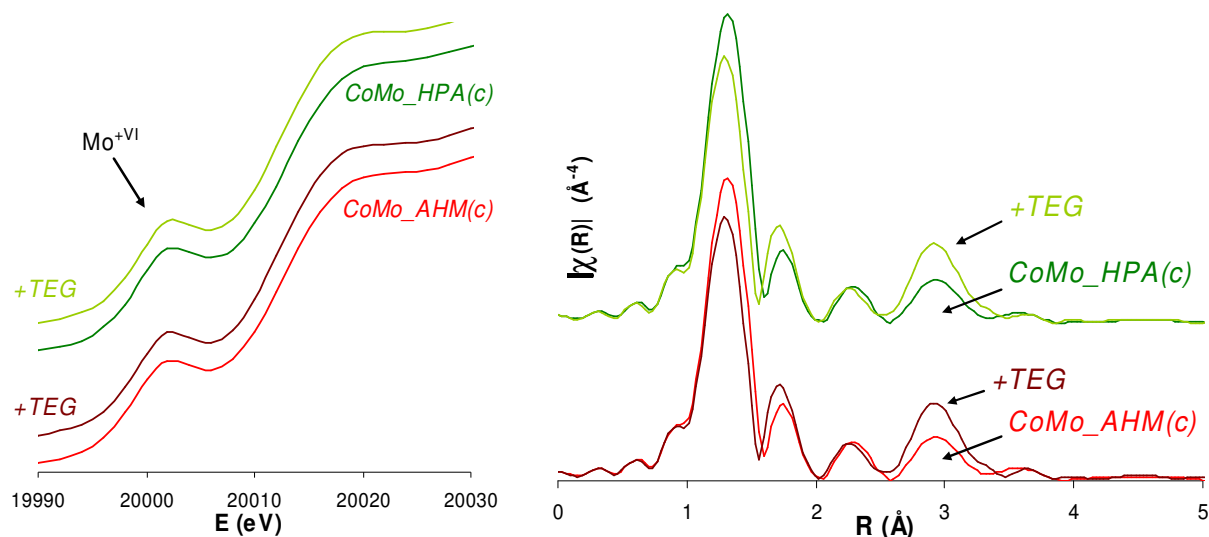


Figure IV-8: Mo K-edge XANES (left) and k^3 -weighted EXAFS Fourier Transforms (FT) (right) of CoMo_AHM(c), CoMo_HPA(c) and corresponding additive-containing catalysts. FT Hanning window from 3 to 13; $\tau=2.5$.

The shape and position of the pre-edge peak in the XANES spectra indicate a 6+ oxidation state of molybdenum in an octahedral symmetry [8]. The additive does not modify the average oxidation stage or the local average geometry. In terms of the EXAFS spectra, only modifications on the peaks intensities are observed. In particular, the peak at 3 Å (not phase corrected) increases, assigned to the formation of more molybdenum-metal or molybdenum-phosphorus bonds [7,8]. This is consistent with polyoxomolybdates conversion into Anderson HPAs, as shown by Raman spectroscopy.

Based on the different characterization methods used, it becomes possible to describe the nature of the species inside the catalyst.

Table IV-2: Speciation results for the calcined CoMo catalysts prior to and after TEG impregnation.

	Prior to TEG	After TEG
CoMo_AHM(c) and CoMo_HPA(c)	cobalt aluminate polyoxomolybdates	cobalt aluminate $\text{Co}_{3/2}[\text{AlMo}_6\text{O}_{24}\text{H}_6]$

IV.2.3. METALS DISTRIBUTION

Electronic probe microanalysis (EPMA) is conducted to determine how the elements are distributed inside the catalysts body and if the additive modifies that distribution.

All calcined catalysts showed a good molybdenum and cobalt dispersion over the alumina extrudate body. A distribution coefficient R of 1 is found for these metals using EPMA. A preliminary essay showed that dried and calcined catalysts exhibit the same distribution profile.

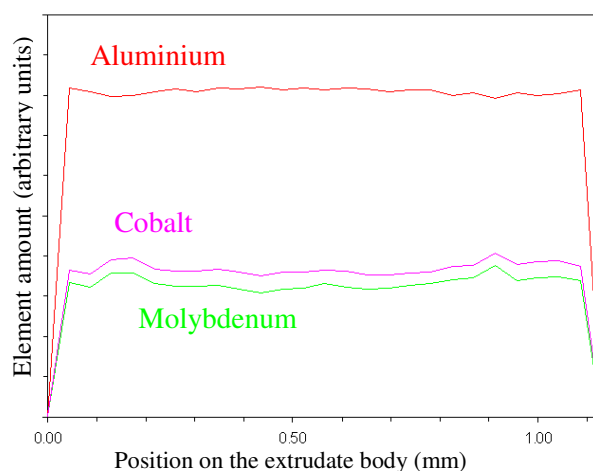


Figure IV-9: Aluminium, molybdenum and cobalt electron probe microanalysis of the CoMo_AHM(c) catalyst.

IV.2.4. THERMAL BEHAVIOR

Thermogravimetric analysis (TGA) is carried out to study the temperature stability domain of the different surface species and how they are affected by the additive. In this sense, the additive-free catalysts are firstly analyzed and the collected data will then be used to interpret the analysis results for the additive-containing catalysts. Like in the dried catalysts case, the derivative thermogravimetry (DTG) curves are calculated from the thermogravimetric analysis and then decomposed into linear combinations of Lorentz curves. A detailed description of the model is reported to Appendix C.

IV.2.4.1. Additive-free calcined CoMo catalysts analysis

The calcined CoMo_AHM(c) and CoMo_HPA(c) exhibit similar thermogravimetric behaviors, with total weight losses of 10.8 and 10.6 wt%, respectively. The DTGs show only one inflexion at about 90 °C.

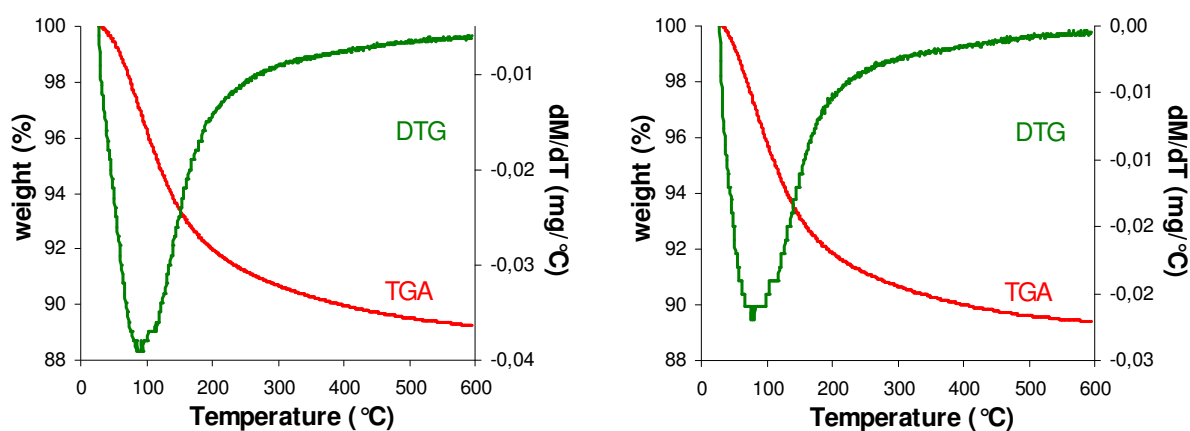


Figure IV-10: Thermogravimetric analysis (TGA) and, derivative thermogravimetry (DTG) of the CoMo_AHM(c) (left) and CoMo_HPA(c) (right) catalysts.

The analysis of the gas effluents by mass spectroscopy reveals only the water removal with a maximum at about 100 °C for the calcined AHM-based (Figure IV-11) and HPA-based (not shown here) catalysts, which corresponds to physisorbed water. The fact that the water removal is not detected in the 150-350 °C region shows that no heteropolyanions are present at the catalysts surface. The absence of nitrogen-containing mass fragments confirms that both ammonium and nitrates counter-ions are destroyed during the calcination stage.

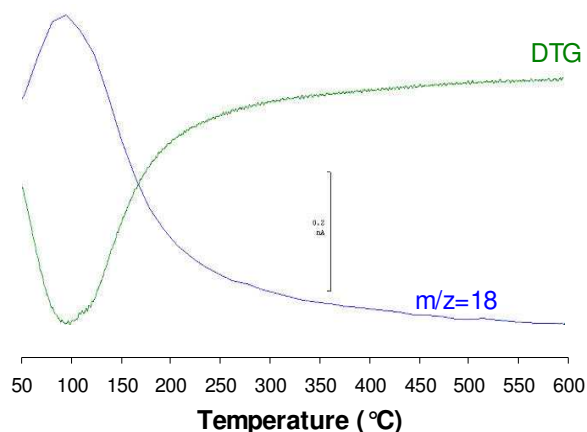


Figure IV-11: Mass spectroscopy follow-up of the CoMo_AHM(c) catalyst.

The DTGs spectra are decomposed in order to obtain more precise qualitative and quantitative information about the thermal stability of the deposited surface species.

In the case of the calcined CoMo catalysts, only one contribution is necessary to simulate the experimental curve, revealing that Lorentz curves satisfactorily describe the experimental DTG data (Figure IV-12).

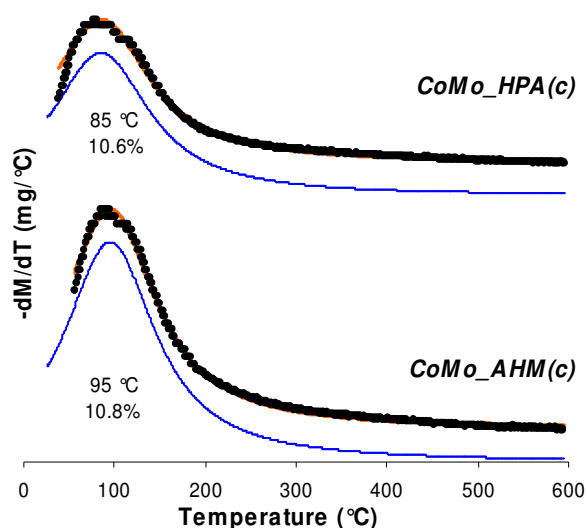


Figure IV-12: DTG decomposition of the calcined CoMo_AHM(c) and CoMo_HPA(c) catalysts.

IV.2.4.2. Additive-containing calcined CoMo catalysts analysis

The CoMo_AHM(c)+TEG catalyst exhibits a total loss of 18.6 wt% with two local DTG minimums at about 80 and 240 °C. Mass spectroscopy shows that the water removal occurs before 100 °C and also at about 240 °C. In addition, a major CO₂ emission centered at 250 °C is observed. Traces of m/z 12 (carbon-type fragment) and 58 (ketone-type fragment) are also observed (Figure IV-13).

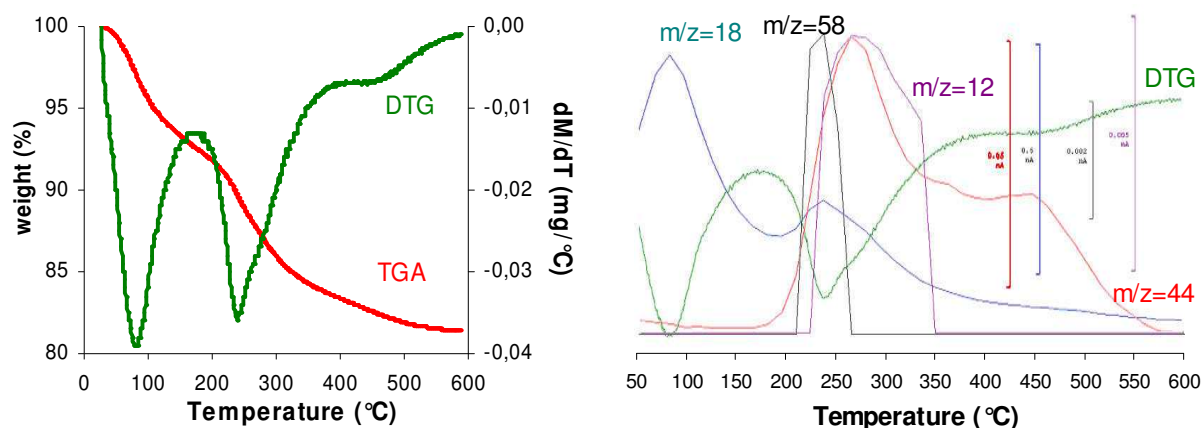


Figure IV-13: Thermogravimetric analysis (TGA), derivative thermogravimetry (DTG) and mass spectroscopy (right) of the CoMo_AHM(c)+TEG sample.

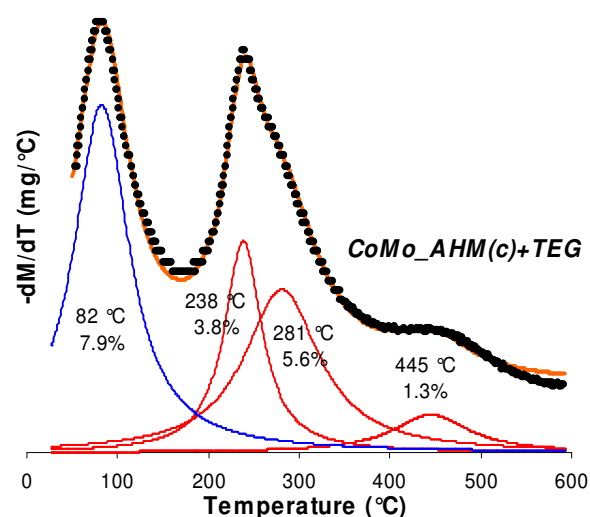


Figure IV-14: DTG decomposition of the CoMo_AHM(c)+TEG sample.

The additive-containing CoMo_AHM(c) catalyst DTG is decomposed into 4 curves (Figure IV-14). The first curve is attributed to physisorbed water (7.9 wt%). The other 3 curves are assigned to three different TEG thermal decomposition products, observed at about 238, 281 °C and 445 °C, corresponding to weight losses of 3.8, 5.6 and 1.3%, respectively. These temperatures are close to those observed in the CoMo_AHM(d)+TEG catalyst (241, 281 and 442 °C).

The second water loss maximum in the mass spectroscopy reveals the presence of heteropolyanions, which according to Raman spectroscopy are the Anderson hexamolybdoaluminate HPAs. However, no additional curve is detected in the DTGs decompositions. Reaction IV-1 is used to determine the amount of water arising from this HPA decomposition, assuming that all molybdenum participates in the HPA.



Table IV-3 shows that the amount of TEG is overestimated, meaning that the contribution due to the $\text{AlMo}_6\text{O}_{24}\text{H}_6^{3-}$ constitutional and coordination water is included in the TEG decomposition curves.

Table IV-3: DTG decomposition assignments of the CoMo_AHM(c)+TEG sample.

T (°C)	Experimental weight loss (%)	Assignment	Expected weight loss (%)
82	7.9	Physisorbed water	-
-	-	HPA coordination water	-
-	-	HPA constitutional water	0.9
241	3.8	TEG (sum=10.8%)	8.8
281	5.6		
445	1.3		

The CoMo_HPA(c)+TEG catalyst exhibits a total loss of 18.0 wt% with two local DTG minimums at about 80 and 240 °C. Mass spectroscopy reveals a major depart from 100 to the end of the analysis. In addition, a major CO₂ emission beginning at 200 °C is observed (Figure IV-15). Traces of m/z 12 (carbon-type fragment) and 58 (ketone-type fragment) are also observed (not shown here).

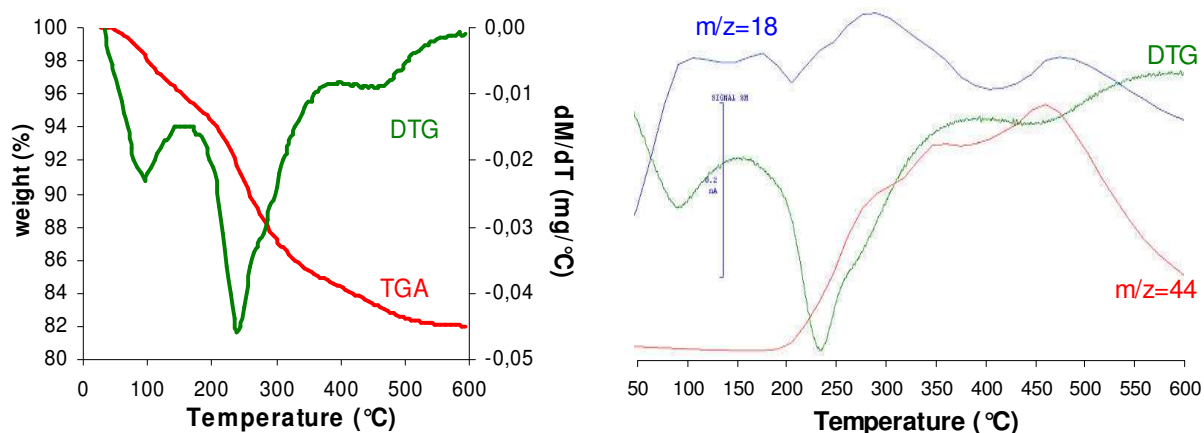


Figure IV-15: Thermogravimetric analysis (TGA), derivative thermogravimetry (DTG) and mass spectroscopy results (right) of the CoMo_HPA(c)+TEG sample.

The additive-containing CoMo_HPA(c) catalyst DTG is decomposed into 5 different curves (Figure IV-16). The first curve is attributed to physisorbed water (4.2 wt%). The second curve, centered at about 170 °C (0.9 wt%) is assigned to the coordination water of the AlMo₆O₂₄H₆³⁻ HPA. The other 3 curves are assigned to three different TEG thermal decomposition products, observed at about 237, 278 °C and 444 °C, corresponding to weight losses of 4.7, 6.3 and 2.0%, respectively.

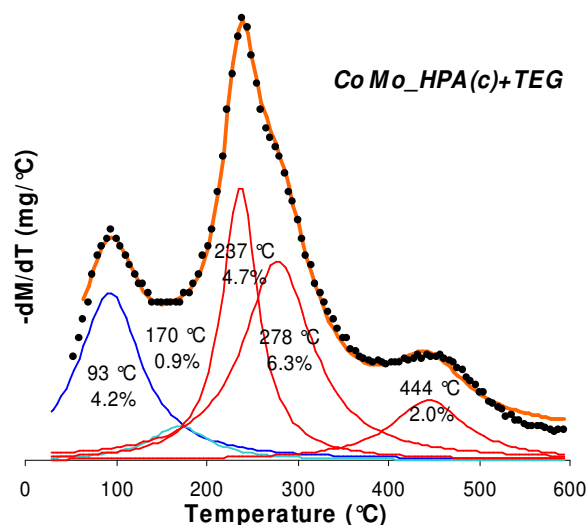


Figure IV-16: DTG decomposition of the CoMo_HPA(c)+TEG sample.

Table IV-4: DTG decomposition assignments of the CoMo_AHM(c)+TEG sample.

T (°C)	Experimental weight loss (%)	Assignment	Expected weight loss (%)
93	4.2	Physisorbed water	-
170	0.9	HPA constitution water	1.1
		HPA coordination water	-
237	4.7	TEG (sum=12.9%)	11.8
278	6.3		
444	2.0		

IV.2.5. SURFACE MECHANISM

The speciation methods showed the evolution from a dispersed polyoxomolybdates phase towards an Anderson hexamolybdoaluminate phase after the additive impregnation, while cobalt aluminate remains untouched. When the additive-containing solution is introduced, part of the deposited polyoxomolybdates is dissolved. At the same time, the alumina support is partially dissolved and reacts with the polyoxomolybdates to form the Anderson HPA that precipitates. As for the dried CoMo-based catalysts, this precipitation displaces the dissolution equilibrium towards the HPA formation. Nevertheless, calcination leads to stronger precursor-support interactions and prevents species redissolution. Consequently, the redispersion phenomenon occurs to less extent.

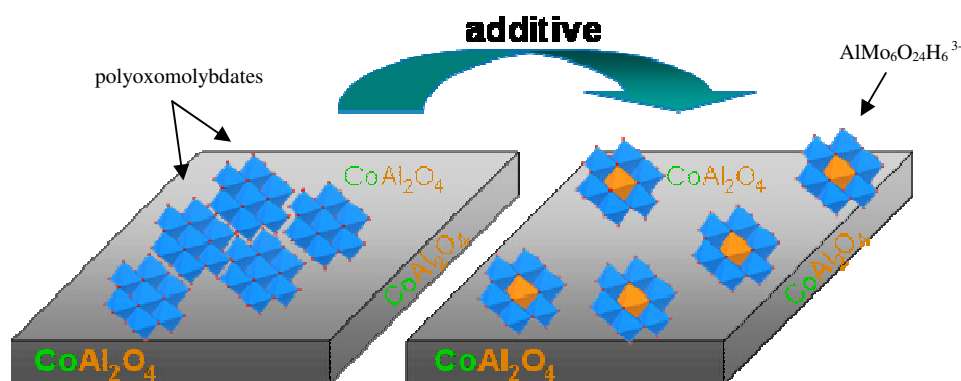


Figure IV-17: Schematic representation of the redispersion mechanism induced by the additive for the alumina-supported calcined CoMo-based catalysts.

IV.3. IMPACT OF THE ADDITIVE WHEN IMPREGNATED ON CALCINED COMOP CATALYSTS

This section is dedicated to understand if and how the additive impregnation modifies the deposited surface species and also the elements distribution inside the catalysts extrudates. To do so, the dried CoMoP catalysts studied in Chapter III are calcined and afterwards impregnated with the additive. In a first step, the textural properties of the starting calcined catalysts are characterized. Then, the surface species and the elements distribution inside the catalyst body are characterized prior to and after additive impregnation.

IV.3.1. TEXTURAL PROPERTIES OF THE CALCINED CoMoP CATALYSTS

Nitrogen adsorption studies were carried out to characterize the porosity of the catalysts. The objective is to study some of the differences of the catalysts.

Table IV-5 shows that increasing amounts of phosphorus result in a decrease in the available surface area while the average pore diameter stays constant. Using the CoMo_AHM(c) catalyst as a reference (255 m²/g), an amount of 5 wt% P₂O₅ leads to a BET surface loss of about 50 m²/g.

Table IV-5: Surface area and average pore diameter of calcined CoMoP catalysts.

Catalyst	BET surface area [m ² /g]	BJH adsorption surface area [m ² /g]	Average pore diameter (APD) (nm)*
CoMoP(1c)	240	219	9.8
CoMoP(2c)	223	202	10.0
CoMoP(3c)	219	194	10.0
CoMoP(5c)	205	187	10.1

* Calculated using the BJH adsorption surface area (APD=4V/S).

Phosphorus deposition in the catalyst pores is a plausible interpretation to explain the decrease in surface area: first phosphate ions react with the alumina surface to form AlPO₄. When the phosphate surface concentration increases, aluminophosphate groups tend to form supported P₂O₅ particles, especially after calcination. These particles decrease the available surface area. At the same time, because the average pore diameter is practically the same, it is plausible to admit that the BET surface area decrease is related to the loss of microporosity by phosphate micropore blockage. This hypothesis is supported by the fact that BJH studies are not sensible to microporosity modifications.

The porous distribution is plotted as a function of the pore volume derivative, which was calculated using the BJH nitrogen desorption branch. Figure IV-18 shows that an increasing amount of phosphorus leads to a loss of smaller pores, shifting the population maximum towards higher pore diameters.

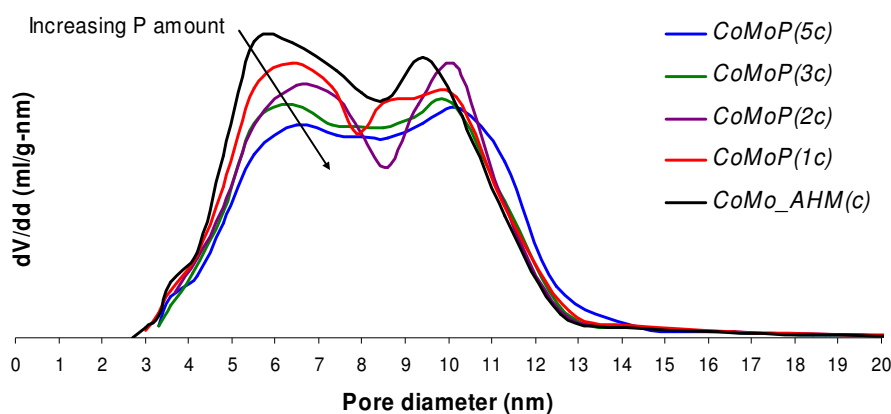


Figure IV-18: BJH porous distribution of calcined CoMoP catalysts.

To better understand this phenomenon, MoP catalysts were also an object of a BJH study. The results summarized in Table IV-6 show that although the BET surface area remains the same for all calcined MoP catalysts, the surface area given by the BJH method decreases with the amount of phosphorus.

Table IV-6: Surface area and average pore diameter of calcined CoMoP catalysts.

Catalyst	BET surface area [m ² /g]	BJH adsorption surface area [m ² /g]	Average pore diameter (APD) (nm)*
MoP(2c)	246	197	10.8
MoP(3c)	249	188	10.5
MoP(5c)	244	177	11.3

* Calculated using the BJH adsorption surface area (APD=4V/S); n.d.: not determined.

Since the BJH method refers to the catalyst mesoporosity and the BET method refers both to the meso and microporosity, the results show that microporosity is being created while mesoporosity is being lost. The reason behind these observations is possibly related to support dissolution caused by the aggressive pH of the impregnation solutions (pH~0.2). New micropores are created but at the same time lead to mesopore collapse.

The same behavior in porous distribution than the CoMoP catalysts is observed: increased amounts of phosphorus lead to a loss in small pores and a shift of the population maximum towards higher pore diameters (Figure IV-19).

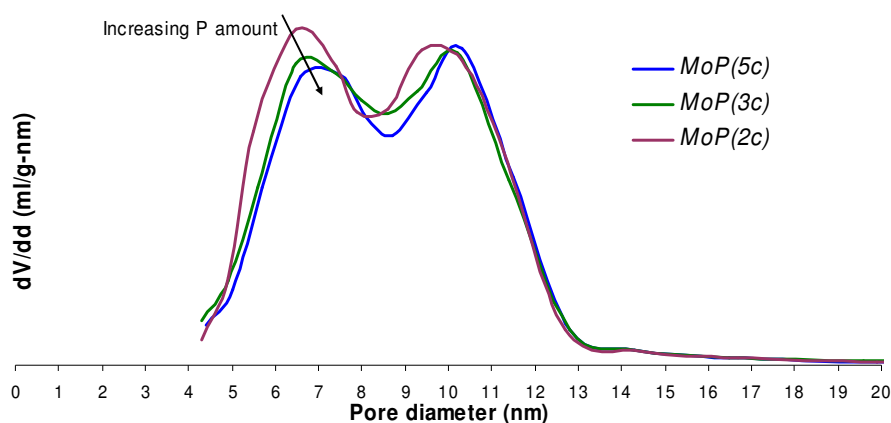


Figure IV-19: BJH porous distribution of calcined MoP catalysts.

To study the impact of the impregnation solution formulation on textural properties, the BJH porous distribution of CoMoP(5c), MoP(5c), P(5c) and alumina samples is superposed. Figure IV-20 shows that the surface area decreases when molybdenum and cobalt are impregnated.

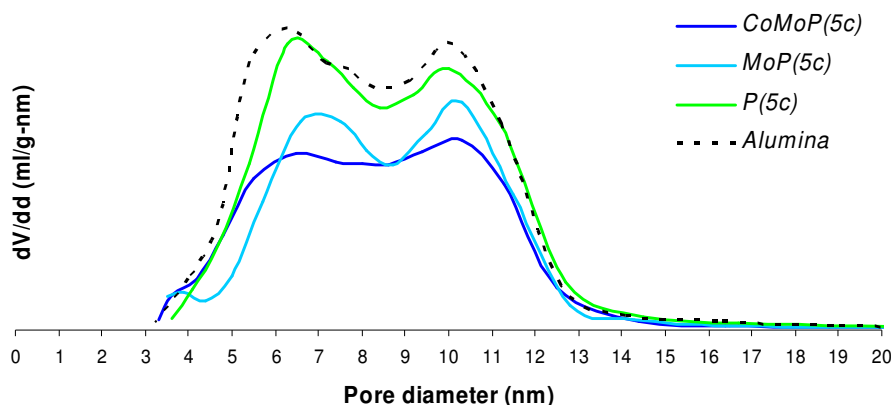


Figure IV-20: BJH porous distribution of CoMoP(c), MoP(c), P(c) and alumina solids.

As mentioned above, the BJH study is not sensible to microporosity and consequently does not account for micropore-blocking or microporosity gains. In this sense, the available surface area of the catalysts correlates with their phosphorus loading (Figure IV-21, left). However, the introduction of ortho-phosphoric acid in the impregnation solutions leads to a decrease in the solution pH, which favors alumina dissolution. The plot of the available surface area as a function of the impregnation solution pH shows that for the same pH, the same surface area is achieved. Moreover, for each formulation, the increase in the impregnation solution acidity results in a decrease in the final surface area (Figure IV-21, right).

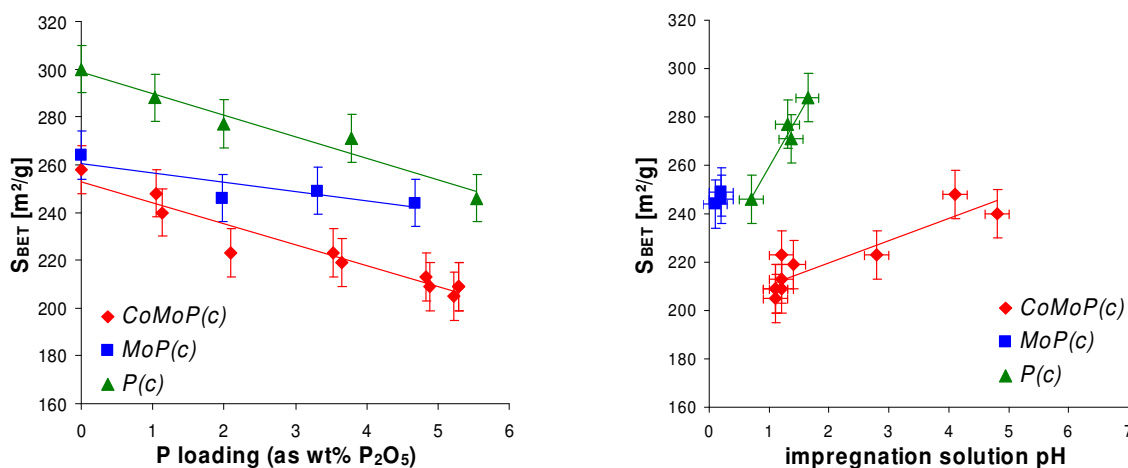


Figure IV-21: BET surface area as a function of phosphorus loading (left) and impregnation solution pH (right). The 0 wt% phosphorus point in the left image corresponds to alumina for P(c) formulations, Mo_AHM for the MoP(c) catalysts and CoMo_AHM(c) for the CoMoP(c) catalysts.

A hypothesis to explain the previous results is that acidic solutions lead to alumina dissolution and favor the formation of micropore-blocking phosphate groups. However, in very acidic solutions ($\text{pH} \leq 1$) this loss is compensated by the creation of new microporosity.

IV.3.2. SPECIATION OF THE CALCINED CoMoP CATALYSTS

This section is dedicated to the study of the deposited surface species in the CoMoP catalysts prior to and after additive impregnation. First, the cobalt-containing species are characterized and how they evolve after additive impregnation. Then, the molybdenum-containing species are determined and finally the phosphorus-containing surface species are studied. By studying the precursor structures, it is possible to have a global vision of the catalyst surface and how it is affected by the additive.

IV.3.2.1. Influence of the additive on cobalt species

Like in the CoMo catalysts case, UV-Visible diffuse reflectance spectroscopy is privileged to provide qualitative information about the cobalt-containing surface species. This study was complemented by cobalt K-edge X-ray absorption spectroscopy to study if the additive changes the local environment of cobalt atoms.

The UV-Visible DRS features of the calcined CoMoP catalysts (Figure IV-22) are similar to those of the calcined CoMo catalysts, exhibiting bands at about 545, 580 and 650 nm. These bands are assigned to cobalt aluminate in which cobalt is in tetrahedral symmetry (545, 580 and 630 nm) [3]. The spectral features of CoMoO_4 (main bands at 525 and 587 nm) are also found, especially when the P/Mo molar ratio is inferior to 2/5. The band appearing in the 600-900 nm region, assigned to reduced species, is no longer visible, meaning that these species are destroyed upon calcination.

After additive impregnation, the CoMoP(1c) spectral line is slightly affected. However, this is not the case for the CoMoP(3c) and CoMoP(5c) samples: the local maximum is shifted towards low wavelengths and the spectral lines evolve to the cobalt aluminate typical spectrum.

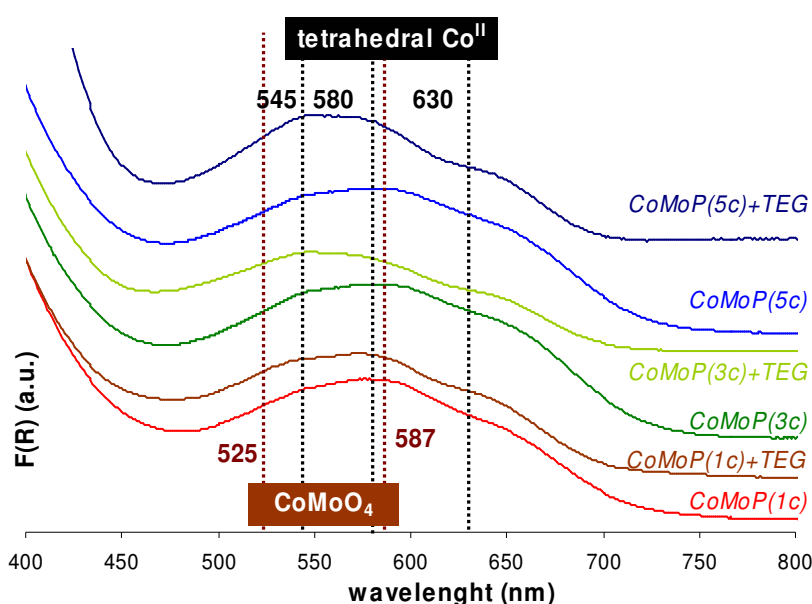


Figure IV-22: UV-Visible DRS of calcined CoMoP and corresponding additive-containing catalysts.

An hypothesis to explain the evolution of the spectral lines may be related to the conversion of CoMoO_4 species to form cobalt aluminate or the cobalt aqua complex (main band at 513 nm) or even $\text{PCoMo}_{11}\text{O}_{40}^{7-}$ (main band at 557 nm), as shown by Raman spectroscopy for the dried catalysts. However, XRD measurements did not detected the presence of a CoMoO_4 phase, which means that the amount formed is small. Besides this, it is know that both CoMoO_4 and CoAl_2O_4 species have very high absorption coefficients in the UV-Visible region, which renders the detection of other phases rather difficult.

Like in the calcined CoMo catalysts case, the absence of Co(III) species was confirmed by the cobalt K-edge XANES study. The maximum at about 7725 eV is typical of Co(II) and no shoulder at about 7733 eV corresponding to Co(III) [5,9] is visible (Figure IV-23). No modifications are shown in the XANES spectra after additive impregnation.

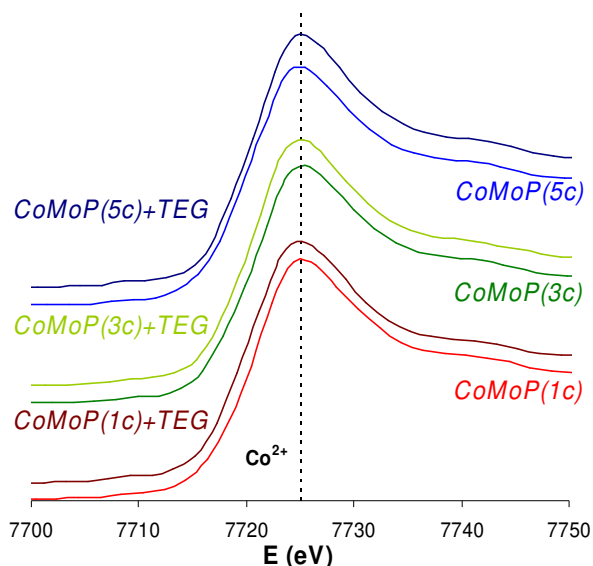


Figure IV-23: Cobalt K-edge spectra of calcined CoMoP and corresponding additive-containing catalysts.

The cobalt K-edge k^3 -weighted EXAFS Fourier Transforms (FT) features are the same for the additive-free and additive-containing calcined CoMoP catalysts (Figure IV-24). The average cobalt local structure is dominated by an oxygen shell at about 1.5 Å (not phase corrected). No modifications are observed after the additive introduction. Unfortunately, due to the quality of the raw signal, the FT is calculated in a rather small interval which results in less-defined EXAFS spectra.

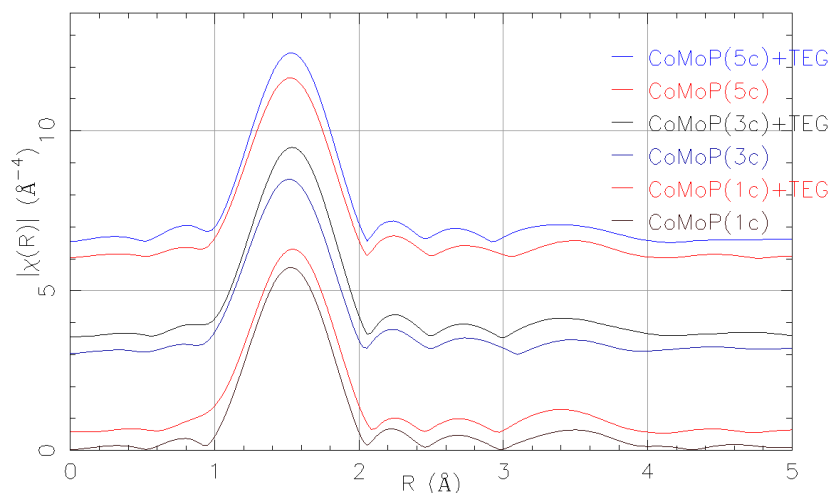


Figure IV-24: Cobalt K-edge k^3 -weighted EXAFS Fourier Transforms (FT) of calcined CoMoP and corresponding additive-containing catalysts. FT Hanning window from 2 to 9; $\tau=2.5$.

The XANES and EXAFS spectra are not affected neither by the presence of the additive nor by increasing amounts of phosphorus, contrarily to the UV-Visible results. Since the XAS measurements only provide information about the average structure, it may be concluded that cobalt structures are similar after calcination independently of the different P/Mo ratio. Thus, the catalysts are only slightly affected by the additive impregnation. This seems logic because calcination leads to stronger active phase precursors-alumina interactions and therefore, it is more difficult to modify these structures.

IV.3.2.2. Influence of the additive on molybdenum species

Raman analyses are carried out on the calcined CoMoP catalysts to characterize the molybdenum-containing surface species prior to and after the additive impregnation. XAS measurements are also conducted to verify if the average molybdenum local environment is modified by the additive.

The Raman spectra of the additive-free calcined CoMoP catalysts (Figure IV-25) exhibit the same features as the calcined CoMo-based samples. The wide band at about 955-950 cm^{-1} and the shoulder at about 860 cm^{-1} , are typical of dispersed polyoxomolybdate structures.

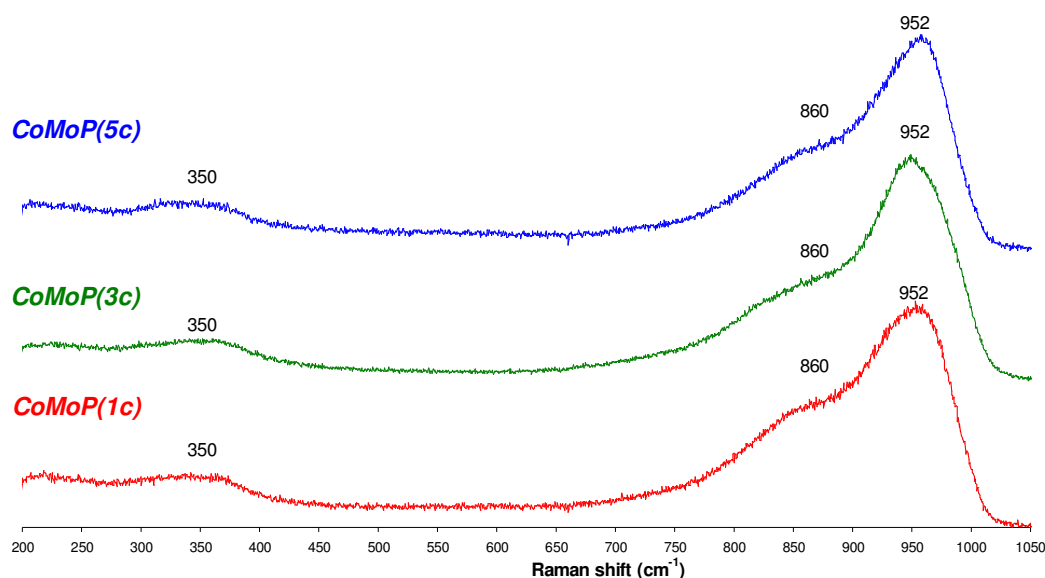


Figure IV-25: Raman spectra of calcined CoMoP catalysts.

Like in the calcined CoMo catalysts case, the absence of signal in the 500-600 cm^{-1} region indicates that no HPA species survived the calcination stage. Indeed, the spectra of all calcined catalysts are similar showing that the calcination stage leads to the formation of a polyoxomolybdates phase.

Once the additive is impregnated, the Raman features of calcined CoMoP samples (Figure IV-26) are similar to those observed for dried CoMoP catalysts containing the additive: an intense sharp peak at 952 cm^{-1} , a shoulder at 835 cm^{-1} (assigned to TEG) and a new peak appearing at about 565 cm^{-1} . Moreover, when the phosphorus loading is superior or equal to 3.5 wt% P_2O_5 (P/Mo molar ratio $\geq 2/5$), a new sharp peak appears at about 971 cm^{-1} .

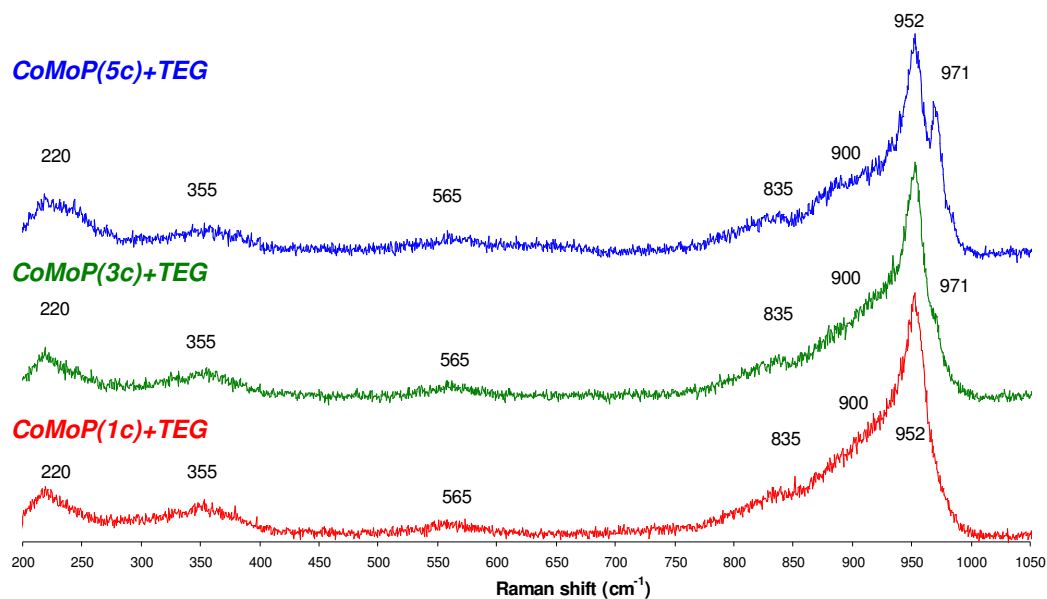


Figure IV-26: Raman spectra of additive-containing calcined CoMoP catalysts.

As for all dried CoMo(P) and calcined CoMo catalysts, the additive leads to the Anderson $\text{AlMo}_6\text{O}_{24}\text{H}_6^{3-}$ HPA formation (peaks at 952 and 565 cm^{-1} [7]). For catalysts with a high phosphorus content, the $\text{PCoMo}_{11}\text{O}_{40}^{7-}$ HPA formation (peak at 971 cm^{-1} [10]) is also observed. This result shows that even on calcined catalysts, the additive promotes a redissolution-reprecipitation mechanism evolving the molybdenum-assisted alumina dissolution.

The Raman analysis of the deposited molybdenum-containing species is complemented by XAS measurements at the molybdenum K-edge.

The molybdenum K-edge XANES of calcined CoMoP catalysts (Figure IV-27, left) present the same features. However, the EXAFS spectra show significant modifications are observed after the additive impregnation (Figure IV-27, right). Although the distances are the same, TEG leads to a decrease in the first two peaks intensity, assigned to molybdenum-oxygen bonds, and also to an intensity increase in the peak centered at about 3 Å (not phase corrected).

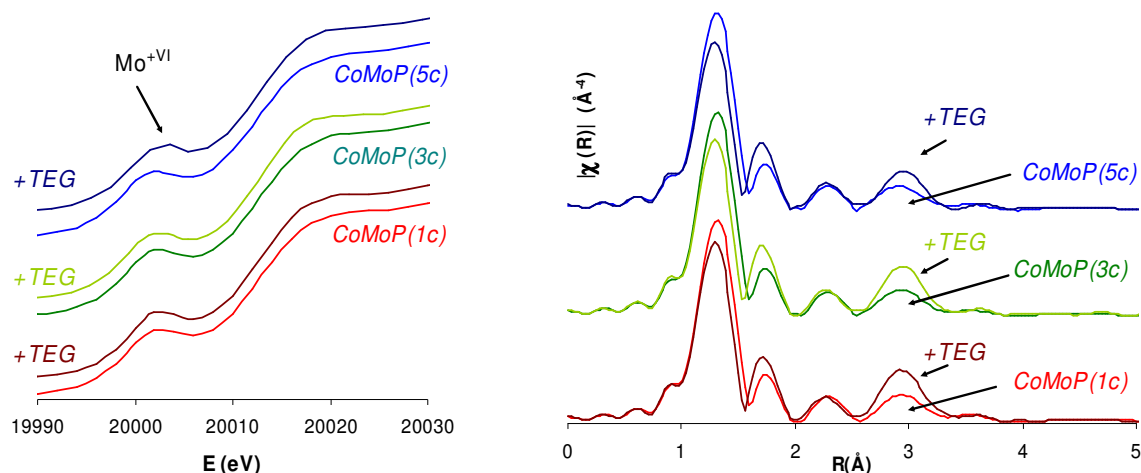


Figure IV-27: Mo K-edge XANES (left) and k^3 -weighted EXAFS Fourier Transforms (FT) (right) of CoMo_AHM(c), CoMo_HPA(c) and corresponding additive-containing catalysts. FT Hanning window from 3 to 13; $\tau=2.5$.

The XANES part of the XAS spectra reveals that neither the additive, nor phosphorus modifies the average oxidation state or average local symmetry. The large pre-edge observed at about 20005 eV is associated to a 6+ oxidation state for molybdenum in octahedral geometry [8]. In terms of k^3 -weighted EXAFS FT, the band at about 3 Å comes from the Mo-metal or Mo-phosphorus shell [7,8], which means that more metals or phosphorus are in the vicinity of molybdenum after additive impregnation. This is consistent with the polyoxomolybdates conversion into HPAs, as shown by Raman.

IV.3.2.3. Influence of the additive on phosphorus species

It was discussed that the additive may significantly alter the structure of the molybdenum active phase precursors as well as cobalt species. Moreover, the study of the phosphorus species on the dried catalysts showed that apart from the $\text{PCoMo}_{11}\text{O}_{40}^{7-}$ HPA formation, no major modifications are induced by the additive. However, the initial state of the calcined catalysts is different due to the thermal treatment, which may have a strong impact on the deposited phosphorus species. For this reason and to refine the Raman observations, a ^{31}P NMR study is conducted. Due to the paramagnetic effect of cobalt species, the study was carried out in the absence of this element.

Before studying the catalysts, a series of dried phosphorus-impregnated aluminas were calcined and then impregnated with the additive. They are previously analyzed to collect reference data about the different phosphate phases and also to characterize the effect of the additive on these samples. Then, the CoMoP and MoP catalysts spectra are acquired and interpreted using the data previously obtained.

The spectra of the additive-free calcined $\text{P}/\text{Al}_2\text{O}_3$ samples exhibit a wide non-symmetrical band with a maximum at about -14 ppm whose intensity increases with the amount of phosphorus. After the additive introduction, the signal is shifted towards the downfield (Figure IV-28).

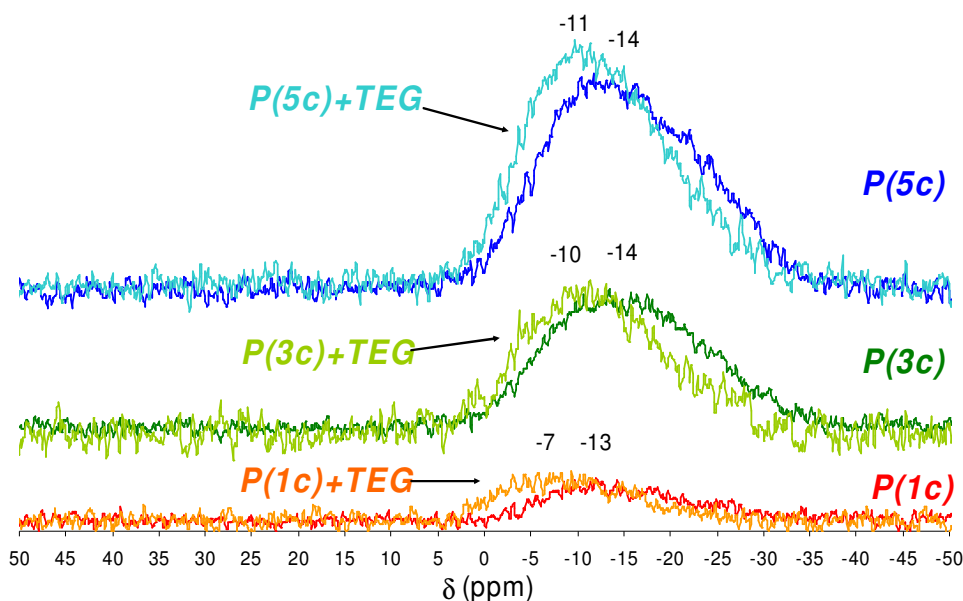


Figure IV-28: ^{31}P MAS NMR spectra of calcined $\text{P}/\text{Al}_2\text{O}_3$ and corresponding additive-containing solids.

The spectra are mathematically decomposed to elucidate about the different phosphated species that are deposited on the catalyst surface. The additive-free samples spectra show three contributions at about -21, -14 and -11 ppm (Figure IV-29). After the additive introduction, the signal at about -11 ppm is kept unaltered while the signal at about -21 ppm decreases drastically. A new signal appears at about -5 ppm.

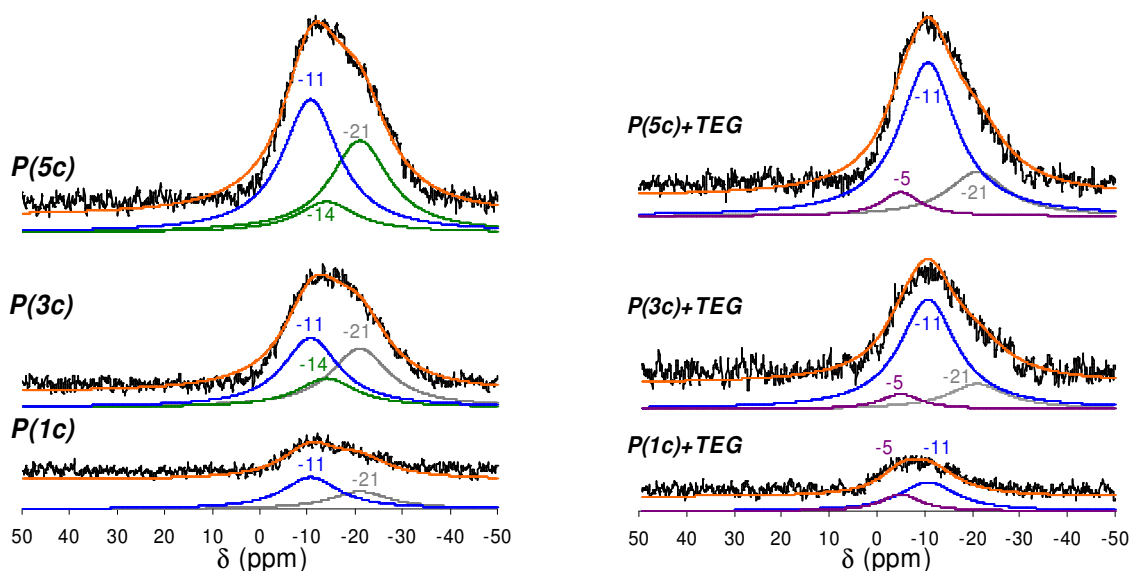


Figure IV-29: ^{31}P MAS NMR spectra decomposition of calcined $\text{P}/\text{Al}_2\text{O}_3$ (left) and corresponding additive-containing solids (right).

As for the dried catalysts, the resonance at about -11 ppm is assigned to dispersed monophosphates [11,12], the resonance at about -14 ppm is assigned to polyphosphates [13,14] and the resonance at

about -21 ppm is assigned to aluminophosphates [11,12,13,14,15]. The new resonance at -5 ppm is assigned to a phosphoric acid derivate, $H_xPO_4^{3-x}$ [16]. The NMR results suggest that the additive leads to the partial conversion of the $AlPO_4$ species. Besides this, the additive also promotes the formation of phosphoric acid derivatives. It seems plausible to propose that in presence of TEG, some of the $Al-PO_4$ bonds are broken and dissolve, then the phosphate groups physisorb on the alumina surface after protonation.

Table IV-7 summarizes the NMR resonances obtained from the experimental data decomposition.

Table IV-7: ^{31}P MAS NMR data extracted from experimental data decompositions.

δ (ppm)	assignment
-5	physisorbed phosphoric acid derivate
-11	monophosphates
-14	polyphosphates
-21	aluminophosphates

The paramagnetic effect of cobalt species was confirmed by a preliminary ^{31}P MAS NMR analysis of the CoMoP(5c) catalyst. It exhibits a weak and broad band centered at about -18 ppm (Figure IV-30). Although the shifting of the NMR signal may be expected due to cobalt, the position and shape of the main resonance reveal the formation of aluminophosphates.

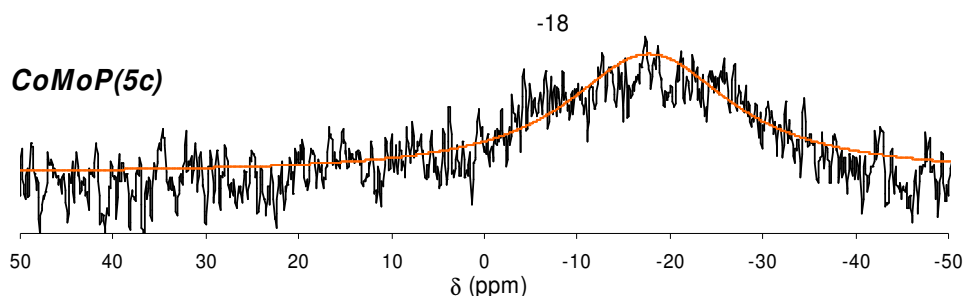


Figure IV-30: ^{31}P MAS NMR spectra of the CoMoP(5c) catalyst.

The spectra of the additive-free calcined MoP catalysts (Figure IV-31) exhibit a broad non symmetrical resonance with a maximum in the -25 to -20 ppm region. After the additive introduction, the signal is shifted towards the upfield and reveals a new sharp resonance at about -3.8 ppm when the P/Mo molar ratio is superior to 2/5.

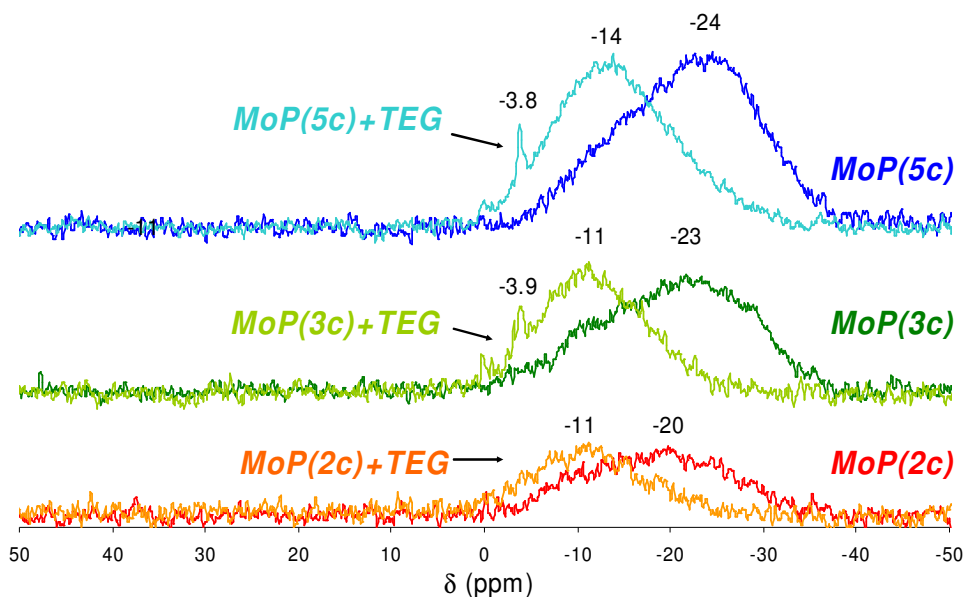


Figure IV-31: ^{31}P MAS NMR spectra of calcined MoP and corresponding additive-containing catalysts.

Resonances lower than -20 ppm indicate presence of AlPO_4 , formed during the calcination stage. After additive impregnation, the shift towards the upfield means that the phosphates interaction with alumina is less intense. Thus, a sharp resonance at about -3.8 ppm appears, already observed in the dried MoP catalysts and assigned to Keggin $\text{PMo}_{12}\text{O}_{40}^{3-}$ entities [14,17].

The mathematical decomposition of the spectra is once again used to elucidate about the precise nature of the phosphated species. The resulting contributions are plotted in Figure IV-32.

The additive-free calcined MoP catalysts DTGs are decomposed into 3 contributions at about -26, -21 and -14 ppm. After additive impregnation, the downfield contributions at about -26 and -21 ppm disappear almost completely and the spectra are mainly composed of a resonance at about -11 ppm, except for the MoP(5c)+TEG catalyst. In this particular case, the spectra decomposition shows an important contribution of the resonance at about -14 ppm as well as a small contribution located at about -21 ppm.

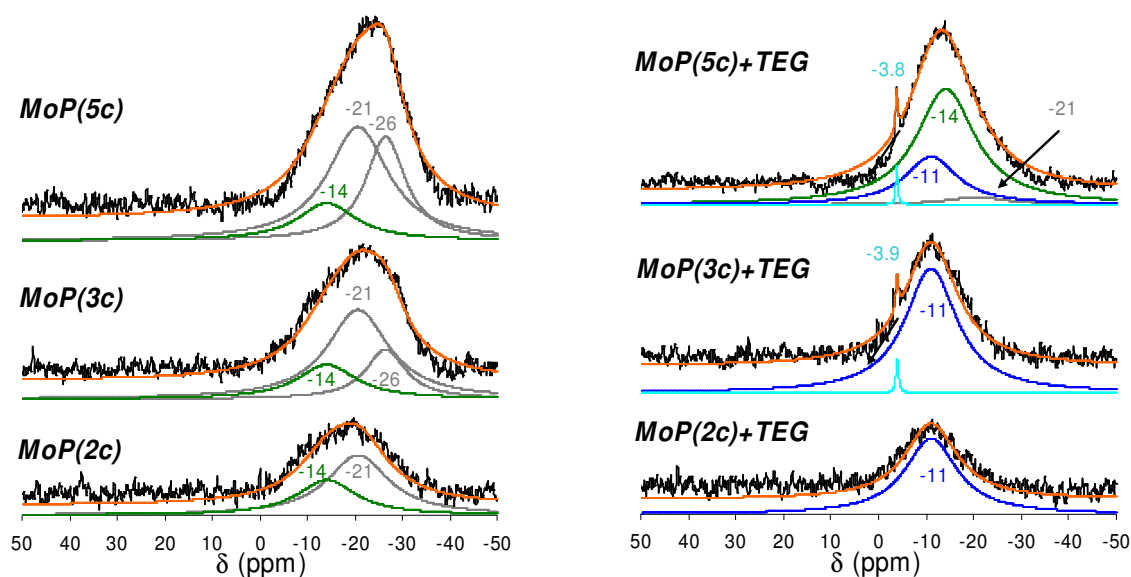


Figure IV-32: ^{31}P MAS NMR spectra decomposition of calcined MoP (left) and corresponding additive-containing solids (right).

The contributions centered at about -21 and -14 ppm were already observed for the calcined $\text{P}/\text{Al}_2\text{O}_3$ samples and also in the dried MoP catalysts. They correspond to polyphosphates and amorphous aluminophosphates, respectively. The curve centered at about -26 ppm is assigned to crystalline AlPO_4 . Indeed, DeCanio *et al.* [15] reported the formation of crystalline AlPO_4 at high phosphorus loadings on calcined MoP/ Al_2O_3 samples, which gave rise to a NMR resonance located at about -26 ppm.

When compared to the additive-free calcined $\text{P}/\text{Al}_2\text{O}_3$ samples, it becomes clear that competitive adsorption between molybdates and phosphate groups is taking place, resulting in less alumina adsorption sites and as a consequence phosphate groups tend to condensate. The same result was widely reported in the literature [11,15,16].

Figure IV-32 shows that the additive induces, besides the formation of Keggin-like HPAs (sharp resonance at about -3.8 ppm), the conversion of both the amorphous and crystalline aluminophosphates into dispersed monophosphates and also polyphosphates at high phosphorus loadings. The phosphorus speciation of the additive-containing MoP catalysts is finally the same for dried or calcined catalysts. This result is in line with the observations made by Raman spectroscopy where molybdenum speciation was the same for the additive-containing dried and calcined CoMoP catalysts.

Raman analyses are carried out on calcined MoP catalysts to refine the phosphorus speciation and to better understand the impact of the additive. This allows to determine which phosphomolybdic heteropolyanions are deposited on the non-promoted catalysts surface. The impact of the additive is necessarily different in absence of cobalt: the $\text{PCoMo}_{11}\text{O}_{40}^{7-}$ HPA can no longer be formed.

The spectrum of the calcined MoP(5c) catalyst (not shown here) is similar to the CoMoP(5c) spectrum, revealing the formation of a polyoxomolybdate phase.

Upon additive impregnation, the MoP(5c)+TEG catalyst spectrum (Figure IV-33) reveals, besides the Anderson hexamolybdoaluminate HPA (intense band at about 952 cm^{-1}), the formation of a Keggin-like HPA (band at 983 cm^{-1}).

These results are in agreement with the NMR observations, showing the formation of Keggin-like HPAs upon additive impregnation.

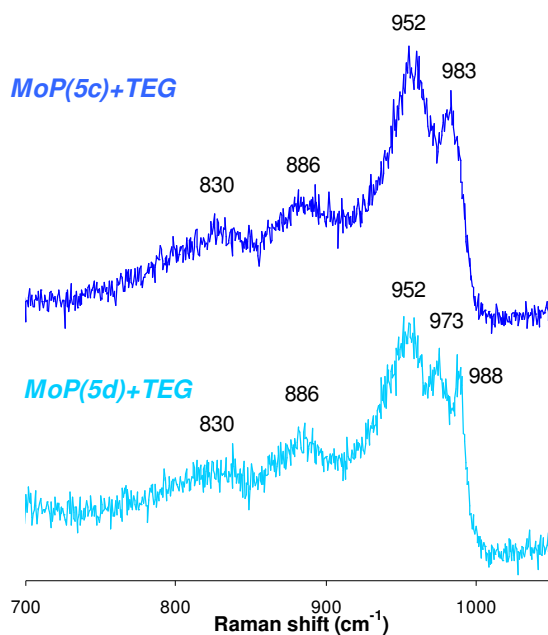


Figure IV-33: Raman spectra of additive-containing dried and calcined MoP(5) catalysts.

As a conclusion in terms of phosphorus-containing species, the combined NMR and Raman study showed the formation of Keggin-like HPAs upon TEG impregnation, also observed in the dried catalysts case. Besides the appearance of these HPAs, the additive also leads to the aluminophosphates and polyphosphates conversion into dispersed monophosphates, except when the P/Mo molar ratio is superior to 2/5. In this case, polyphosphates and traces of aluminophosphates are still on the catalysts surface.

Table IV-8 summarizes the speciation results for the calcined CoMoP catalysts.

Table IV-8: Speciation results for calcined CoMoP catalysts prior to and after TEG impregnation.

	Prior to TEG	After TEG
CoMoP(1c)	cobalt aluminate polyoxomolybdates polyphosphates aluminophosphates	cobalt aluminate $\text{Co}_{3/2}[\text{AlMo}_6\text{O}_{24}\text{H}_6]$ monophosphates
CoMoP(3c)	cobalt aluminate polyoxomolybdates polyphosphates aluminophosphates	cobalt aluminate $\text{Co}_{3/2}[\text{AlMo}_6\text{O}_{24}\text{H}_6]$ $\text{Co}_{7/2}[\text{PCoMo}_{11}\text{O}_{40}]$ monophosphates
CoMoP(5c)	cobalt aluminate polyoxomolybdates polyphosphates aluminophosphates	cobalt aluminate $\text{Co}_{3/2}[\text{AlMo}_6\text{O}_{24}\text{H}_6]$ $\text{Co}_{7/2}[\text{PCoMo}_{11}\text{O}_{40}]$ monophosphates polyphosphates

IV.3.3. METALS AND PHOSPHORUS DISTRIBUTION

Electronic probe microanalysis (EPMA) is conducted to determine how the elements are distributed inside the catalysts body and if the additive modifies that distribution.

All calcined CoMoP catalysts showed a good molybdenum and cobalt distribution over the alumina extrudate body: using EPMA, a distribution coefficient of 1 is found for these metals. This coefficient evaluates the homogeneity of an element throughout the catalyst body; $R=1$ for flat profiles, $R<1$ for eggshell profiles and $R>1$ for egg-yolk profiles. However, Figure IV-34 shows these catalysts exhibit an eggshell profile for phosphorus ($R<1$) that becomes flatter as the phosphorus loading increases.

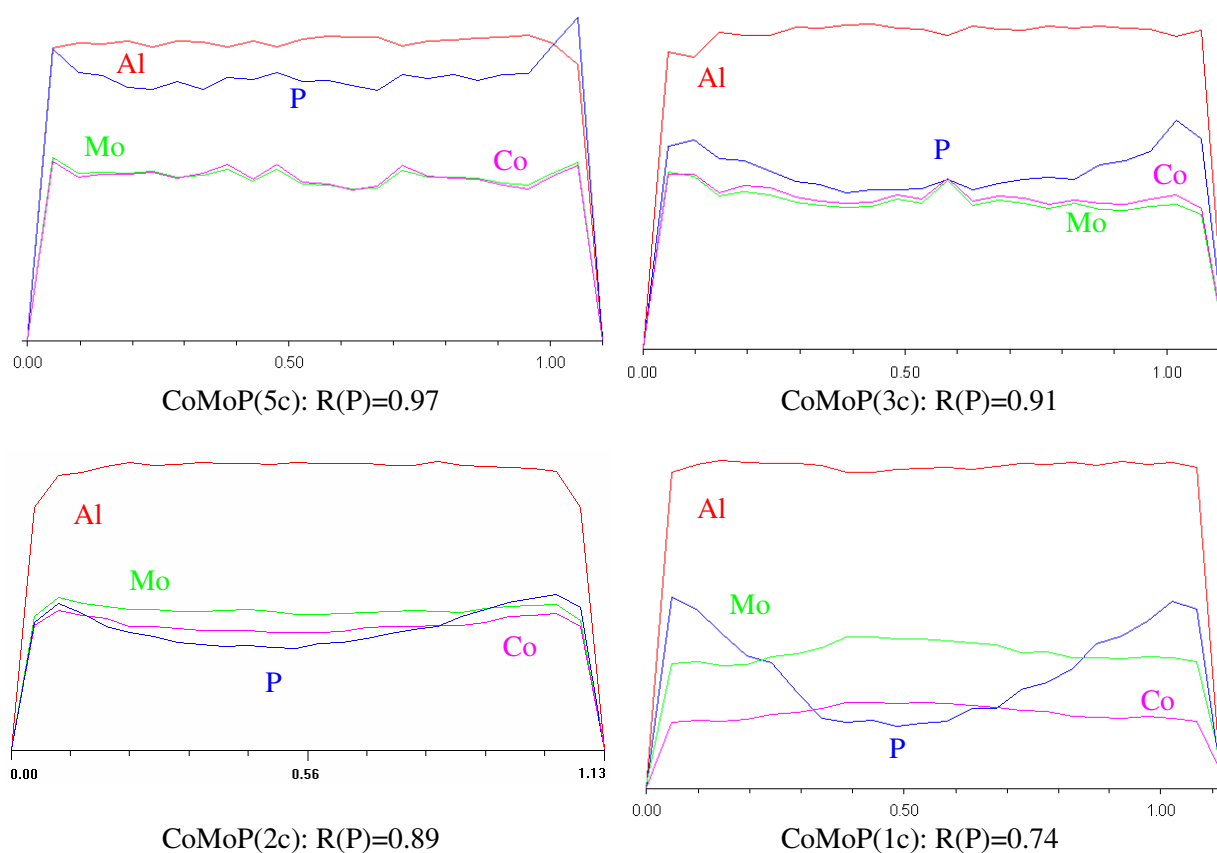


Figure IV-34: Aluminium, molybdenum, cobalt and phosphorus Electron Probe Microanalysis of the calcined CoMoP(c) catalysts.

The phosphorus eggshell profile is mainly due to the reaction between free phosphates and alumina surface hydroxyls, which leads to phosphorus fixation [10]:



, where Al_s corresponds to surface aluminium atoms. When the phosphorus loading increases, the alumina reactive sites become saturated and the excess phosphorus is dispersed towards the extrudate

center. Thus, at high P loadings, the excess phosphorus prevents $P_2Mo_5O_{23}^{6-}$ decomposition upon impregnation, as confirmed by Raman experiments.

After additive impregnation, the phosphorus distribution profile tends to become flatter. Such an effect is also achieved by water impregnation, although to a lesser extent, as shown in Figure IV-35.

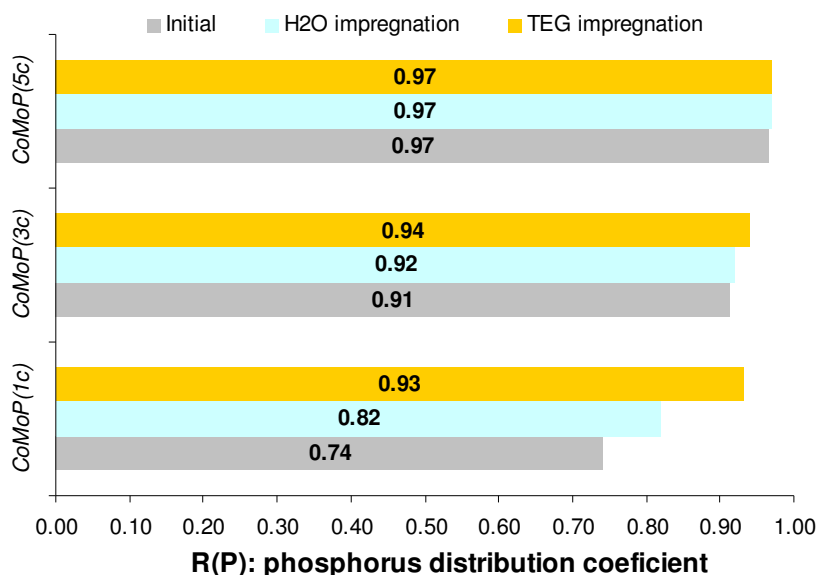
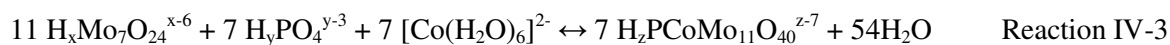


Figure IV-35: Electron Probe Microanalysis for phosphorus distribution of the calcined CoMoP catalysts.

An explanation for the enhanced redistribution induced by the additive is related to the $PCoMo_{11}O_{40}^{7-}$ HPA. Indeed, the substituted Keggin HPA species are instable during impregnation [10]: the reaction between free phosphates and alumina tends to decrease the local phosphorus concentration in the solution inside the alumina pores and consequently, $PCoMo_{11}O_{40}^{7-}$ evolves into $Mo_7O_{24}^{6-}$, displacing Reaction IV-3 towards the reactants side:



As shown by ^{31}P NMR, TEG diffusion into the catalyst porosity tends to release free phosphates, which react with molybdate and cobalt species, displacing the Reaction IV-3 equilibrium towards the $PCoMo_{11}O_{40}^{7-}$ formation. Therefore, the phosphorus distribution is improved.

To verify if the beneficial effect of the additive is related to the substituted-Keggin HPA, the phosphorus distribution profile of MoP catalysts and P/Al_2O_3 samples is determined. Both cases showed a limited enhancement, similar to the one achieved by water impregnation (Figure IV-36). Moreover, the P/Al_2O_3 samples exhibit a low distribution coefficient when compared to the MoP and CoMoP catalysts.

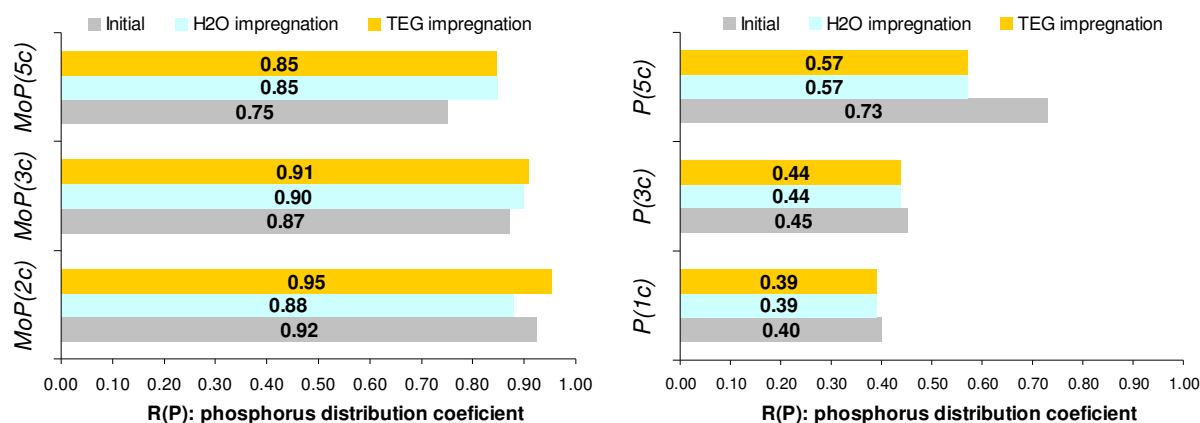


Figure IV-36: Electron Probe Microanalysis for phosphorus distribution of the calcined MoP catalysts (left) and the calcined P/Al₂O₃ samples (right).

The poor distributions of the P/Al₂O₃ samples may be explained by the absence of competitive adsorption between molybdates and phosphates. In this case, Reaction IV-2 is strongly favored.

The fact that the additive does not improve the phosphorus distribution coefficient in samples without cobalt, support the hypothesis that the PCoMo₁₁O₄₀⁷⁻ HPA formation is responsible for the enhanced phosphorus distribution.

IV.3.3.1. Phosphorus reaction with the additives

Phosphorus redistribution induced by the additive is related not exclusively related to a dissolution mechanism but because TEG tends to release free phosphates, as discussed above. In order to reveal the mechanism behind this behavior and based on the known reactivity between phosphorous oxides and alcohols to form phosphate ethers [18,19], a reaction with glycol and P₂O₅ is carried out in aqueous solution.

Preliminary essays showed that the reaction with TEG was very exothermic and dangerous. For this reason, diethyleneglycol monobutyl ether (DEGbe) is used instead. The reaction consists in dissolving anhydrous P₂O₅ (97%, Aldrich) in DEGbe at room temperature to obtain a P₂O₅ concentration of 1.0 mol.dm⁻³. Water is avoided because it leads to the formation of hydrolyzed species, like phosphoric acid. After a 24 hour period, a liquid sample is collected and the solution is refluxed for an additional 20 hour period. At the end of this period, another sample is collected. Figure IV-37 summarizes the reaction protocol.

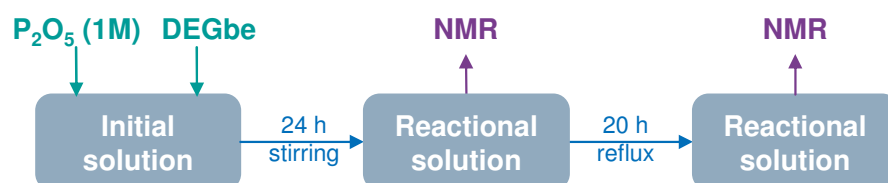


Figure IV-37: Schematic representation of the P₂O₅ reaction with DEGbe experimental protocol.

Prior to the reaction, DEGbe was characterized by ^{13}C NMR. The DEGbe molecule has 5 types of carbon atoms that give rise to 8 resonances in the ^{13}C NMR spectrum (Figure IV-38):

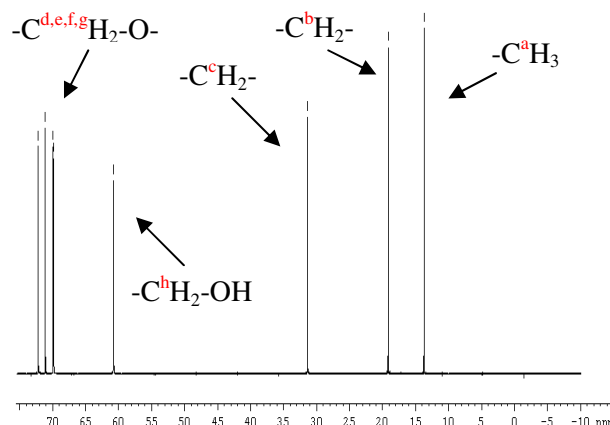


Figure IV-38: ^{13}C NMR of liquid DEGbe.

Figure IV-39 shows that the reaction products of P_2O_5 and DEGbe exhibit 8 peaks. After 20 hours of reflux (not shown here) the same peaks are observed. The absence of new peaks in the ^{13}C NMR spectra show that the DEGbe skeleton is maintained during the reaction.

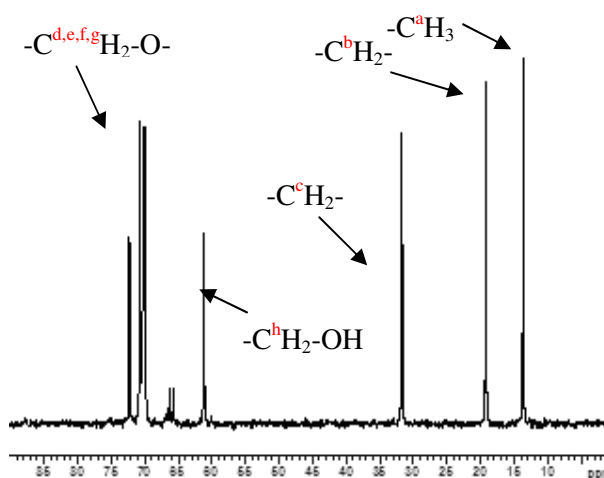


Figure IV-39: ^{13}C NMR of a P_2O_5 +DEGbe solution after 24h reaction at room temperature.

^1H NMR spectrum confirms that the DEGbe structure is retained after 24 hours of reaction at room temperature (Figure IV-40) and also after 20 hours of reflux (not shown here). These spectra exhibit a triplet at 1.0 ppm, corresponding to a terminal $-\text{CH}_3$ group ($\text{C}^{\text{a}}\text{H}_3$), a doublet at 1.6 ppm, corresponding to $-\text{CH}_2-$ groups ($\text{C}^{\text{b}}\text{H}_2$ and $\text{C}^{\text{c}}\text{H}_2$), a multiplet at about 3.7 ppm, corresponding to a $-\text{CH}_2\text{-O}$ group ($\text{C}^{\text{d}}\text{H}_2$, $\text{C}^{\text{e}}\text{H}_2$, $\text{C}^{\text{f}}\text{H}_2$, $\text{C}^{\text{g}}\text{H}_2$ and $\text{C}^{\text{h}}\text{H}_2$) and a singlet at about 8.9 ppm, corresponding to the hydroxyl hydrogen.

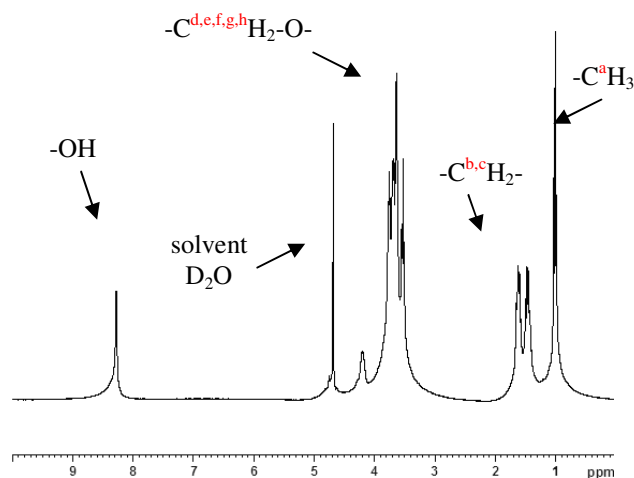


Figure IV-40: ^1H NMR of a P_2O_5 +DEGbe solution after 24h reaction at room temperature.

The ^{31}P NMR spectrum (Figure IV-41, left) shows the formation of phosphate mono- (-0.2 ppm) and di-DEGbe ethers (-0.8 ppm), as well as H_3PO_4 (1.8 ppm) after 24 hours of reaction at room temperature. Dimeric phosphate species (P-O-P: -12.9 ppm) and traces of trimeric species (P-O-P-O-P: -11.7 ppm) are also observed in the spectra. After 20 hours of reflux (Figure IV-41, right), the signal corresponding to the dimeric and trimeric species disappears, the phosphoric acid signal intensity increases and the peaks observed for the phosphate ethers shift upfield to 0.1, 1.1 and 2.0 ppm. The phosphate mono-DEGbe ether is the predominant species in both spectra.

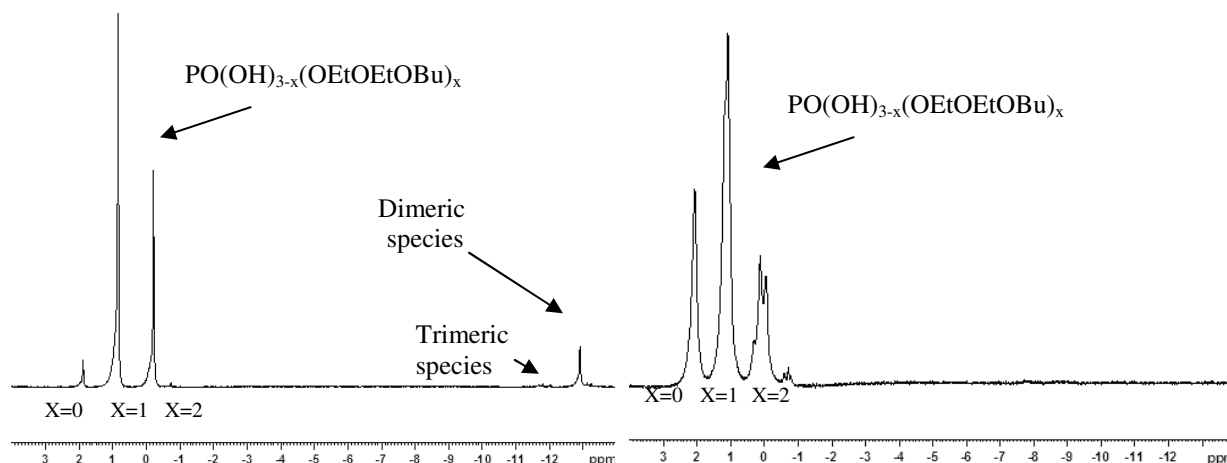


Figure IV-41: ^{31}P NMR of $\text{P}_2\text{O}_5 + \text{DEGbe}$ after 24h at room-temperature (left) and after 20h reflux (right).

In terms of reactivity, NMR spectra confirmed the reaction of solid P_2O_5 with liquid DEGbe to form phosphate mono- and di-DEGbe ethers, according to Reaction IV-4:



, where Et corresponds to an ethyl group and Bu corresponds to a butyl group.

The ^{31}P NMR spectrum evolution after reflux indicates that the monomer species are more stable than the polymeric species and that the reflux favors the formation of phosphorus mono-DEGbe ethers. However, the reflux also increases the amount of phosphoric acid. A hypothesis is that the same reaction occurs on the catalyst surface, leading to the dissolution of bulk P_2O_5 and AlPO_4 -like phases to form phosphate ethers or phosphoric acid that would transport phosphorus with posterior formation of HPA species. However, no evidence of these ethers was found in the calcined catalysts.

IV.3.4. THERMAL BEHAVIOR

The temperature stability domain of the surface species is evaluated by thermogravimetric analysis (TGA). To determine if the additive as in impact on this property, analyses are carried out in absence and in presence of TEG. As for the dried catalysts, the derivative thermogravimetry (DTG) curves are decomposed according to the model described in Appendix C.

IV.3.4.1. Additive-free calcined CoMoP catalysts analysis

The calcined CoMoP(1c) and CoMoP(5c) catalysts exhibit similar thermogravimetric behaviors, with total weight losses of 10.4 and 8.8 wt%, respectively. The CoMoP(1c) catalyst DTG shows only one inflexion at about 85 °C and the CoMoP(5c) at about 105 °C (Figure IV-42).

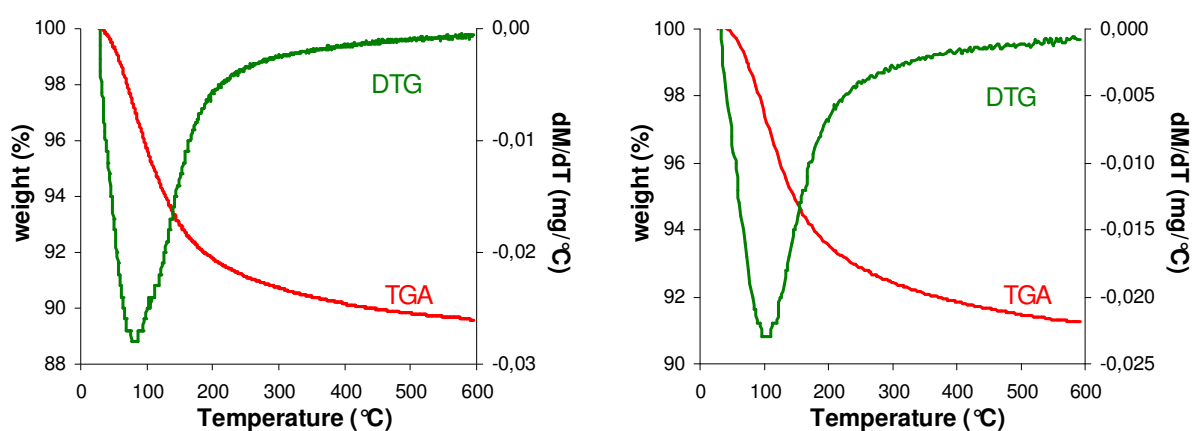


Figure IV-42: Thermogravimetric analysis (TGA) and, derivative thermogravimetry (DTG) of the CoMoP(1c) (left) and CoMoP(5c) (right) catalysts.

The mass spectroscopy features of the CoMoP(1c) (Figure IV-43) and CoMoP(5c) (not shown here) catalysts thermal decomposition is the same: only water is detected in the gas effluents. The maximum of the water removal occurs at about 100 °C, corresponding to the physisorbed water on the catalysts. The absence of other inflexions in the water spectra indicates that no heteropolyanions are present, in agreement with Raman and UV-Visible spectroscopies.

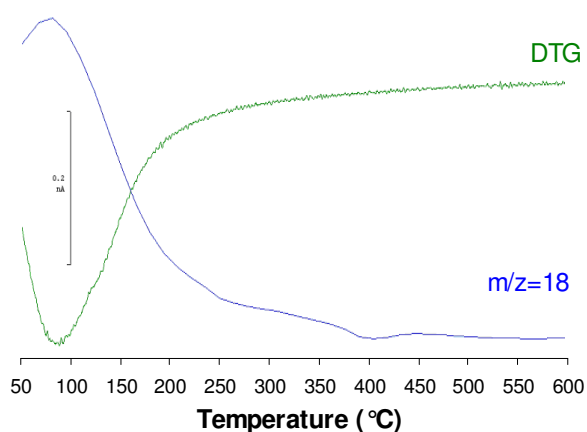


Figure IV-43: Mass spectroscopy follow-up of the CoMoP(1c) catalyst.

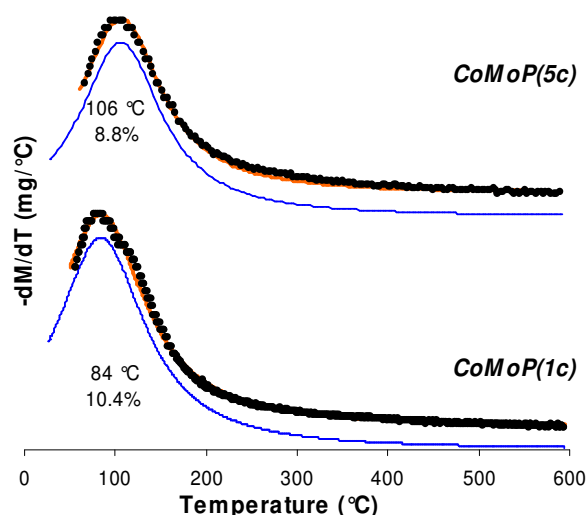


Figure IV-44: DTG decomposition of the calcined CoMoP (1c) and CoMoP(5c) catalysts.

The thermal behavior of calcined CoMoP catalysts is the same as observed for calcined CoMo catalysts, showing only the removal of physisorbed water. This shows that the HPA species were decomposed during the calcination stage.

IV.3.4.2. Additive-containing calcined CoMoP catalysts analysis

The CoMoP(1c)+TEG catalyst exhibits a total loss of 20.9 wt% with two local DTG minimums at about 75 and 230 °C and a two shoulders at about 270 and 420 °C. Mass spectroscopy reveals a major water removal before 100 °C and a second one at about 230 °C. In addition, a major CO₂ emission centered at 260 °C is observed. Traces of *m/z* 12 (carbon-type fragment) and 58 (ketone-type fragment) are also observed (Figure IV-45).

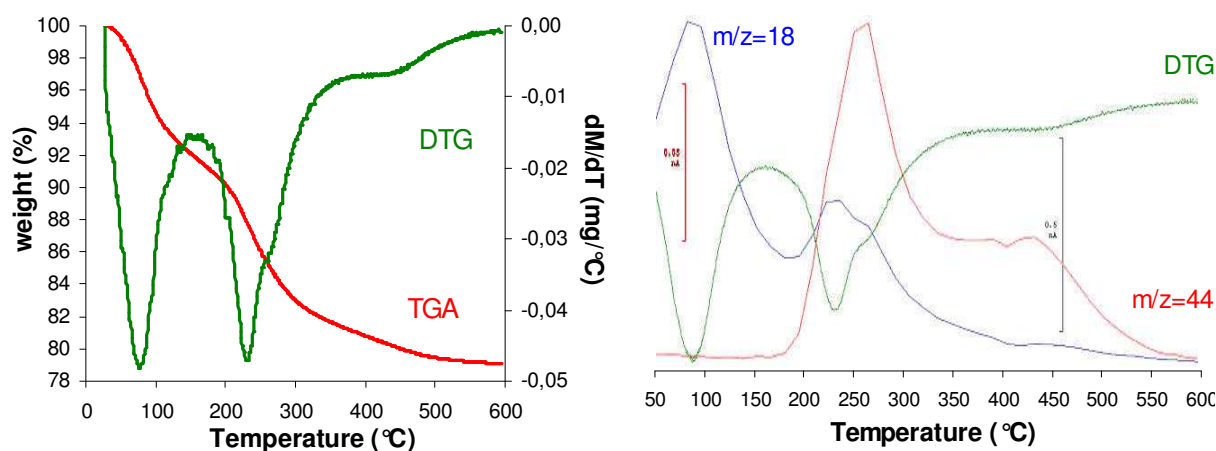


Figure IV-45: Thermogravimetric analysis (TGA), derivative thermogravimetry (DTG) and mass spectroscopy (right) of the CoMoP(1c) sample.

The CoMoP(1c)+TEG catalyst DTG is decomposed into 5 contributions (Figure IV-46). They are centered at about 76, 169, 228, 264 and 421 °C, which correspond to weight losses of 8.2, 1.1, 4.5, 5.7 and 1.4%, respectively. Based on the MS results, the first curve is assigned to physisorbed water and the second curve to the coordination water of the Anderson HPA. The remaining three curves are assigned to TEG thermal decomposition products.

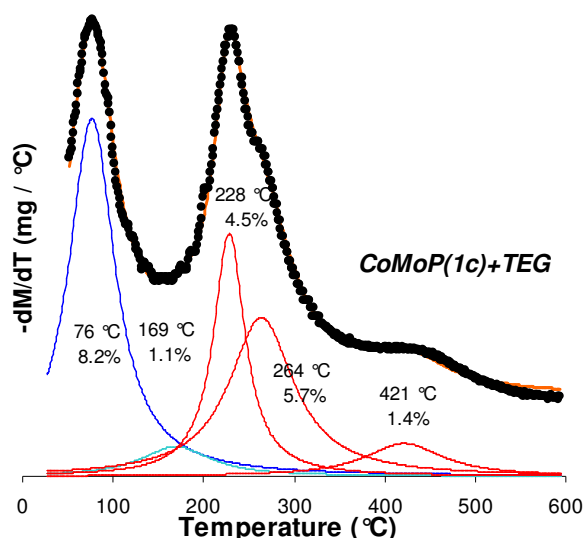


Figure IV-46: DTG decomposition of the CoMoP(1c)+TEG sample.

Using Reaction IV-1 (§IV.2.4.2), it becomes possible to estimate the amount of constitutional water arising from the Anderson salt decomposition.

Table IV-9: DTG decomposition assignments of the CoMoP(1c)+TEG sample.

T (°C)	Experimental weight loss (%)	Assignment	Expected weight loss (%)
76	8.2	Physisorbed water	-
169	1.1	HPA coordination water HPA constitutional water	- 1.0
228	4.5	TEG (sum=11.3)	11.3
264	5.7		
421	1.4		

The CoMoP(5c)+TEG catalyst (12.4 wt% TEG) exhibits a total loss of 18.9 wt% with two local DTG minimums at about 110 and 220 °C and a two shoulders at about 270 and 440 °C. Mass spectroscopy shows a continuous water removal. In addition, a major CO₂ emission is observed between 200 and 600 °C. Traces of m/z 12 (carbon-type fragment) and 58 (ketone-type fragment) are also observed (Figure IV-47).

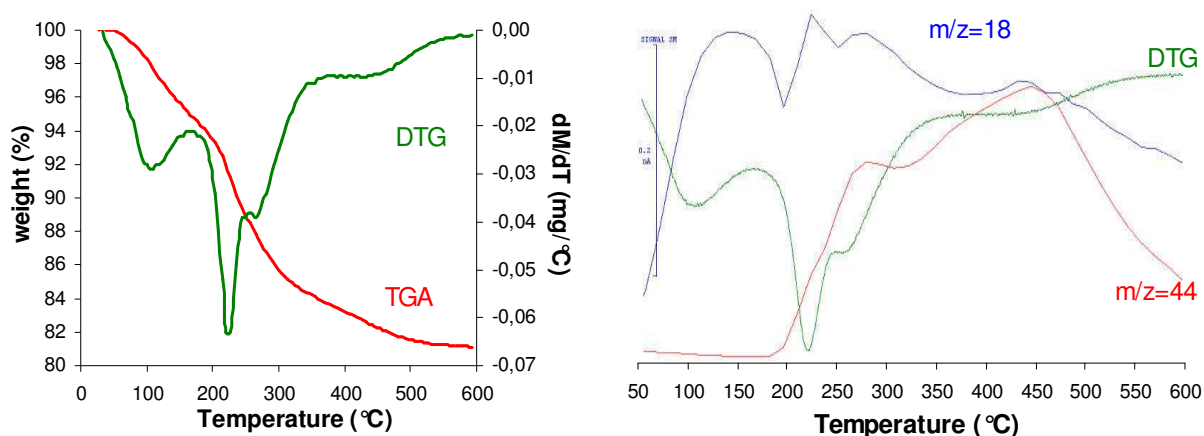
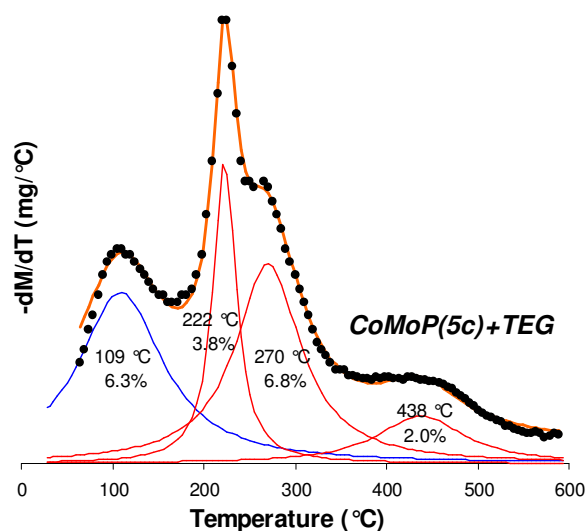


Figure IV-47: Thermogravimetric analysis (TGA), derivative thermogravimetry (DTG) and mass spectroscopy results (right) of the CoMoP(5c) sample.



The CoMoP(5c)+TEG catalyst DTG is decomposed into 4 contributions (Figure IV-48). The curve centered at about 109 °C is assigned physisorbed water (6.3 wt%) and the other 3 curves are assigned to the TEG thermal decomposition: 222, 270 and 438 °C (3.8, 6.8 and 2.0 wt%).

Figure IV-48: DTG decomposition of the CoMoP(5c)+TEG sample.

Table IV-10: DTG decomposition assignments of the CoMo_AHM(c)+TEG sample.

T (°C)	Experimental weight loss (%)	Assignment
109	6.3	Physisorbed water
222	3.8	TEG (sum=12.5%)
270	6.8	
438	2.0	

IV.3.4.3. Additives long-term stability

The thermal study showed that TEG decomposition may start before its normal boiling point (285 °C). Thus, thermodynamic liquid-vapor equilibrium is established that may lead to partial evaporation even at room temperature. Several parameters may accelerate the additive decomposition

or evaporation, like storage temperature, humidity or atmospheric pressure. To evaluate the impact of these effects on the catalysts TEG loading, the same additive-containing CoMoP(5c) sample was submitted to periodic CHNS elemental analysis and lost-on-ignition (LOI) measurements. Figure IV-49 shows that the TEG loading remains unaltered, showing that TEG remains stable inside the catalyst porosity without evaporation.

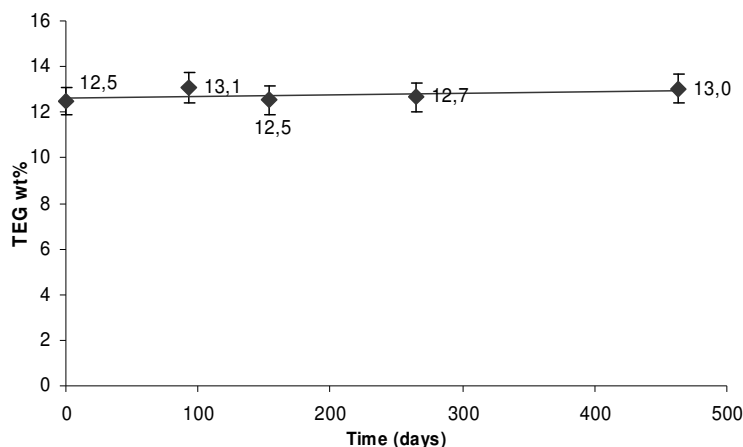


Figure IV-49: Additive-containing CoMoP(5c) catalyst long term stability. Loadings are water-corrected.

IV.3.5. SURFACE MECHANISM

Based on the speciation results, it is possible to propose a mechanism to explain the modifications observed inside the catalyst porosity after the additive impregnation. Two distinct behaviors are observed depending on the phosphorus loading.

When the P/Mo ratio is inferior to 2/5, the additive does not induce any modification to the cobalt aluminate phase. In the same way as described for the calcined CoMo-based catalysts, part of the deposited polyoxomolybdates are redissolved and redispersed. These polyoxomolybdates then react with the aluminium ions that were dissolved from the alumina matrix to form Anderson hexamolybdoaluminates HPAs. Due to their poor solubility they precipitate and displace the alumina dissolution equilibrium towards the formation of more Al^{3+} entities. Since calcination leads to stronger support-precursor interactions, this effect is limited because less phosphate groups are available. At the same time, the additive also blocks part of the alumina adsorption sites but because the P loading is low, phosphate groups adsorb as monomers on alumina surface. Figure IV-50 summarizes the transformations induced by the additive in calcined CoMoP catalysts with a P/Mo molar ratio inferior to 2/5.

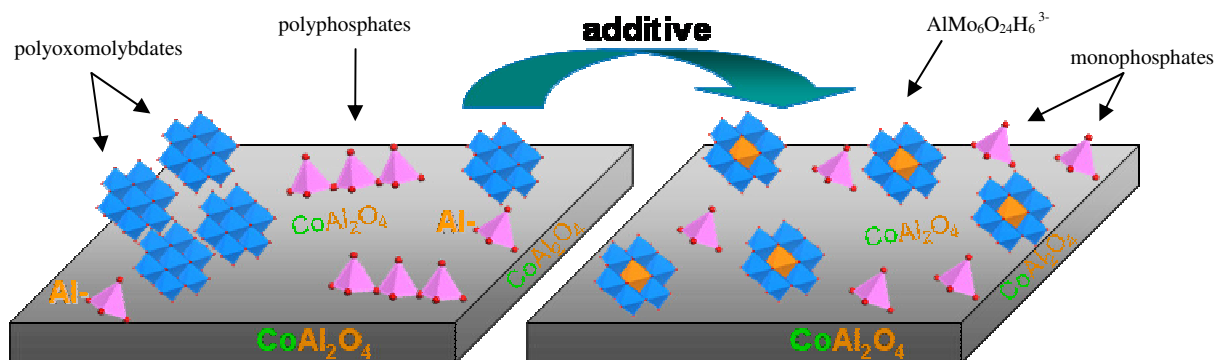


Figure IV-50: Schematic representation of the redispersion mechanism induced by the additive for the alumina-supported CoMoP(1c) catalysts.

When the P/Mo is superior to 2/5, besides the modifications discussed above, the excess phosphate groups or those coming from the AlPO_4 decomposition induced by TEG, react with molybdates to form substituted Keggin $\text{PCoMo}_{11}\text{O}_{40}^{7-}$ HPAs on top of Anderson $\text{AlMo}_6\text{O}_{24}\text{H}_6^{3-}$ HPAs. The remaining phosphate groups adsorb into the alumina surface as monomers or as polymers if the P loading is elevated. This redispersion mechanism is consistent with the Raman and Electron Probe Microanalysis characterization results. The mechanism is schematized in Figure IV-51.

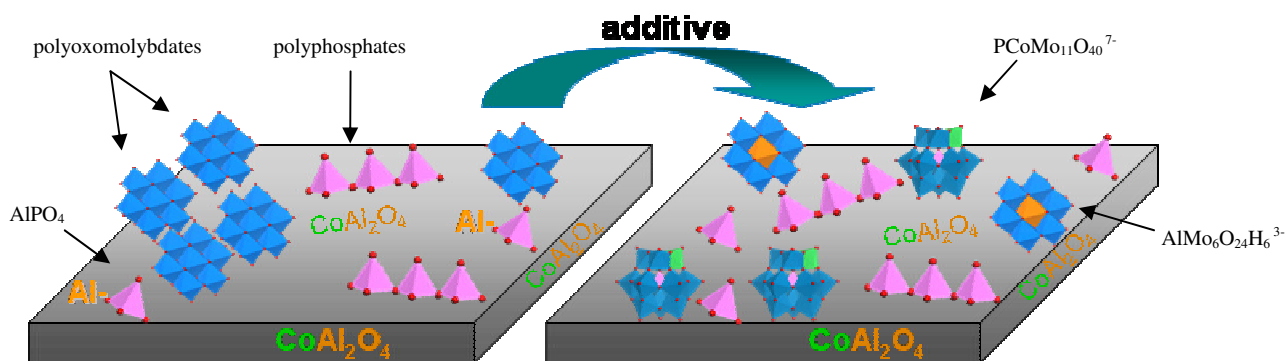


Figure IV-51: Schematic representation of the redispersion mechanism induced by the additive for the alumina-supported CoMoP(5c) catalysts.

IV.4. CHAPTER CONCLUSION

After calcination, all catalysts exhibit similar phases: polyoxomolybdates and cobalt aluminates. For CoMoP catalysts, phosphorus is present as phosphate polymers or bonded to alumina as AlPO_4 species. In these catalysts, no proof of P_2O_5 is found. After additive impregnation, the polyoxomolybdates lead to the same Anderson hexamolybdoaluminates heteropolyanions by support dissolution, also observed in the additive-containing dried catalysts cases. Furthermore, substituted Keggin heteropolyanions are also formed after additive impregnation when the P/Mo molar ratio is superior to 2/5. Like in the dried catalysts case, these heteropolyanions lead to an overall redispersion of the active phase precursors. However, because calcination leads to stronger precursor-support

interactions, the species redissolution is prevented and the redispersion mechanism is limited compared to the dried catalysts.

In terms of distribution profiles, phosphorus tends to assume an eggshell profile that results from the phosphorus interaction with aluminium entities to form surface AlPO_4 groups. This profile becomes flatter upon the introduction of TEG. This behavior is attributed to the redissolution and transport by the additive solution and also by the reactivity of the additive towards phosphate groups. Indeed, NMR spectroscopy showed a specific reactivity between P_2O_5 with DEGbe in solution even at room-temperature to form phosphate ethers. However, no evidence of these ethers or even phosphorous oxide was found at the catalyst surface prior to or after the additive impregnation.

Key-points

1. *As for the dried catalysts, the additive favors the formation of $\text{AlMo}_6\text{O}_{24}\text{H}_6^{3-}$ in all calcined catalysts. In addition, when the P/Mo molar ratio is superior to 2/5, the additive also induced the formation of $\text{PCoMo}_{11}\text{O}_{40}^{7-}$. These heteropolyanions lead to an overall redispersion of the active phase precursors. However, because calcination leads to stronger precursor-support interactions, the redispersion mechanism is limited.*
2. *The additive impregnation corrects the phosphorus eggshell distribution profiles.*

IV.5. BIBLIOGRAPHIC REFERENCES

-
- 1 WO96/41848A1, *Hydrotreating catalyst: composition, preparation and use thereof*, **1996**.
 - 2 P. Mazoyer-Galliou, Ph.D. thesis, Université Claude Bernard – Lyon I, **1998**.
 - 3 J. Vakros, K. Bourickas, S. Perlepes, C. Kordulis and A. Lycourghiotis, *Am. Chem. Soc., Langmuir* 20, 10542, **2004**.
 - 4 C. Cabello, I. Botto and H. Thomas, *Appl. Catal. A* 197, 79, **2000**.
 - 5 C. Martin, Ph.D. thesis, Université des Sciences et Technologies de Lille, **2003**.
 - 6 C. Martin, C. Lamonier, M. Fournier, O. Mentré, V. Harlé, D. Guillaume and E. Payen, *Chem. Mater.* 17, 4438, **2005**.
 - 7 X. Carrier, E. Marceau and M. Che, *Pure Appl. Chem.*, Vol. 78, No. 5, 1039, **2006**.
 - 8 D. Nicosia and R. Prins, *J. Catal.* 229, 424, **2005**.
 - 9 C. Martin, C. Lamonier, M. Fournier, O. Mentré, V. Harlé, D. Guillaume and E. Payen, *Chem. Mater.* 17, 4438, **2005**.

- 10 J.A. Bergwerff, L.G.A. van der Water, T. Wissner, P. de Peinder B.R.G. Leliveld, K.P. de Jong and B.M. Weckhuysen, *Chem. Eur. J.* 11, 4591, **2005**.
- 11 H. Kraus and R. Prins, *J. Catal.* 164, 251, **1996**.
- 12 E. R. H. van Eck, A.P.M. Kentgens, H. Kraus and R. Prins, *J. Phys. Chem.* v. 99, 43, 16085, **1995**.
- 13 T.R. Krawietz, P. Lin, K.E. Lotterhos, P.D. Torres, D.H. Barich, A. Clearfield and J.F. Haw, *J. Am. Chem. Soc.* 120, 8502, **1998**.
- 14 R. Iwamoto and J. Grimblot, *Adv. Catal.* 44, 417, **2000**.
- 15 E.C. DeCanio, J.C. Edwards, T.R. Scalzo, D.A. Storm and J.W. Bruno, *J. Catal.* 132, 498, **1991**.
- 16 J.A.R. van Veen, P.A.J.M. Hendricks, E.J.G.M. Romers and R.R. Andrea, *J. Phys. Chem.* 94, 5282, **1990**.
- 17 A. Griboval, Ph.D. thesis, Université des Sciences et Technologies de Lille, **1998**.
- 18 J. Livage, P. Barboux, M. Vandenborre, C. Schmutz and F. Taulelle, *J. Non-Cryst. Sol.* 147, 18, **1992**.
- 19 W. Weng and J. Batista, *J. Sol-Gel Sci. Tech.* 8, 654, **1997**.

CHAPTER V: THE ROLE OF GLYCOL-TYPE ADDITIVES ON CoMo(P) CATALYSTS PREPARED FROM AN ADDITIVE-CONTAINING ALUMINA

V.1. Introduction	155
V.2. Characterization of the alumina support	155
V.2.1. Infrared analysis and surface acidity	156
V.2.2. Thermal behavior of the alumina support	157
V.3. Impact of the additive on the alumina support.....	158
V.3.1. Study of the additive structure after impregnation	158
V.3.2. Study of the additive-support interaction	159
V.3.3. Thermal behavior of the additive-impregnated alumina	161
V.3.4. Additive adsorption on alumina study.....	163
V.3.4.1. <i>Excess impregnation</i>	165
V.3.4.2. <i>Incipient wetness impregnation</i>	166
V.3.4.3. <i>Additives adsorption mechanism on the alumina support</i>	168
V.4. Impact of the additive on additive pre-impregnated CoMo(P) catalysts	169
V.4.1. Influence of the additive on the deposited cobalt species.....	169
V.4.2. Influence of the additive on the deposited molybdenum species	172
V.4.3. Metals and phosphorus distribution.....	174
V.4.4. Thermal behavior	175
V.5. Surface mechanism.....	176
V.6. Chapter conclusions	177
V.7. Bibliographic references	178

CHAPTER V: THE ROLE OF GLYCOL-TYPE ADDITIVES ON CoMo(P) CATALYSTS PREPARED FROM AN ADDITIVE-CONTAINING ALUMINA

V.1. INTRODUCTION

The previous chapters showed that the additive induced the redispersion of metals and phosphorus species through a redissolution-reprecipitation mechanism when impregnated on dried and calcined catalysts. In the case of additive impregnation directly on the alumina support and posterior CoMo(P) solution impregnation, the proposed redissolution-reprecipitation mechanism is no longer possible because the active phase precursors are not submitted to a posterior impregnation stage. For this reason, the role of glycol-type additives is necessarily different.

Therefore, the chapter objective is to provide answers to the following questions: 1) Does the additive modifies the alumina support surface and properties? 2) Does the additive modify the catalysts surface species prior to the sulfidation stage when compared to the dried catalysts? 3) What is the mechanism behind the activity enhancements reported in the patent applications?

To determine the influence of the additive on the alumina support surface and properties, alumina is characterized as-is and after additive impregnation. Then, the deposited precursors structures are determined in pre-impregnated CoMo(P) catalysts. To complete this study, the impact of the additive on the elements distribution in the catalyst body will be also studied.

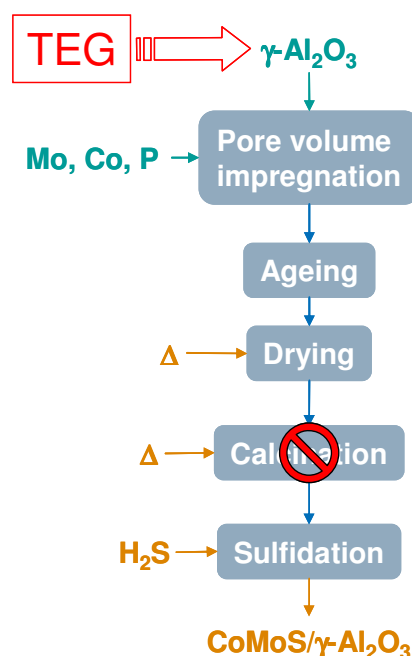


Figure V-1: Preparation of CoMoP catalysts using a TEG pre-impregnated alumina.

V.2. CHARACTERIZATION OF THE ALUMINA SUPPORT

This section is dedicated to the study of the alumina support properties: nature of Al-OH groups, support acidity and thermal stability. The support used to prepare all catalysts is a commercial γ -alumina shaped as trilobe extrudates with a specific surface area of $300 \text{ m}^2/\text{g}$.

V.2.1. INFRARED ANALYSIS AND SURFACE ACIDITY

The diffuse reflection infrared (DRIFT) spectra were registered following the temperature program described in section II.2.3.1 in argon atmosphere. The analyzed γ -alumina DRIFT spectra shows that after 200 °C, the wide band centered at about 3246 cm^{-1} , assigned to physisorbed water, begins to decrease (Figure V-2).

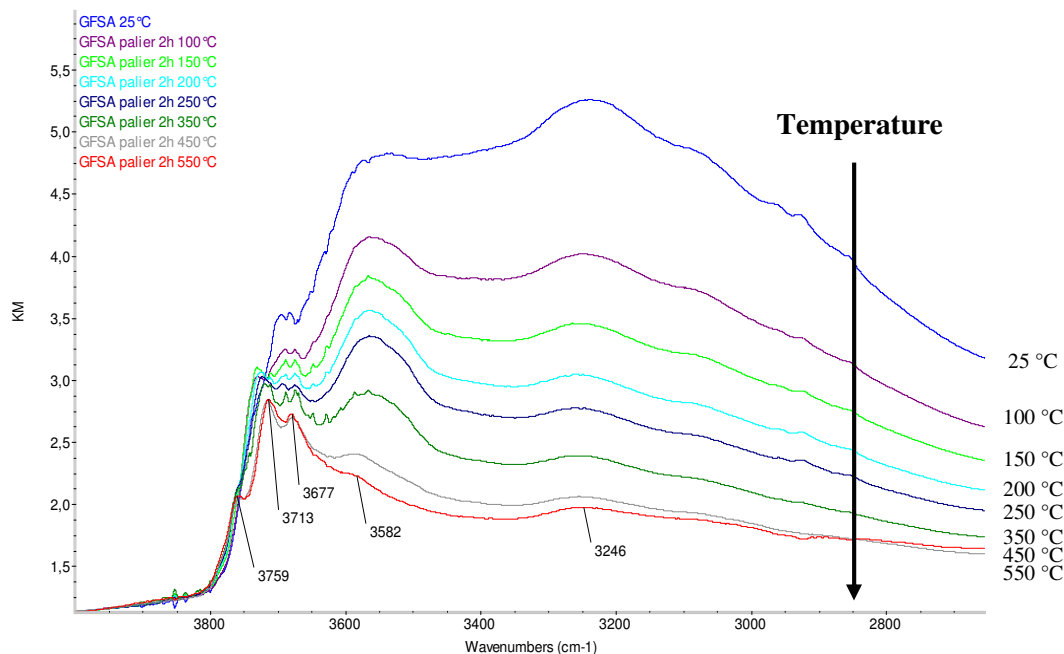


Figure V-2: DRIFT spectra in the 2800-3800 cm^{-1} region of the γ -alumina support from 25 to 550 °C.

When the temperature increases, the adsorbed water and CO_2 molecules that were in interaction with the different alumina surface groups tend to evaporate and the bands corresponding to the hydroxyl groups begin to appear in the spectra. Therefore, the minimal activation temperature required to observe alumina surface groups is 200 °C.

The transmission IR spectrum acquired at 530 °C is shown in Figure V-3.

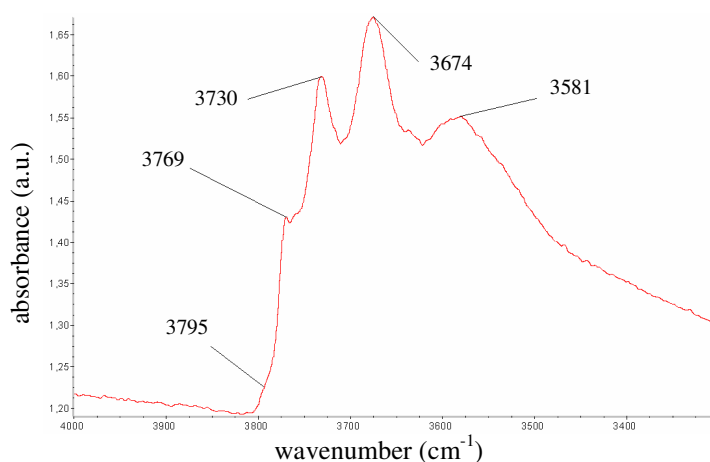


Figure V-3: Transmission infrared spectrum in the 2800-3800 cm^{-1} region of the γ -alumina support at 530 °C pretreated during 10 hours under vacuum.

The transmission IR spectrum shows a main infrared band at about 3674 cm^{-1} corresponding to acidic $\text{Al}^{\text{VI}}\text{-OH}$ groups. Smaller bands are observed at about 3730 and 3769 cm^{-1} , as well as a shoulder at about 3795 cm^{-1} . These bands are assigned to neutral $\text{Al}^{\text{VI}}\text{-OH}$, basic $\text{Al}^{\text{VI}}\text{-OH}$ and $\text{Al}^{\text{IV}}\text{-OH}$ groups, respectively [1].

Further support acidity characterization was carried out by means of CO adsorption at $-150\text{ }^{\circ}\text{C}$. This experimental technique allows monitoring the coordinatively unsaturated (CUS) surface aluminum atoms, responsible for the Lewis acidity, and the surface hydroxyl groups, responsible for the Brønsted acidity. The study revealed that the Lewis to Brønsted acid sites ratio is 1.1, meaning that the studied alumina support possesses slightly more Lewis acid sites than Brønsted.

V.2.2. THERMAL BEHAVIOR OF THE ALUMINA SUPPORT

Thermogravimetric analysis (TGA) is carried out to study the thermal behaviour of alumina.

The alumina support TGA revealed a total loss of 8.3 wt% with a DTG minimum at about $80\text{ }^{\circ}\text{C}$, corresponding to water removal, as shown by the mass spectroscopy (Figure V-4).

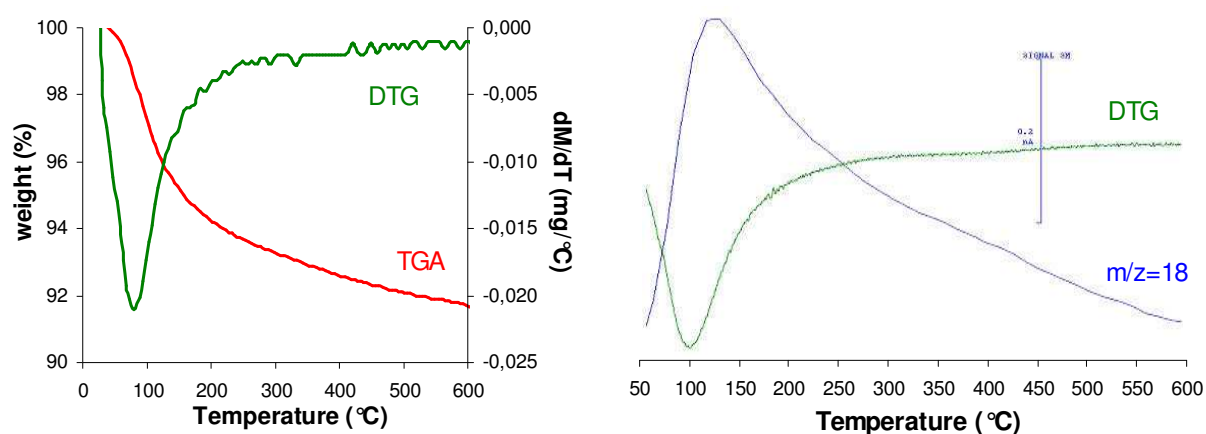


Figure V-4: Thermogravimetric analysis (TGA), derivative thermogravimetry (DTG) and mass spectroscopy results (right) of the alumina support.

In order to obtain more precise qualitative and qualitative information about the thermal behavior of the alumina support, the DTGs are decomposed according to the above-mentioned method. For the sake of simplicity, the decomposition plots are inverted.

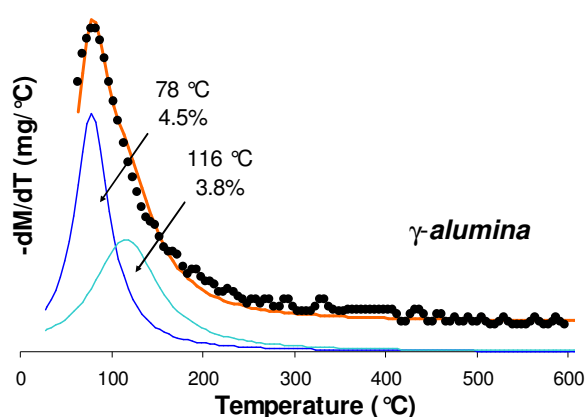


Figure V-5: Alumina support DTG decomposition.

The alumina support DTG is decomposed into 2 contributions. They are centered at about 78 and 116 °C that correspond to weight losses of 4.5 and 3.8%, respectively (Figure V-5). These losses are assigned to the removal of physisorbed and structural water molecules (by deshydroxylation). At 200 °C, the main part of physisorbed water has been removed in agreement with DRIFT analysis. From 400 to 600 °C, the derivative is not null, meaning that a weight loss is taking place due to chemisorbed water removal by alumina deshydroxylation.

V.3. IMPACT OF THE ADDITIVE ON THE ALUMINA SUPPORT

Several analytical techniques are used to provide qualitative information about the nature of the bonds established between the additive and the alumina support to determine if the additive modifies the alumina surface. In this sense, samples with two additive loadings (0.2 and 1.1 DEGbe/nm²) prepared by incipient wetness impregnation were characterized by TGA, Raman and DRIFT spectroscopy. Details about the experimental analysis techniques are discussed in section II.2.

V.3.1. STUDY OF THE ADDITIVE STRUCTURE AFTER IMPREGNATION

The DEGbe Raman spectrum at room temperature (Figure V-6) reveals bands corresponding to C-O stretching (842 and 892 cm⁻¹), C-H bending (1302 and 1459 cm⁻¹) and C-H stretching vibrations (2846, 2914 and 2938 cm⁻¹).

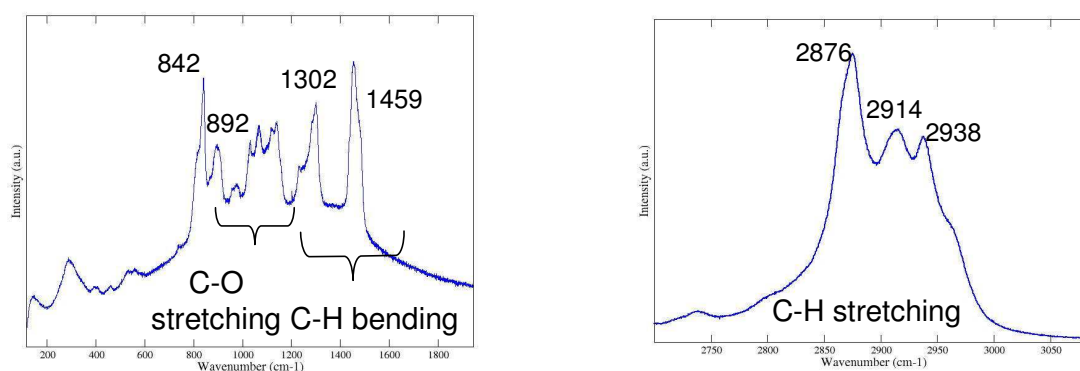


Figure V-6: Raman spectrum of liquid DEGbe.

The Raman bands of deposited DEGbe are kept unchanged when alumina is impregnated with an aqueous DEGbe solution (Figure V-7).

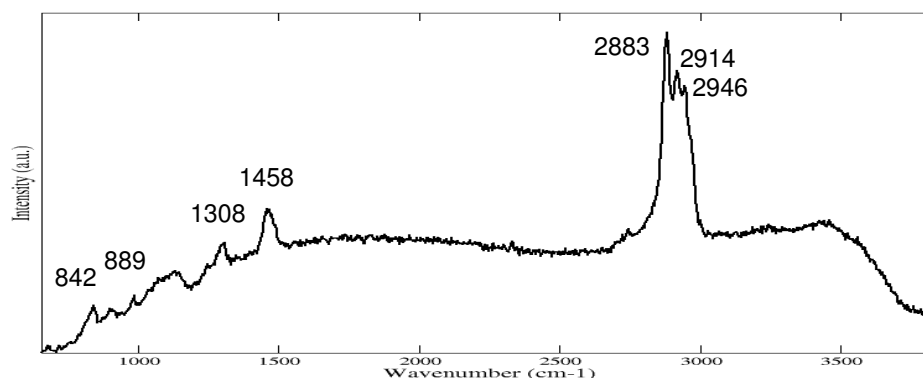


Figure V-7: Raman spectrum of additive-containing alumina (1.1 DEGbe/nm²).

This fact evidences a weak interaction between DEGbe and alumina, excluding chemisorption of DEGbe molecules on alumina.

V.3.2. STUDY OF THE ADDITIVE-SUPPORT INTERACTION

The additives interaction with the support at different temperatures is studied using DRIFT spectroscopy. The spectra are registered in argon atmosphere according to the temperature program described in section II.2.3.1. The analyzed sample has a loading of 1.1 DEGbe/nm².

All spectra recorded prior to 250 °C showed a broad signal between 3000 and 2750 cm⁻¹, which is due to DEGbe C-H vibrations. After 250 °C, beyond the DEGbe normal boiling point, this broad signal tends to disappear. The presence of water is indicated by the broader signal from 3800 to 3000 cm⁻¹ that progressively disappears, revealing Al-OH bands in the 3800-3600 cm⁻¹ region after 200 °C (Figure V-8). After 150 °C, a new signal appears at about 1580 cm⁻¹ which has been assigned in the literature to an Al-O-C vibration [2]. Moreover, after the additive decomposition, which occurs before 250 °C (the C-H bands at 3000–2750 cm⁻¹ disappear), the band at 1580 cm⁻¹ shifts slightly to lower wavenumbers (1565 cm⁻¹) but does not disappear.

The band assigned to an Al-O-C vibration is still visible at 550°C, suggesting either a partial additive anchorage to alumina, with water departure ($\text{Al-OH} + \text{OH-R} \rightarrow \text{Al-O-R} + \text{H}_2\text{O}$) or a surface carboxylation due to thermal decomposition or reduction of DEGbe. However, only traces of carbon (less than 0.1 wt%) are found after the thermal treatment.

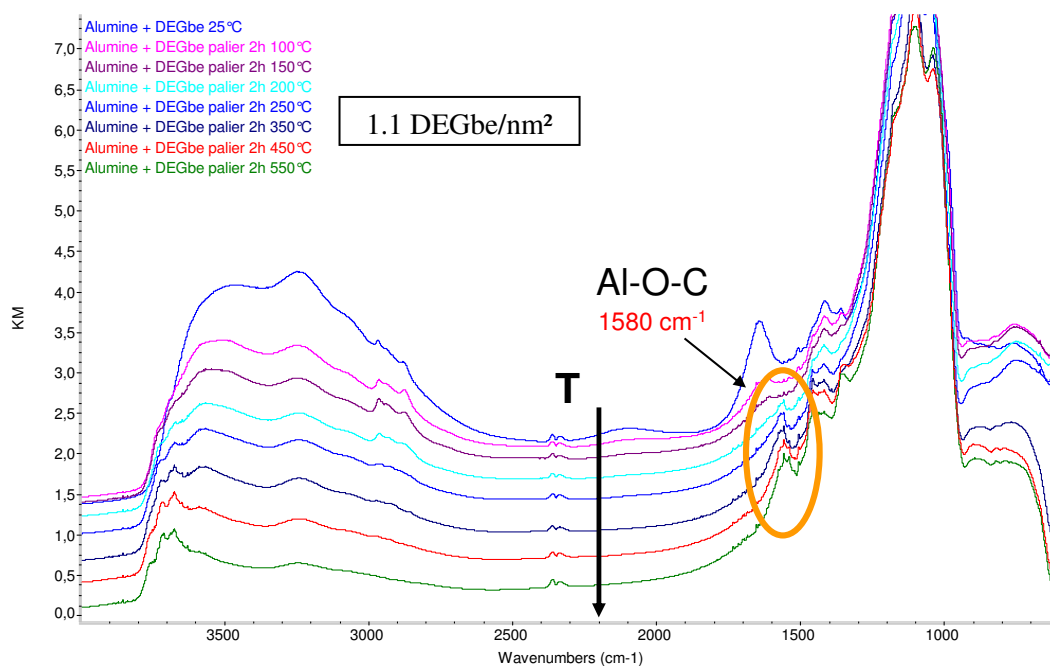


Figure V-8: DRIFT spectrum of an additive-containing alumina (1.1 DEGbe/nm²) from 25 to 550 °C.

Figure V-9 shows the DRIFT spectra at 200 °C in argon atmosphere of two aluminas with different additive loadings (0.2 and 1.1 DEGbe/nm²) and the alumina support, where the Al-O-C peak at 1580 cm⁻¹ is present even for low additive loadings.

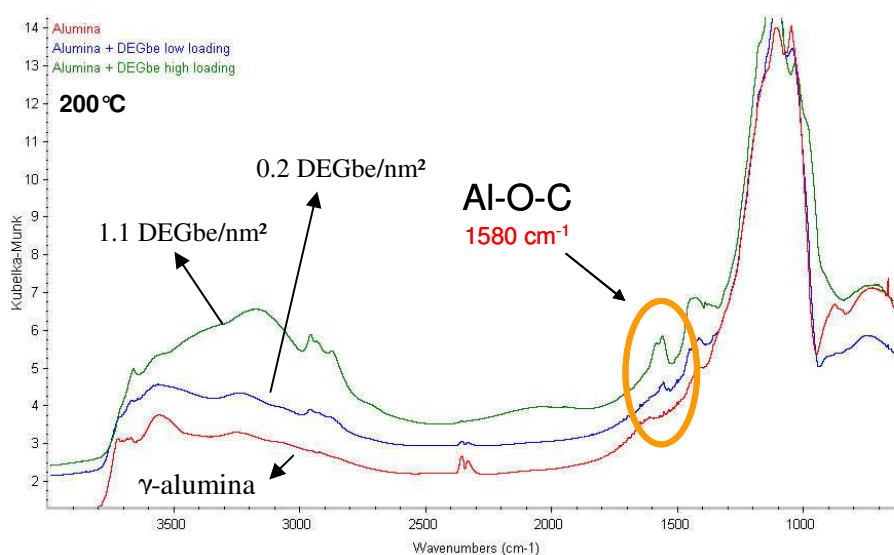


Figure V-9: DRIFT spectra at 200 °C of additive-free and additive-containing aluminas (1.1 and 0.2 DEGbe/nm²).

The additive interaction with alumina hydroxyl groups is evidenced by changes in the DRIFT spectra in the high wavenumbers region. The subtraction spectra between the additive-containing alumina and the alumina support are shown in Figure V-10. In such spectra, a spectral line decrease when compared to the base line at the left side of the spectra means that the band that existed on the

alumina support was removed after additive impregnation. The spectra show that the band at about 3733 cm^{-1} disappears in the additive-containing alumina from room temperature to $250\text{ }^{\circ}\text{C}$. After this temperature, the signal shifts towards 3714 cm^{-1} . Another signal is visible at about 3767 cm^{-1} at $250\text{ }^{\circ}\text{C}$.

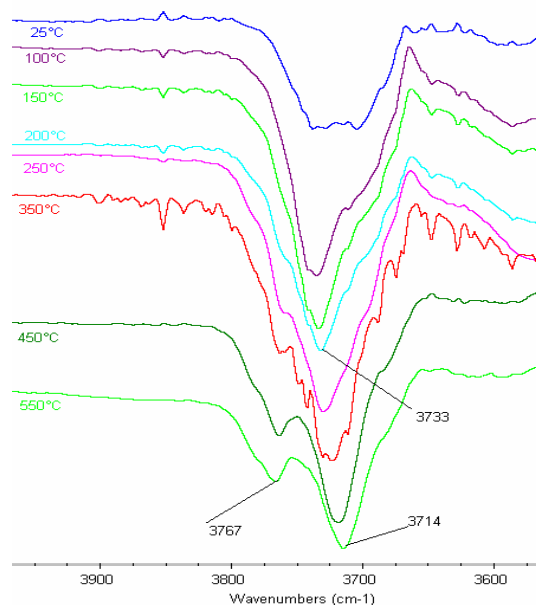


Figure V-10: DRIFT spectra subtraction of the additive-containing alumina (1.1 DEGbe/nm^2) and the alumina support in the hydroxyl region.

The disappearance of the band at about 3733 cm^{-1} means that the neutral mono-coordinated Al-OH groups ($3710\text{--}3735\text{ cm}^{-1}$) are in interaction with the additive from room temperature to $250\text{ }^{\circ}\text{C}$. Likewise, other type of interaction is revealed by the signal that appears at 3767 cm^{-1} , assigned to basic mono-coordinated Al-OH groups. Moreover, DRIFT experiments conducted by Nicosia and Prins [2] using triethyleneglycol dimethyl ether did not showed the formation of Al-O-C linkages, meaning that the interaction of the additive with the support is made trough the terminal hydroxyl groups and not by the ethoxy oxygens.

V.3.3. THERMAL BEHAVIOR OF THE ADDITIVE-IMPREGNATED ALUMINA

Thermogravimetric analysis (TGA) is carried out to study the thermal behaviour of the additive-impregnated alumina support using DEGbe and TEG as additives.

The DEGbe-impregnated alumina support revealed a total loss of $23.1\text{ wt}\%$ with two DTG local minima at about 80 and $250\text{ }^{\circ}\text{C}$ and a shoulder at about $400\text{ }^{\circ}\text{C}$. The mass spectroscopy shows two major emissions of water and CO_2 starting at about $250\text{ }^{\circ}\text{C}$ (Figure V-11). Traces of mass fragments $m/z\ 12$ and 58 were also found (not shown here).

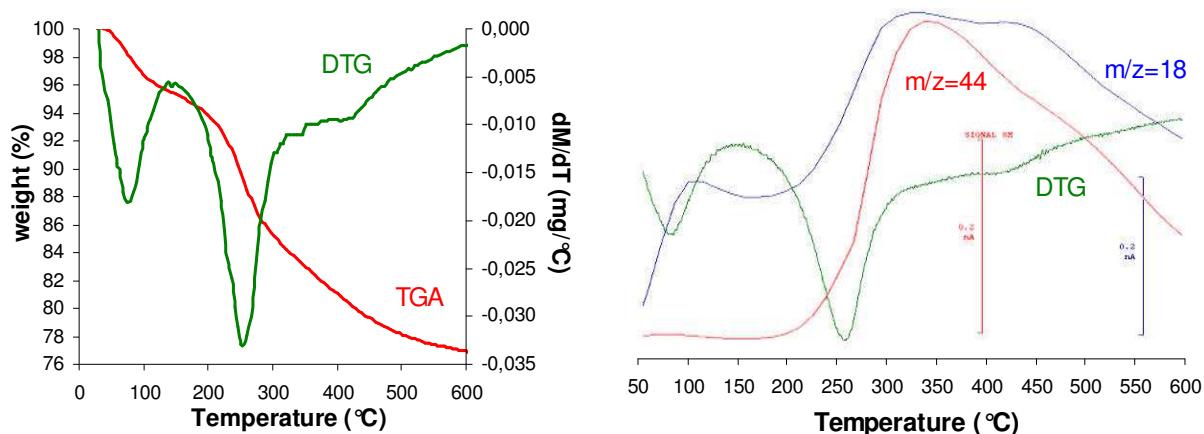


Figure V-11: Thermogravimetric analysis (TGA), derivative thermogravimetry (DTG) and mass spectroscopy results (right) of the alumina support.

On the other hand, the TEG-impregnated alumina support revealed a total loss of 17.2 wt% with two DTG local minima at about 95 and 250 °C and a shoulder at about 300 °C. The mass spectroscopy shows two major emissions of water and CO₂ starting at about 250 °C (Figure V-11). Traces of mass fragments m/z 12, 30 (carbon-type) and 58 (ketone-type) were also found (not shown here).

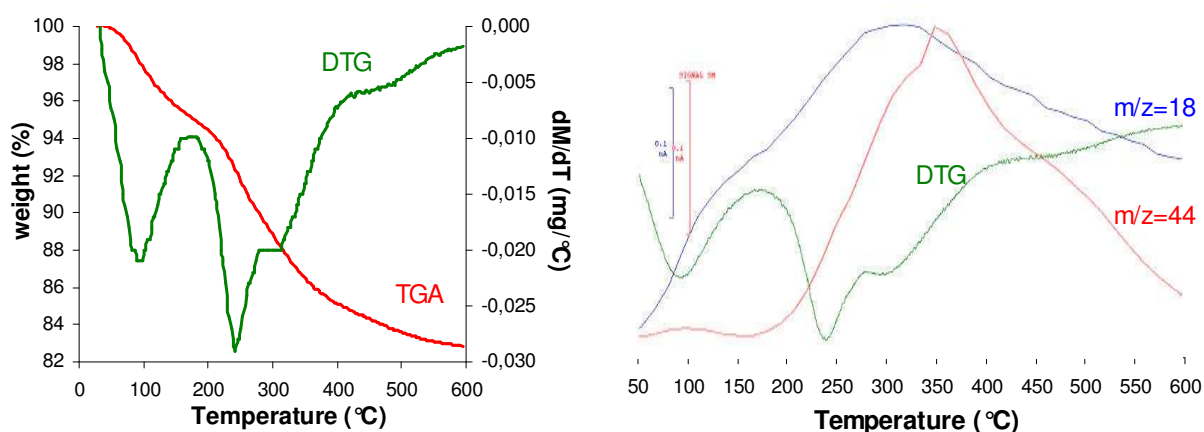


Figure V-12: Thermogravimetric analysis (TGA), derivative thermogravimetry (DTG) and mass spectroscopy results (right) of the alumina support.

In order to obtain more precise qualitative and qualitative information about the thermal behavior of the alumina support, the DTGs are decomposed according to method described in Appendix C. For the sake of simplicity, the decomposition plots are inverted.

The thermal gravimetric analysis of the DEGbe-impregnated alumina plotted as a function of the DTG decomposition shows 4 contributions (Figure V-13). The first curve, centered at about 77 °C is assigned to physisorbed water, corresponding to a weight loss of 4.7%. The remaining 3 curves centered at about 253 (12.3 wt%), 345 (1.4 wt%) and 418 °C (4.7 wt%) are assigned to thermal

decomposition products of DEGbe. The sum of these three weight losses corresponds to 18.4 wt% against the 13.3 wt% DEGbe determined by carbon quantification. Using the same DTG decomposition method, the TEG-impregnated alumina also shows 4 contributions: physisorbed water (94 °C) and 3 thermal decomposition products (241, 312 and 472 °C). They correspond to weight losses of 5.3, 4.3, 7.2 and 0.4 wt%, respectively. The sum of these three weight losses corresponds to 11.9 wt% against the 10.0 wt% TEG determined by carbon quantification.

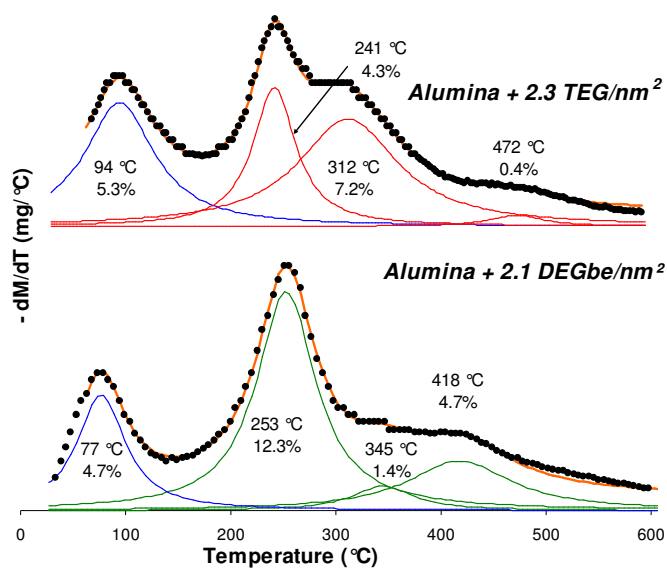


Figure V-13: TEG- and DEGbe-impregnated aluminas DTG decomposition curves.

V.3.4. ADDITIVE ADSORPTION ON ALUMINA STUDY

An adsorption study is carried out to assess the strength of the bonds between additives and the alumina support. In order to investigate the established interaction, two glycol-type additives are chosen: triethyleneglycol (TEG) and diethyleneglycol monobutyl ether (DEGbe). The choice was made in function of their water solubility, number of carbon atoms, viscosity and boiling point (not too close to water boiling point).

The TEG molecule was chosen because according to patent applications [3,4], it is the most efficient additive, leading to better catalytic performances. It is a non-ionic tensioactive, infinitely soluble in water, relatively viscous and contains two terminal hydroxyl groups as well as two ethoxy groups, resulting in a symmetric molecule. The DEGbe molecule was chosen because it contains two ethoxy groups and a terminal hydroxyl groups. Besides that, it is infinitely solute in water and possesses a low viscosity. This molecule is also a non-ionic tensioactive and several authors have studied its adsorption [5,6,7]. Table V-1 summarizes physical properties of the chosen molecules:

Table V-1: Physical properties of TEG and DEGbe molecules.

Compound	Molecule	B.P. [°C]	Viscosity [cP]	M.W. [g/mol]	Density	Water solub. [g/100 ml]
DEGbe	<chem>CCCCOCCOCCO</chem>	231	4.7 ^{25 °C}	162.23	0.967	∞
TEG	<chem>OCCOCCOCCO</chem>	285	48 ^{20 °C}	150.17	1.125	∞

Two simple models are postulated to describe the additives adsorption onto alumina: a chemical and a geometric model. The use of an indirect approach based on carbon quantification of the additive-containing alumina will allow verifying the validity of both models.

The chemical model assumes that surface alumina hydroxyl groups are responsible for the interaction with the adsorbed molecules, which implies that the adsorption is limited by the support. In the specific case of DEGbe adsorption, this model considers that up to three alumina OH groups may be in interaction with the hydroxyl and the two ethoxy groups of DEGbe molecules, as represented in Figure V-14:

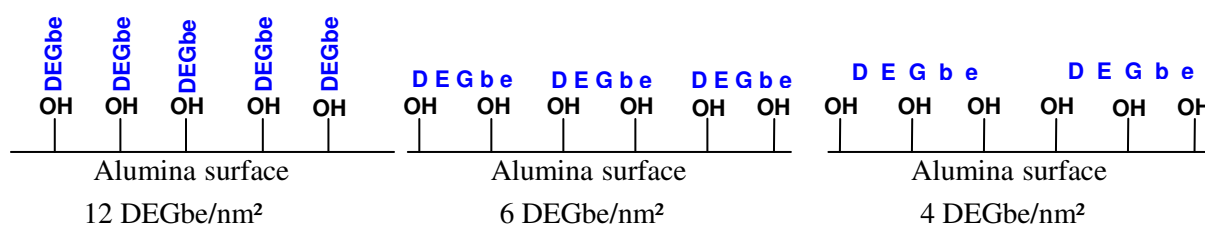


Figure V-14: Chemical adsorption model for DEGbe molecules onto γ -alumina (12 OH/nm^2 and S_{BET} of $300 \text{ m}^2/\text{g}$). Left: 1 Al-OH group in interaction with DEGbe molecules; center: 2 Al-OH groups in interaction with DEGbe molecules; right: 3 Al-OH groups in interaction with DEGbe molecules.

The geometrical model is based in the molecules dimensions and their deposition onto alumina surface, which implies that the adsorption is limited by the additive size. Two types of adsorption are considered: parallel and perpendicular to the alumina surface. Molecular dimensions have been calculated and optimized using the Universal Force Field (U.F.F). The molecule size is obtained from the optimized geometry calculating the molecular shadow indices, as implemented in the *MS Modeling* software (*Accelrys*). Figure V-15 represents the geometrical adsorption model for DEGbe and Table V-2 reports the dimensions of both molecules and also the calculated molecular densities for parallel and perpendicular adsorption.

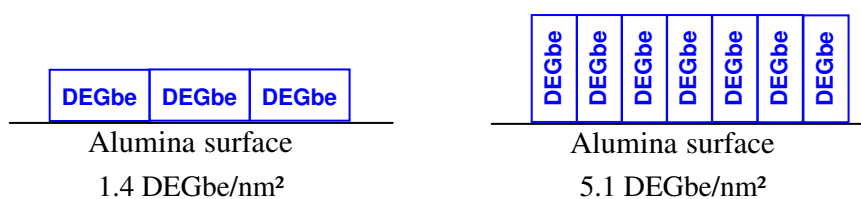


Figure V-15: Geometrical adsorption model for DEGbe molecules on the alumina support (S_{BET} of $300 \text{ m}^2/\text{g}$). Left: parallel deposition; right: perpendicular deposition.

Table V-2: Calculated molecular dimensions and adsorbed densities on the alumina support (S_{BET} of $300 \text{ m}^2/\text{g}$).

Molecule	Length [nm]	Width [nm]	Height [nm]	Molecular Density [molecules/nm ²]	
				Parallel	Perpendicular
Diethyleglycol monobutyl ether	1.56	0.46	0.43	1.4	5.1
Triethyleneglycol	1.24	0.54	0.53	1.5	3.5

V.3.4.1. Excess impregnation

Figure V-16 shows the additive amount determined by CHNS elemental analysis of a 96 hours excess impregnation with DEGbe on alumina at room temperature, prior to and after 3 washing operations with 50 ml of water.

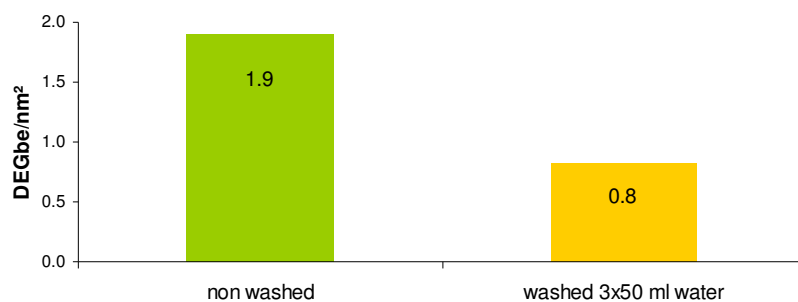


Figure V-16: DEGbe adsorbed onto alumina by excess impregnation for 96h at room temperature, prior to and after washing.

The resulting washing solutions, as well as the mother impregnation solution, were analyzed to measure their additive loading. In Figure V-17, the first point of the curve corresponds to the mother solution which had originally a DEGbe loading of 49.3 wt%.

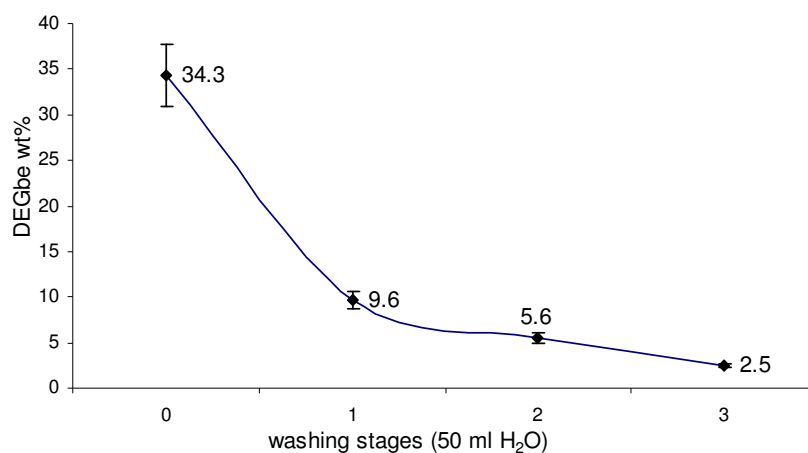


Figure V-17: Additive loading in the mother and washing solutions of DEGbe/Al₂O₃ samples prepared using the excess impregnation method.

The adsorbed DEGbe after the washing stages corresponds to 0.8 DEGbe/nm², which is inferior to the amount predicted by the geometrical model for parallel adsorption (1.4 DEGbe/nm²) and the chemical model considering an interaction with 3 Al-OH groups (4 DEGbe/nm²). However, part of the additive is still present in the last washing solution, meaning that further washing stages may result in less additive on the alumina surface and as consequence, an erroneous description of the additive monolayer.

V.3.4.2. Incipient wetness impregnation

The additive adsorption on the alumina support is also studied using incipient wetness impregnations in order to evaluate the influence of the solutions viscosity and reactivity with the support. The CHNS elemental analysis results for the additive-containing samples are summarized in Figure V-18. These values are corrected with respect to the LOI (550 °C) value.

The DEGbe loading after the washing stage shows that standard ageing leads to weaker Al-DEGbe bonds. This is also visible in Figure V-19 where important amounts of additive are detected in the washing solutions. On the other hand, the ageing time and temperature have a minor effect in the adsorbed additive amount after the washing stages (except for standard ageing). In terms of physisorbed additive, long ageing stages favor the interaction between alumina and DEGbe, leading to less important losses by additive evaporation during the drying stage.

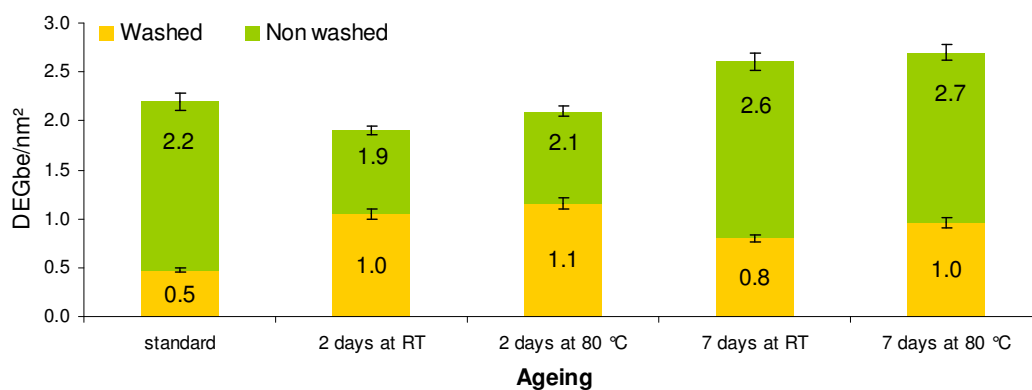


Figure V-18: Adsorbed DEGbe on the alumina support using incipient wetness impregnations with different ageing conditions, prior to and after the washing stage.

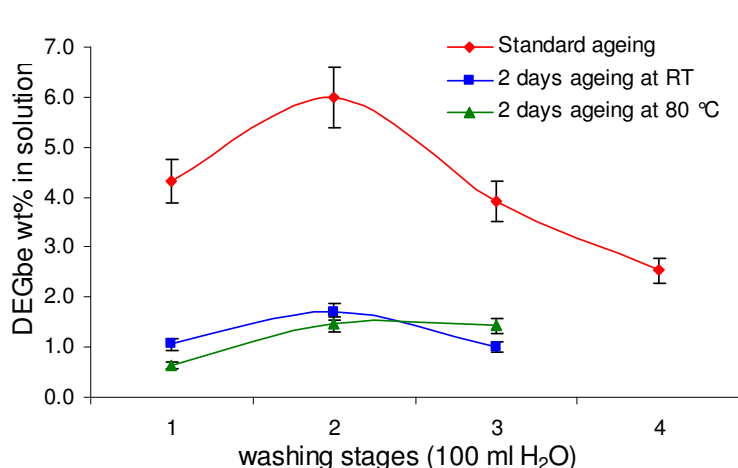


Figure V-19: DEGbe loading in the washing solutions of DEGbe/Al₂O₃ samples impregnated using the incipient wetness method.

The additive concentration in the washing solutions is measured by carbon analysis (Figure V-19). As observed in the excess impregnation case, the amount of additive in the last washing solution is still important. This means that the monolayer coverage is not achieved and that some physisorbed additive is still present.

The DEGbe loading after the washing stages shows that the standard ageing (1 night at room temperature) leads to a weaker adsorption of this additive. This result may be a consequence of the additive viscosity (4.7 cP for DEGbe) that delays the diffusion inside the alumina extrudates, favoring the formation of superposed layers instead of a well dispersed monolayer. Moreover, CHNS elemental analysis show that the 4 washing stages were not enough to eliminate all additive molecules in week interaction with the support. This was the motivation to perform new incipient wetness impregnations, this time introducing a drying stage at 70 °C and 50 mbar prior to the washing stages. The objective is to favor the additive-support interactions established after the ageing and drying states. The CHNS elemental analysis (Figure V-20) reveals that prior to the washing stages, about 0.4 wt% DEGbe is already lost, probably due to the intermediary drying stage. After the washing stages, both additives stay adsorbed on the alumina support with a density of 0.5 molecules/nm².

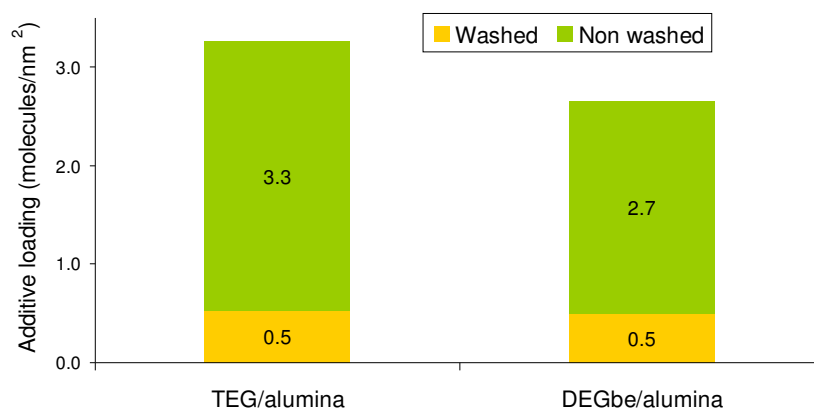


Figure V-20: Adsorbed additive on the alumina support using incipient wetness impregnations, prior to and after the washing stage with an intermediary drying step at 70°C and 50 mbar. Target loading of 3.3 TEG/nm² and 3.1 DEGbe/nm².

The CHNS elemental analysis (Figure V-21) confirmed that almost no additive is present in solution after 5 washing stages.

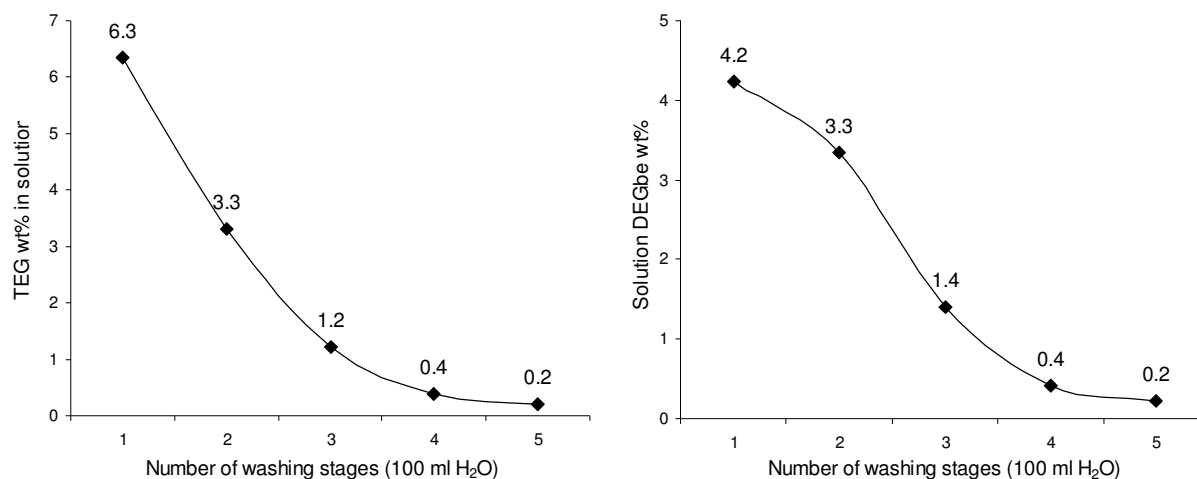


Figure V-21: Additive amount in washing solutions of additive-impregnated aluminas.

Assuming that the additive superposed layers are removed during the washing stage, it may be admitted that the amount that stays in the support is in direct interaction with alumina. Thus, since an excess of additive is used, it is assumed that all possible alumina adsorption sites may be occupied, defining this way an adsorption monolayer. The measured amounts after impregnation and washing stages correspond to about 0.5 additive molecule/nm², which is smaller than the values predicted by the chemical adsorption model (4 molecules/nm² considering 3 Al-OH in interaction with the additive) or the geometrical adsorption model (1.4 DEGbe/nm² or 1.5 TEG/nm² considering parallel adsorption). This evidences steric hindrance of the additives or preferential reaction with certain types of alumina hydroxyl groups.

The chemical model is based on the assumption of 12 Al-OH/nm² and that the additives may be in interaction with 1, 2 or 3 alumina hydroxyl groups. As shown by DRIFTS results for the additive-impregnated alumina samples, not all Al-OH groups are in interaction with the additive. This means that in order to validate this model, the proportion of hydroxyl groups in interaction with the additive needs to be determined. Moreover, this model does not consider the coordinative unsaturated sites (CUS) of alumina that could interact with the additives acting as Lewis acid sites. On the other hand, the geometric model is too simplistic because it does not consider the electrostatic repulsion between two additive molecules and neither the molecular deformation which may modify the dimensions of the molecule. Both models consider that the additive does not decompose into smaller fragments upon adsorption, which was verified by Raman and TGA analysis.

V.3.4.3. Additives adsorption mechanism on the alumina support

Based on the adsorption study and DRIFT spectroscopy, the additives interaction with alumina is governed by basic and neutral alumina hydroxyl groups, as schematized in Figure V-22.

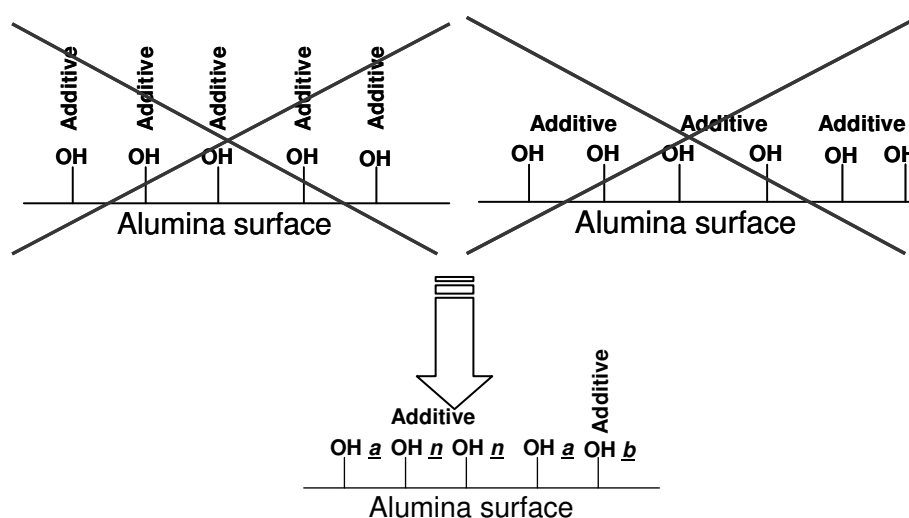


Figure V-22: Schematic representation of additives adsorption monolayer.
"a" corresponds to acidic, "n" to neutral and "b" to basic OH groups.

V.4. IMPACT OF THE ADDITIVE ON ADDITIVE PRE-IMPREGNATED CoMo(P) CATALYSTS

The objective of this section is to determine if the CoMo(P) catalysts surface species and the elements distribution inside the catalysts body are modified when the metal carrier solution is impregnated on an additive-containing alumina, compared to the additive impregnation of dried CoMo(P) catalysts. First, the cobalt-containing species are characterized and compared to those existing in the additive-containing dried catalysts. Then, the molybdenum-containing surface species are determined and compared. By studying the precursor structures, it is possible to have a global vision of the catalyst surface and how it is affected by the additive.

For this purpose, two catalysts with a molybdenum loading of 18 wt% MoO₃ and a TEG/Mo molar ratio of 0.75 were prepared by impregnation of a TEG-containing alumina support. The first catalyst was impregnated with a solution of Co₃[Co₂Mo₁₀O₃₈H₄], noted CoMo_HPA+TEG(PI). The second catalyst was prepared using a phosphorus-containing impregnation solution with a P/Mo molar ratio of 0.57, noted CoMoP(5)+TEG(PI).

V.4.1. INFLUENCE OF THE ADDITIVE ON THE DEPOSED COBALT SPECIES

UV-Visible diffuse reflectance spectroscopy is privileged to provide qualitative information about the cobalt-containing surface species. For the CoMo_HPA catalyst, a semi-quantitative analysis is carried out by XPS. For the CoMoP(5) catalyst, the study was complemented by cobalt K-edge X-ray absorption spectroscopy.

The UV-Visible diffuse reflectance spectrum of TEG pre-impregnated CoMo_HPA catalyst (Figure V-23) reveals the same features as the dried CoMo_HPA catalyst. It reveals the presence of Co(II) hexaaquo complex (bands at about 468 and 523 nm) as well as a Co(III) contribution (610 nm) arising from a molybdocobaltate HPA. As shown for dried and calcined catalysts cases, no significant modification of the spectrum is observed after additive impregnation, meaning that cobalt or molybdenum complexation by the additive is not occurring. However, the CoMo_HPA+TEG(PI) catalyst spectral line slightly evolves: the relative intensity of the Co(III) band increases.

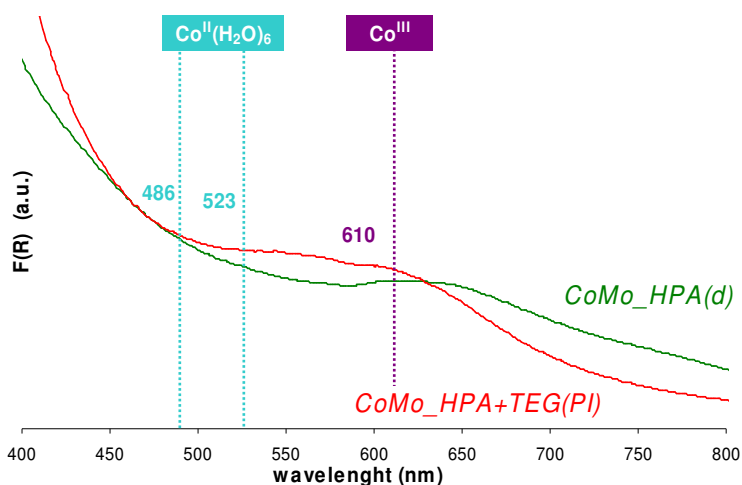


Figure V-23: UV-Visible diffuse reflectance spectra of additive-free dried and TEG pre-impregnated CoMo_HPA catalysts.

The increase of the Co(III) band suggests that the molybdocobaltate HPAs are retained to a greater extent after the $\text{Co}_3[\text{Co}_2\text{Mo}_{10}\text{O}_{38}\text{H}_4]$ solution impregnation compared to the dried CoMo_HPA(d) catalyst.

The XPS analysis is used to confirm evaluate the proportion of Co^{3+} ions in the pre-impregnated CoMo_HPA catalyst (Figure V-24). The spectrum decomposition method described in section III.2.2.1 is used. After the decomposition, it is possible to determine the $\text{Co}^{2+}/\text{Co}^{3+}$ proportion based on the relative areas of each contribution. The TEG pre-impregnated CoMo_HPA catalyst reveals 79/21, equal to the proportion found for the CoMo_HPA(d)+TEG catalyst case.

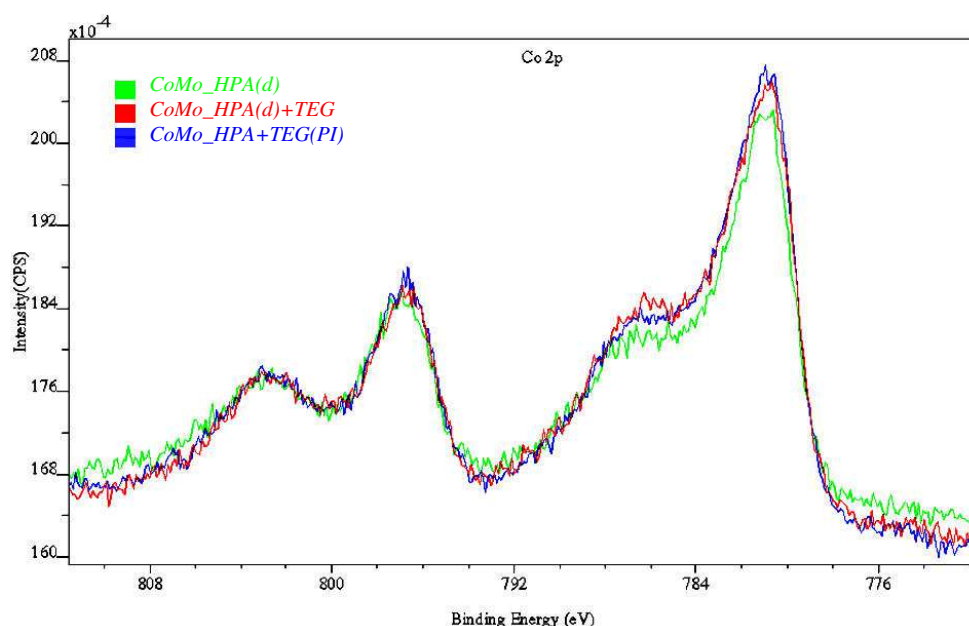


Figure V-24: Co 2p XPS spectra of the CoMo_HPA(d), CoMo_HPA(d)+TEG and CoMo_HPA+TEG(PI) catalysts.

Both additive-containing catalysts exhibit a slight decrease of the Co^{3+} proportion, which was 76/24 in the additive-free sample. This result is in contradiction with the observations made by UV-Visible spectroscopy which revealed that the pre-impregnated catalyst has a higher proportion of Co(III) species than the dried CoMoP(5d) catalyst.

For phosphorus-containing catalysts, no metal complexation is shown when pre-impregnation is used (Figure V-25). The CoMoP(5)+TEG(PI) spectrum shows the same spectral features than the CoMoP(5d)+TEG catalyst, revealing the presence of cobalt hexaquo complex (486 and 523 nm) and $\text{PCoMo}_{11}\text{O}_{40}^{7-}$ (557 nm). Besides these features, a broad band in the 700-900 nm region appears, also observed in the CoMoP(5d) catalyst and assigned to a reduced HPA. The fact that the additive is introduced prior to the impregnation of the active phase precursors limits the disappearance of this reduced compound.

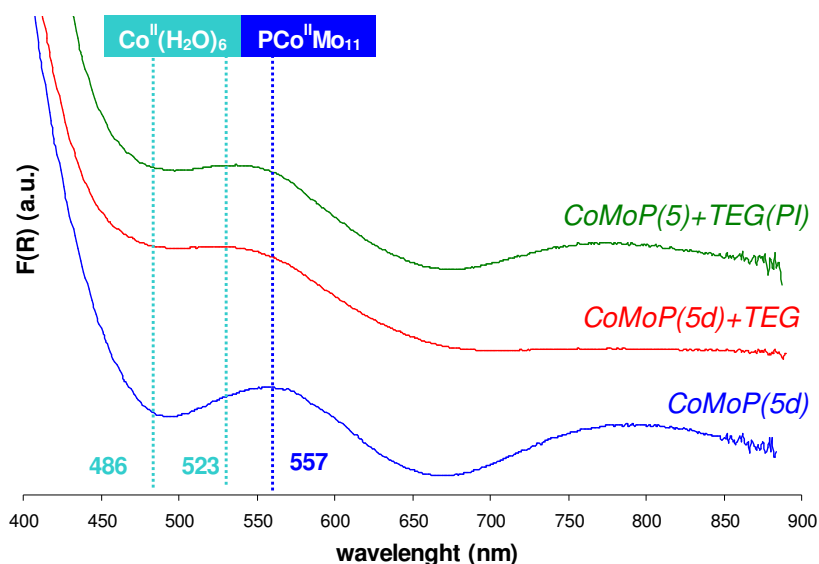


Figure V-25: UV-Visible diffuse reflectance spectra of the CoMoP(5d), CoMoP(5d)+TEG and pre-impregnated CoMoP(5)+TEG(PI) catalysts.

Based on the UV-Visible observations for the pre-impregnated CoMo_HPA and CoMoP(5) catalysts, it is plausible to conclude that the CoMo(P) solution species are partially preserved when the additive is previously impregnated on the alumina support.

The cobalt K-edge XANES of the CoMoP(5)+TEG(PI) sample shows the same features as those observed for the CoMoP(5d) and corresponding additive-containing catalyst (Figure V-26, left), exhibiting an adsorption maxima at about 7725 eV, assigned to Co^{2+} . On the other hand, the cobalt K-edge k^3 -weighted EXAFS Fourier Transforms modulus (Figure V-26, right) show minor variations with respect to the first and second coordination shells (Co-O bonds).

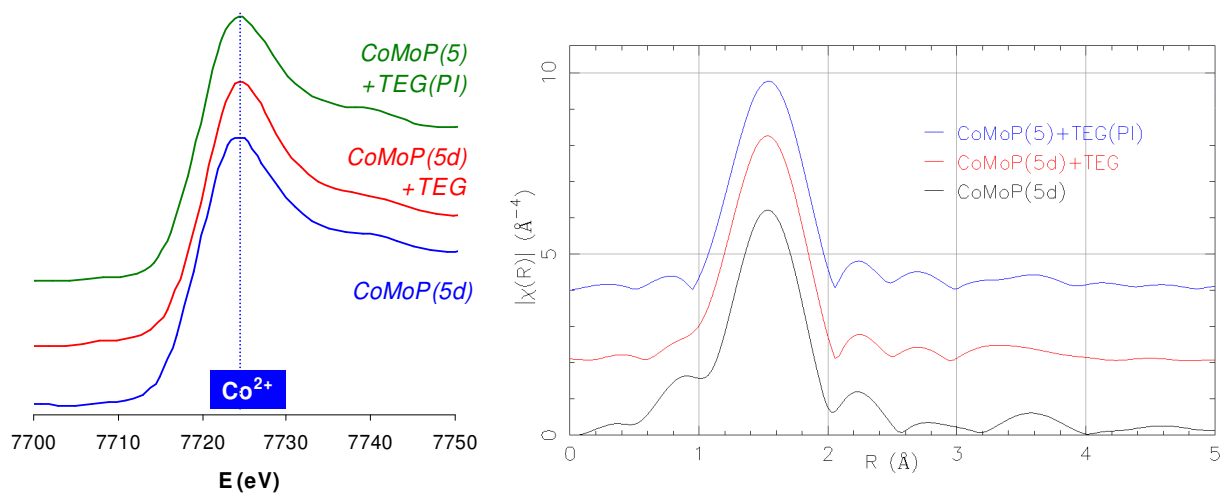


Figure V-26: Cobalt K-edge XANES (left) and k^3 -weighted EXAFS Fourier Transforms (FT) of CoMoP(5d), CoMoP(5d)+TEG and CoMoP(5)+TEG(PI) catalysts. FT Hanning window from 2 to 9; $\tau=2.5$.

V.4.2. INFLUENCE OF THE ADDITIVE ON THE DEPOSED MOLYBDENUM SPECIES

Raman analyses were conducted to determine the molybdenum-containing surface species on the additive pre-impregnated catalysts. The Raman spectra are then compared to the dried and additive-containing dried and calcined catalysts. In the case of the phosphorus-containing catalysts, the speciation was complemented by X-ray absorption spectroscopy.

The Raman spectrum of the CoMo_HPA+TEG(PI) catalyst shows the same features as the additive-containing CoMo_HPA catalysts (Figure V-27). Besides the band at about 835 cm^{-1} , assigned to TEG, the spectrum exhibits features of the $\text{Co}_2\text{Mo}_{10}\text{O}_{38}\text{H}_4^{6-}$ HPA (bands at 954 and 603 cm^{-1}).

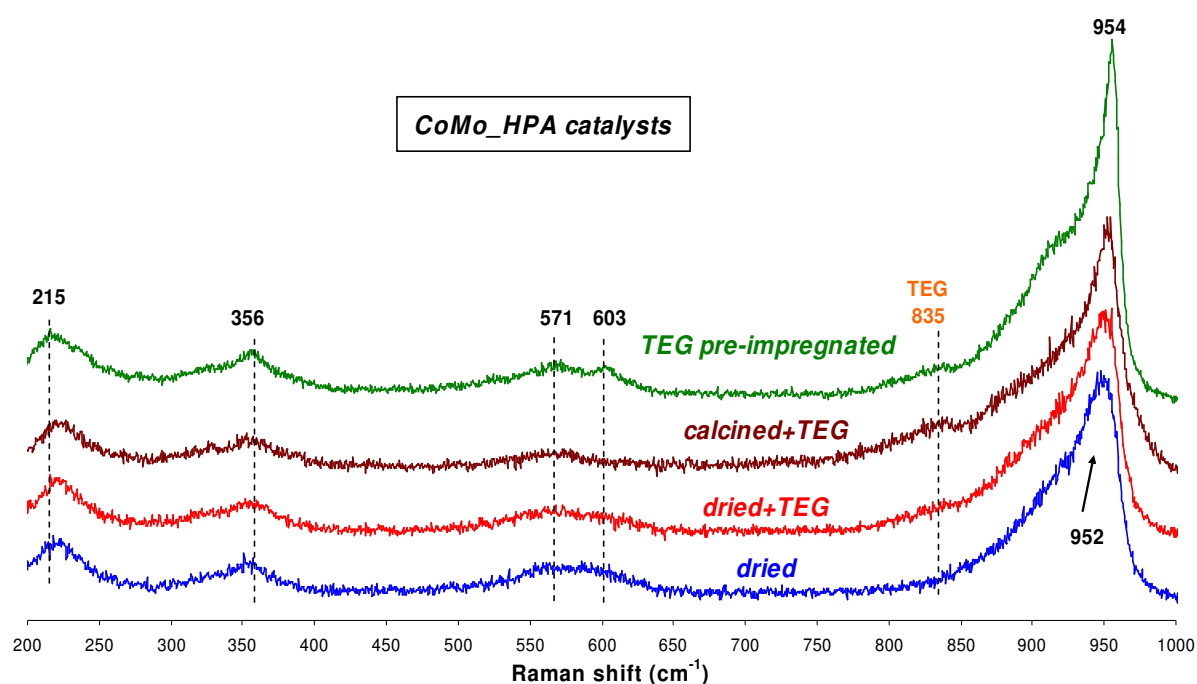


Figure V-27: Raman spectra of additive-containing CoMo_HPA catalysts.

The spectrum of the CoMo_HPA+TEG(PI) catalyst is very close to that of the $\text{Co}_2\text{Mo}_{10}\text{O}_{38}\text{H}_4^{6-}$ solution (Figure III-3). This HPA is deposited on the surface layer of physisorbed TEG molecules. Consequently, there is no direct interaction with the alumina surface groups, preventing the HPA decomposition.

In terms of phosphorus-containing catalyst, the Raman spectrum of the CoMoP(5)+TEG(PI) catalyst (Figure V-28) reveals the presence of $\text{PCoMo}_{11}\text{O}_{40}^{7-}$ (971 cm^{-1}), $\text{AlMo}_6\text{O}_{24}\text{H}_6^{3-}$ (952 cm^{-1}) and $\text{P}_2\text{Mo}_5\text{O}_{23}^{5-}$ (944 cm^{-1}) heteropolyanions, besides the band assigned of TEG (835 cm^{-1}). The proportion between the Anderson HPAs band in and the substituted Keggin-type HPAs band decreases in comparison to other additive-containing CoMoP(5) catalysts.

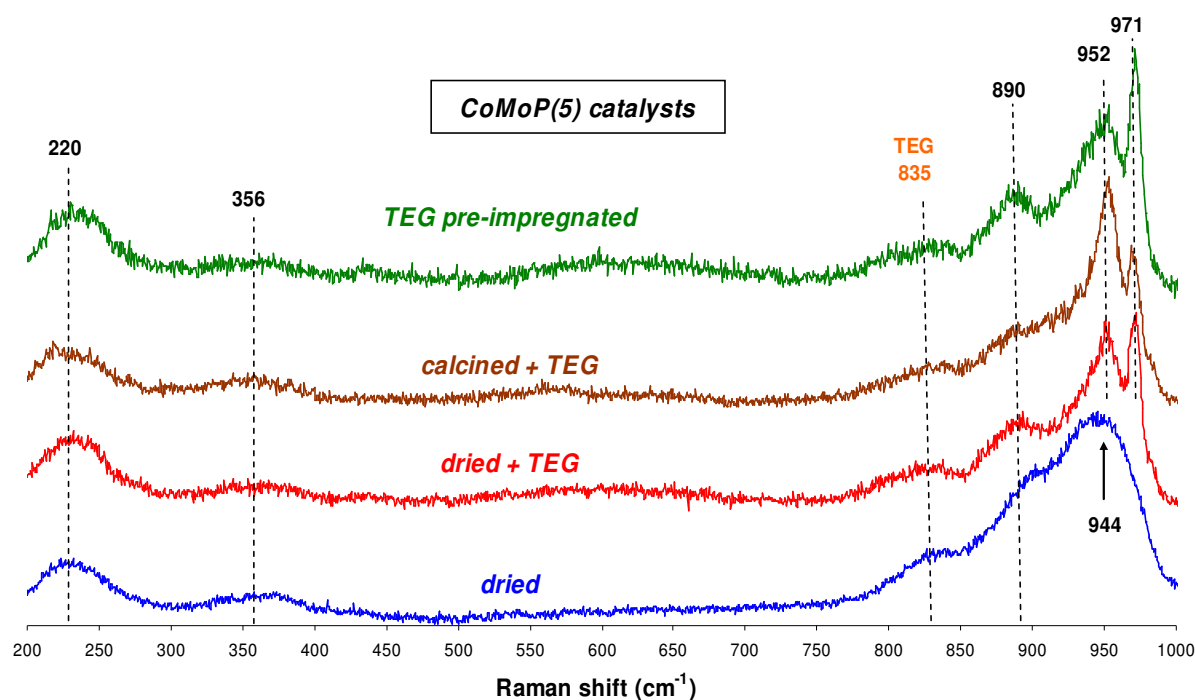


Figure V-28: Raman spectra of additive-containing CoMoP(5) catalysts.

Molybdenum speciation indicates that the diphosphopentamolybdate species, present in the impregnation solution (Figure III-25), are preserved upon impregnation. This is consistent with the previous Raman results of the CoMo_HPA+TEG (PI) catalyst. This means that a surface layer of physisorbed TEG molecules is formed. Therefore, there is no direct interaction with the alumina surface groups, preventing the HPA disintegration. In addition, the modification of the Anderson to Keggin HPAs proportion indicates that TEG pre-impregnation favors $\text{PCoMo}_{11}\text{O}_{40}^{7-}$ formation and prevents to some extent alumina dissolution.

Molybdenum K-edge XAS was also conducted for the CoMoP(5)+TEG(PI) sample. The XANES spectra (Figure V-29, left) shows the same broad pre-edge as the CoMoP(5d) catalysts, corresponding to molybdenum atoms in octahedral symmetry with a 6+ oxidation state. With respect to the EXAFS FT modulus, identical features are observed for the CoMoP(5)+TEG(PI) and CoMoP(5d)+TEG catalysts, meaning that the pre-impregnation leads to the same "average" molybdenum local environment as the sequentially impregnated dried catalyst.

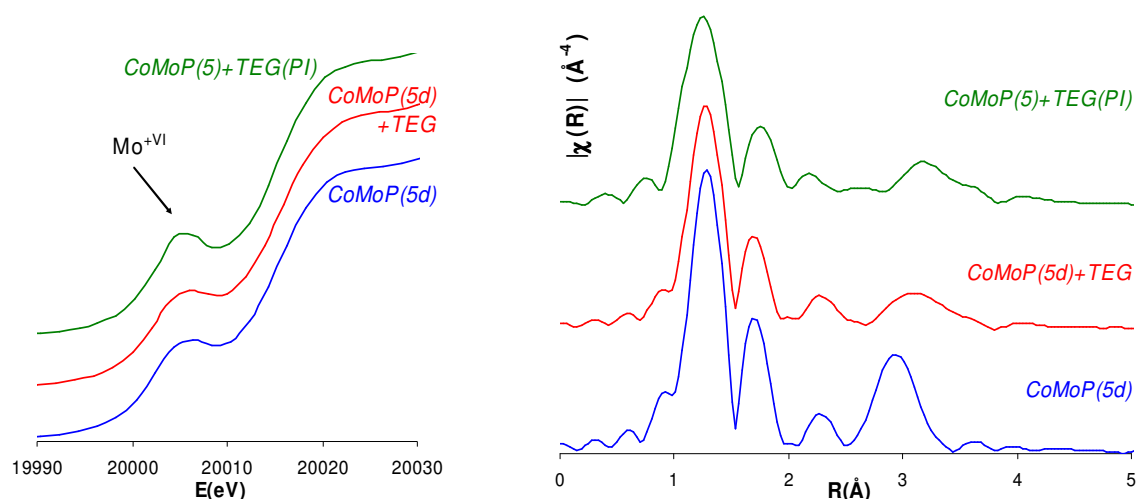


Figure V-29: Molybdenum K-edge XANES (left) and k^3 -weighted EXAFS Fourier Transforms (FT) of CoMoP(5d), CoMoP(5d)+TEG and CoMoP(5)+TEG(PI) catalysts. FT Hanning window from 2 to 11; $\tau=2.5$.

V.4.3. METALS AND PHOSPHORUS DISTRIBUTION

Electronic probe microanalysis (EPMA) is conducted to determine how the elements are distributed inside the catalysts body.

The CoMo_HPA+TEG(PI) catalyst has a good metal dispersion, as showed by the EPMA distribution coefficients near 1 (Figure V-30, left). This is not the case for the CoMoP(5)+TEG(PI), where phosphorus exhibits an eggshell profile corresponding to a distribution coefficient of about 0.78 (Figure V-30, right).

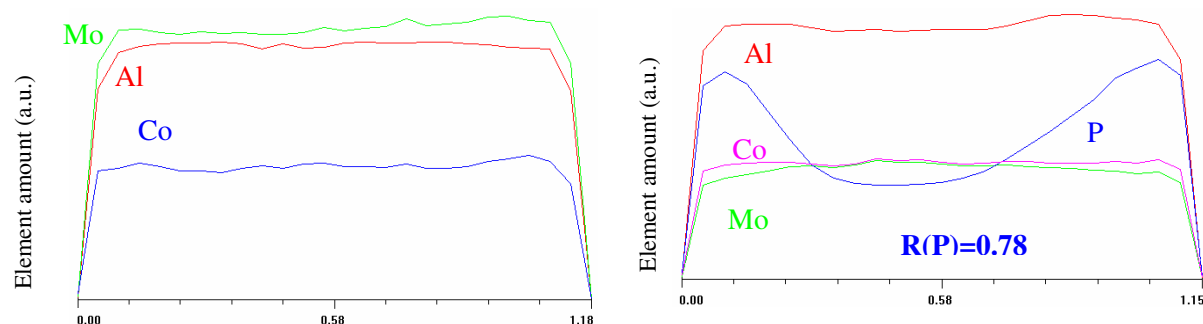
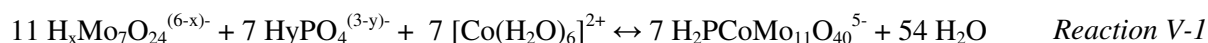


Figure V-30: EPMA of the CoMo_HPA+TEG(PI) (left) and CoMoP(5)+TEG(PI) (right) catalysts.

The causes of the phosphorus eggshell profile are discussed in section IV.3.3. It arises from the reaction of free phosphates and alumina surface hydroxyl groups, leading to phosphorus fixation.

However, a flat P distribution profile ($R=0.97$) is found for CoMoP(5c) catalysts: the free phosphate groups disperse towards the extrudate center after the alumina reactive sites saturation. In the pre-impregnated case, the free phosphate groups react with molybdates resulting from the

diphosphopentamolybdate HPA decomposition to form $\text{PCoMo}_{11}\text{O}_{40}^{7-}$ entities (Reaction V-1 [8]) that precipitate, leading to phosphorus fixation.



V.4.4. THERMAL BEHAVIOR

Thermogravimetric analyses (TGA) are carried out to study the thermal stability of the deposited species in the CoMoP(5) catalyst prepared using an additive-containing alumina support.

The CoMoP(5)+TEG(PI) catalyst revealed a total loss of 20.7 wt% with two DTG local minima at about 100 and 225 °C and a shoulder at about 250 °C. The mass spectroscopy shows two major emissions of water and CO_2 starting at about 200 °C (Figure V-30). Traces of mass fragments m/z 12 (carbon-type) and 58 (ketone-type) were also found (not shown here).

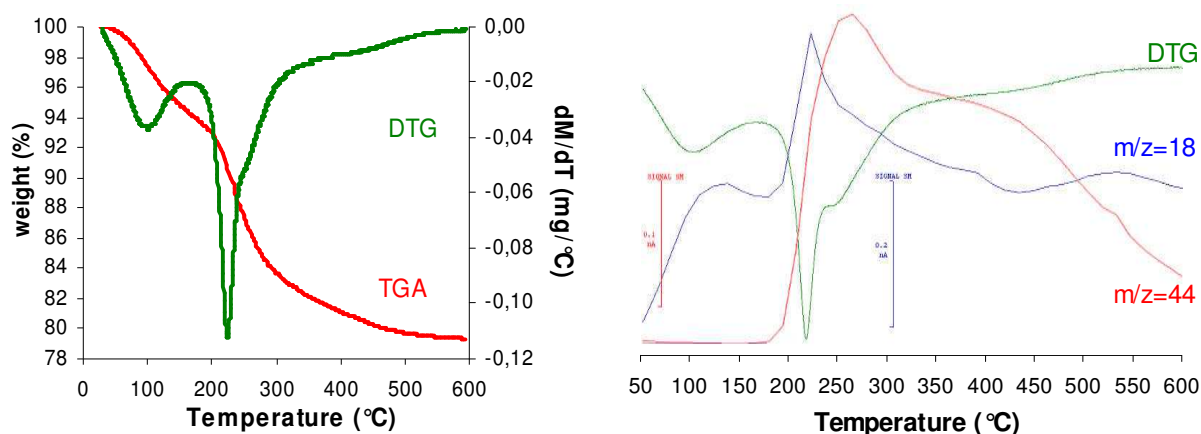
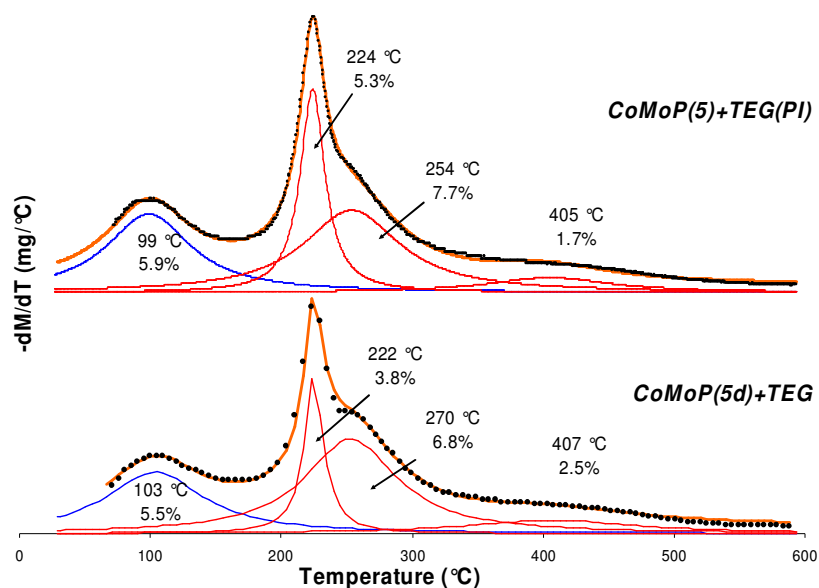


Figure V-31: Thermogravimetric analysis (TGA), derivative thermogravimetry (DTG) and mass spectroscopy results (right) of the CoMoP(5)+TEG(PI) catalyst.

More precise qualitative and qualitative information about the thermal stability of the catalyst is obtained using the DTG decomposition method described in Appendix C. For the sake of simplicity, the decomposition plots are inverted.

The thermogravimetric behavior of the pre-impregnated CoMoP(5)+TEG(PI) catalyst is similar to the CoMoP(5d)+TEG catalyst (Figure V-32), showing water removal at about 99 °C (5.9 wt%) and TEG decomposition and removal (224, 254 and 405 °C), corresponding to weight losses of 5.3, 7.7 and 1.7 wt%, respectively. The sum of the TEG decomposition curves equals 14.7 wt% against 11.8 wt% TEG determined by carbon quantification using CHNS elemental analysts. This difference may be assigned to coordination and constitution water of the existing HPAs, which leave the catalyst at about 150 °C and 300 °C, respectively.

DTG decompositions show that TEG interacts with the catalyst surface in the same way when impregnated directly on alumina or after the precursor solution impregnation. When compared to



TEG-impregnated alumina, the decomposition products for the additive-impregnated catalysts appear at significant lower temperatures (224, 254 and 405 °C against 241, 312 and 472 °C), revealing that the TEG interaction with surface are weakened in presence of the active phase precursors, independently of the impregnation order.

Figure V-32: TEG pre- or sequentially-impregnated CoMoP(5) DTG decomposition curves.

V.5. SURFACE MECHANISM

When the additive is impregnated on the alumina support, it forms a surface layer of physisorbed molecules. Upon the precursor solution impregnation, the solution HPA precursors deposit on this physisorbed layer and the direct interaction between the HPA species and the alumina surface groups is limited. Therefore, the decomposition of the HPA species is prevented. Moreover, the additive induces the formation of the Anderson hexamolybdoaluminate HPAs and the substituted Keggin $\text{PCoMo}_{11}\text{O}_{40}^{7-}$ HPAs when the P/Mo molar is superior to 2/5, which leads to improved dispersion of the metals. In addition, the physisorbed surface layer of the additive limits the dissolution of the alumina support and consequent formation of $\text{AlMo}_6\text{O}_{24}\text{H}_6^{3-}$ species.

Figure V-33 exemplifies the surface mechanism when the CoMoP(5) solution is impregnated on a TEG-containing alumina support. The precursor solution is mainly composed of $\text{P}_2\text{Mo}_5\text{O}_{23}^{5-}$, $[\text{Co}(\text{H}_2\text{O})_6]^{2+}$ and free phosphate species. Upon impregnation, part of the $\text{P}_2\text{Mo}_5\text{O}_{23}^{5-}$ HPA deposits intact and the other part is decomposed to form molybdates and phosphate groups. These anions then react to form $\text{PCoMo}_{11}\text{O}_{40}^{7-}$ HPA. A portion of the molybdates ions also reacts with the Al^{3+} ions arising from alumina dissolution to form $\text{AlMo}_6\text{O}_{24}\text{H}_6^{3-}$ species. The remaining cobalt precipitates as counter-ion of the existing HPAs. Considering the excess phosphate groups, they adsorb as polyphosphates in presence of TEG, as showed by ^{31}P NMR of the dried CoMoP(5d)+TEG catalysts.

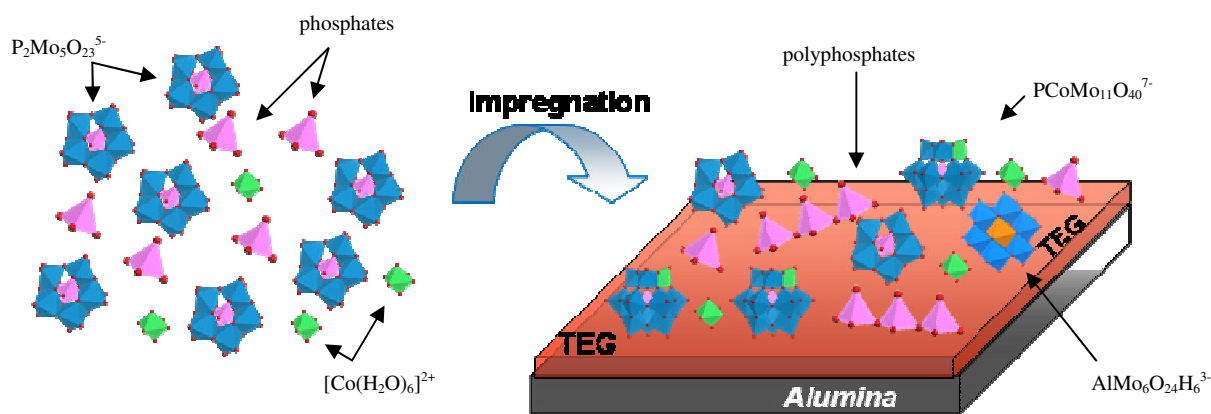


Figure V-33: Schematic representation of the surface mechanism for the CoMoP(5)+TEG(PI) catalyst.

V.6. CHAPTER CONCLUSIONS

The first part of this chapter is dedicated to the additive adsorption on alumina. Characterization reveals a weak support-glycol interaction at room temperature. However, after 150 °C, an Al-O-C bond is established that remains at least up to 550 °C. Moreover, DRIFT spectroscopy shows that the additive is in interaction mainly with basic and neutral alumina hydroxyl groups. The adsorption study on alumina shows a coverage of about 0.5 molecules/nm² for both DEGbe and TEG, meaning that the adsorption is not governed by geometrical factors but by the availability of the surface alumina hydroxyl groups.

The second part of this chapter focuses on the TEG pre-impregnated CoMo(P) catalysts. It was shown that the HPA decomposition is limited due to the existence of an additive physisorbed layer on the alumina surface. In this way, the interaction between the initial HPA species in solution and the alumina surface sites is prevented. The alumina dissolution is also limited: the formation of $\text{AlMo}_6\text{O}_{24}\text{H}_6^{3-}$ species is observed but it occurs to a lesser extent when compared to the catalysts sequentially impregnated with TEG. Moreover, enhanced metal dispersion is achieved by formation of $\text{PCoMo}_{11}\text{O}_{40}^{7-}$ heteropolyanions when the P/Mo ratio is superior to 2/5.

Key-points

1. The adsorption of the additives on alumina is governed by the availability of the surface alumina hydroxyl groups.
2. The additive leads to the formation of $\text{AlMo}_6\text{O}_{24}\text{H}_6^{3-}$ and in addition, $\text{PCoMo}_{11}\text{O}_{40}^{7-}$ when the P/Mo molar ratio is superior to 2/5.
3. The additive pre-impregnation increases the proportion of $\text{PCoMo}_{11}\text{O}_{40}^{7-}$ with respect to $\text{AlMo}_6\text{O}_{24}\text{H}_6^{3-}$ compared to the additive impregnation on dried and calcined catalysts.
4. The additive is deposited on alumina and forms a layer between the active phase precursors and alumina. In this way, the decomposition of the solution heteropolyanions is limited.

V.7. BIBLIOGRAPHIC REFERENCES

- 1 M. Digne, Ph.D. thesis, École Normale Supérieure de Lyon, **2003**.
- 2 D. Nicosia and R. Prins, J. Catal. 229, 424, **2005**.
- 3 WO96/41848A1, **1996**.
- 4 EP0601722A1, **1994**.
- 5 P. Mazoyer-Galliou, Ph.D. thesis Université Claude Bernard – Lyon I, **1998**.
- 6 R. Iwamoto, N. Kagami and A. Lino, J. Jpn. Petrol. Inst. 48, 4, 234, **2005**.
- 7 M. Tunius and R. Sköld, Coll. Surf. 46, 379, **1990**.
- 8 J.A. Bergwerff, L.G.A. van der Water, T. Wisser, P. de Peinder B.R.G. Leliveld, K.P. de Jong and B.M. Weckhuysen, Chem. Eur. J. 11, 4591, **2005**.

CHAPTER VI: THE ROLE OF GLYCOL-TYPE ADDITIVES ON CoMo(P) CATALYSTS PREPARED BY CO-IMPREGNATION

VI.1. Introduction.....	181
VI.2. Impact of the additive on the impregnation solutions	181
VI.2.1. Influence of the additive on the cobalt species in solution	182
VI.2.2. Influence of the additive on the molybdenum species in solution	183
VI.2.3. Influence of the additive on the phosphorus species in solution.....	184
VI.3. Impact of the additive on the catalysts prepared by co-impregnation.....	185
VI.3.1. Influence of the additive on the deposited cobalt and molybdenum species	185
VI.3.2. Metals and phosphorus distribution	187
VI.3.3. Thermal stability	188
VI.4. Surface mechanism	189
VI.5. Chapter conclusions.....	190
VI.6. Bibliographic references.....	191

CHAPTER VI: THE ROLE OF GLYCOL-TYPE ADDITIVES ON CoMo(P) CATALYSTS PREPARED BY CO-IMPREGNATION

VI.1. INTRODUCTION

It was shown in the previous chapters that the additive leads to enhanced metal dispersion by favoring the formation of Anderson and substituted-Keggin HPAs. An additional effect was shown when the additive is impregnated on the alumina support prior to the CoMo(P) precursors: the additive forms a surface layer between the support and the metal precursors and thus limits the solution HPAs disintegration. When the additive and the CoMo(P) precursors are mixed in the same impregnation solution, two different aspects have to be considered: 1) Are the solution species modified by the presence of the additive? 2) Are those species preserved after impregnation?

To provide answer to these questions, the impact of the additive on the impregnation solution will be firstly determined, followed by the speciation of the deposited species on alumina surface. To complete this study, the impact of the additive on the elements distribution in the catalyst body will be also studied.

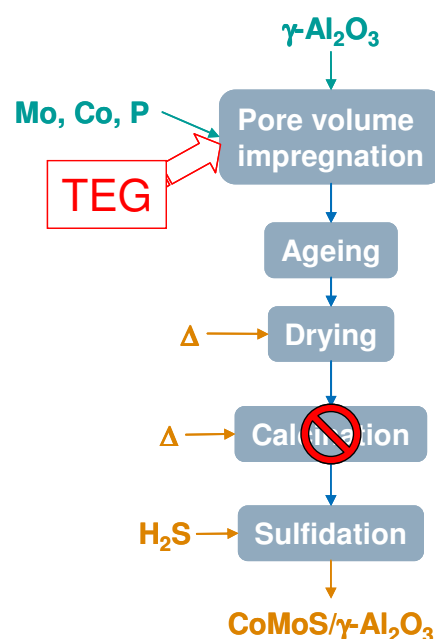


Figure VI-1: Preparation of additive-containing CoMoP catalysts using co-impregnation.

VI.2. IMPACT OF THE ADDITIVE ON THE IMPREGNATION SOLUTIONS

The speciation of the impregnation solutions is conducted in absence and in presence of TEG to study the impact of the additive on the impregnation solutions. First, the cobalt-containing species are determined, followed by the molybdenum-containing species. For CoMoP solutions, the phosphorus-containing species are also determined.

The additive-containing impregnation solutions were prepared by adding TEG (0.75 TEG/Mo molar ratio) to the impregnation solutions studied in Chapter III. The introduction of the additive in the impregnation solutions slightly changes the solution pH: a maximum increase of 0.5 was measured. In terms of visible modifications in the solutions induced by the additive, only the CoMoP(5) solution changed from blue to green.

VI.2.1. INFLUENCE OF THE ADDITIVE ON THE COBALT SPECIES IN SOLUTION

UV-Visible spectroscopy was the privileged experimental technique to determine the cobalt species in solution. The spectra of the $\text{Co}(\text{NO}_3)_2$, CoMo_AHM and CoMo_HPA solutions (Figure VI-2) exhibits identical spectral lines after the additive introduction. The cobalt nitrate and CoMo_AHM (cobalt nitrate and ammonium heptamolybdate) aqueous solutions are not affected by the additive, revealing the presence of hexaaquo complex $[\text{Co}(\text{H}_2\text{O})_6]^{2+}$ (460, 513 and 615 nm). Furthermore, the CoMo_HPA aqueous solution is also not affected by the introduction of the additive. The presence of Co(III) (610 nm) and Co(II) (513 nm) species is still observed, revealing the presence of molybdocobaltate cobalt salts.

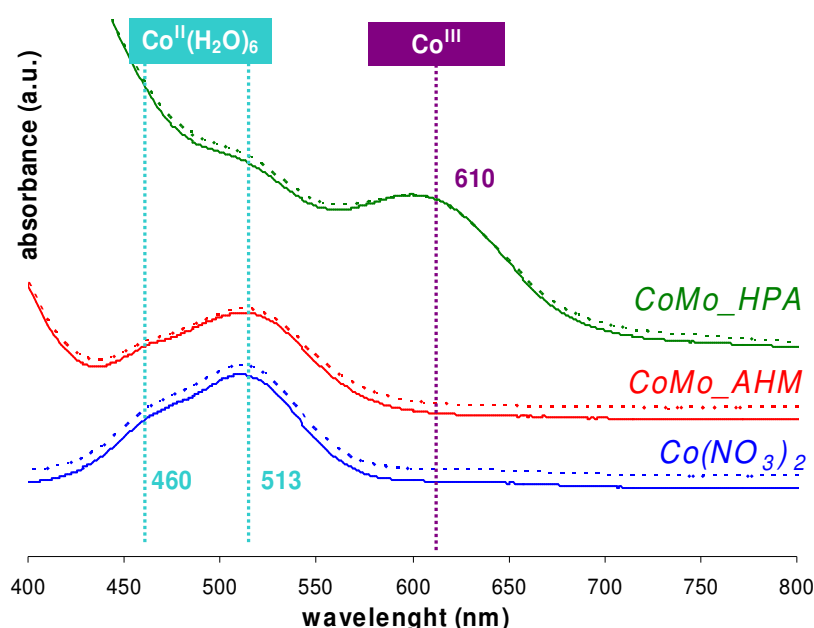


Figure VI-2: UV-Visible spectra of additive-free (— solid lines) and additive-containing $\text{Co}(\text{NO}_3)_2$ and CoMo-based solutions (--- dashed lines).

Concerning the phosphorus-containing solutions, the UV-Visible spectra of the CoMoP(5) and CoMoP(3) solutions exhibit a broad band in the 600-900 nm region (Figure VI-3). The intensity of this band increases when the phosphorus content increases. These spectra also exhibit a smaller band at about 513 nm, assigned to the hexaaquo complex $[\text{Co}(\text{H}_2\text{O})_6]^{2+}$. The CoMoP(5) and the CoMoP(1) solutions present a band at about 564 nm, assigned to the $\text{PCoMo}_{11}\text{O}_{40}^{7-}$ HPA.

After impregnation of the additive, no significant modifications are observed in the CoMoP(1) solution spectrum. However, this is not the case for spectra of the CoMoP(5) and CoMoP(3) solutions, where the relative intensity of the broad band in the 600-900 nm region decreases.

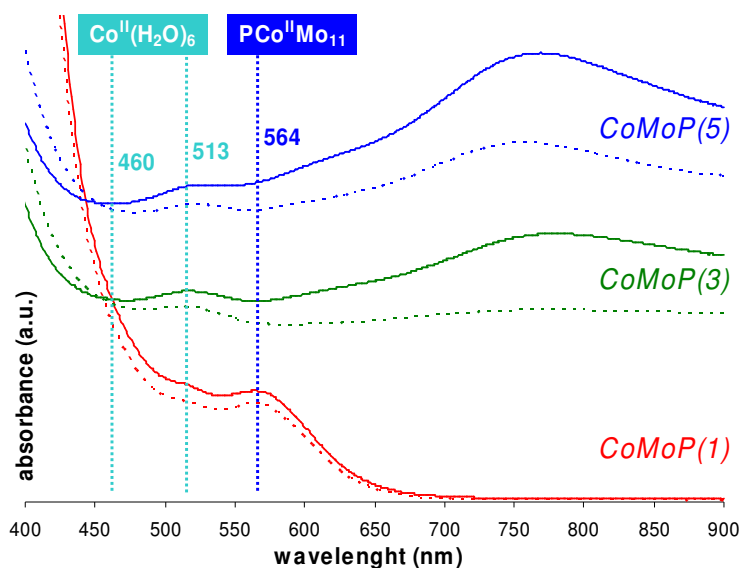


Figure VI-3: UV-Visible spectra of additive-free (— solid lines) and additive-containing CoMoP-based solutions (--- dashed lines).

As mentioned in Chapter III (§III.3.1), the broad band centered at about 750 nm is assigned to the 4-electron reduced Keggin $\text{PMo}_{12}\text{O}_{40}^{3-}$ HPA [1]. Griboval reported that some HPAs may exchange electrons in multiple reversible steps and that reduced entities are stabilized by acidic pH [2]. It is unlikely that a TEG redox reaction is occurring, since TEG is a primary alcohol. The partial conversion of the reduced species seems most likely to result from a pH effect.

VI.2.2. INFLUENCE OF THE ADDITIVE ON THE MOLYBDENUM SPECIES IN SOLUTION

The Raman analysis of the CoMoP(5) solution prior to and after TEG introduction shows minor changes in molybdenum speciation. The main species is still the $\text{P}_2\text{Mo}_5\text{O}_{23}^{6-}$ HPA (944 cm^{-1}) but the sharp shoulder observed at about 977 cm^{-1} assigned to the Dawson $\text{P}_2\text{Mo}_{18}\text{O}_{62}^{6-}$ HPA, gives place to two new sharp shoulders at about 971 and 993 cm^{-1} . The first peak is assigned to $\text{PCoMo}_{11}\text{O}_{40}^{7-}$ [3] and the second to the Keggin $\text{PMo}_{12}\text{O}_{40}^{3-}$ HPA [4]. However, the weak band at about 720 cm^{-1} is typical from $\text{P}_2\text{Mo}_{18}\text{O}_{62}^{6-}$ and $\text{PMo}_9\text{O}_{34}\text{H}_4^{6-}$ [4], which means that these entities are also present.

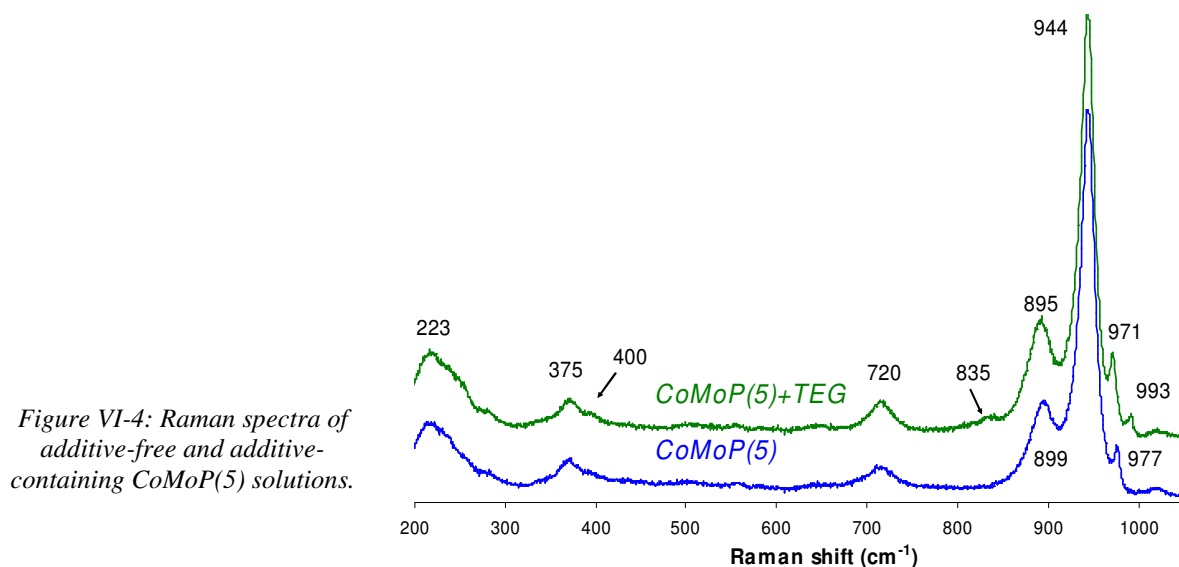


Figure VI-4: Raman spectra of additive-free and additive-containing CoMoP(5) solutions.

VI.2.3. INFLUENCE OF THE ADDITIVE ON THE PHOSPHORUS SPECIES IN SOLUTION

The use of ^{31}P NMR spectroscopy allows to better describe the HPA entities present in the impregnation solutions, as well as other phosphorus-containing species. As mentioned before, only MoP solutions are analyzed due to the broadening and shifting of the NMR signal induced by the paramagnetic nature of cobalt. However, the absence of cobalt hydroxide renders the solution pH more acidic: MoP solutions have a pH value in the 0 to 0.5 interval, while CoMoP solutions are situated in the 1-1.5 interval, except for the CoMoP(1) solution which has a pH value of 4.1. TEG introduction slightly modifies the solution pH towards higher values ($\Delta \text{pH} < 0.3$). These differences in pH may completely change the nature of the dissolved species.

The starting solutions exhibit resonances at about -1.0, 0.5 and 2.0 ppm (Figure VI-5, left), assigned to $\text{PMo}_9\text{O}_{34}\text{H}_6^{3-}$, $\text{H}_x\text{PO}_4^{3-x}$ and $\text{P}_2\text{Mo}_5\text{O}_{23}^{6-}$, respectively. After TEG introduction, the same peaks are visible and a new weak peak at about -1.7 ppm appears in all solutions (Figure VI-5, right). This resonance is assigned to the Dawson $\text{P}_2\text{Mo}_{18}\text{O}_{62}^{6-}$ heteropolyanion [4,5,6]. The peaks integrals show a decrease in $\text{P}_2\text{Mo}_5\text{O}_{23}^{6-}$ and free phosphates while $\text{PMo}_9\text{O}_{34}\text{H}_6^{3-}$ and $\text{P}_2\text{Mo}_{18}\text{O}_{62}^{6-}$ increase when the additive is introduced.

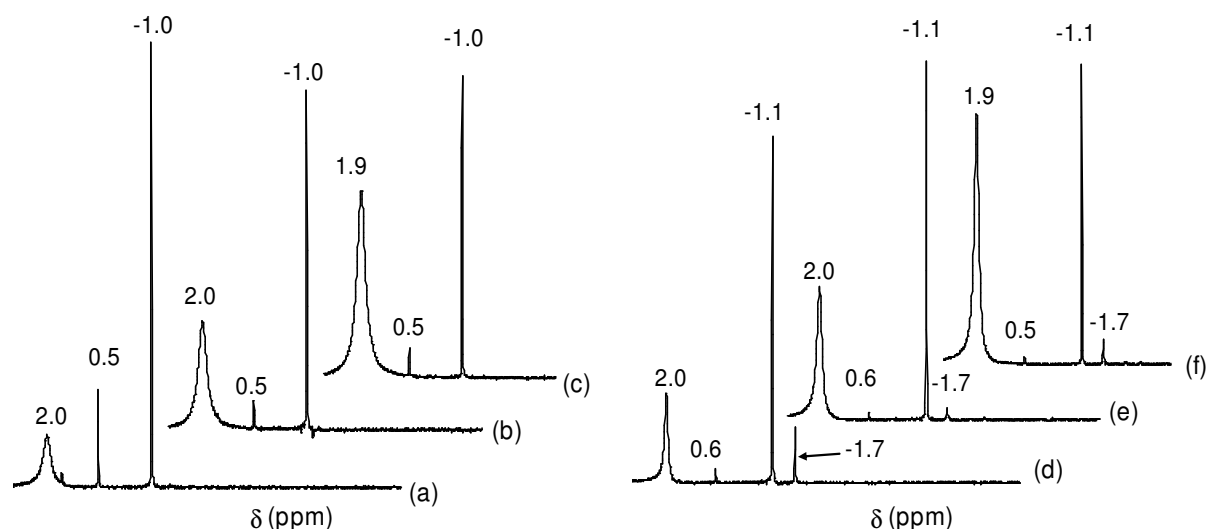
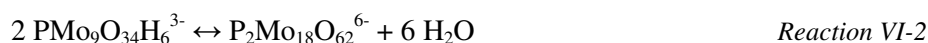
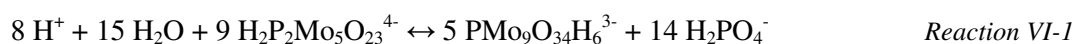


Figure VI-5: ^{31}P NMR spectra of: (a) MoP(2), (b) MoP(3) and (c) MoP(5) precursor solutions. Spectra (d), (e) and (f) are from the corresponding additive-containing solutions, respectively.

When the P/Mo ratio increases, the solution equilibria (Reaction VI-2) are displaced towards the formation of diphosphopentamolybdate ions while $\text{PMo}_9\text{O}_{34}\text{H}_6^{3-}$ is consumed. On the other hand, results show that TEG favors the formation of HPAs with a P/Mo molar ratio inferior to 2/5 (Reaction VI-2 and Reaction VI-2). No evidence of phosphate glycol ethers is found (cf. §IV.3.3.1).



Based on the combined NMR and Raman results, the CoMoP(5) solution is composed mainly of $\text{P}_2\text{Mo}_5\text{O}_{23}^{6-}$ and an equilibrium is established between $\text{PMo}_9\text{O}_{34}\text{H}_6^{3-}$ and $\text{P}_2\text{Mo}_{18}\text{O}_{62}^{6-}$ species. When glycol is introduced, the main species remains the same but new $\text{PCoMo}_{11}\text{O}_{40}^{7-}$ and $\text{PMo}_{12}\text{O}_{40}^{3-}$ HPAs are formed. $\text{PMo}_9\text{O}_{34}\text{H}_6^{3-}$ and $\text{P}_2\text{Mo}_{18}\text{O}_{62}^{6-}$ species are also present. Table VI-1 summarizes the dissolved species prior to or after TEG introduction. For the sake of simplicity, only the main components are taken into account.

Table VI-1: Speciation results for CoMoP precursor solutions prior to and after TEG impregnation.

Solution	Prior to TEG	After TEG
CoMoP(1)	$[\text{Co}(\text{H}_2\text{O})_6]^{2+}$	$[\text{Co}(\text{H}_2\text{O})_6]^{2+}$
P/Mo = 0.11	$\text{PCoMo}_{11}\text{O}_{40}^{7-}$	$\text{PCoMo}_{11}\text{O}_{40}^{7-}$
CoMoP(3)	$[\text{Co}(\text{H}_2\text{O})_6]^{2+}$	$[\text{Co}(\text{H}_2\text{O})_6]^{2+}$
P/Mo = 0.40	$\text{P}_2\text{Mo}_5\text{O}_{23}^{6-}$	$\text{P}_2\text{Mo}_5\text{O}_{23}^{6-}$
CoMoP(5) P/Mo = 0.57	$[\text{Co}(\text{H}_2\text{O})_6]^{2+}$	$[\text{Co}(\text{H}_2\text{O})_6]^{2+}$
	$\text{P}_2\text{Mo}_5\text{O}_{23}^{6-}$	$\text{P}_2\text{Mo}_5\text{O}_{23}^{6-}$
	$\text{PMo}_9\text{O}_{34}\text{H}_6^{3-}$	$\text{PMo}_9\text{O}_{34}\text{H}_6^{3-}$
	$\text{P}_2\text{Mo}_{18}\text{O}_{62}^{6-}$	$\text{P}_2\text{Mo}_{18}\text{O}_{62}^{6-}$
		$\text{PCoMo}_{11}\text{O}_{40}^{7-}$
		$\text{PMo}_{12}\text{O}_{40}^{3-}$

VI.3. IMPACT OF THE ADDITIVE ON THE CATALYSTS PREPARED BY CO-IMPREGNATION

This section is consecrated to the study of the deposited surface species when prepared from a solution containing the CoMo(P) precursors and the additive. The study is also comprises the elements distribution inside the catalysts extrudates. For this purpose, a catalyst with a molybdenum loading of 18 wt% MoO_3 was prepared by co-impregnation using for the CoMoP(5)+TEG solution. This catalyst is noted with the (CI) suffix: CoMoP(5)+TEG(CI).

VI.3.1. INFLUENCE OF THE ADDITIVE ON THE DEPOSED COBALT AND MOLYBDENUM SPECIES

The UV-Visible spectroscopy of the co-impregnated CoMoP(5)+TEG(CI) catalyst (Figure VI-6) revealed the same features as the dried CoMoP(5d) catalyst: a shoulder at 468 and 523 nm (cobalt hexaaquo complex), a band at 557 nm ($\text{PCoMo}_{11}\text{O}_{40}^{7-}$) and a broad band in the 600-900 nm region (reduced Keggin HPA). In this particular case, the relative intensity of the reduced compound increases when compared to the only dried catalyst and it does not disappear, in opposition to the CoMoP(5d)+TEG catalyst.

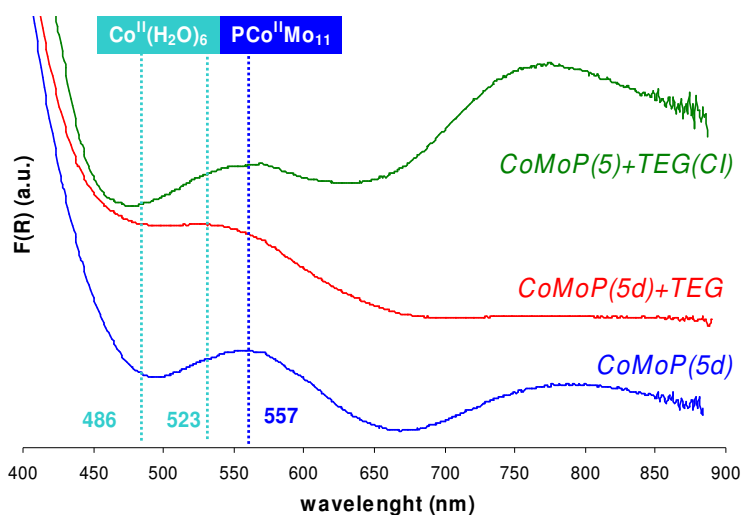


Figure VI-6: UV-Visible diffuse reflectance spectra of CoMoP(5d), CoMoP(5d)+TEG and co-impregnated CoMoP(5)+TEG(Cl) catalysts.

Cobalt speciation indicates that the co-impregnation limits the disintegration of the surface species: reduced Keggin and $\text{PCoMo}_{11}\text{O}_{40}^{7-}$ HPAs. A similar result was observed for pre-impregnated catalysts.

The Raman spectrum reveals the formation of the Anderson $\text{AlMo}_6\text{O}_{24}\text{H}_6^{3-}$ HPA (952 nm) and the substituted Keggin $\text{PCoMo}_{11}\text{O}_{40}^{7-}$ HPA (971 cm^{-1}) HPAs. Moreover, the wide band at 944 cm^{-1} and the shoulder at about 890 nm also indicates the presence of $\text{P}_2\text{Mo}_5\text{O}_{23}^{6-}$ (Figure VI-7). As observed in the pre-impregnated CoMoP(5)+TEG(PI) case, the relative proportion of the $\text{PCoMo}_{11}\text{O}_{40}^{7-}$ band also increases when compared to other additive-containing CoMoP(5) catalysts.

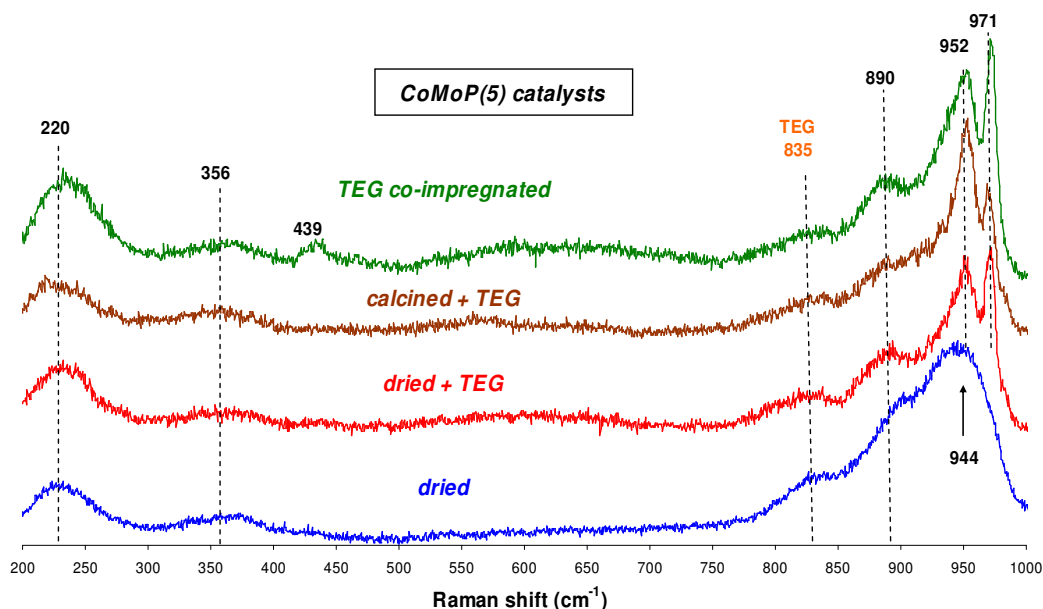


Figure VI-7: Raman spectra of additive-containing CoMoP(5) catalysts.

TEG prevents the HPA direct interaction with the alumina support and thus prevents their disintegration, besides inducing the formation of Anderson $\text{AlMo}_6\text{O}_{24}\text{H}_6^{3-}$ HPA.

VI.3.2. METALS AND PHOSPHORUS DISTRIBUTION

Electronic probe microanalysis (EPMA) is conducted on the co-impregnated catalysts to determine how the elements are distributed inside the catalysts body.

The co-impregnated CoMoP(5)+TEG(CI) catalyst (Figure VI-8) exhibits a homogeneous metal distribution: the molybdenum, cobalt and aluminium distribution coefficients determined by EPMA are close to 1.00. This is not the case of phosphorus, where an eggshell profile is observed: the EPMA revealed a phosphorus distribution coefficient of 0.81.

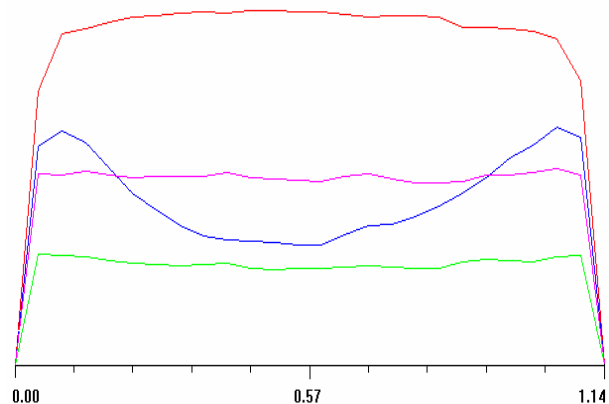
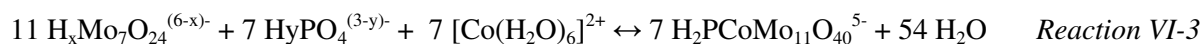


Figure VI-8: Electron Probe Microanalysis of the CoMoP(5)+TEG(CI) catalyst.

The phosphorus distribution in the co-impregnated CoMoP(5) catalyst is similar to that of the pre-impregnated CoMoP(5) catalyst ($R(P)=0.81$). Based on the surface speciation results and as proposed for the pre-impregnated catalysts, the free phosphate groups tend to react with molybdates resulting from the diphosphopentamolybdate HPA decomposition to form $\text{PCoMo}_{11}\text{O}_{40}^{7-}$ entities (Reaction VI-3 [3]) that precipitate, leading to phosphorus fixation.



To study the impact of the additive loading on the phosphorus distribution, a series of TEG co-impregnated CoMoP(5) catalysts with different additive loadings was prepared and characterized by EPMA. The experimental results show that the metals distribution is still flat ($R=1$) and a correlation is found between the TEG/Mo ratio and the phosphorus dispersion coefficient (Figure VI-9): increasing amounts of TEG lead to more accentuated eggshell profiles.

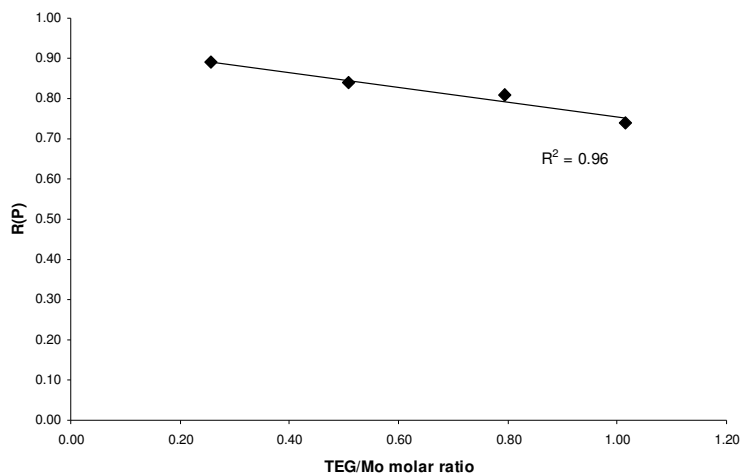


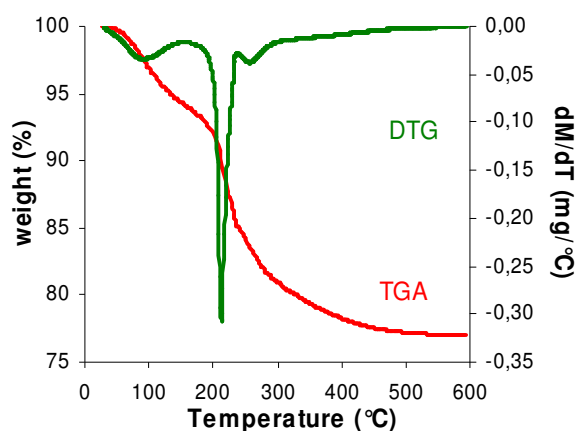
Figure VI-9: EPMA phosphorus dispersion coefficient $R(P)$ as a function of the TEG/Mo molar ratio in CoMoP(5)+TEG(CI) catalysts.

UV-Visible and Raman spectroscopies allow determining the impact of increasing amounts of the additive on the surface species and therefore to infer about the proposed mechanism of $\text{PCoMo}_{11}\text{O}_{40}^{7-}$ fixation. Moreover, EPMA conducted on other series of CoMoP catalysts with different P/Mo ratios may also bring light to this particular aspect.

Another approach to explain this eggshell profile is related to the impregnation solution viscosity. TEG has a relatively elevated viscosity (48 cP at room temperature) and consequently, concentrated TEG solutions become viscous. Because of this, the solution has more difficulty to penetrate into the alumina porosity and the species transport is necessarily slower. However, the flat distribution profiles exhibited by the metal elements, even at high TEG loadings, indicate that the viscosity is not the main effect in this case.

VI.3.3. THERMAL STABILITY

Thermogravimetric analysis (TGA) is carried out to study the thermal stability of the deposited species in the CoMoP(5) catalyst prepared using co-impregnation. In this case, the TEG/Mo molar ratio on the catalyst was 1.0.



The CoMoP(5)+TEG(CI) catalyst revealed a total loss of 23.0 wt% with three DTG local minima at about 100, 215 and 260 °C (Figure VI-10). The mass spectroscopy shows two major emissions of water and CO_2 starting at about 200 °C (not shown here). Traces of mass fragments m/z 12 (carbon-type) and 58 (ketone-type) were also detected.

Figure VI-10: Thermogravimetric analysis (TGA) and derivative thermogravimetry (DTG) of the CoMoP(5)+TEG(CI) catalyst.

As previously, to obtain further information about the thermal stability of the catalyst, the DTG decomposition method described in Appendix C is used. For the sake of simplicity, the decomposition plots are inverted.

The DTG decomposition of the co-impregnated CoMoP(5)+TEG(CI) catalyst (Figure VI-11) shows the water removal at about 93 °C (6.0 wt%) and four TEG decomposition and removal contributions (214, 260, 311 and 370 °C), corresponding to weight losses of 10.8, 2.6, 1.9 and 1.7 wt%, respectively. The sum of the TEG decomposition curves equals 17.0 wt% against 14.6 wt% TEG determined by carbon quantification using CHNS elemental analysts. This difference may be assigned to coordination and constitution water of the existing HPAs, which leave the catalyst at about 150 °C and 300 °C, respectively.

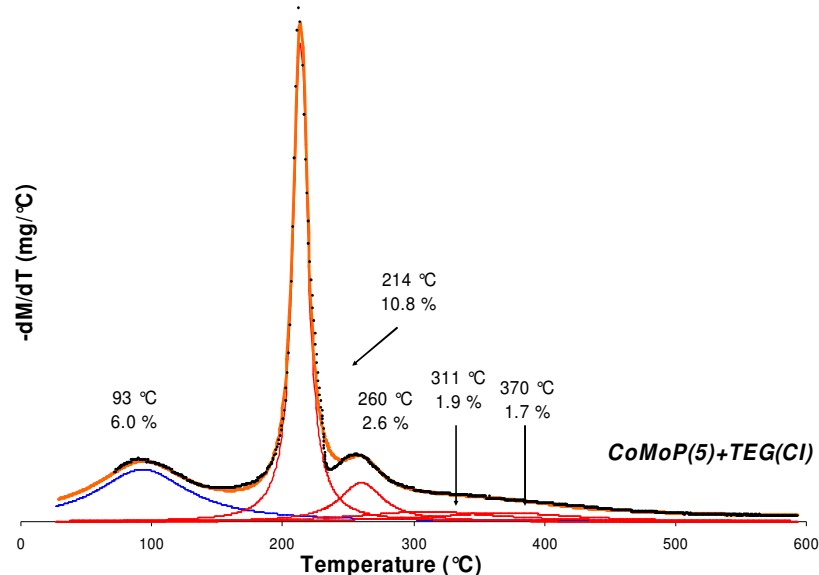


Figure VI-11: TEG co- or sequentially-impregnated CoMoP(5) DTG decomposition curves.

VI.4. SURFACE MECHANISM

The surface mechanism is almost identical to that proposed for TEG pre-impregnated catalysts. When the additive is impregnated simultaneously with CoMo(P) precursors on alumina, it forms a surface layer on the alumina support. The HPA of the solution deposit on this additive layer and the interactions between the alumina surface groups and the HPAs are limited. Consequently, the disintegration of these species is prevented. Moreover, like for all the additive-containing species, Anderson and substituted Keggin HPA species (if the P/Mo molar ratio is superior to 2/5) lead to improved metal dispersion.

The surface mechanism of the CoMoP(5)+TEG(CI) catalyst is represented in Figure VI-12. The precursor solution is mainly composed of $\text{P}_2\text{Mo}_5\text{O}_{23}^{5-}$, $[\text{Co}(\text{H}_2\text{O})_6]^{2+}$, $\text{PCoMo}_{11}\text{O}_{40}^{7-}$ and free phosphate groups. Upon impregnation, the $\text{PCoMo}_{11}\text{O}_{40}^{7-}$ and portion of the $\text{P}_2\text{Mo}_5\text{O}_{23}^{5-}$ HPA deposit intact. The other portion of this HPAs is disintegrated to form molybdates and phosphate groups. Molybdates species then react with the Al^{3+} ions (alumina dissolution) to form $\text{AlMo}_6\text{O}_{24}\text{H}_6^{3-}$ species. Moreover, molybdates and phosphate groups also react to form more $\text{PCoMo}_{11}\text{O}_{40}^{7-}$ HPAs. Improved metal dispersion is thus achieved. Finally, the remaining phosphate groups adsorb as polyphosphates in presence of TEG, as shown by the ^{31}P NMR study in Chapter III.

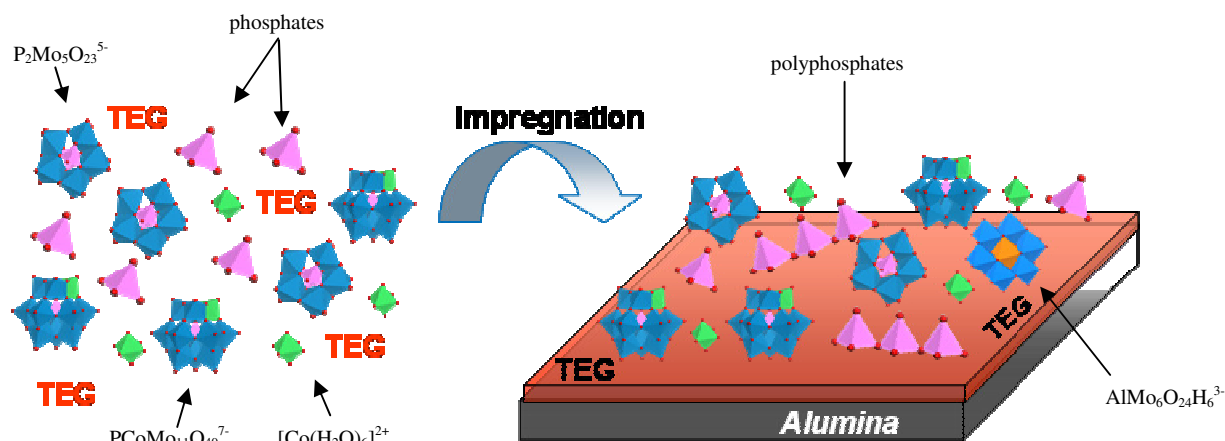


Figure VI-12: Schematic representation of the surface mechanism for the CoMoP(5)+TEG(CI) catalyst.

VI.5. CHAPTER CONCLUSIONS

Concerning the impact of TEG on the solution speciation, no major modifications are observed in solution prior to or after glycol introduction. The role of the additive on the catalysts prepared by co-impregnation is similar to that observed on the pre-impregnated alumina: the solution HPAs decomposition is limited due to the existence of an additive physisorbed layer deposited on the alumina surface. In this way, the interaction between the initial HPA species in solution and the alumina surface sites is prevented. The alumina dissolution is also limited: the formation of $\text{AlMo}_6\text{O}_{24}\text{H}_6^{3-}$ species is observed but it occurs to a lesser extent when compared to the catalysts sequentially impregnated with TEG. Moreover, enhanced metal dispersion is achieved by formation of $\text{PCoMo}_{11}\text{O}_{40}^{7-}$ HPAs when the P/Mo ratio is superior to 2/5.

Key-points

1. No significant modifications are induced by the additive in the impregnation solution.
2. The additive leads to the formation of $\text{AlMo}_6\text{O}_{24}\text{H}_6^{3-}$ and in addition, $\text{PCoMo}_{11}\text{O}_{40}^{7-}$ when the P/Mo molar ratio is superior to 2/5.
3. The additive pre-impregnation increases the proportion of $\text{PCoMo}_{11}\text{O}_{40}^{7-}$ with respects to $\text{AlMo}_6\text{O}_{24}\text{H}_6^{3-}$ compared to the additive impregnation on dried and calcined catalysts.
4. The additive is deposited on alumina and forms a layer between the active phase precursors and alumina. In this way, the decomposition of the solution heteropolyanions is limited.

VI.6. BIBLIOGRAPHIC REFERENCES

- 1 A. Griboval, P. Blanchard, L. Gengembre, E. Payen, M. Fournier, J.L. Dubois and J.R. Bernard, J. Catal. 188, 102, **1999**.
- 2 A. Griboval, Ph.D. thesis, Université des Sciences et Technologies de Lille, **1998**.
- 3 J.A. Bergwerff, L.G.A. van der Water, T. Wissner, P. de Peinder B.R.G. Leliveld, K.P. de Jong and B.M. Weckhuysen, Chem. Eur. J. 11, 4591, **2005**.
- 4 J.A.R. van Veen, O. Sudmeijer, C.A. Emeis and H. de Wit, J. Chem. Soc. Dalton Trans. 1825, **1986**.
- 5 L. Pattersson, I. Andersson and L.O. Ohman, Inorg. Chem. 25, 4726, **1986**.
- 6 L.E. Briand, G.M. Valle and H.J. Thomas, J. Mater. Chem. 12, 299, **2002**.

CHAPTER VII: IMPACT OF THE ADDITIVE ON THE ACTIVATION STAGE AND EVALUATION OF CATALYTIC PERFORMANCES

VII.1. Introduction	195
VII.2. Impact of the additive on sulfided catalysts	195
VII.2.1. Influence of the additive on the final sulfided state (<i>ex situ</i> sulfidation)	195
VII.2.1.1. Influence of the additive on cobalt structure	196
VII.2.1.2. Influence of the additive on molybdenum structure	202
VII.2.1.3. Influence of the additive on the active phase morphology.....	208
VII.2.2. Influence of the additive during the sulfidation stage (<i>in situ</i> sulfidation)	210
VII.2.2.1. Influence of the additive on cobalt structure	210
VII.2.2.2. Influence of the additive on molybdenum structure	213
VII.2.3. Conclusion on the additive impact on the sulfidation stage	216
VII.3. Impact of the additive on catalytic performances	216
VII.3.1. Hydrogenation and isomerization reactions	217
VII.3.1.1. Screening of additive-free dried and calcined CoMo(P) catalysts	217
VII.3.1.2. Influence of the additive on the hydrogenation and isomerization catalytic performances of dried and calcined catalysts.....	218
VII.3.1.3. Influence of the additive impregnation step location on the catalytic activity.....	220
VII.3.1.4. Influence of the additive loading on the catalytic activity	222
VII.3.2. Hydrodesulfurization reaction	223
VII.3.3. Conclusion on the additive impact on the catalytic tests	224
VII.4. Chapter conclusion.....	225
VII.5. Bibliographic references	226

CHAPTER VII: IMPACT OF THE ADDITIVE ON THE ACTIVATION STAGE AND EVALUATION OF CATALYTIC PERFORMANCES

VII.1. INTRODUCTION

The previous chapters were dedicated to the study of the active phase precursor phases and how they are affected by the additive prior to the activation stage. This allowed establishing that glycol-type additives act as a solvent and favor the formation of heteropolyanions. In this way, improved metals dispersion is achieved, mainly due to hexamolybdoaluminates formation and also phosphomolybdates when the P/Mo molar ratio is superior to 2/5.

The study of sulfidation stage as well as the catalytic performances will allow determining the impact of these additive-induced modifications and more precisely the impact of improved metals dispersion.

VII.2. IMPACT OF THE ADDITIVE ON SULFIDED CATALYSTS

As discussed in the bibliographic chapter, the additives play an important role during the activation stage by modifying the sulfidation mechanism but lead to the same final sulfided state. However, controversial explanations about the sulfidation mechanism in the literature.

This was the motivation to study the final catalysts state after sulfidation in presence or absence of the additive as well as the activation stage. For this purpose, gas-phase activation procedures were conducted *ex situ* on the prepared catalysts and characterized at the final state in terms of structure and morphology. In addition, an EXAFS *in situ* gas phase sulfidation follow-up provided important structural information concerning the role of the additive during the activation stage.

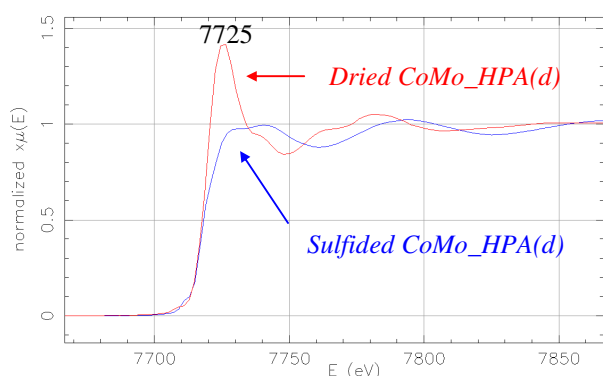
VII.2.1. INFLUENCE OF THE ADDITIVE ON THE FINAL SULFIDED STATE (*EX SITU* SULFIDATION)

To determine if the additive modifies the final sulfided state of the CoMo(P) catalysts, the cobalt and molybdenum structures are characterized after sulfidation, as well as the active phase morphology. For this purpose, the prepared catalysts were sulfided *ex situ* using a 15% H₂S/H₂ gas mixture at 400 °C for 2 hours and afterwards sealed in a vacuum container. XAS, XPS and TEM characterizations were then conducted. The experimental facilities and conditions are described in Chapter II.

VII.2.1.1. Influence of the additive on cobalt structure

The influence of the additive is determined by describing the cobalt structure after the activation stage in presence or in absence of the additive. In this sense, XAS and XPS analysis are carried out on sulfided catalysts.

The cobalt K-edge XANES spectrum of the sulfided CoMo_HPA(d) catalyst reveals that the white line feature observed at about 7725 eV, visible in the fresh dried sample, has disappeared (Figure VII-1). Indeed, cobalt in the oxide form presents a strong white line due to Co(1s)→Co(4p) transition, whereas in the sulfided state the white line disappears [1,2,3].



All sulfided samples with or without additive impregnation exhibit similar near edge spectra (Figure VII-1). This means that the additive induces no significant modifications on the final sulfided state of different catalysts formulations in terms of average geometry and oxidation state.

Figure VII-1: Normalized Co K-edge XANES spectra of the dried CoMo_HPA(d) and corresponding *ex situ* sulfided catalyst.

The k^3 -weighted Fourier Transforms (FT) modulus of the cobalt K-edge EXAFS show a broad signal between about 1 and 2 Å (not phase corrected) for all sulfided dried catalysts (Figure VII-2), which is due to a Co-S contribution. No significant change is observed after additive impregnation.

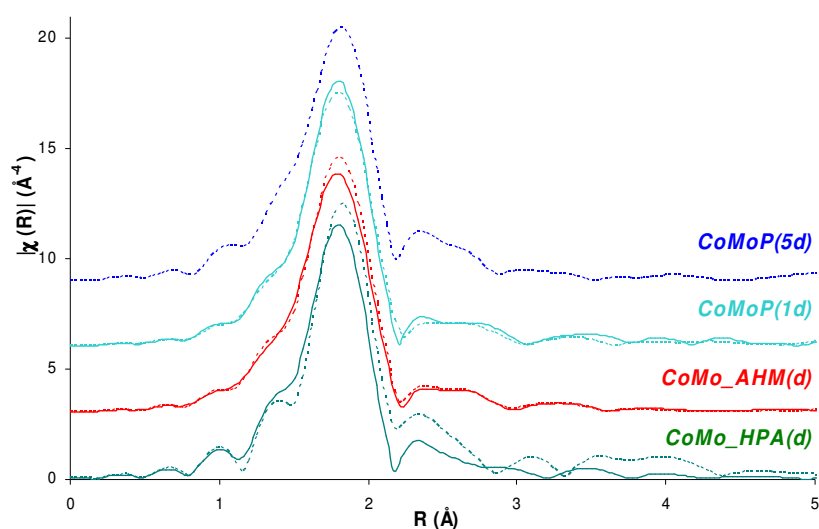


Figure VII-2: Co K-edge k^3 -weighted EXAFS Fourier Transforms modulus of sulfided dried CoMo(P) (— solid lines) and corresponding TEG-containing catalysts (--- dashed lines). FT Hanning window from 3 to 13 Å⁻¹ except for the CoMo_HPA(d)+TEG sample (3 to 9 Å⁻¹); $\tau=2.5$.

In order to estimate locally the extent of cobalt sulfidation as well as the modifications according to the catalyst formulation or additive presence, the structural parameters were fitted (Table VII-1 and Table VII-2). The fitting revealed that a single Co-S contribution is enough to simulate the first coordination sphere of the experimental spectra. As an example, the filtered EXAFS and corresponding FT modulus of the CoMo_HPA(d) sample fitting are plotted in Figure VII-3.

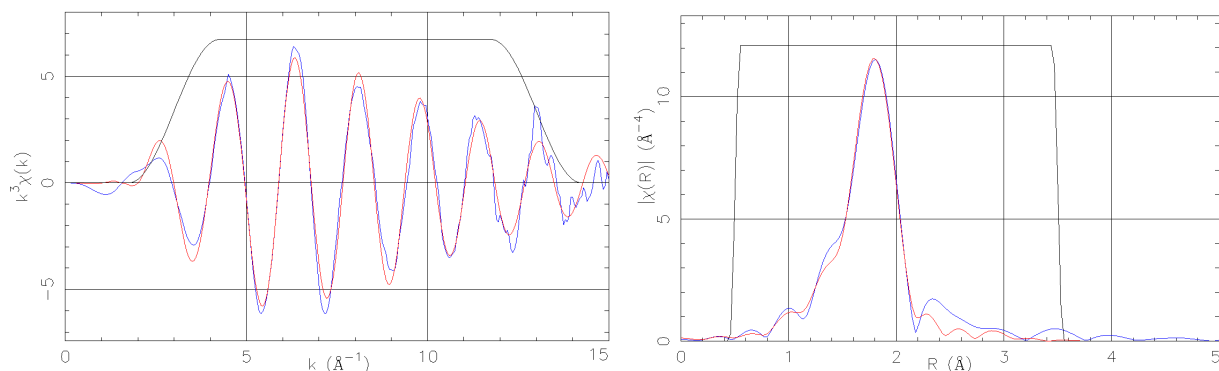


Figure VII-3: Co K-edge k^3 -weighted filtered EXAFS signal (left) and corresponding Fourier Transforms modulus (right) of CoMo_HPA(d) catalyst. FT Hanning window from 3 to 13 \AA^{-1} , inverse FT window from 0.5 to 3.5 \AA ; $\tau = 2.5$. Blue: experimental signal, red: fitted signal, green: extraction window.

EXAFS fitting leads to a constant Co-S bond length of 2.21 \AA for all samples. Concerning the coordination environment, the calculated number of sulfur neighbors ranges from 2.8 to 3.2, excluding the CoMo_HPA(d)+TEG sample that due to the poor quality of the raw data forced a narrower FT extraction and consequently a FT modulus peak amplitude loss. No significant differences in the cobalt coordination sphere are observed in presence of the additive.

Table VII-1: Structural parameters resulting from the Co K-edge Fourier-filtered k^3 -weighed EXAFS functions of the ex situ sulfided additive-free dried catalysts ($\Delta R = 0.5\text{--}3.5 \text{\AA}$).

	CoMo_HPA(d)	CoMo_AHM(d)	CoMoP(1d)
$N_{\text{Co-S}}$	2.8	3.3	3.2
$R_{\text{Co-S}} (\text{\AA})$	2.21	2.21	2.21
$10^3 \cdot \Delta\sigma^2 (\text{\AA}^2)$	4.6	6.2	5.3
$\Delta E_0 (\text{eV})$	-2.7	-2.2	-1.6

Table VII-2: Structural parameters resulting from the Co K-edge Fourier-filtered k^3 -weighed EXAFS functions of the ex situ sulfided additive-containing dried catalysts ($\Delta R = 0.5\text{--}3.5 \text{\AA}$).

	CoMo_HPA(d)+TEG	CoMo_AHM(d)+TEG	CoMoP(1d)+TEG	CoMoP(5d)+TEG
$N_{\text{Co-S}}$	2.0	3.2	3.2	3.1
$R_{\text{Co-S}} (\text{\AA})$	2.21	2.21	2.21	2.21
$10^3 \cdot \Delta\sigma^2 (\text{\AA}^2)$	1.5	5.7	5.7	5.3
$\Delta E_0 (\text{eV})$	-1.7	-1.2	-1.2	-3.5

The calculated Co-S bond length of 2.21 Å is assigned to the presence of bulk Co₉S₈ and cobalt in decoration of MoS₂ structures. Indeed, Bouwens *et al.* [4] determined the same Co-S distance for pure Co₉S₈ and for the phase. Several authors report experimental Co-S distances in sulfided CoMo catalysts between 2.19 and 2.23 Å [1,4,5,6].

To study further the nature of the different cobalt phases formed during sulfidation, all samples were analyzed using XPS. After acquisition, the cobalt 2p raw spectra were decomposed into Co(II) in oxygen environment, Co₉S₈ and "CoMoS" contributions, each one associated to 2 main peaks (2p_{3/2} and 2p_{1/2}) that are correlated with smaller satellite peaks, as shown in Figure VII-4. The position of the main decomposition peaks is summarized in Table VII-3.

Table VII-3: XPS parameters used for the Co2p spectra decomposition of sulfided samples.

Phase	Contribution	Binding energy (eV)
Co(II)	Co2p _{3/2}	781.5
	Co2p _{1/2}	797.3
Co ₉ S ₈	Co2p _{3/2}	778.1
	Co2p _{1/2}	793.2
"CoMoS"	Co2p _{3/2}	778.6
	Co2p _{1/2}	793.5

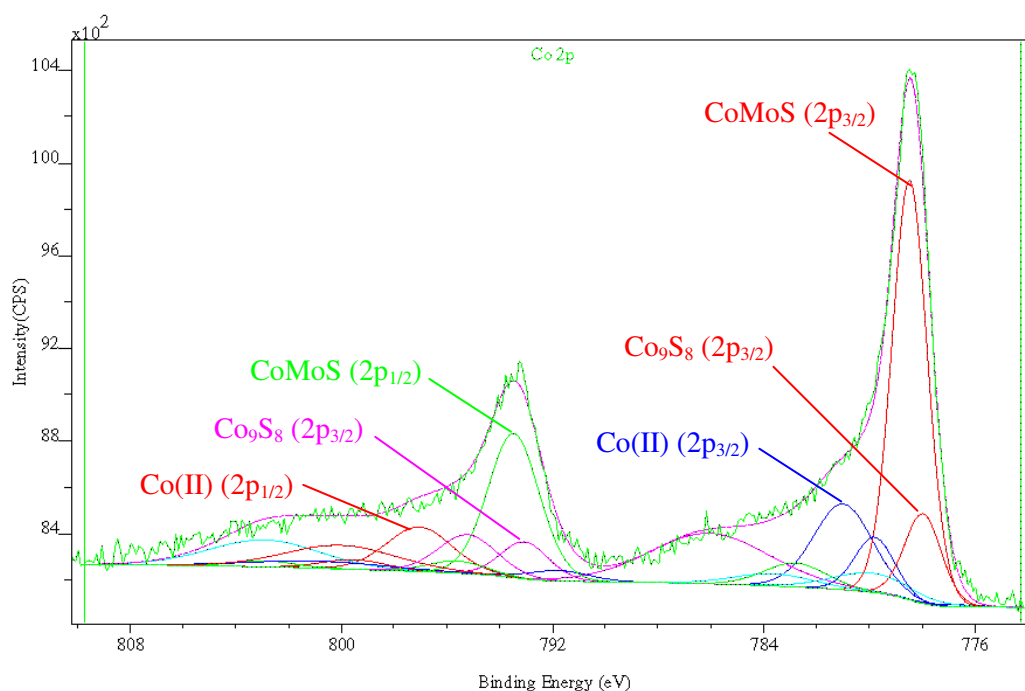


Figure VII-4: Cobalt 2p XPS spectrum decomposition of the sulfided CoMoP(5d) catalyst.

This methodology allows quantifying the amount of cobalt atoms participating in each phase [7]. The results presented in Figure VII-5 show that the Co species distribution is strongly dependant of the

catalyst formulation. The phase yield (or promotion ratio) ranges from 20 to 58%, while the oxide phase quantities are relatively constant, corresponding to about 30%.

The additive-free samples containing a P/Mo molar ratio equal or superior to 2/5 exhibit the highest promotion ratios (superior to 50%). The CoMo_HPA(d) catalyst occupies the second place in the promotion ratio hierarchy (about 40%). Finally, the CoMoP(1d) and CoMo_AHM(d) samples have rather similar phase distributions (promotion ratio between 20 and 25%).

The additive impregnation leads to an important increase in promotion ratios except for the cases where this ratio is already elevated (variations are within the 5% decomposition method incertitude).

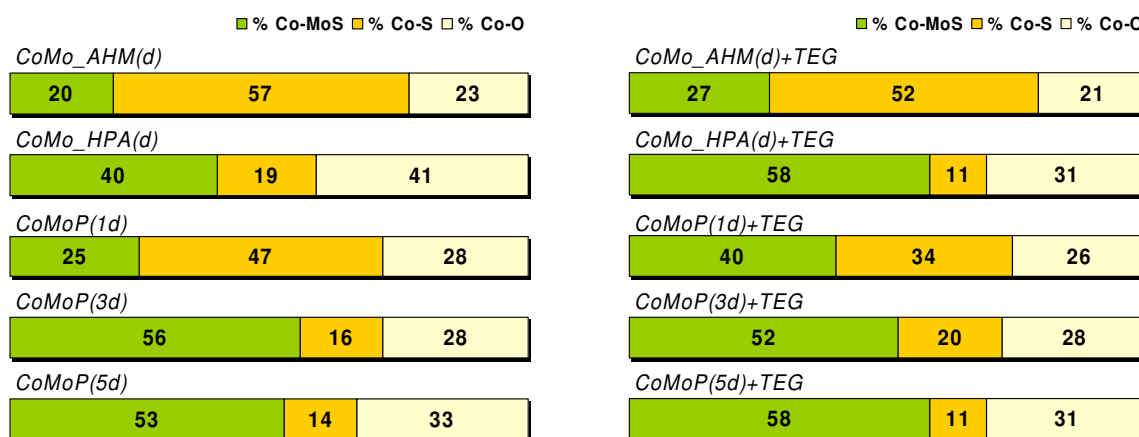


Figure VII-5: Cobalt 2p XPS spectrum decomposition results for additive-free (left) and additive-containing dried CoMo(P) catalysts (right).

The elevated promotion ratio of the CoMoP(3d) and CoMoP(5d) catalysts is explained by the presence of $\text{Co}_3[\text{P}_2\text{Mo}_5\text{O}_{23}]$ and $\text{Co}_{7/2}[\text{PCoMo}_{11}\text{O}_{40}]$ heteropolycompounds before sulfidation, as deduced by Raman, UV-Visible and NMR spectroscopies. These heteropolycompounds appear as an efficient precursor for the "CoMoS" phase formation. In the case of the CoMo_HPA(d) catalysts, the promoter and molybdenum atoms are in close proximity in the molybdocobaltate HPAs and therefore enhance the "CoMoS" phase formation. The fact that the CoMoP(1d) and CoMo_AHM(d) catalysts exhibit similar promotion ratios reinforces the idea that this ratio is strongly associated to the nature of the deposited species before sulfidation, since both catalysts are mainly constituted of Anderson hexamolybdoaluminate HPAs. However, the AHM-based has the lowest promotion ratio and the highest Co_9S_8 relative amount. This appears to be a consequence of the double impregnation method used, leading to poor metals dispersion. Moreover, the presence of nitrate ions favors the formation of Co_9S_8 instead of "CoMoS" phase formation.

The gains in promotion ratio after additive impregnation are correlated with losses in the Co_9S_8 proportion. The redissolution/reprecipitation mechanism proposed in Chapter III provides a plausible explanation for this promotion enhancement: the metal components are redispersed and therefore the overall Co-Mo proximity is optimized. The fact that Co_9S_8 amount decreases supports this idea.

In terms of calcined catalysts, the sulfidation stage leads to the same XANES features (not shown here) than the sulfided dried catalysts. The white line observed in fresh catalysts disappears, indicating that cobalt atoms are mainly in a sulfided state. No significant modifications are observed after TEG impregnation. The same observations are also valid for the EXAFS spectra: all samples give rise to similar features even when the additive is present (Figure VII-6).

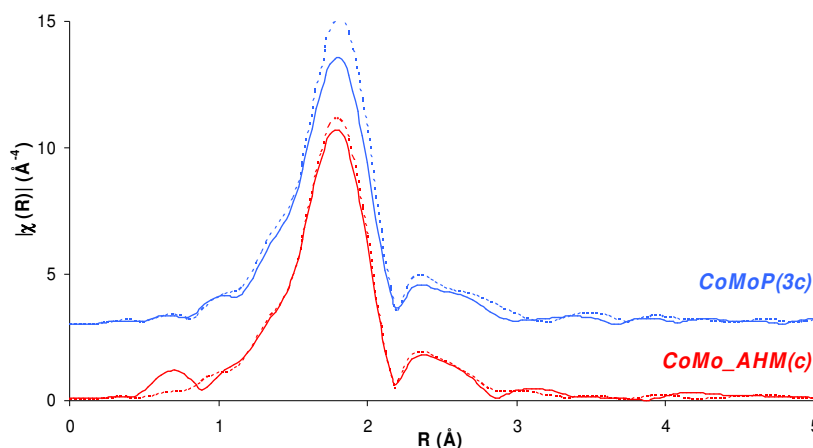


Figure VII-6: Cobalt K-edge k^3 -weighted EXAFS Fourier Transforms of sulfided calcined CoMo(P) catalysts (— solid lines) and corresponding TEG-containing catalysts (--- dashed lines). FT Hanning window from 3 to 13 \AA^{-1} ; $\tau=2.5$.

The structural parameters were fitted (Table VII-4): like the dried samples, a single Co-S contribution is enough to simulate the first coordination sphere of the experimental spectra. Moreover, the fitting reveals the same Co-S coordination distance of about 2.21 \AA for all samples and the number of sulfur neighbors ranges from 2.8 to 3.1. Therefore, according to X-ray absorption measurements, all dried and calcined samples have the same average cobalt environment.

Table VII-4: Structural parameters resulting from the Co K-edge Fourier-filtered k^3 -weighted EXAFS functions of the ex situ sulfided calcined catalysts ($\Delta R=0.5\text{-}3.5 \text{ \AA}$).

	CoMo_AHM(c)	CoMoP(3c)
$N_{\text{Co-S}}$	2.9	2.8
$R_{\text{Co-S}} (\text{\AA})$	2.20	2.21
$10^3 \Delta\sigma^2 (\text{\AA}^2)$	5.2	5.2
$\Delta E_0 (\text{eV})$	-6.0	-3.6
	CoMo_AHM(c)+TEG	CoMoP(3c)+TEG
$N_{\text{Co-S}}$	2.9	3.1
$R_{\text{Co-S}} (\text{\AA})$	2.20	2.21
$10^3 \Delta\sigma^2 (\text{\AA}^2)$	5.1	5.0
$\Delta E_0 (\text{eV})$	-3.7	-1.4

A more precise picture of the sulfidation may be achieved through XPS analysis. Using the decomposition described in the case of the sulfided dried catalysts, the cobalt species distribution is determined (Figure VII-7): cobalt atoms participating in the phase range from 35 to 57%, while the

oxide phases are relatively constant, corresponding to about 30%. Moreover, all additive-free samples except the CoMoP(1c) exhibit a promotion ratio superior to 50%. It should be noticed that for the particular case of the AHM-based catalyst, a dramatic increase in promotion is observed after calcination: from 20% on the dried catalyst to 51% on the calcined catalyst.

As for the dried catalysts, the promotion ratios are improved after additive impregnation except when the samples already have a good promotion ratio (superior to 50%). However, this is not the case for the CoMo_HPA(c) catalyst where a 14% loss is observed, mainly in favor of Co₉S₈ species.

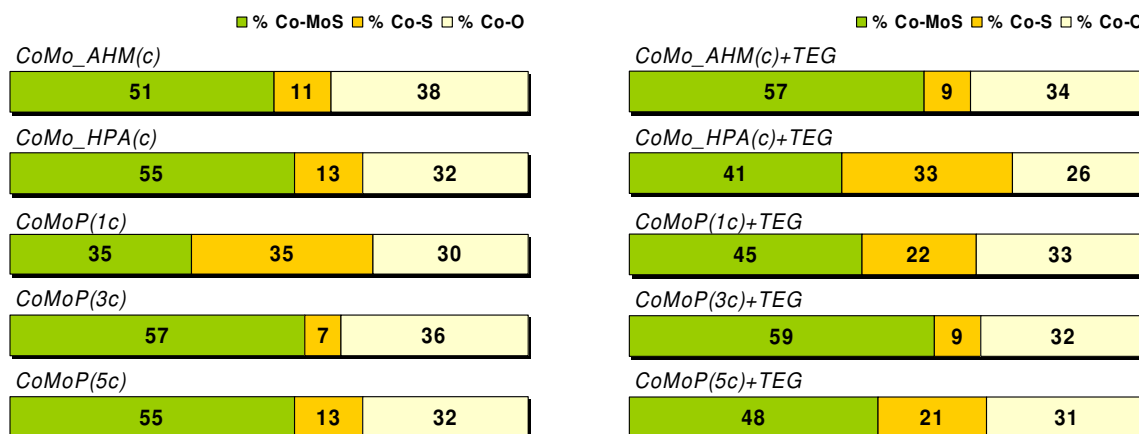


Figure VII-7: Cobalt 2p XPS spectrum decomposition results for additive-free (left) and additive-containing calcined CoMo(P) catalysts (right).

The increase of the promotion ratio in the CoMo_AHM sample after calcination shows that the presence of nitrogen-containing ions, which are destroyed during the calcination stage (as shown by Raman spectroscopy and TGA), inhibits the phase formation. Concerning the inferior promotion ratio shown by the CoMoP(1c) catalyst, it seems related to the amount of Co₉S₈ formed, which is the highest for calcined catalysts. This suggests that molybdenum and cobalt atoms are not in close proximity. Since the CoMo_AHM(c) sample exhibited similar surface species before calcination (mainly Anderson HPAs) than the CoMoP(1c) sample and also after calcination (ill-defined polyoxomolybdates), it may be concluded that the nature of the active phase precursors is not the reason behind this low promotion ratio. A possible explanation may be related to phosphorus eggshell profile observed in EPMA, leading to limited metals dispersion.

The decrease on the phase yield observed after additivation of the CoMo_HPA(c) catalyst is related to the redispersion mechanism: molybdenum atoms are redispersed via AlMo₆O₂₄H₆³⁻ formation, but the close Co-Mo vicinity inherited from the molybdocobaltate HPAs is degraded. As a consequence, the beneficial effect of these starting HPA precursors is lost, leading to lower promotion ratios. For the CoMoP(1c) case, the "CoMoS" phase yield of this catalyst is strongly improved after additive impregnation. This may be a consequence of the phosphorus distribution coefficient improvement which increases from 0.74 to 0.93 after additive impregnation (*cf.* section IV.4.3).

VII.2.1.2. Influence of the additive on molybdenum structure

The influence of the additive is determined by describing the molybdenum structure after the activation stage in presence or in absence of the additive. In this sense, XAS and XPS analysis are carried out on sulfided catalysts.

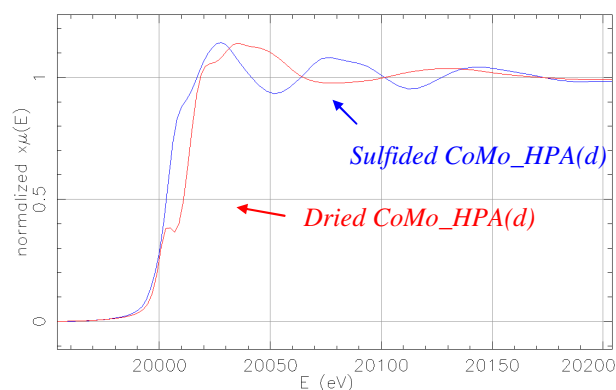


Figure VII-8: Normalized Mo K-edge XANES spectra of the dried CoMo_HPA(d) and corresponding *ex situ* sulfided catalyst.

The molybdenum K-edge XANES spectra of the sulfided dried catalysts show the absence of a pre-edge peak in all cases (for example, CoMo_HPA(d) in Figure VII-8): during sulfidation Mo(VI) species are replaced by Mo(IV) species. This means that the majority of Mo is in a sulfided state, as MoS₂ [8].

Two major bands are visible in the FT modulus of the k^3 -weighted Mo K-edge EXAFS of dried catalysts sulfided *ex situ* (Figure VII-9). A first impression is that all spectra are equivalent, even when the additive is present.

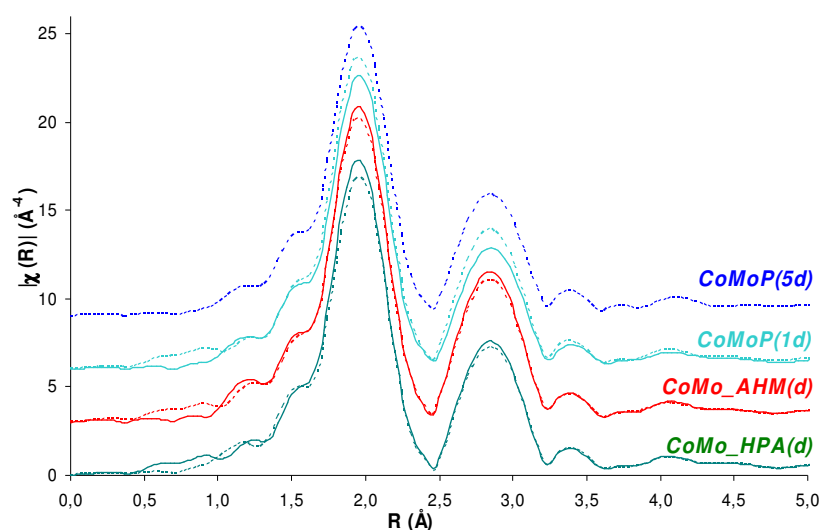


Figure VII-9: Mo K-edge k^3 -weighted EXAFS Fourier Transforms of sulfided dried CoMo(P) (— solid lines) and corresponding TEG-containing catalysts (--- dashed lines).
FT Hanning window from 2.5 to 13.5 Å⁻¹; $\tau=2.5$.

In order to locally estimate the extent of the sulfidation, as well as the modifications induced by the catalyst formulation or additive presence, the structural parameters are fitted (Table VII-5 and Table VII-6). The fitting reveals that a single Mo-S contribution is enough to simulate the first coordination shell. The second shell is also successfully fitted only using a single Mo-Mo contribution. For example, the filtered EXAFS and corresponding FT modulus of the CoMo_HPA(d) sample fitting are plotted in Figure VII-10.

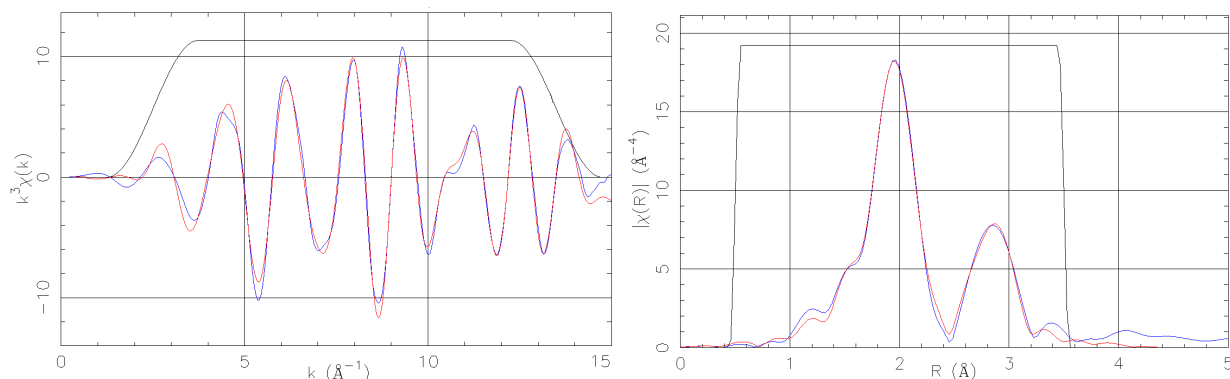


Figure VII-10: Mo K-edge k^3 -weighted filtered EXAFS signal (left) and corresponding Fourier Transforms modulus (right) of CoMo_HPA(d) catalyst. FT Hanning window from 2.5 to 13.5 \AA^{-1} , inverse FT window from 0.5 to 3.5 \AA ; $\tau = 2.5$. Blue: experimental signal, red: fitted signal, green: extraction window.

The fitting reveals the same distances of 2.41 \AA and 3.16 \AA for the first (Mo-S) and second (Mo-Mo) coordination shells in all samples. The coordination number in the first shell varies between 5.0 and 5.6, and between 2.8 and 3.4 in the second shell. The EXAFS fitting also revealed similar Debye-Waller factors (σ^2), meaning that the sulfided catalysts have comparable static orders. No significant differences in the molybdenum coordination sphere are observed in presence of the additive.

Table VII-5: Structural parameters resulting from the Mo K-edge Fourier-filtered k^3 -weighed EXAFS functions of the ex situ sulfided additive-free dried catalysts ($\Delta R = 0.5\text{--}3.5 \text{\AA}$).

	CoMo_HPA(d)	CoMo_AHM(d)	CoMoP(1d)
$N_{\text{Mo-S}}$	5.6	5.4	5.1
$R_{\text{Mo-S}} (\text{\AA})$	2.41	2.41	2.41
$10^3 \cdot \Delta\sigma^2 (\text{\AA}^2)$	3.8	3.7	3.8
$\Delta E_0 (\text{eV})$	1.7	1.8	2.7
$N_{\text{Mo-Mo}}$	3.2	3.4	2.9
$R_{\text{Mo-Mo}} (\text{\AA})$	3.16	3.16	3.16
$10^3 \cdot \Delta\sigma^2 (\text{\AA}^2)$	5.0	4.7	5.1
$\Delta E_0 (\text{eV})$	1.3	1.0	1.7

Table VII-6: Structural parameters resulting from the Mo K-edge Fourier-filtered k^3 -weighed EXAFS functions of the ex situ sulfided additive-containing dried catalysts ($\Delta R=0.5-3.5$ Å).

	CoMo_HPA(d)+TEG	CoMo_AHM(d)+TEG	CoMoP(1d)+TEG	CoMoP(5d)+TEG
$N_{\text{Mo-S}}$	5.0	5.2	5.3	5.0
$R_{\text{Mo-S}}$ (Å)	2.41	2.41	2.41	2.41
$10^3 \cdot \Delta\sigma^2$ (Å ²)	3.6	3.8	3.7	3.8
ΔE_0 (eV)	1.9	2.2	1.9	2.2
$N_{\text{Mo-Mo}}$	2.9	3.2	3.2	2.8
$R_{\text{Mo-Mo}}$ (Å)	3.16	3.16	3.16	3.16
$10^3 \cdot \Delta\sigma^2$ (Å ²)	4.8	4.7	4.8	4.9
ΔE_0 (eV)	1.6	1.3	1.0	1.0

The calculated Mo-S and Mo-Mo bond lengths are typical of MoS₂ clusters and are in agreement with data in the literature for sulfided Mo-based catalysts [1,2,6,7,8,9,10]. With respect to the first coordination shell, a full octahedral coordination of 6 sulfur atoms is expected, which is not the case. This indicates that either not all MoS₂ crystallite edges are saturated with sulfur or that some of the molybdenum edge atoms are coordinated to oxygen [2]. Concerning the second coordination shell, the variation of the Mo-Mo coordination number is related to the average MoS₂ crystallite size of each sample. Indeed, molybdenum atoms at the core of the MoS₂ crystallites are surrounded by 6 molybdenum atoms, which is not the case at the edge of the crystallites. As EXAFS data arises from the average of all molybdenum atoms, the Mo-Mo coordination number increases when the average crystallite size increases (the core/edge atoms ratio increases) [10,11].

The XAS analysis is complemented with XPS measurements: an analog decomposition method than that described for cobalt is used [7]. In the case of molybdenum each entity is associated to two contributions: Mo3d_{5/2} and Mo3d_{3/2}. A third contribution is detected in the same region corresponding to sulfur S2s (main peak at 226.5 eV), which has to be considered in order to fully simulate the spectral envelope but is not taken into account in the quantification. Three molybdenum entities are considered: MoS₂, Mo(V) and Mo(IV). The first corresponds to the active phase crystallites where molybdenum is in a 4+ oxidation state, the second corresponds to oxysulfided species MoS_xO_y and the third to residual Mo⁶⁺, arising from non sulfided precursors. Figure VII-11 shows an example of a Mo 3d decomposed spectrum and Table VII-7 summarizes the position of the decomposition peaks.

Table VII-7: XPS parameters used for the Mo3d spectra decomposition of sulfided samples.

Phase	Contribution	Binding energy (eV)
Mo(VI)	Mo3d _{5/2}	232.0
	Mo3d _{3/2}	235.1
Mo(V)	Mo3d _{5/2}	229.8
	Mo3d _{3/2}	232.9
MoS ₂	Mo3d _{5/2}	228.8
	Mo3d _{3/2}	231.9

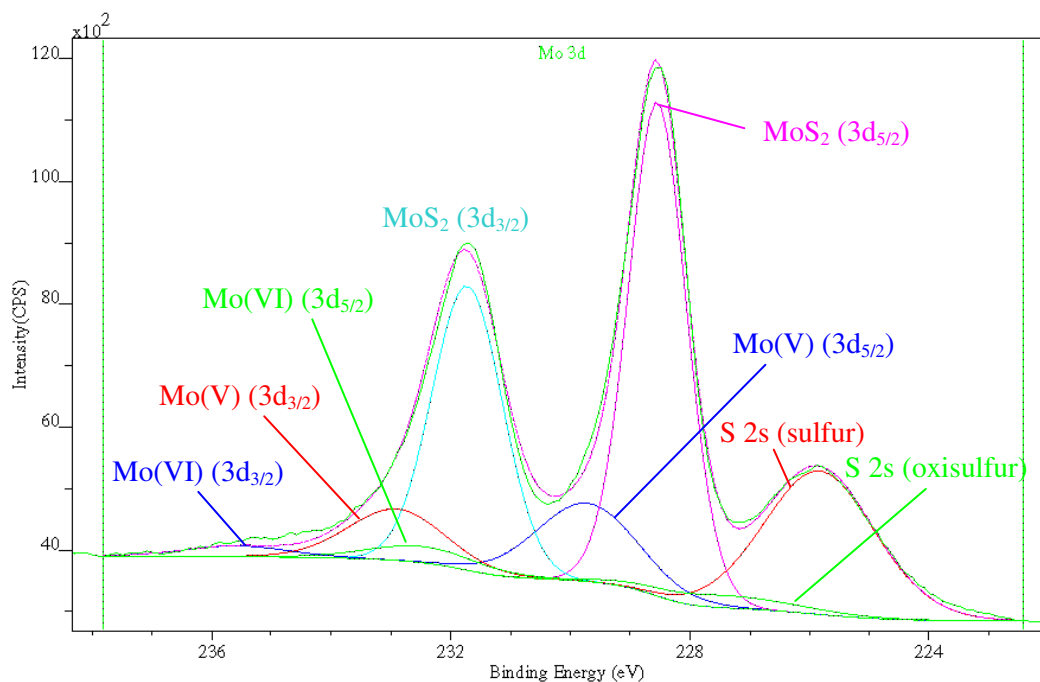


Figure VII-11: Molybdenum 3d XPS spectrum decomposition of the sulfided CoMoP(5d) catalyst.

The Mo 3d spectrum decomposition (Figure VII-12) revealed that most molybdenum atoms are in a sulfided state. Oxy-sulfided compounds, associated to Mo(V) species are also detected corresponding to 10 to 20% of the metal loading. Residual Mo(VI) entities represent less than 10%, except for the CoMo_HPA(d) catalyst. This catalyst shows the lowest Mo sulfidation percentage.

The additive impregnation slightly increases the proportion of MoS₂ species in all catalysts while the proportion of Mo(V) species decreases.

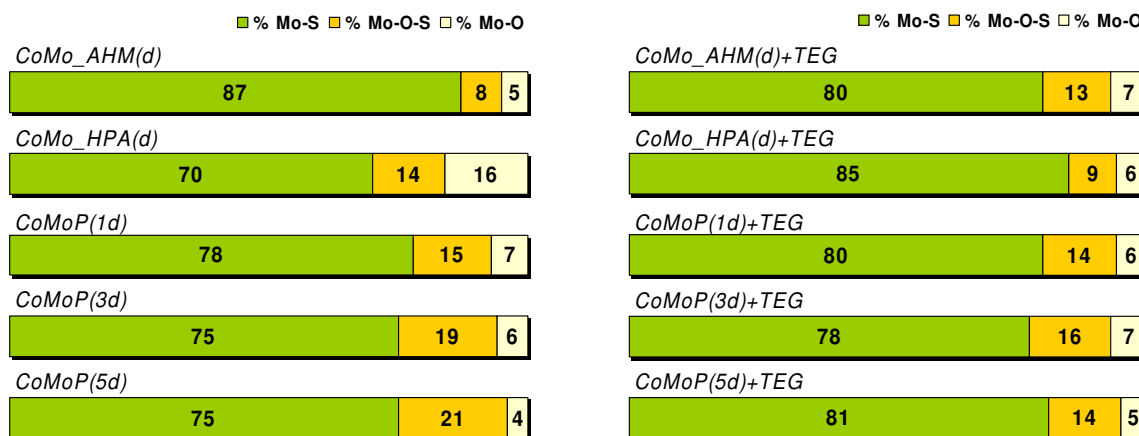


Figure VII-12: Molybdenum 3d XPS spectrum decomposition results for additive-free (left) and additive-containing dried CoMo(P) catalysts (right).

The poor molybdenum sulfidation of the CoMo_HPA(d) sample, as well as the important amount of non sulfided cobalt (40%), may be explained by an insufficient sulfidation of the active phase precursors. Indeed, Raman and UV-Visible spectroscopies show that cobalt and molybdenum are

deposited on the catalyst surface in the same heteropolyanion salts ($\text{Co}_{3/2}[\text{CoMo}_6\text{O}_{24}\text{H}_6]$ and $\text{Co}_3[\text{Co}_2\text{Mo}_{10}\text{O}_{38}\text{H}_4]$). Therefore, insufficient sulfidation of molybdocobaltate salts leads to poor sulfidation of molybdenum and cobalt atoms.

After additive impregnation, the enhanced dispersion via Anderson hexamolybdoaluminates and substituted Keggin HPAs when the P/Mo molar ratio is superior to 0.40 leads to better yields in molybdenum sulfidation. This effect is particularly important in the CoMo_HPA(d) catalyst, where a gain of 15% in MoS_2 phase is attained after additive impregnation: molybdocobaltate HPAs are partially replaced by the molybdoaluminate HPA and as a consequence, molybdenum atoms are better sulfided.

For calcined catalysts, the molybdenum K-edge XANES (not shown here) and EXAFS (Figure VII-13) spectra are rather similar to the only dried catalysts. The k^3 -weighted Fourier Transform modulus of the calcined CoMo_AHM(c) and CoMoP(3c) catalysts exhibit mainly two contributions, between 1.5 and 2.5 Å (Mo-S, not phase corrected) and between 2.5 and 3.3 Å (Mo-Mo, not phase corrected). On a first approach, the additive only induces minor changes to the average local environment of molybdenum.

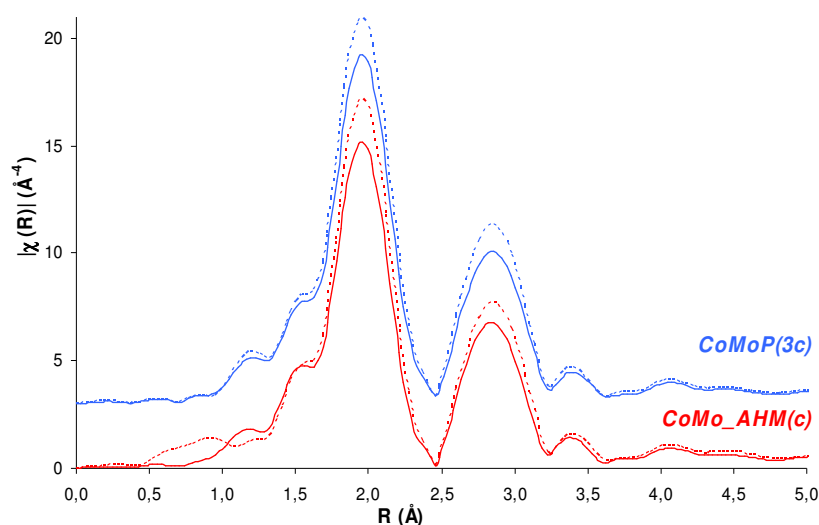


Figure VII-13: Molybdenum K-edge k^3 -weighted EXAFS Fourier Transforms modulus of sulfided calcined CoMo(P) (— solid lines) and corresponding TEG-containing catalysts (--- dashed lines). FT Hanning window from 2.5 to 13.5 Å⁻¹; $\tau=2.5$.

The fitting revealed the same Mo-S and Mo-Mo distances as those found for the dried catalysts: 2.41 and 3.16 Å, respectively (Table VII-8). These distances are typical of a MoS_2 phase. Concerning the coordination number, a small increase is observed after additive impregnation (Table VII-9).

Table VII-8: Structural parameters resulting from the Mo K-edge Fourier-filtred k^3 -weighed EXAFS functions of the ex situ sulfided additive-free calcined catalysts ($\Delta R=0.5-3.5 \text{ \AA}$).

	CoMo_AHM(c)	CoMoP(3c)
$N_{\text{Mo-S}}$	4.7	5.0
$R_{\text{Mo-S}} (\text{\AA})$	2.41	2.41
$10^3 \cdot \Delta\sigma^2 (\text{\AA}^2)$	3.8	3.9
$\Delta E_0 (\text{eV})$	1.1	2.8
$N_{\text{Mo-Mo}}$	2.6	2.8
$R_{\text{Mo-Mo}} (\text{\AA})$	3.16	3.16
$10^3 \cdot \Delta\sigma^2 (\text{\AA}^2)$	4.6	4.8
$\Delta E_0 (\text{eV})$	0.4	1.9

Table VII-9: Structural parameters resulting from the Mo K-edge Fourier-filtred k^3 -weighed EXAFS functions of the ex situ sulfided additive-containing calcined catalysts ($\Delta R=0.5-3.5 \text{ \AA}$).

	CoMo_AHM(c)+TEG	CoMoP(3c)+TEG
$N_{\text{Mo-S}}$	5.0	5.4
$R_{\text{Mo-S}} (\text{\AA})$	2.41	2.41
$10^3 \cdot \Delta\sigma^2 (\text{\AA}^2)$	3.6	3.7
$\Delta E_0 (\text{eV})$	2.8	2.0
$N_{\text{Mo-Mo}}$	3.0	3.3
$R_{\text{Mo-Mo}} (\text{\AA})$	3.16	3.16
$10^3 \cdot \Delta\sigma^2 (\text{\AA}^2)$	4.7	4.8
$\Delta E_0 (\text{eV})$	2.2	1.5

The Mo-S coordination number increase after additive impregnation indicates that the MoS_2 crystallites edges are more saturated by sulfur [2]. Moreover, the Mo-Mo coordination number increase after additive impregnation shows that the average crystallite size has increased [10,11].

XPS analyses are conducted on the sulfided calcined samples to further describe the catalysts structure and how they evolve after additive impregnation. The XPS Mo 3d spectra are decomposed using the method described for the sulfided dried catalysts. Figure VII-14 summarizes the results for the additive-free and additive-containing calcined catalysts.

No major modifications are observed between the sulfided dried catalysts and the sulfided calcined catalysts, except for the CoMo_AHM sample (21% decrease on the MoS_2 proportion) and the CoMo_HPA sample (11% increase). Likewise, the additive impregnation does not induce significant modifications on the molybdenum state. The only exception is the calcined CoMo_AHM(c), which exhibits a gain of 10% on the sulfided molybdenum percentage, in disfavor of oxysulfided species.

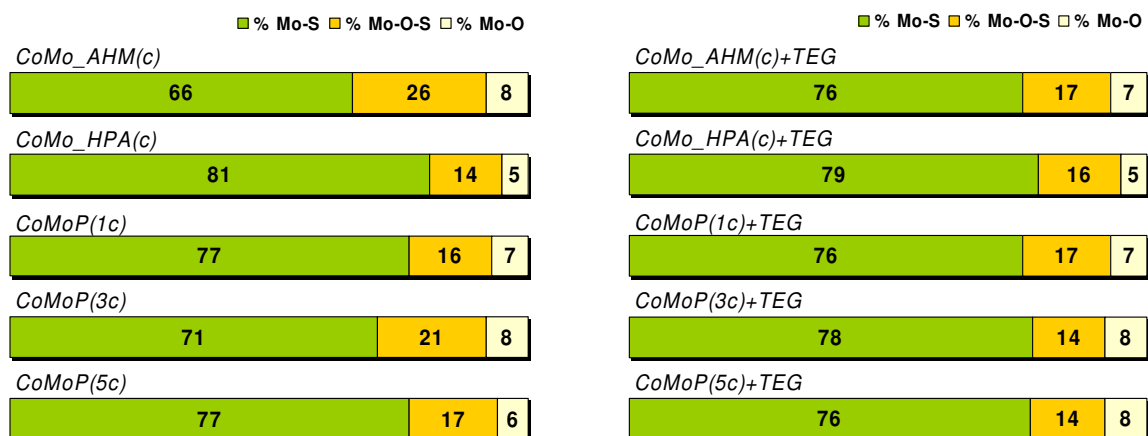


Figure VII-14: Molybdenum 3d XPS spectrum decomposition results for additive-free (left) and additive-containing calcined CoMo(P) catalysts (right).

The fact that the sulfided calcined CoMo_AHM(c) sample exhibits lower MoS₂ percentage than the corresponding sulfided dried sample may be explained by poor molybdenum dispersion. Indeed, this catalyst was prepared by double-impregnation with an intermediary calcination. This leads to stronger active phase precursors-support interactions before the second impregnation which limits the molybdenum species dispersion upon the second impregnation. The important proportion of non sulfided cobalt (40%) in the same catalyst confirms the limited dispersion of metals. In the case of the sulfided CoMo_HPA(c) catalyst, the molybdocobaltate HPAs are destroyed upon calcination and therefore better Mo sulfidation ratios are obtained: it was shown for dried samples that these HPA are not efficient precursors for the MoS₂ formation.

The improvement on molybdenum sulfidation after additive impregnation of the CoMo_AHM(c) may be explained by an increase of the Mo atoms dispersion via hexamolybdoaluminates formation.

VII.2.1.3. Influence of the additive on the active phase morphology

The characterization of the active phase morphology on sulfided catalysts prior to an after additive impregnation is used to complement the previous XAS and XPS analyses.

TEM analyses conducted on sulfided catalysts showed the presence of metal-containing aggregates for the additive-free and additive-containing sulfided dried AHM-based catalysts (Figure VII-15). Energy Dispersive X-ray (EDS) analysis revealed that these aggregates are composed of cobalt and sulfur, possibly corresponding to Co₉S₈-like bulks. These results are in agreement with the XPS observations, where the majority of cobalt participates in these structures.

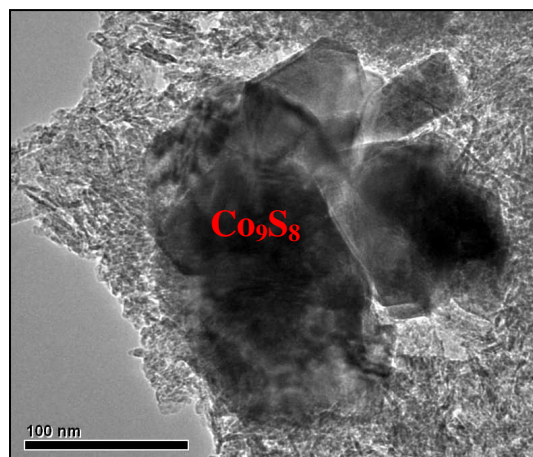


Figure VII-15: TEM image of a Co₉S₈ particle on the sulfided CoMo_AHM(d) catalyst.

TEM images allow visualizing the MoS_2 structures deposited on the alumina support. Each sharp black line represents a MoS_2 slab. As an example, Figure VII-16 shows TEM images of sulfided AHM-based catalysts, representative of all *ex situ* sulfided catalysts.

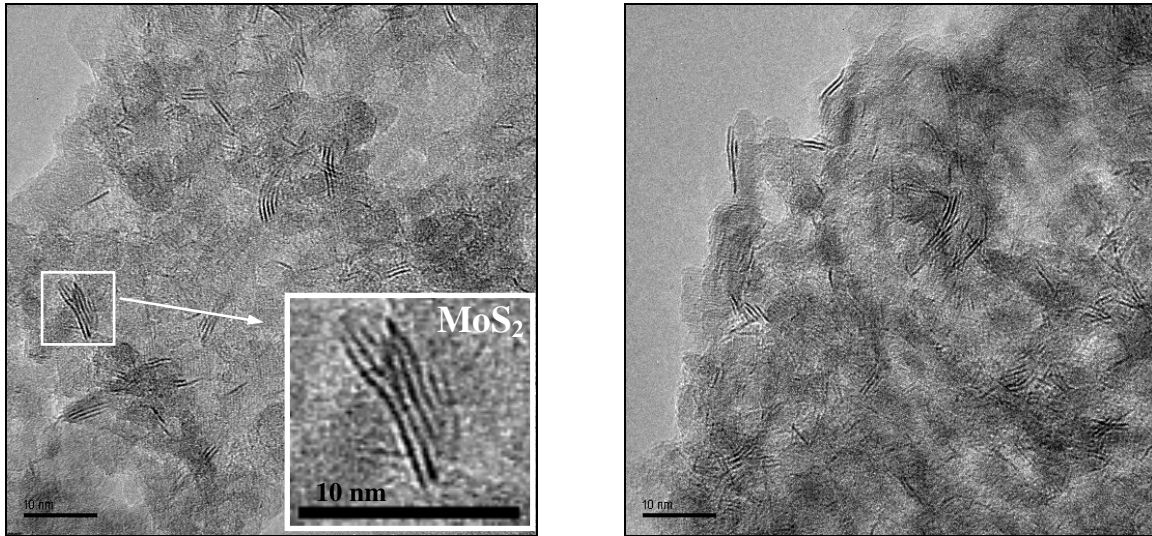


Figure VII-16: TEM images of the sulfided CoMo_AHM(d) (left) and CoMo_AHM(d)+TEG catalysts (right).

Using the TEM images, statistics were made over about 200 structures With respect to their length and stacking. The results are plotted in Figure VII-17 and Figure VII-18 for the dried AHM-based catalysts.

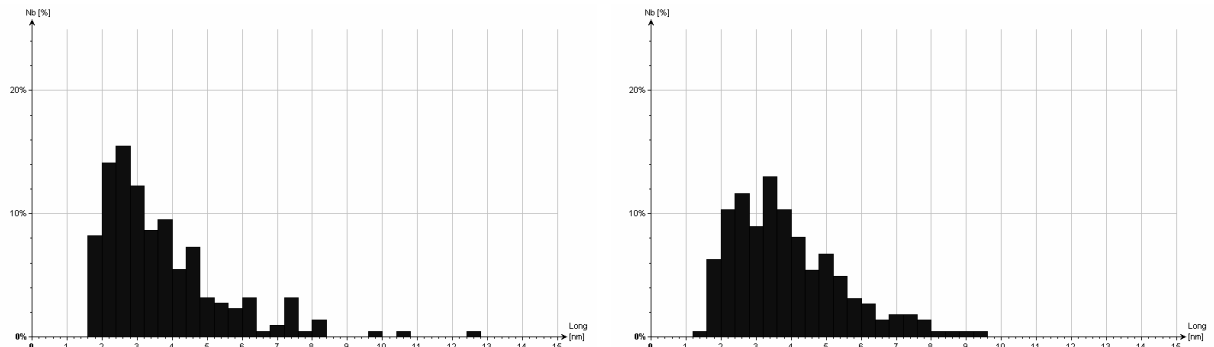


Figure VII-17: MoS_2 slab length histogram of the CoMo_AHM(d) (left) and CoMo_AHM(d)+TEG catalysts (right).

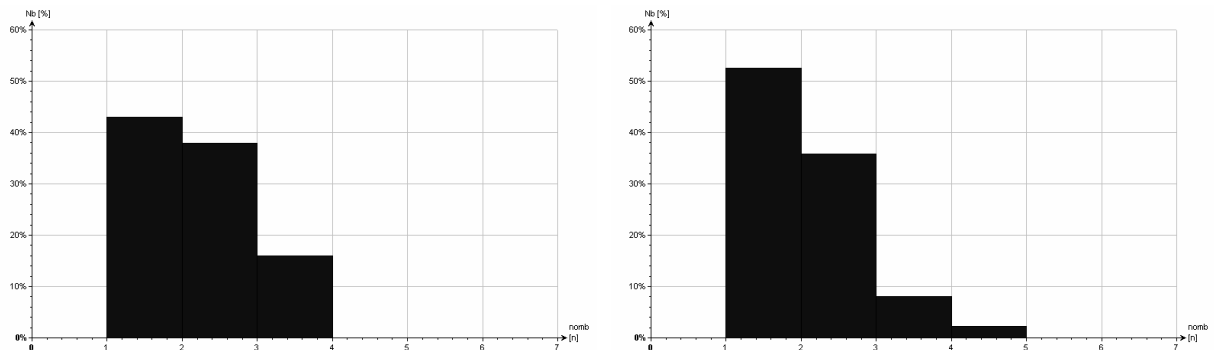


Figure VII-18: MoS_2 slab stacking histogram of the CoMo_AHM(d) (left) and CoMo_AHM(d)+TEG catalysts (right).

Table VII-10 summarizes the average slab length and staking of the analyzed sulfided samples. It may be seen that stacking is not affected by the catalyst formulation, by the thermal treatment and by the additive. In terms of slab length, the average value is slightly superior when the additive is present, although this increase is quite close to the analysis incertitude of 0.5 nm.

Table VII-10: MoS_2 morphology of *ex situ* sulfided CoMo(P) catalysts as observed by TEM.

	Average MoS_2 slab length (nm)	Average MoS_2 slab stacking
CoMo_AHM(d)	3.7	1.8
CoMo_AHM(d)+TEG	3.9	1.6
CoMo_AHM(c)	3.1	1.7
CoMo_AHM(c)+TEG	3.8	1.6
CoMoP(3c)	3.0	1.6
CoMoP(3c)+TEG	3.6	1.8

The observed stacking of about 1.7 is in agreement with literature data when similar gas-phase sulfidation conditions are used [1,7]. The increase of the average slab length after additive impregnation reinforces the EXAFS observations: larger MoS_2 crystallites explain the Mo-Mo coordination number increase.

VII.2.2. INFLUENCE OF THE ADDITIVE DURING THE SULFIDATION STAGE (*IN SITU* SULFIDATION)

According to published studies devoted to glycol-type additives, the activation stage is a crucial step to understand the role of glycol-type additives [1,5]. The X-ray absorption spectroscopy (XAS) allows to separately follow the local environment evolution of cobalt and molybdenum atoms during sulfidation. In this sense, the additive-free and additive-containing CoMoP(5d) catalysts were sulfided *in situ* and simultaneously analyzed by XAS.

VII.2.2.1. Influence of the additive on cobalt structure

The cobalt K-edge XANES provides a clear image of the sulfidation evolution when comparisons are made at the same temperature for the additive-free and additive-containing samples (Figure VII-19). In order to compare the near edge spectra, the raw signal was normalized and calibrated with the help of a reference metallic cobalt foil introduced in series with the analyzed sample. The maximum of the reference spectrum derivative was fixed to 7709 eV for cobalt.

As mentioned for the *ex situ* activations, the decrease of the white line intensity typical from non sulfided states allows to evaluate the cobalt sulfidation rate. The XANES spectra superposition at 100 °C shows that the additive-containing CoMoP(5d) catalyst is slightly more sulfided than the additive-free catalyst because its spectral line is closer to the final sulfided state spectral line.

However, this difference is no longer observed at 150 °C, 200 °C (Figure VII-19) and higher temperatures (not shown here).

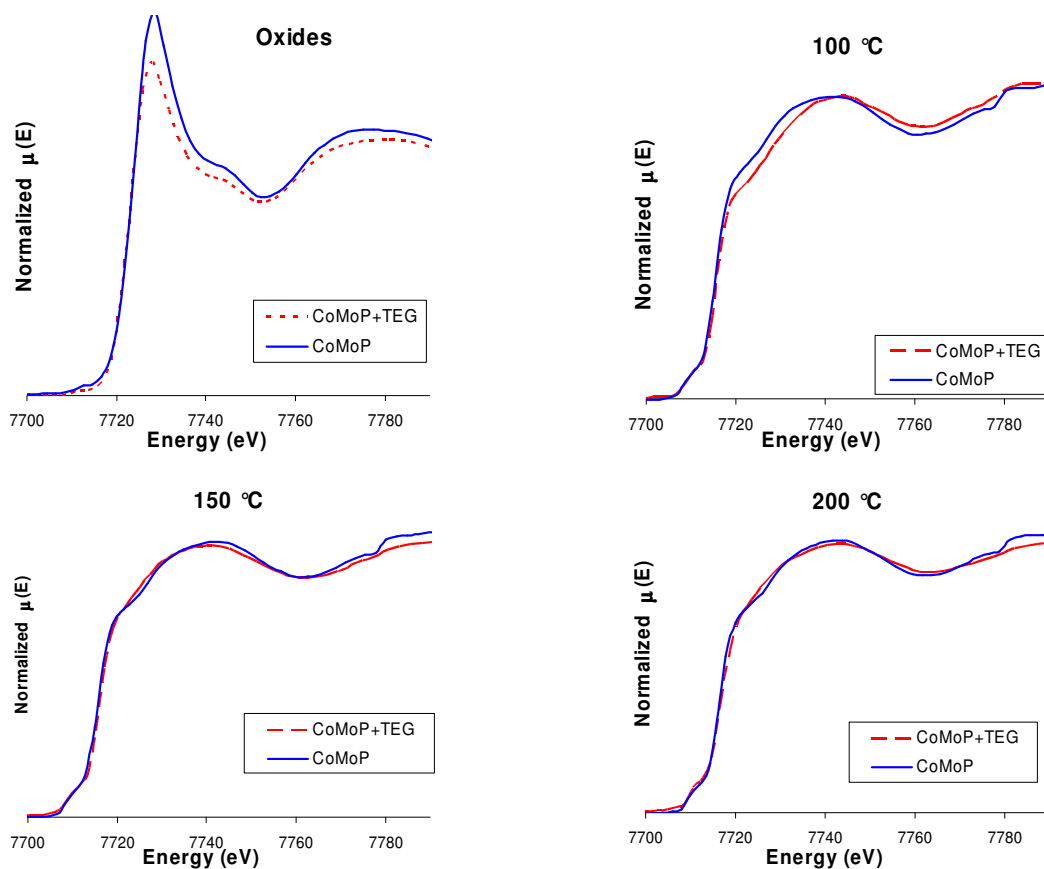


Figure VII-19: In situ sulfidation follow-up using the Co K-edge XANES spectra of the additive-free and additive-containing CoMoP(5d) catalysts.

In agreement with the XPS and XAS results of the *ex situ* sulfidations, the final sulfidation state is similar for all samples. *In situ* activation shows that before 150 °C, cobalt atoms are slightly more sulfided in presence of the additive.

The sulfided samples exhibit an EXAFS broad band from 1.0 to 2.0 Å (not phase corrected) assigned to a sulfur coordination shell. In opposition to the XANES results, the sulfidation follow-up by cobalt k^3 -weighted EXAFS spectra reveals the same Co-S contribution already at 100 °C (Figure VII-20). In other words, according to the EXAFS FT modulus, cobalt atoms are already sulfided at 100 °C with or without the additive, mainly because all spectra are rather close to the spectrum recorded at 400 °C.

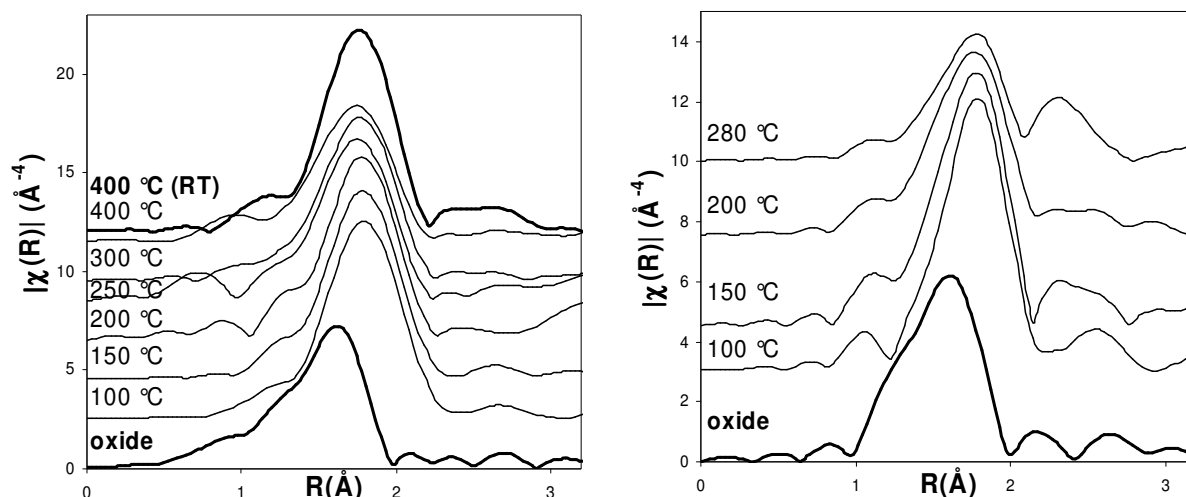


Figure VII-20: Cobalt K-edge k^3 -weighted EXAFS Fourier Transforms of the additive-free CoMoP(5d) (left) and additive-containing CoMoP(5d)+TEG catalysts (right) during in situ sulfidations. Hanning window from 2.5 to 11.5 Å⁻¹; $\tau=2.5$.

The spectra are successfully fitted using a single Co-S contribution (Table VII-11 and Table VII-12). The fit reveals that the Co-S bond lengths evolve from 2.24 to 2.20 Å and that the number of sulfur atoms neighbors evolves from 3.5 at 100 °C to 2.7 at 400 °C in the additive-free sample.

When the additive is introduced, the Co-S distances are slightly smaller before 200 °C when compared to the additive-free samples. However, after this temperature, the quality of the FT extraction decreases, leading to less accurate fits.

Table VII-11: Structural parameters resulting from the Co K-edge Fourier-filtred k^3 -weighed EXAFS functions of the in situ sulfided additive-free CoMoP(5d) catalyst ($\Delta R=1.0-2.5$ Å).

	100 °C	150 °C	200 °C	250 °C	300 °C	400 °C	RT *
$N_{\text{Co-S}}$	3.5	3.3	3.2	3.0	3.0	2.7	2.7
$R_{\text{Co-S}}$ (Å)	2.24	2.23	2.23	2.21	2.21	2.20	2.20
$10^3 \cdot \Delta\sigma^2$ (Å ²)	6.6	6.7	6.9	7.3	7.2	7.9	4.4
ΔE_0 (eV)	2.4	-0.3	1.8	-0.7	1.3	0.1	0.1

* acquisition after cooling at room temperature.

Table VII-12: Structural parameters resulting from the Co K-edge Fourier-filtred k^3 -weighed EXAFS functions of the in situ sulfided additive-containing CoMoP(5d) catalyst ($\Delta R=1.0-2.5$ Å).

	100 °C	150 °C	200 °C	250 °C	280 °C
$N_{\text{Co-S}}$	2.8	3.0	2.8	2.9	3.9
$R_{\text{Co-S}}$ (Å)	2.22	2.20	2.21	2.24	2.23
$10^3 \cdot \Delta\sigma^2$ (Å ²)	6.6	7.4	9.8	14	12
ΔE_0 (eV)	-0.6	-3.3	-1.3	2.0	0.9

The calculated Co-S bond length at 400 °C is quite close to the value observed in the *ex situ* sulfidations, which is in agreement with literature data [1]. Contrarily to the XANES results that show that before 150 °C cobalt atoms are more sulfided in presence of the additive, the EXAFS fit reveals

the opposite: cobalt coordination by sulfur atoms is always inferior in presence of the additive. However, the differences on the coordination number in presence and in absence of the additive are rather small. For this reason, it may be concluded that the additive does not significantly impact the cobalt atoms sulfidation.

VII.2.2.2. Influence of the additive on molybdenum structure

The molybdenum K-edge XANES spectrum is used to provide a clear image of the sulfidation evolution. To do so, comparisons are made at the same temperature for the additive-free and additive-containing samples. The raw signal was normalized and calibrated with the help of a reference metallic molybdenum foil introduced in series with the analyzed sample. The maximum of the reference spectra derivate was fixed to 20000 eV for molybdenum.

The molybdenum K-edge near edge spectra (Figure VII-21) reveal that at the same temperature, the molybdenum atoms are slightly more sulfided in the additive-containing sample than in the corresponding additive-free sample. This results from the fact that the spectral line of the additive-containing sample is closer to the final sulfided state spectral line. However, this effect disappears after 150 °C. Therefore, the additive lowers the temperature at which Mo atoms begin to be sulfided.

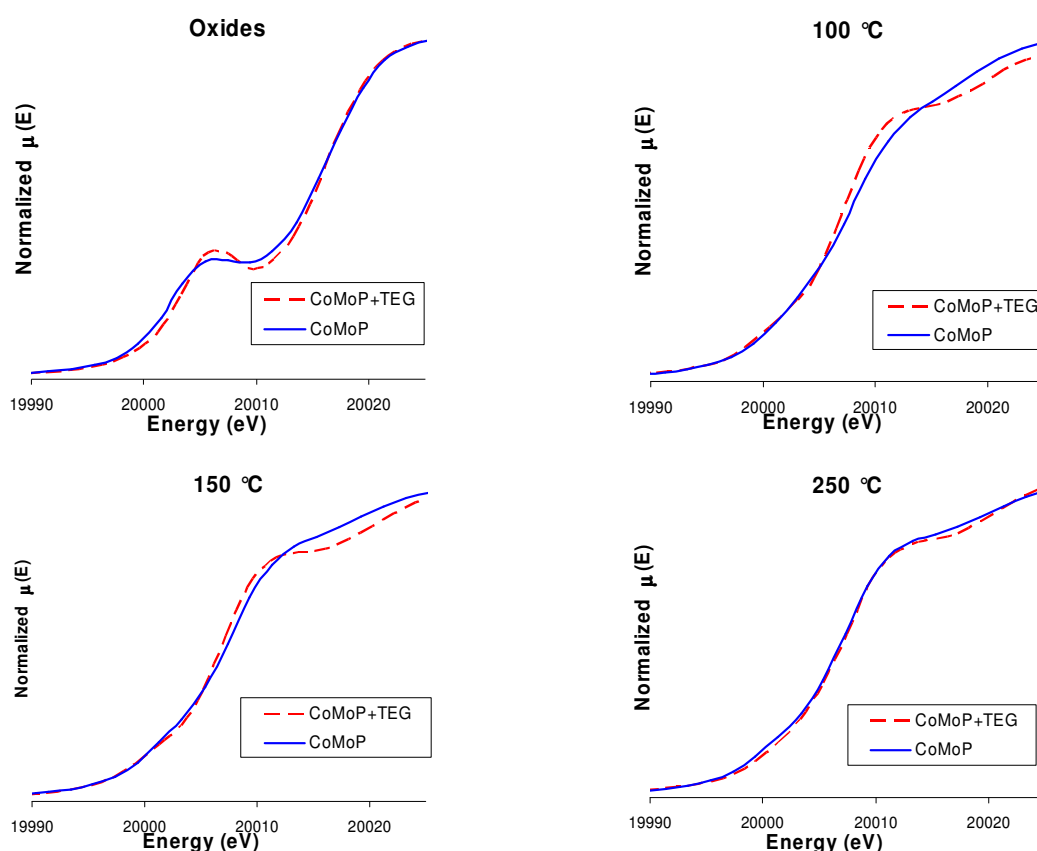


Figure VII-21: In situ sulfidation follow-up using the Mo K-edge XANES spectra of the additive-free and additive-containing CoMoP(5d) catalysts.

As for the cobalt case, the sulfidation follow-up using the Mo k^3 -weighted EXAFS spectra reveals similar features from 100 °C to 400 °C for both samples (Figure VII-22), exhibiting a main FT modulus contribution between 1.5 and 2.5 Å (not phase corrected).

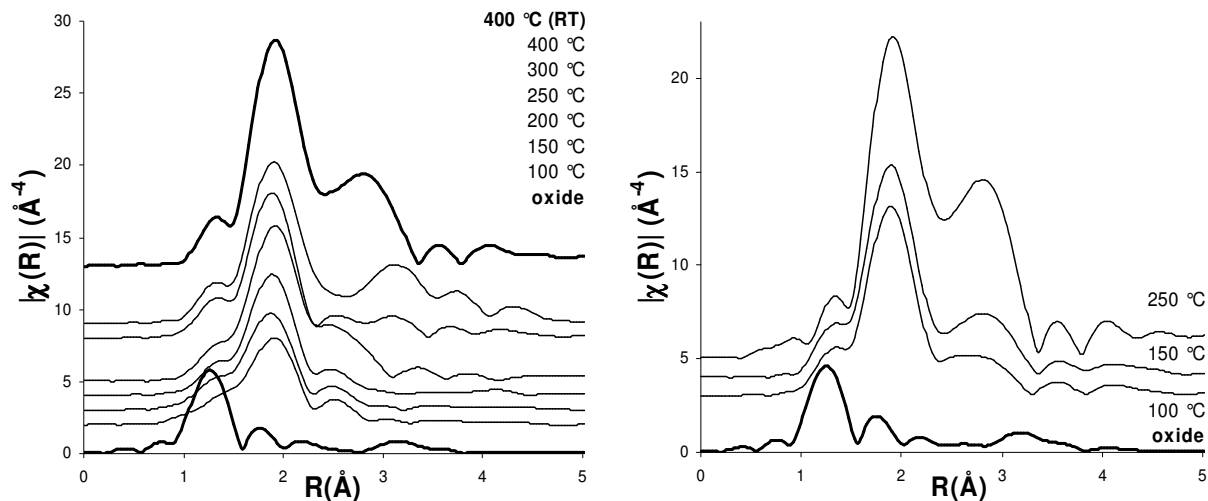


Figure VII-22: Molybdenum K-edge k^3 -weighted EXAFS Fourier Transforms of additive-free CoMoP(5d) (left) and additive-containing CoMoP(5d)+TEG catalysts (right) during in situ sulfidations. Hanning window from 2 to 11 Å⁻¹; $\tau=2.5$.

However, the fitting reveals significant differences between the additive-containing and additive-free samples. For the CoMoP(5d) catalyst, a Mo-O contribution is needed in order to fully simulate the first FT modulus curve (Table VII-13). This Mo-O contribution is needed up to 300 °C and it is not needed in the additive-containing sample case (Table VII-14). The fit also reveals a constant Mo-S distance of about 2.41 Å, typical in MoS₂ structures. Concerning the Mo-Mo distance, the fit revealed a value of about 2.81 Å for the additive-free catalysts which evolves to 3.16 Å at 400 °C. Besides this, the additive-containing catalyst shows a constant Mo-Mo distance of about 3.16 Å. The Mo-Mo coordination numbers gradually increase from 4.2 to 5.5 for sulfur neighbors in the additive-free catalyst while in the additive-containing they increase from 4.7 to 5.6.

The absence of a Mo-O contribution in the EXAFS spectra of the additive-containing sample and the higher Mo-S coordination number at each temperature indicates that the additive promotes molybdenum sulfidation even at low temperatures.

Table VII-13: Structural parameters resulting from the Mo K-edge Fourier-filtered k^3 -weighed EXAFS functions of the in situ sulfided additive-free CoMoP(5d) catalyst ($\Delta R=0.5-3.5 \text{ \AA}$).

	100 °C	150 °C	200 °C	250 °C	300 °C	400 °C	RT *
$N_{\text{Mo-O}}$	0.4	0.2	0.2	0.5	0.4	-	-
$R_{\text{Mo-O}} (\text{\AA})$	1.64	1.61	1.61	1.67	1.60	-	-
$10^3 \cdot \Delta\sigma^2 (\text{\AA}^2)$	4.4	0.8	1.2	8.4	5.9	-	-
$\Delta E_0 (\text{eV})$	1.6	2.7	-0.3	6.9	-3.0	-	-
$N_{\text{Mo-S}}$	4.2	4.1	4.4	4.7	4.5	4.8	5.5
$R_{\text{Mo-S}} (\text{\AA})$	2.41	2.39	2.40	2.40	2.40	2.42	2.41
$10^3 \cdot \Delta\sigma^2 (\text{\AA}^2)$	11.0	9.9	7.9	6.0	6.0	5.0	3.3
$\Delta E_0 (\text{eV})$	3.5	-0.9	1.7	1.7	1.0	3.3	2.5
$N_{\text{Mo-Mo}}$	0.6	0.9	0.8	0.9	n.d.	n.d.	3.8
$R_{\text{Mo-Mo}} (\text{\AA})$	2.80	2.81	2.81	2.82	n.d.	n.d.	3.16
$10^3 \cdot \Delta\sigma^2 (\text{\AA}^2)$	5.2	8.0	7.6	2.0	n.d.	n.d.	4.5
$\Delta E_0 (\text{eV})$	5.6	4.5	7.3	11.6	n.d.	n.d.	1.1

* acquisition after cooling at room temperature; n.d. stands for non determined.

Table VII-14: Structural parameters resulting from the Mo K-edge Fourier-filtered k^3 -weighed EXAFS functions of the in situ sulfided additive-containing CoMoP(5d) catalyst ($\Delta R=0.5-3.5 \text{ \AA}$).

	100 °C	150 °C	250 °C
$N_{\text{Mo-S}}$	4.7	5.2	5.6
$R_{\text{Mo-S}} (\text{\AA})$	2.40	2.40	2.41
$10^3 \cdot \Delta\sigma^2 (\text{\AA}^2)$	6.2	5.8	2.5
$\Delta E_0 (\text{eV})$	2.2	1.3	2.6
$N_{\text{Mo-Mo}}$	1.8	3.2	4.7
$R_{\text{Mo-Mo}} (\text{\AA})$	3.13	3.16	3.16
$10^3 \cdot \Delta\sigma^2 (\text{\AA}^2)$	7.0	7.7	3.2
$\Delta E_0 (\text{eV})$	-3.0	-0.2	0.9

Figure VII-23 shows the evolution of the Mo-S coordination number as a function of temperature. It is observed that for each temperature, the sample containing the additive has a higher Mo coordination by sulfur atoms, at least up to 200 °C, indicating that the additive favors molybdenum sulfidation, especially at lower temperatures.

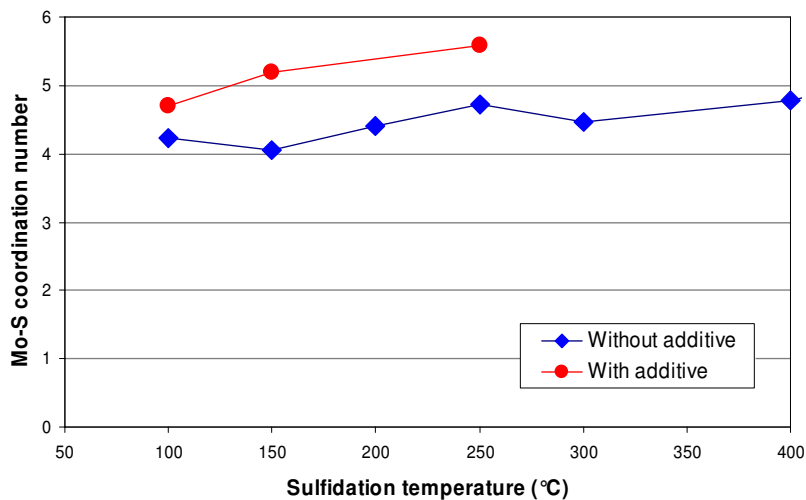


Figure VII-23: Mo-S coordination number evolution with temperature during the in situ sulfidations.

VII.2.3. CONCLUSION ON THE ADDITIVE IMPACT ON THE SULFIDATION STAGE

The first part of this section was consecrated to the additive influence on the final sulfided state of the catalysts. It was shown that the "CoMoS" phase yield in dried catalysts is strongly dependant on the deposited surface species prior to the sulfidation stage: $\text{Co}_3[\text{P}_2\text{Mo}_5\text{O}_{23}]$ and $\text{Co}_{7/2}[\text{PCoMo}_{11}\text{O}_{40}]$ heteropolycompounds are the most efficient precursors, followed by the molybdocobaltate cobalt salts and finally, the Anderson hexamolybdoaluminates salts. Furthermore, it was shown that nitrogen-containing ions are inhibitors of the "CoMoS" phase formation, leading to important amounts of Co_9S_8 species. For the additive-containing catalysts, improved metal dispersions were shown by the increase of the molybdenum atoms yield on MoS_2 structures and also by the increase of the cobalt atoms yield on "CoMoS" phase. These gains are associated to a decrease on the formation of the parasite phases, like oxysulfided molybdenum and Co_9S_8 species. Concerning the calcined catalysts, the additives also have a positive effect on the MoS_2 and "CoMoS" phase yields although inferior to that observed for the dried catalysts. In this case, the active phase precursors-support interactions are stronger due to the calcination stage and consequently the metals redispersion is limited. The morphology of the catalysts is not significantly modified by the additive besides a slight increase in the average crystallites size.

The second part of this section focused on the role of the additive during the sulfidation stage. The *in situ* sulfidation follow-up by XAS revealed that the cobalt atoms sulfidation is not significantly affected by the presence of the additive. However, this is not the case for the molybdenum atoms sulfidation. The molybdenum K-edge XANES spectra showed that at temperatures inferior to 250 °C, the molybdenum atoms on the additive-containing catalyst are more sulfided than on the corresponding additive-free catalyst. Moreover, bellow that temperature, the EXAFS fitting revealed higher Mo-S coordination numbers for the additive-containing sample. Since the final sulfided state is similar for both catalysts, as shown by XPS, this means that the additive accelerates the molybdenum atoms sulfidation at low temperatures.

VII.3. IMPACT OF THE ADDITIVE ON CATALYTIC PERFORMANCES

The previous section was dedicated to the study of the sulfidation stage, where it was shown that the promotion ratio is strongly dependent of the active phase precursors. Thus, it was shown that the additive limits the formation of parasite phases and as consequence improves both the promotion ratio and MoS_2 formation. The EXAFS *in situ* sulfidation study also revealed that in presence of the additives, molybdenum atoms are sulfided at lower temperatures, although the final sulfided state of the catalysts is similar.

The catalytic tests will allow to determine if the nature of the active phase precursors and additive induced modifications are correlated to for the catalysts performances. In this sense, molecule model tests and real feed HDS tests were conducted over additive-free and additive-containing catalysts.

Moreover, to evaluate the influence of the additive impregnation step location, these tests were conducted using different types of additive impregnation method.

VII.3.1. HYDROGENATION AND ISOMERIZATION REACTIONS

Catalysts were tested in toluene hydrogenation (HYD) and cyclohexane isomerization (ISOM) to evaluate the catalysts performances and the impact of the additives. Toluene reaction rates are expressed in converted toluene per molybdenum and per hour. The cyclohexane reaction rate is expressed in converted cyclohexane per catalyst gram per hour.

VII.3.1.1. Screening of additive-free dried and calcined CoMo(P) catalysts

The hydrogenation activity results show that the AHM-based catalyst has the lowest performance and that the CoMoP(5d) catalyst has the highest one, while the remaining catalysts have similar activities. In terms of isomerization activity results, the catalysts may be grouped in two groups: CoMoP catalysts with a P/Mo molar ratio superior or equal to 2/5, exhibiting ISOM reaction rates of about $0.45 \text{ mmol.g}^{-1}.\text{h}^{-1}$ and the CoMo-based and CoMoP catalysts with a P/Mo molar ratio inferior to 2/5, exhibiting ISOM reaction rates of about $0.22 \text{ mmol.g}^{-1}.\text{h}^{-1}$.

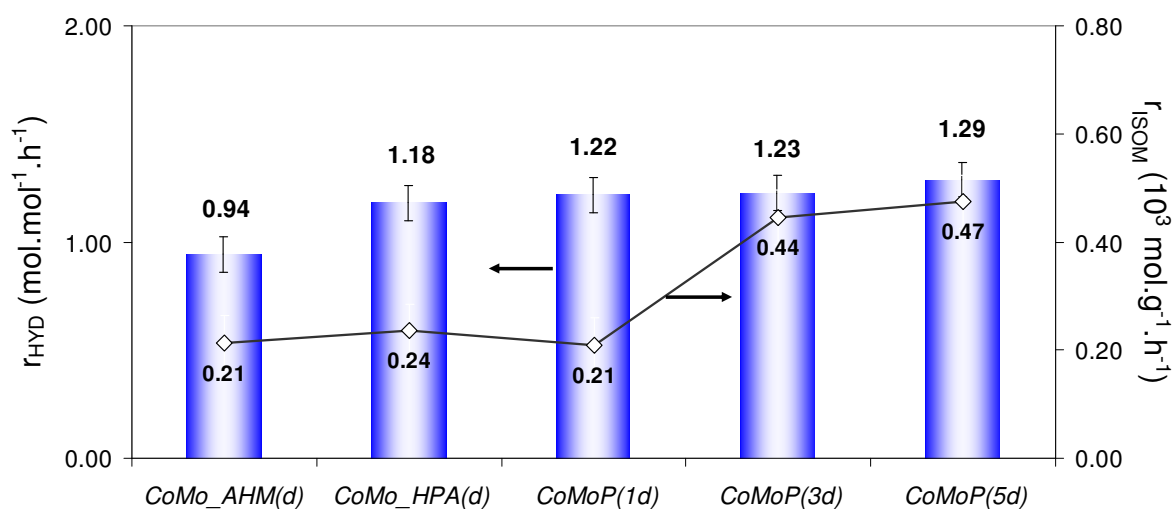


Figure VII-24: Toluene hydrogenation (HYD) and cyclohexane isomerization (ISOM) reaction rates of the additive-free dried CoMo(P) catalysts (350°C , 40 bar, $\text{LHSV}=2 \text{ h}^{-1}$).

The low HYD activity of the CoMo_AHM(d) catalyst is related to the poor dispersion resulting from the double-impregnation method used and also due to the presence of nitrate and ammonium ions, which are inhibitors of the phase formation: Co_9S_8 is formed instead of the phase, as shown by XPS. In opposition, the CoMoP(5d) catalyst reveals the highest HYD activity of this series, explained by the partial preservation of the $\text{P}_2\text{Mo}_5\text{O}_{23}^{6-}$ HPA on the catalyst before sulfidation, as shown by Raman spectroscopy. The CoMoP(3d), CoMoP(1d) and CoMo_HPA(d) catalysts have similar HYD performances, as well as similar active phase precursors, mainly composed of Anderson HPAs. These

results show that toluene hydrogenation performances are governed by the surface species present before sulfidation. However, this is not the case for the cyclohexane isomerization, where important amounts of phosphorus lead to higher ISOM activities. The presence of phosphorus increases the overall acidity of the catalyst and therefore enhances the isomerization performances.

The toluene hydrogenation activities of calcined catalysts are almost the same, except for the CoMoP(1c) catalyst, and slightly superior to the dried catalysts. In terms of cyclohexane isomerization, the same results as for the dried catalysts are observed, revealing two different behaviors due to phosphorus content.

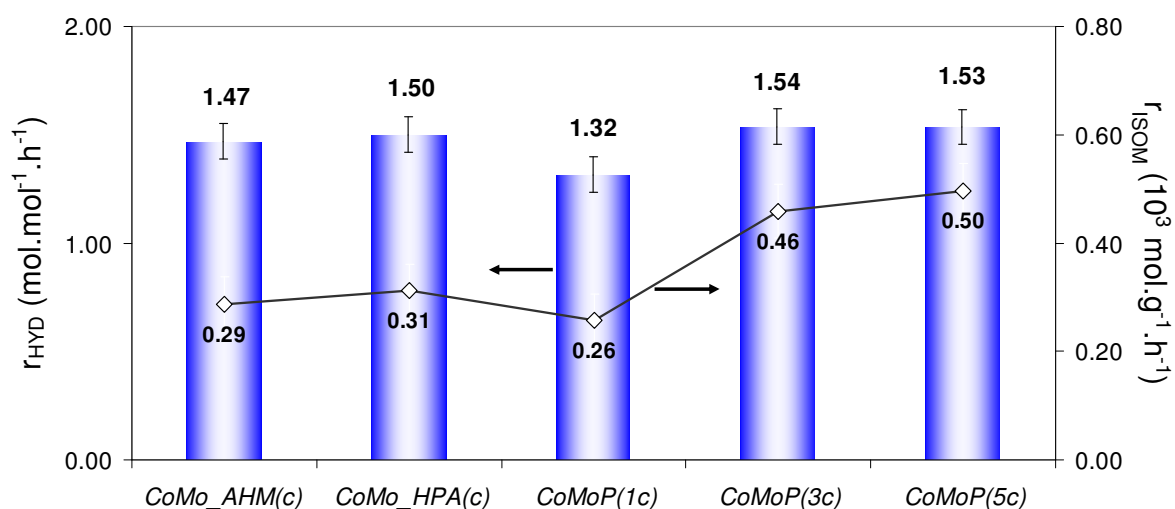


Figure VII-25: Toluene hydrogenation (HYD) and cyclohexane isomerization (ISOM) reaction rates of the additive-free calcined CoMo(P) catalysts (350 °C, 40 bar, LHSV=2 h⁻¹).

Once the catalysts undergo calcination, the existing heteropolyanions and nitrogen-containing ions are destroyed and the surface species are converted into ill-defined polyoxomolybdates. In this case, the fact that similar HYD activities are observed reinforce the idea that the surface species govern the HYD catalytic performance. The lower hydrogenation activity observed for the CoMoP(1c) catalyst is a consequence of the lower promotion ratio (35%) compared to the other calcined catalysts (more than 50%). Like in the dried catalysts case, the ISOM activities are related to the presence of phosphorus.

VII.3.1.2. Influence of the additive on the hydrogenation and isomerization catalytic performances of dried and calcined catalysts

The HYD reaction rate improvements due to additive impregnation of dried catalysts are summarized in Figure VII-26. All HYD performances are enhanced after additive impregnation and they can be separated into 2 groups: Group 1, containing the CoMoP(5d) and CoMoP(3d) catalysts (improvement of about 50%) and Group 2, containing the CoMoP(1d), CoMo_HPA(d) and CoMo_AHM catalysts (improvement of about 25%, except for the AHM-based case, where the

improvement is about 10%). In opposition, the additive has a negative impact on cyclohexane isomerization except when the catalysts have an important amount of phosphorus.

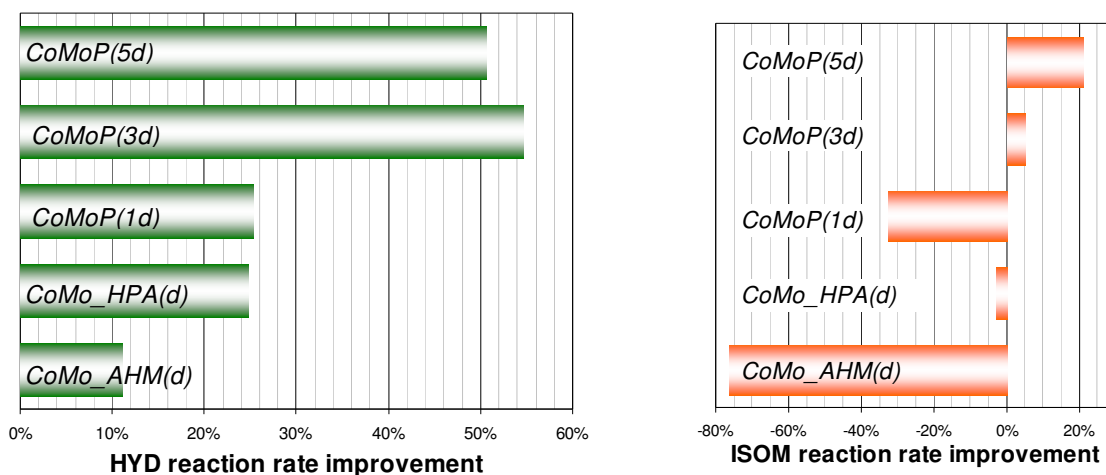


Figure VII-26: Improvements in toluene hydrogenation and cyclohexane isomerization reactions due to TEG impregnation of dried catalysts.

The catalytic improvement observed for Group 1 is consistent with surface species present on the additive-containing dried catalysts. Both exhibit formation of $\text{PCoMo}_{11}\text{O}_{40}^{7-}$ on top of $\text{AlMo}_6\text{O}_{24}\text{H}_6^{3-}$ heteropolyanions, combined with weak precursor-support interaction (the aluminophosphates are inexistent or in residual quantity, as shown by ^{31}P NMR). Therefore, molybdenum dispersion is enhanced and consequently leads to improved HYD activities. In Group 2 catalysts, this additional phosphomolybdate HPA is not formed and due to the low solubility of the Anderson hexamolybdoaluminate HPA, the metals redispersion is limited. Although this mechanism is also valid for the dried AHM-based catalysts, the presence of nitrogen-containing ions inhibits the phase formation when compared to the other catalysts, as shown by XPS.

The collected experimental data is insufficient to propose a plausible explanation for the modifications on the ISOM conversions after additive impregnation.

The improvements observed after additive impregnation of calcined catalysts are represented in Figure VII-27. Like in the dried catalysts case, the additive impregnation has a positive effect over the HYD activity of all calcined samples. In this case, phosphorus-containing catalysts exhibit about 10% of improvement while the CoMo formulations are only slightly affected (about 2%). On the other hand, all calcined catalysts reveal a negative influence of the additive in the isomerization reaction rates, except for the CoMoP(5c) catalyst.

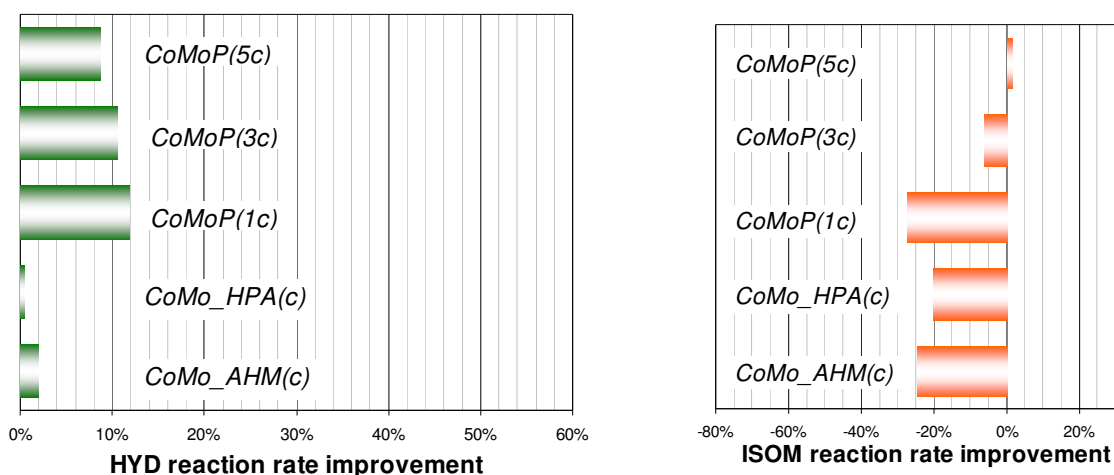


Figure VII-27: Improvements in toluene hydrogenation and cyclohexane isomerization reactions due to TEG impregnation of calcined catalysts.

The characterization results discussed in Chapter IV showed similar surface species after additive impregnation of calcined catalysts compared to the corresponding dried catalysts. Based on this, a similar redispersion mechanism was proposed. The improvements in HYD performances due to additive impregnation are in agreement with the proposed redispersion mechanism, although smaller improvements are observed compared to the dried catalysts. This is mainly due to stronger active phase-support interactions established during calcination.

Like in the dried catalysts case, the collected experimental data is insufficient to propose a plausible explanation for the modifications on the ISOM conversions after additive impregnation.

VII.3.1.3. Influence of the additive impregnation step location on the catalytic activity

A series of CoMoP(5) catalysts prepared according to different additive impregnation methods was tested in toluene hydrogenation and cyclohexane isomerization in order to evaluate the impact of the additive impregnation step location. The additive was thus introduced previously and simultaneously to the active phase precursor solution, as well as after the drying and calcination steps. A CoMoP(5d) catalyst impregnated only with water was also prepared and tested to study the differences in catalytic performances between water and TEG aqueous solutions.

The results summarized in Figure VII-28 show that water impregnation leads to a 17% increase in the hydrogenation reaction rate compared to the starting dried catalyst. In the cases of TEG impregnation of dried catalysts and TEG simultaneous impregnation, an increase of about 50% is observed, while the pre-impregnation method lead to the highest HYD improvement corresponding to a 66% increase when compared to the dried CoMoP(5d) catalyst. The results also show that the HYD activity of the CoMoP(5c)+TEG catalyst is the lowest of the additive-containing catalysts.

The isomerization reaction rate slightly changes after water and TEG impregnation. The highest ISOM performance is observed for the water impregnated sample, corresponding to an increase of

about 32%. It may be also observed that the pre-impregnation of the alumina support leads to the lowest isomerization activity.

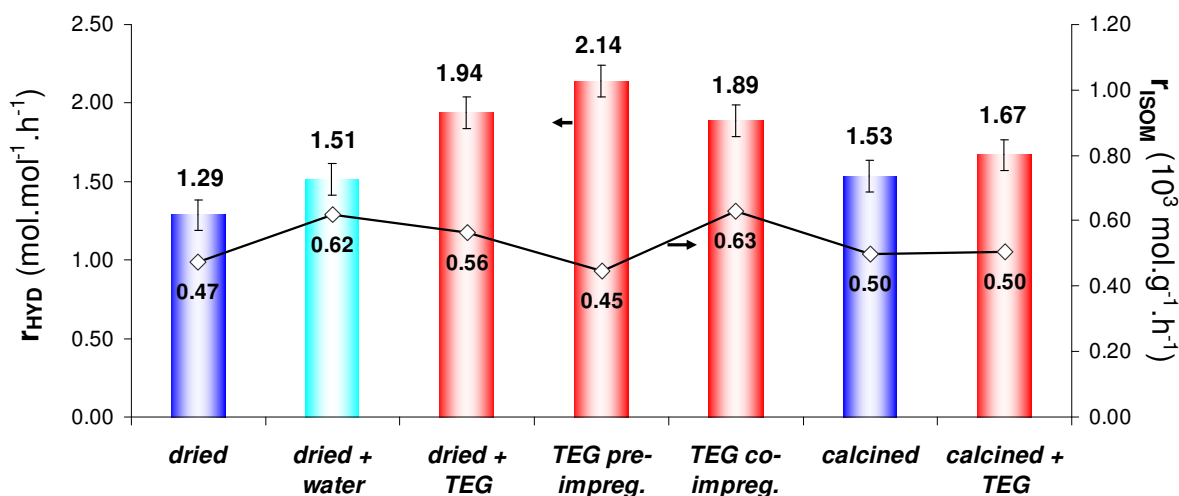


Figure VII-28: Impact of the additive impregnation stage location on toluene hydrogenation (HYD) and cyclohexane isomerization (ISOM) reaction rates of CoMoP(5) catalysts (350 °C, 40 bar, LHSV=2 h⁻¹).

A similar series of CoMo_HPA catalysts was also prepared and tested (Figure VII-29). The results are similar to those obtained for the CoMoP(5) formulations presented above. The toluene hydrogenation reaction rate increases of almost 50% in the case when previous alumina impregnation is used. Thus, the cyclohexane isomerization reaction rates are similar for all tested samples.

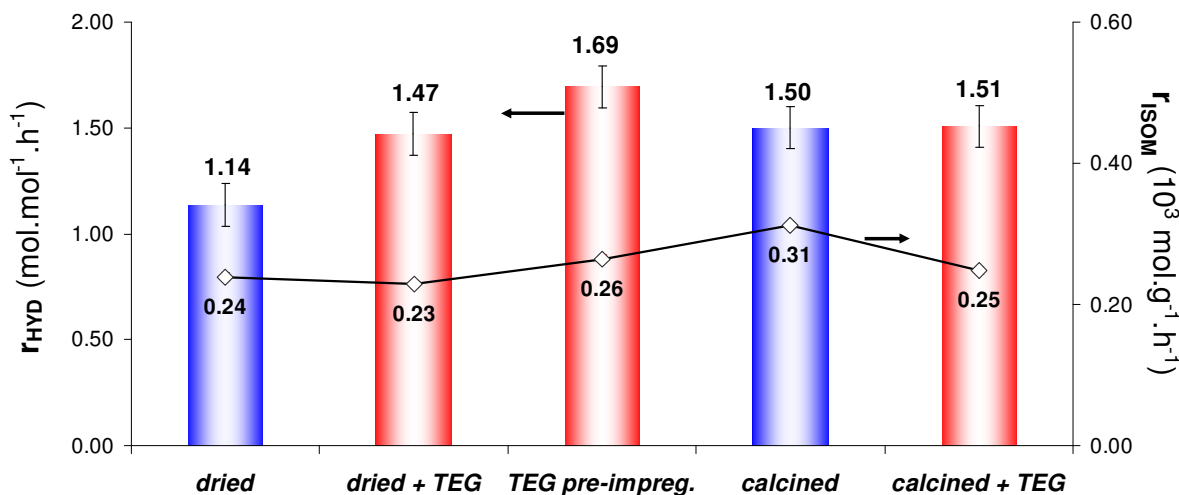


Figure VII-29: Impact of the additive impregnation stage location on toluene hydrogenation (HYD) and cyclohexane isomerization (ISOM) reaction rates of CoMo_HPA catalysts (350 °C, 40 bar, LHSV=2 h⁻¹).

The catalytic activities of the CoMoP(5) and CoMo_HPA catalysts series reveal that the most efficient additive impregnation method is when the additive is directly impregnated over alumina. It was discussed in Chapter V that in this case, TEG forms a physisorbed layer on the alumina support

and consequently blocks the alumina surface groups. When the HPA salts precipitate, their interaction with the alumina surface groups is prevented. As a consequence, their disintegration is limited.

The additive-containing catalysts have in general similar HYD activities which support the fact that the improved metal dispersion leads to better "CoMoS" phase yields catalytic and consequently to better "CoMoS" phase yields.

VII.3.1.4. Influence of the additive loading on the catalytic activity

To better understand the additive impact in the catalytic performances of dried catalysts, a series of samples was prepared with an increasing TEG/Mo molar ratio (Figure VII-30). The toluene hydrogenation reaction rates show that the optimal TEG quantity corresponds to a TEG/Mo ratio of 0.25, leading to a 64% improvement compared to the corresponding additive-free sample. Increasing amounts of additive lead to a steady conversion level of about $1.85 \text{ mol.mol}^{-1}.\text{h}^{-1}$ (40% improvement). In terms of cyclohexane isomerization conversion, a correlation is found with the amount of impregnated additive: the ISOM reaction rate decreases with increasing amounts of additive.

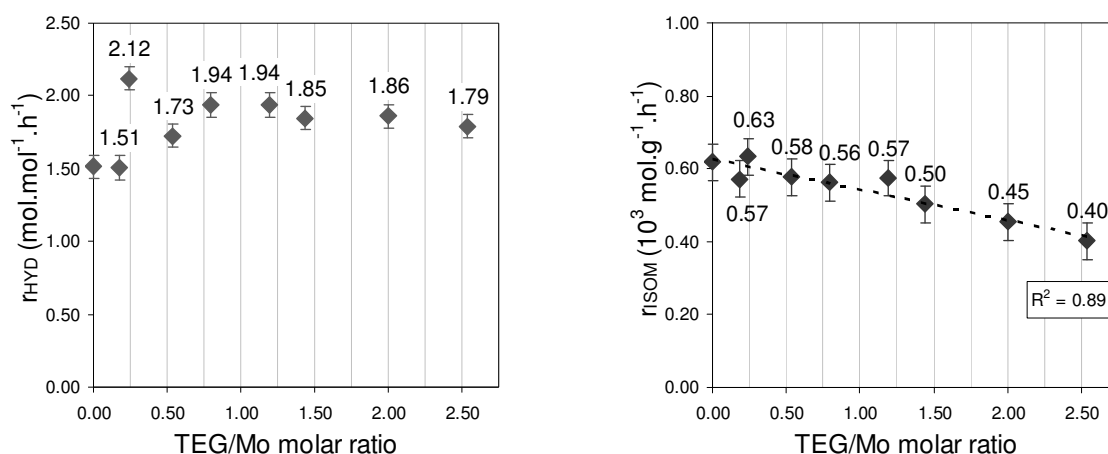


Figure VII-30: Impact of the additive loading on the toluene hydrogenation (HYD) (left) and cyclohexane isomerization (ISOM) (right) reaction rates for the dried CoMoP(5d) catalysts (350 °C, 40 bar, LHSV=2 h⁻¹). The first point (TEG/Mo=0.0) corresponds to a catalyst only impregnated with water.

The collected experimental data is insufficient to propose an explanation to the HYD reaction rates evolution with the TEG/Mo ratio. Further research on the deposited surface species and on the catalyst properties in general using different TEG/Mo loadings are required.

With respect to isomerization, the linear decrease observed in the ISOM catalytic performances are may be explained by the hindrance of the acidic alumina surface groups: the additive blocks part of the alumina adsorption sites and leads to a decrease in the support acidity. This decreases the capability of alumina to convert cyclohexane into its isomerization products. Therefore, more additive leads to less available alumina sites and as a consequence, lower ISOM reaction rates.

When the additive is simultaneously impregnated with the CoMoP(5) solution, the hydrogenation reaction rate maximum is displaced towards a higher TEG/Mo molar ratio of 0.50 (Figure VII-31). In this case, the activity reaches about $2.0 \text{ mol} \cdot \text{mol}^{-1} \cdot \text{h}^{-1}$ and remains relatively constant when further additive is impregnated. The same behavior is observed for the isomerization reaction, in opposition to the case of additive impregnation over a dried catalyst.

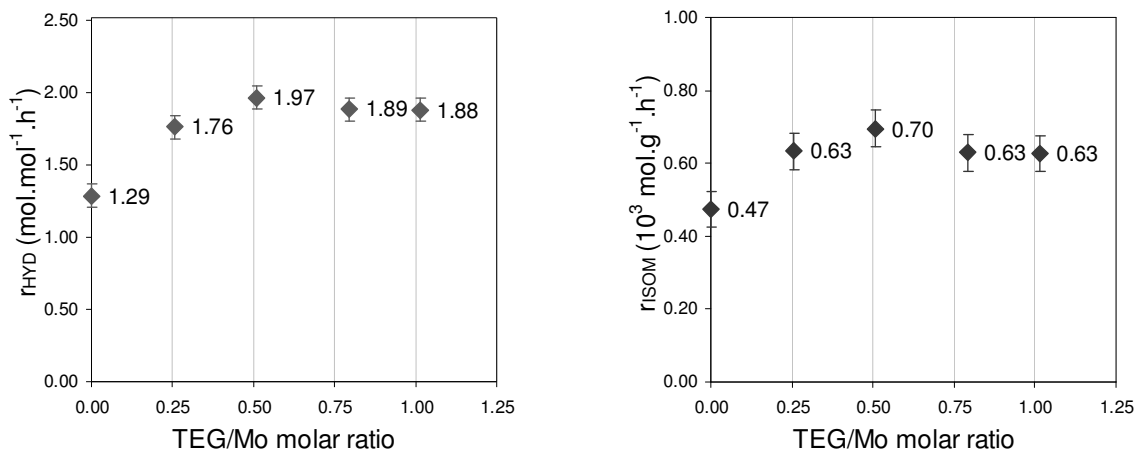


Figure VII-31: Impact of the additive loading on the toluene hydrogenation (HYD) (left) and cyclohexane isomerization (ISOM) (right) reaction rates for the co-impregnated CoMoP(5) catalysts (350 °C, 40 bar, LHSV=2 h⁻¹). The first point (TEG/Mo=0.0) corresponds to the dried CoMoP(5d) catalyst.

The reason for this behavior in the HYD reactions may be explained by the formation of substituted Keggin heteropolyanions. When more additive is present in solution, more $\text{PCoMo}_{11}\text{O}_{40}^{7-}$ is formed from free phosphates. When all free phosphates are converted, the additional quantity of TEG has no beneficial effect and therefore the HYD reaction rates remain constant.

VII.3.2. HYDRODESULFURIZATION REACTION

It has been shown in the literature that the HDS mechanism involves two different pathways: the hydrogenation (HYD) and the direct desulfurization (DDS) pathways [12,13]. The catalytic tests presented in the previous section may be extrapolated to the hydrogenation pathway but the DDS pathway may be differently affected by the additive. Therefore, the CoMoP(5) catalysts prepared according to different additive-impregnation methods were also tested in real feed HDS reactions.

The results reveal the following catalysts hierarchy in terms of HDS performance:



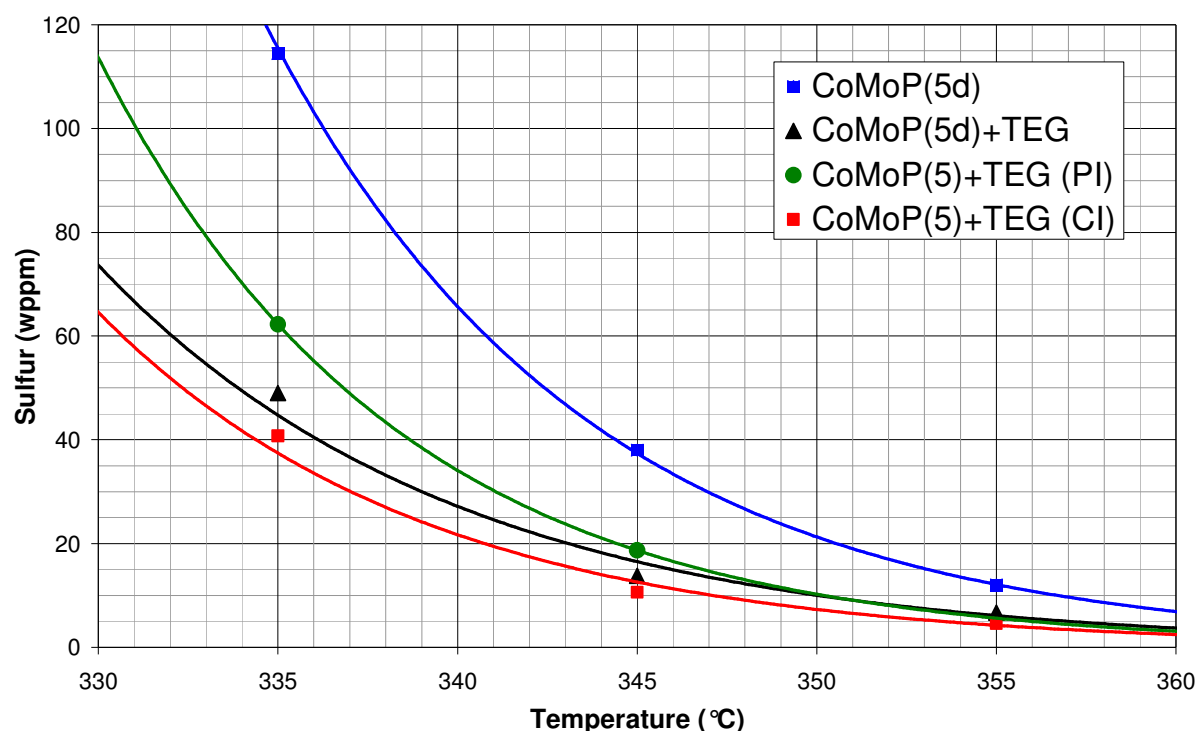


Figure VII-32: Diesel sulfur content after HDS reaction at different temperatures using CoMoP(5) catalysts (30 bar, LHSV=1 h⁻¹). PI stands for pre-impregnation and CI for co-impregnation.

In agreement with the results observed in toluene hydrogenation tests, the performances of the CoMoP(5d)+TEG and CoMoP(5)+TEG (CI) are quite similar. However, the pre-impregnated catalyst leads to an inferior gain although the toluene hydrogenation test showed the highest enhancement. This suggests that the DDS route is not affected in a similar way by the additive impregnation for all the catalysts. Further research is required to explain this behavior.

VII.3.3. CONCLUSION ON THE ADDITIVE IMPACT ON THE CATALYTIC TESTS

The additive impact in catalytic performances was evaluated in toluene hydrogenation and cyclohexane isomerization reactions. For this purpose, additive-free and additive-containing samples prepared using different additive impregnation stage locations were tested, as well as different TEG loadings. This allowed to establish a catalyst hierarchy and to quantify the impact of the additives. Results show that the nature of the active phase precursors governs the HYD catalytic performances and that the ISOM reactions are related to the presence of phosphorus which modifies the catalyst acidity. When the additive is introduced, a hydrogenation reaction rate increase is observed that is consistent with the redispersion phenomena presented in the previous chapters, especially when free phosphates are available. The catalytic results also show that this booster effect is limited in calcined catalysts, where stronger active phase precursors-support interactions are established. Thus, the TEG co-impregnation and impregnation on a dried catalyst lead to similar catalytic results, revealing a common solvent effect that favors molybdenum dispersion. Moreover, the highest enhancements were

observed for the TEG pre-impregnated case. In this case, besides the solvent effect, an additional hindering effect over the alumina absorption sites may explain the activity improvement.

The HDS test revealed similar activity enhancements for all the additive-containing samples when compared to the fresh catalyst. This is the consequence of improved metal dispersion due to the formation of Anderson and Keggin phosphomolybdic HPAs, like observed in the HYD tests.

VII.4. CHAPTER CONCLUSION

The catalysts study of the at the sulfided state showed that the additive leads to improved promotion ratios, mainly due to a decrease on the formation of parasite phases, especially bulk Co_9S_8 . Thus, the amount of molybdenum participating on MoS_2 structures also increases, which supports the hypotheses of enhanced metals dispersion. In terms of active phase morphology, no modification in MoS_2 layers stacking was observed and only a slight increase on the average crystallite size was shown. Besides this, the *in situ* sulfidation XAS study revealed that the presence of the additive accelerates the sulfidation of molybdenum. However, this effect disappears when the temperature reaches 150-200 °C.

In terms of catalytic performances, the toluene hydrogenation and cyclohexane isomerization reactions were used to establish a catalyst hierarchy and to quantify the impact of the additives. It was shown that when the additive is introduced in the catalysts, the hydrogenation reaction rate increases and that this booster effect is limited in calcined catalysts, where stronger active phase precursors-support interactions are established. Concerning the additive introduction stage location, similar HYD performances were observed while using co-impregnation and impregnation on a dried catalyst. However, highest enhancements were observed for the TEG pre-impregnated case. In this case, besides the solvent effect, an additional hindering effect of the alumina absorption sites may explain the activity improvement. The HDS tests are in agreement with the previous results, revealing a gain that can reach 10 °C.

Key-points

1. *The additive impregnation leads to improved promotion ratios and improved molybdenum sulfidation.*
2. *The in situ sulfidations XAS study revealed that the molybdenum sulfidation is accelerated bellow 150-200 °C.*
3. *No significant modifications on the active phase morphology were observed after additive impregnation, besides a slight increase in the average MoS_2 crystallite size.*
4. *The hydrogenation activities are governed by the surface species present on the catalysts prior to the activation stage.*

5. *The hydrogenation activities are enhanced in presence of the additive. HDS performances are also improved using CoMoP catalysts ($P/Mo=0.57$).*
6. *Similar hydrogenation activities are observed for the additive impregnation on dried catalysts and for the TEG co-impregnated catalysts. The highest enhancement is observed for the TEG pre-impregnated catalyst.*

VII.5. BIBLIOGRAPHIC REFERENCES

- 1 P. Mazoyer, C. Geantet, F. Diehl, C. Pichon, T.S. Nguyen and M. Lacroix, Oil&Gas Sci. Tech. – Rev. IFP, Vol. 60, 5, 791, **2005**.
- 2 D. Nicosia and R. Prins, J. Catal. 231, 258, **2005**.
- 3 C. Geantet, Y. Soldo, C. Glasson, N. Matsubayashi, M. Lacroix, O. Proux, I. Ulrich and J.-L. Hazeman, Cat. Lett. Vol. 73, No. 2-4, 95, **2001**.
- 4 S.M.A.M. Bouwens, J.A.R. van Veen, D.C. Koningsberger, V.H.J. de Beer and R. Prins, J. Phys. Chem. 95, 123, **1991**.
- 5 D. Nicosia, Ph.D. thesis Swiss Federal Institute of Technology Zurich, **2005**.
- 6 S.M.A.M. Bouwens, F.B.M. van Zon, M.P. van Dijk, A.M. van der Kraan, V.H.J. de Beer, J.A.R. van Veen and D.C. Koningsberger, J. Catal. 146, 375, **1994**.
- 7 A. Gandubert, Ph.D. thesis Université des Sciences et Technologies de Lille, **2006**.
- 8 R.G. Leliveld, A.J. van Dillen, J.W. Geus and D.C. Koningsberger, J. Catal. 171, 115, **1997**.
- 9 T.G. Parham and R.P. Merrill, J. Catal. 85, 295, **1984**.
- 10 G. Plazenet, Ph.D. thesis Université des Sciences et Technologies de Lille, **2001**.
- 11 T. Shido and R. Prins, J. Phys. Chem. B 102, 8426, **1998**.
- 12 F. Bataille, J.L. Lemberon, P. Michaud, G. Pérot, M. Vrinat, M. Lemaire, E. Schulz, M. Breyse and S. Kasztelan, J. Catal. 191, 409, **2000**.
- 13 H. Topsøe, B. Hinnemann, J.K. Nørskov, J.V. Lauritsen, F. Besenbacher, P.L. Hansen, G. Hytoft, R.G. Egeberg and K.G. Knudsen, Catal. Today 107–108, 12, **2005**.

GENERAL CONCLUSION

The introduction of a glycol-type additive in hydrotreating catalysts is an efficient procedure to improve catalytic activity. However, controversial explanations about the activity enhancement mechanism exist in the literature. This may be due to different catalyst preparation procedures, different location of the additive impregnation step, or simply because several phenomena are implied in these improvements. The aim of this thesis was thus to rationalize the roles of these additives with respect to (i) species present in the impregnation solution as well as on the catalyst surface, (ii) the preparation step where the additive impregnation is carried out. By preparing catalysts using different impregnation solutions and varying the location of the additive impregnation stage, it was possible to verify if the additive has an impact on the catalyst properties prior to, during and after the activation stage.

It was shown that for dried or calcined CoMo and CoMoP catalysts with a P/Mo molar ratio lower than 0.4, the additive promotes a redissolution phenomenon through formation of the Anderson heteropolyanion $\text{AlMo}_6\text{O}_{24}\text{H}_6^{3-}$. This redissolution phenomenon is however limited by the low solubility of this Anderson HPA. In the case of CoMoP dried catalysts with a P/Mo molar ratio greater than 0.4, characterization of additive-containing catalysts evidenced $\text{PCoMo}_{11}\text{O}_{40}^{7-}$, on top of $\text{AlMo}_6\text{O}_{24}\text{H}_6^{3-}$ formation. Redissolution and redispersion due to the additive impregnation are thus enhanced. TEG acts as a solvent and favors the formation and dispersion of heteropolycompounds. Consequently, improved metals dispersion is achieved and the formation of the "CoMoS" phase is favored. However, the redispersion phenomenon is limited on calcined catalysts due to stronger active phase precursors-support interactions established during the calcination stage. The catalytic performances tested on toluene hydrogenation match perfectly with the dispersion enhancement: the catalytic improvement due to the additive impregnation is higher when $\text{PCoMo}_{11}\text{O}_{40}^{7-}$ heteropolyanions are formed. Moreover, the catalytic improvements after additive impregnation of calcined catalysts are limited.

Concerning the impregnation of the additive directly on the alumina support or simultaneously with the precursor solution impregnation, the same surface species were found as for the additive-containing dried and calcined catalysts. This revealed that the additive plays the same role, acting as a solvent and thus favoring HPA formation and dispersion. For the CoMoP(5) formulation, the proportion of $\text{PCoMo}_{11}\text{O}_{40}^{7-}$ species increased with respect to $\text{AlMo}_6\text{O}_{24}\text{H}_6^{3-}$ species. Moreover, the surface species observed in solution were retained to a greater extent on the catalyst surface after the drying stage. This behavior may be explained by the formation of a TEG physisorbed layer on alumina. The heteropolyanions in solution precipitate on this layer and their direct interaction with the alumina surface groups is limited. Consequently, the heteropolyanion decomposition is prevented.

The catalytic performances tested on toluene hydrogenation revealed that this hindrance effect may further increase the catalysts activity. Indeed, the highest activities were obtained when the additive was previously impregnated on the alumina support. However, this latter effect is not as extensive in the co-impregnated catalyst, where they exhibit similar activities compared to the TEG-impregnated dried catalysts.

The study of *ex situ* sulfided catalysts showed that the "CoMoS" phase yield in dried catalysts is correlated to the deposited surface species prior to the sulfidation stage. The phosphomolybdic heteropolyanions revealed to be the most efficient active phase precursors, followed by the molybdocobaltate cobalt salts and finally, the Anderson hexamolybdoaluminates salts. When the additive is impregnated, enhanced metals dispersion is achieved and as a consequence, the molybdenum yield on MoS₂ and the cobalt yield on the "CoMoS" phase are improved. No modification in the stacking of the MoS₂ layers occurs after additive impregnation and only a slight increase on the average crystallite size was observed.

On the other hand, the *in situ* sulfidation XAS study of a CoMoP catalyst revealed that the presence of the additive does not have a significant effect on the cobalt atoms sulfidation. For molybdenum, both the XANES and the EXAFS spectra showed that below 250 °C, the molybdenum atoms on the additive-containing catalyst are more sulfided than on the corresponding additive-free catalyst. Since the final sulfided state is similar for both catalysts, the additive accelerates the molybdenum atoms sulfidation below 250 °C.

In conclusion, the physical properties of the additive, namely its solvent properties like polarity and boiling point, stabilize the heteropolyanions on the catalyst surface. As a consequence, the glycol-type additives favor the HPA formation. The active phase precursors are then better dispersed and favor the precipitation of molybdenum and cobalt atoms in close proximity, leading to enhanced "CoMoS" phase yields. Moreover, when the additive is impregnated prior to or simultaneously with the precursor solution, besides the aforementioned effect, the decomposition of the solution HPA species upon contact with alumina is partially avoided.

This work shows that the main role of the additives is due to its physical properties, acting as a solvent.

APPENDIX

APPENDIX A: PREPARED CATALYSTS PROPERTIES

Table 1: Properties of additive-free dried CoMo(P) catalysts.

Catalyst	Co/Mo [mol/mol]	P/Mo [mol/mol]	CoO [wt%]	MoO ₃ [wt%]	P ₂ O ₅ [wt%]	LOI [wt%]
CoMo_AHM(d)	0.40	-	3.46	16.4	-	17.71
CoMo_HPA(d)	0.46	-	3.30	13.7	-	24.97
CoMoP(1d)	0.36	0.14	2.52	13.3	0.92	24.44
CoMoP(3d)	0.38	0.45	3.05	15.5	3.40	15.30
CoMoP(5d)	0.38	0.58	3.09	15.7	4.50	14.34

Table 2: Properties of additive-free calcined CoMo(P)catalysts.

Catalyst	S _{BET} [m ² /g]	Co/Mo [mol/mol]	P/Mo [mol/mol]	CoO [wt%]	MoO ₃ [wt%]	P ₂ O ₅ [wt%]	LOI [wt%]
CoMo_AHM(c)	258	0.41	-	3.63	16.9	-	4.92
CoMo_HPA(c)	260	0.47	-	4.35	17.8	-	0.74
CoMoP(1c)	248	0.36	0.12	3.38	17.6	1.05	0.25
CoMoP(2c)	223	0.38	0.23	3.60	18.3	2.10	0.00
CoMoP(3c)	223	0.37	0.38	3.56	18.4	3.49	1.19
CoMoP(5c)	213	0.38	0.54	3.60	18.0	4.80	0.64

Table 3: Properties of additive-free dried Mo(P) catalysts.

Catalyst	P/Mo [mol/mol]	MoO ₃ [wt%]	P ₂ O ₅ [wt%]	LOI [wt%]
Mo_AHM(d)	-	15.7	-	13.44
MoP(2d)	0.24	15.1	1.76	15.05
MoP(3d)	0.42	14.7	3.03	17.58
MoP(5d)	0.57	14.8	4.19	17.58

Table 4: Properties of additive-free calcined Mo(P)catalysts.

Catalyst	S _{BET} [m ² /g]	P/Mo [mol/mol]	MoO ₃ [wt%]	P ₂ O ₅ [wt%]	LOI [wt%]
Mo_AHM(c)	264	-	18.0	-	0.18
MoP(2c)	246	0.22	17.5	1.92	2.84
MoP(3c)	249	0.38	17.3	3.21	2.85
MoP(5c)	244	0.53	17.4	4.57	2.46

Table 5: Properties of additive-free dried P/Al₂O₃ samples.

Sample	P ₂ O ₅ [wt%]	LOI [wt%]
P(1d)	0.83	23.35
P(3d)	3.09	21.46
P(5d)	4.23	23.60

Table 6: Properties of additive-free calcined P/Al_2O_3 samples.

Sample	S_{BET} [m ² /g]	P_2O_5 [wt%]	LOI [wt%]
P(1c)	288	1.03	4.06
P(2c)	277	2.00	0.11
P(3c)	271	3.79	3.60
P(5c)	246	5.38	2.87

Table 7: Properties of additive-containing dried CoMo(P) catalysts.

Catalyst	Co/Mo [mol/mol]	P/Mo [mol/mol]	TEG/Mo [mol/mol]	TEG [wt%]	CoO [wt%]	MoO ₃ [wt%]	P ₂ O ₅ [wt%]	LOI [wt%]
CoMo_AHM(d)+TEG	0.40	-	0.78	12.1	3.11	14.9	-	24.5
CoMo_HPA(d)+TEG	0.46	-	0.71	10.7	3.48	14.4	-	30.12
CoMoP(1d)+TEG	0.36	0.12	0.85	12.1	2.54	13.6	0.94	30.71
CoMoP(3d)+TEG	0.39	0.45	1.24	17.9	2.76	13.7	3.02	20.42
CoMoP(5d)+TEG	0.39	0.65	0.80	11.70	2.86	14.1	4.50	18.80

Table 8: Properties of additive-containing calcined CoMo(P) catalysts.

Catalyst	Co/Mo [mol/mol]	P/Mo [mol/mol]	TEG/Mo [mol/mol]	TEG [wt%]	CoO [wt%]	MoO ₃ [wt%]	P ₂ O ₅ [wt%]	LOI [wt%]
CoMo_AHM(c)+TEG	0.40	-	0.76	12.0	3.14	15.2	-	17.02
CoMo_HPA(c)+TEG	0.47	-	0.63	9.7	3.59	14.8	-	25.59
CoMoP(1c)+TEG	0.36	0.14	0.80	11.5	2.62	13.8	0.82	28.16
CoMoP(3c)+TEG	0.38	0.38	0.77	11.8	2.94	14.7	2.79	16.19
CoMoP(5c)+TEG	0.39	0.54	0.77	11.9	2.96	14.7	3.92	14.78

Table 9: Properties of additive-containing dried Mo(P) catalysts.

Catalyst	P/Mo [mol/mol]	TEG/Mo [mol/mol]	TEG [wt%]	MoO ₃ [wt%]	P ₂ O ₅ [wt%]	LOI [wt%]
Mo_AHM(d)+TEG	-	0.79	11.8	14.2	-	20.08
MoP(2d)+TEG	0.24	0.71	10.6	14.4	1.68	18.32
MoP(3d)+TEG	0.42	0.75	11.1	14.2	2.94	19.27
MoP(5d)+TEG	0.57	0.76	11.5	14.6	4.14	17.03

Table 10: Properties of additive-containing calcined Mo(P) catalysts.

Catalyst	P/Mo [mol/mol]	TEG/Mo [mol/mol]	TEG [wt%]	MoO ₃ [wt%]	P ₂ O ₅ [wt%]	LOI [wt%]
Mo_AHM(c)+TEG	-	0.73	11.4	15.0	-	21.81
MoP(2c)+TEG	0.22	0.72	10.8	14.4	1.59	17.35
MoP(3c)+TEG	0.38	0.76	11.2	14.2	2.64	19.26
MoP(5c)+TEG	0.53	0.83	12.8	14.7	3.87	16.94

Table 11: Properties of additive-containing dried P/Al_2O_3 samples.

Sample	TEG [wt%]	P_2O_5 [wt%]	LOI [wt%]
P(1d)+TEG	11.4	1.29	15.69
P(3d)+TEG	10.3	4.10	14.90
P(5d)+TEG	11.0	6.71	17.62

Table 12: Properties of additive-containing calcined P/Al_2O_3 samples.

Sample	TEG [wt%]	P_2O_5 [wt%]	LOI [wt%]
P(1c)+TEG	12.4	1.18	15.68
P(3c)+TEG	10.3	4.11	13.94
P(5c)+TEG	10.8	6.69	16.02

Table 13: Properties of a series of additive-containing dried CoMoP(5d)+TEG catalysts.

Catalyst	Co/Mo [mol/mol]	P/Mo [mol/mol]	TEG/Mo [mol/mol]	TEG [wt%]	CoO [wt%]	MoO ₃ [wt%]	P_2O_5 [wt%]	LOI [wt%]
CoMoP(5d)+TEG(0.10)	0.38	0.56	0.18	2.94	3.11	15.7	4.35	13.57
CoMoP(5d)+TEG(0.25)	0.38	0.65	0.24	3.95	3.08	15.5	4.95	15.61
CoMoP(5d)+TEG(0.50)	0.38	0.58	0.53	8.42	2.97	15.1	4.35	16.53
CoMoP(5d)+TEG(0.75)	0.39	0.65	0.80	11.70	2.86	14.1	4.50	18.80
CoMoP(5d)+TEG(1.25)	0.39	0.58	1.19	16.92	2.74	13.6	3.90	20.16
CoMoP(5d)+TEG(1.50)	0.39	0.65	1.44	19.19	2.60	12.8	4.08	26.55
CoMoP(5d)+TEG(2.00)	0.39	0.76	2.00	24.39	2.39	11.7	4.39	32.68
CoMoP(5d)+TEG(2.50)	0.39	0.75	2.54	29.47	2.28	11.1	4.09	35.93

Table 14: Properties of a series of additive co-impregnated CoMoP(5)+TEG(CI) catalysts.

Catalyst	Co/Mo [mol/mol]	P/Mo [mol/mol]	TEG/Mo [mol/mol]	TEG [wt%]	CoO [wt%]	MoO ₃ [wt%]	P_2O_5 [wt%]	LOI [wt%]
CoMoP(5)+TEG(CI)	0.38	0.60	0.26	4.12	3.06	15.5	4.58	15.23
CoMoP(5)+TEG(CI)	0.38	0.64	0.51	8.10	3.00	15.3	4.82	14.16
CoMoP(5)+TEG(CI)	0.38	0.61	0.79	12.38	2.99	14.9	4.51	18.48
CoMoP(5)+TEG(CI)	0.38	0.67	1.01	15.19	2.84	14.4	4.72	19.71

Table 15: Properties of pre-impregnated CoMo_HPA and CoMoP(5) catalysts.

Catalyst	Co/Mo [mol/mol]	P/Mo [mol/mol]	TEG/Mo [mol/mol]	TEG [wt%]	CoO [wt%]	MoO ₃ [wt%]	P_2O_5 [wt%]	LOI [wt%]
CoMo_HPA+TEG(PI)	0.46	-	0.93	12.98	3.19	13.4	-	20.00
CoMoP(5)+TEG(PI)	0.39	0.67	0.86	11.34	2.59	12.7	4.17	20.77

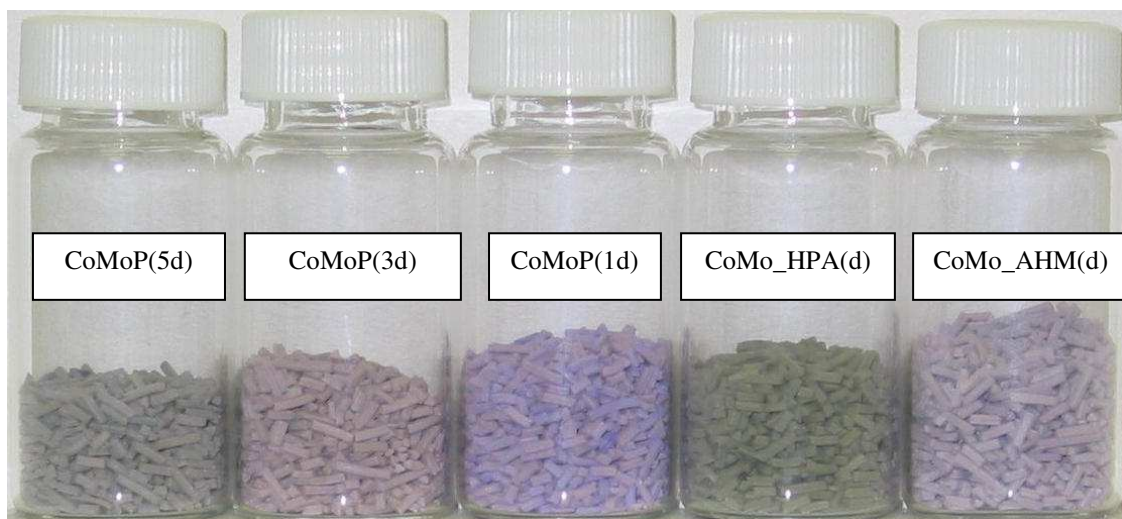
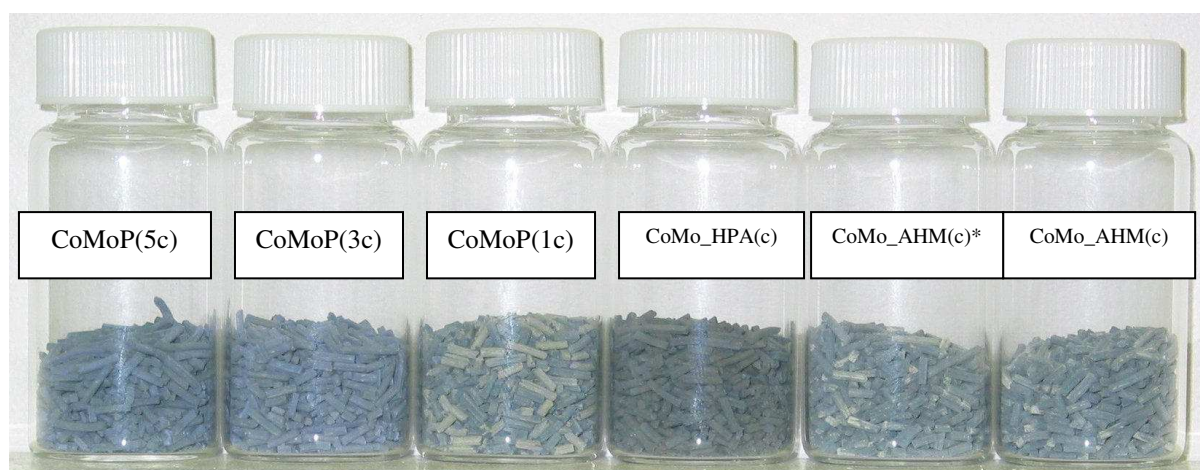


Figure 1: Dried CoMo(P) catalysts.



*Figure 2: Calcined CoMo(P) catalysts. Note: * submitted to an intermediary drying stage*

APPENDIX B: ADDITIVES LIQUID-GAS EQUILIBRIUM

Figure 3 presents the liquid-gas equilibrium of TEG and DEGbe for pressures inferior to 1 bar, based on the Antoine equation.

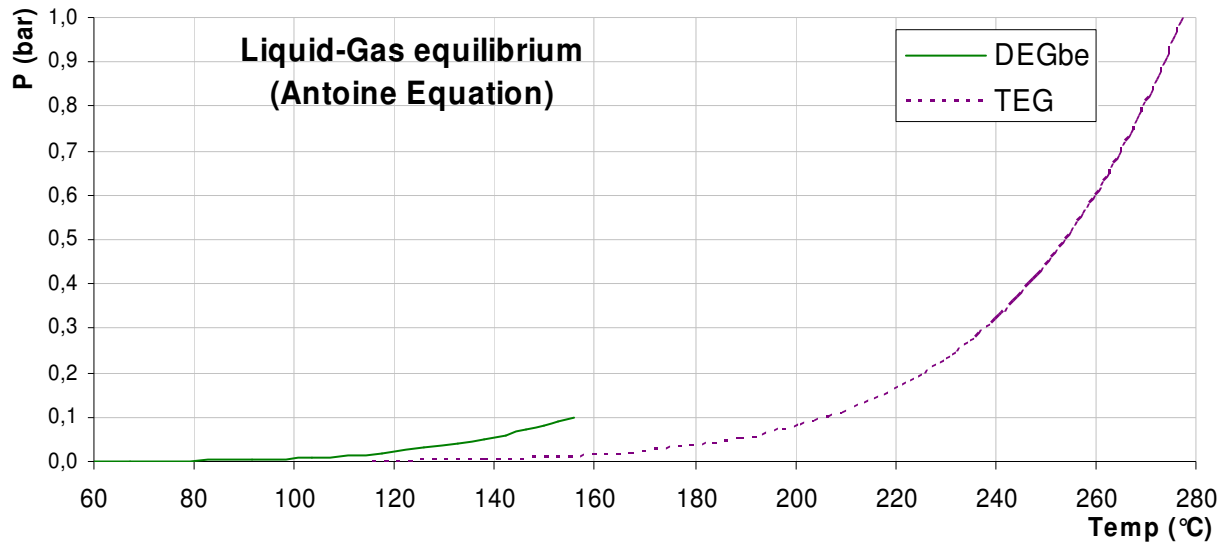


Figure 3: Liquid-Gas equilibrium for $P < 1$ bar of TEG and DEGbe.

Figure 4 presents the liquid-gas equilibrium of TEG and DEGbe for pressures superior to 1 bar up to the critical point. These results are based on the Save-Redlich-Kwong model, using *Pro II – Simulation Sciences Inc.* software.

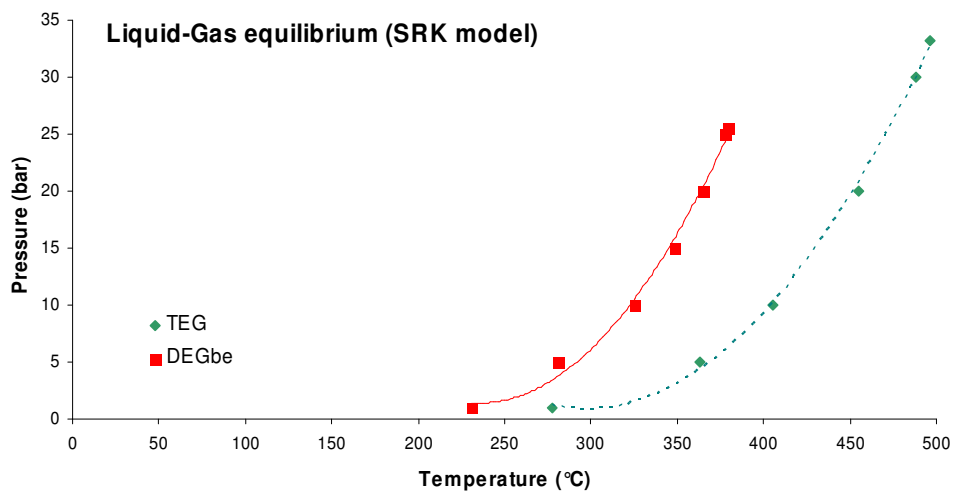


Figure 4: Liquid-Gas equilibrium for $P > 1$ bar of TEG and DEGbe.

APPENDIX C: MATHEMATICAL DECOMPOSITION OF EXPERIMENTAL SPECTRA

The DTG and NMR spectra were simulated by means of Lorentz functions. These functions are widely used in spectroscopy to describe the line shape of spectral lines. Each function is characterized by 3 parameters: amplitude (A), location (x_0) and width at half-maximum (σ):

$$f(x) = A \cdot \frac{\sigma^2}{4} \cdot \frac{1}{\frac{\sigma^2}{4} + (x - x_0)^2} \quad \text{Equation 1}$$

To perform the fit, the baseline was previously defined, which corresponds to the minimum of the spectral line in the fit range. The simulation of the spectral line is then obtained by calculating the sum of all the individual Lorentz function.

The criteria used in the fitting is the least squares method. More precisely, it consists in varying the Lorentz function parameters with the purpose of minimizing the sum (S) expressed in Equation 2.

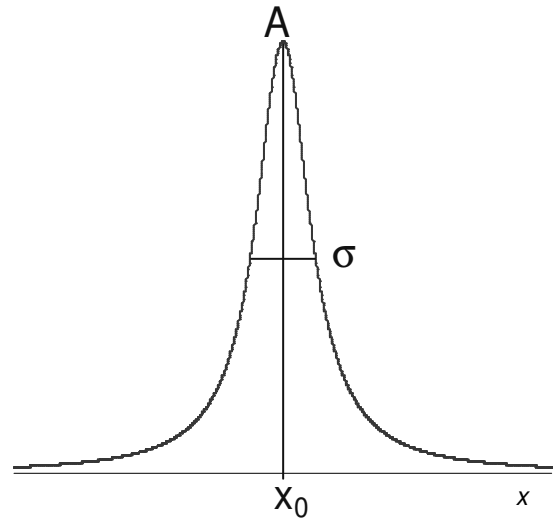


Figure 5: Lorentz function.

$$S = \sum_{i=1}^n |y_i^2 - f(x_i)^2| \quad \text{Equation 2}$$

y_i corresponds to a spectrum point.

Once the spectral line is simulated, the weight of each contribution was measured by determining the area of each function in the fit range. The trapezoidal rule was used for the numerical integration.

$$Area = \sum_{i=1}^n \left[(x_{i+1} - x_i) \cdot \left| \frac{y_{i+1} + y_i}{2} \right| \right] \quad \text{Equation 3}$$

APPENDIX D: TABLES INDEX

CHAPTER I: BIBLIOGRAPHIC STUDY

Table I-1: Oil fractions classification.	6
Table I-2: Most common HDT applications.	8
Table I-3: IR and Raman data of bulk Anderson salts.	16
Table I-4: ³¹ P NMR chemical shift data for reference compounds.	17
Table I-5: Glycol-type molecules suitable to be used as additives.	24
Table I-6: Additives boiling point, melting point, decomposition temperatures and viscosities.	25
Table I-7: IR attributions for alumina hydroxyl groups proposed by Digne.	26
Table I-8: BET surface area and pore volume of an additive-free and additive-containing alumina.	26
Table I-9: Textural properties and thiophene HDS conversion of CoMoP catalysts.	30
Table I-10: Conditions for presulfidation and test reactions used in patent examples.	31

CHAPTER II: EXPERIMENTAL

Table II-1: P/Mo, Co/Mo molar ratios and precursors used in CoMo(P) catalysts.	47
Table II-2: Water pore volume of dried CoMo(P), Mo(P) and P/Al ₂ O ₃ samples.	48
Table II-3: Water pore volume of calcined CoMo(P), Mo(P) and P/Al ₂ O ₃ samples.	48
Table II-4: Experimental conditions for DEGBE pore volume impregnation on alumina.	50
Table II-5: Acquisition parameters used for the molybdenum and cobalt K-edges.	57
Table II-6: Operating conditions for the sulfidation and test stages of the HSC catalytic test.	60
Table II-7: Operating conditions for the sulfidation and test stages of the real feed HDS cat. test.	62

CHAPTER III: THE ROLE OF GLYCOL-TYPE ADDITIVES ON DRIED CoMo(P) CATALYSTS

Table III-1: Raman shift of dried CoMo-based catalysts and reference data.	75
Table III-2: Speciation of CoMo solutions and dried catalysts prior to and after TEG impregnation.	79
Table III-3: DTG decomposition assignments of the Mo_AHM(d) sample.	82
Table III-4: DTG decomposition assignments of the CoMo_AHM(d) sample.	82
Table III-5: DTG decomposition assignments of the CoMo_HPA(d) sample.	84
Table III-6: DTG decomposition assignments of the Mo_AHM(d)+TEG sample.	85
Table III-7: DTG decomposition assignments of the CoMo_HPA(d)+TEG sample.	87
Table III-8: Raman shift of dried CoMoP catalysts and reference data.	95
Table III-9: Raman shift of additive-containing dried CoMoP catalysts and reference data.	97
Table III-10: ³¹ P MAS NMR data extracted from experimental data decompositions.	100
Table III-11: Speciation of CoMoP solutions and dried catalysts prior to and after TEG impregnation.	104
Table III-12: DTG decomposition assignments of the CoMoP(1d) and CoMoP(5d) samples.	106
Table III-13: DTG decomposition assignments of the CoMoP(1d)+TEG and CoMoP(5d)+TEG samples.	108

CHAPTER IV: THE ROLE OF GLYCOL-TYPE ADDITIVES ON CALCINED CoMo(P) CATALYSTS

Table IV-1: Surface area and average pore diameter of calcined CoMo-based catalysts and alumina.	116
Table IV-2: Speciation results for the calcined CoMo catalysts prior to and after TEG impregnation.	121
Table IV-3: DTG decomposition assignments of the CoMo_AHM(c)+TEG sample.	125
Table IV-4: DTG decomposition assignments of the CoMo_AHM(c)+TEG sample.	126
Table IV-5: Surface area and average pore diameter of calcined CoMoP catalysts.	127
Table IV-6: Surface area and average pore diameter of calcined CoMoP catalysts.	128
Table IV-7: ³¹ P MAS NMR data extracted from experimental data decompositions.	136
Table IV-8: Speciation results for calcined CoMoP catalysts prior to and after TEG impregnation.	139
Table IV-9: DTG decomposition assignments of the CoMoP(1c)+TEG sample.	147
Table IV-10: DTG decomposition assignments of the CoMo_AHM(c)+TEG sample.	148

CHAPTER V: THE ROLE OF GLYCOL-TYPE ADDITIVES ON CoMo(P) CATALYSTS PREPARED FROM AN ADDITIVE-CONTAINING ALUMINA

Table V-1: Physical properties of TEG and DEGBE molecules.	164
Table V-2: Calculated molecular dimensions and adsorbed densities on the alumina support.	165

CHAPTER VI: THE ROLE OF GLYCOL-TYPES ADDITIVES ON CoMo(P) CATALYSTS PREPARED BY CO-IMPREGNATION

Table VI-1: Speciation results for CoMoP precursor solutions prior to and after TEG impregnation.	185
---	-----

CHAPTER VII: IMPACT OF THE ADDITIVE ON THE ACTIVATION STAGE AND EVALUATION OF CATALYTIC PERFORMANCES

Table VII-1: Structural parameters resulting from the Co K-edge Fourier-filtered k ³ -weighted EXAFS functions of the ex situ sulfided additive-free dried catalysts.	197
Table VII-2: Structural parameters resulting from the Co K-edge Fourier-filtered k ³ -weighted EXAFS functions of the ex situ sulfided additive-containing dried catalysts.	197
Table VII-3: XPS parameters used for the Co 2p spectra decomposition of sulfided samples.	198
Table VII-4: Structural parameters resulting from the Co K-edge Fourier-filtered k ³ -weighted EXAFS functions of the ex situ sulfided calcined catalysts.	200
Table VII-5: Structural parameters resulting from the Mo K-edge Fourier-filtered k ³ -weighted EXAFS functions of the ex situ sulfided additive-free dried catalysts.	203
Table VII-6: Structural parameters resulting from the Mo K-edge Fourier-filtered k ³ -weighted EXAFS functions of the ex situ sulfided additive-containing dried catalysts.	204
Table VII-7: XPS parameters used for the Mo 3d spectra decomposition of sulfided samples.	204
Table VII-8: Structural parameters resulting from the Mo K-edge Fourier-filtered k ³ -weighted EXAFS functions of the ex situ sulfided additive-free calcined catalysts.	207
Table VII-9: Structural parameters resulting from the Mo K-edge Fourier-filtered k ³ -weighted EXAFS functions of the ex situ sulfided additive-containing calcined catalysts.	207
Table VII-10: MoS ₂ morphology of ex situ sulfided CoMo(P) catalysts as observed by TEM.	210
Table VII-11: Structural parameters resulting from the Co K-edge Fourier-filtered k ³ -weighted EXAFS functions of the in situ sulfided additive-free CoMoP(5d) catalyst.	212
Table VII-12: Structural parameters resulting from the Co K-edge Fourier-filtered k ³ -weighted EXAFS functions of the in situ sulfided additive-containing CoMoP(5d) catalyst.	212
Table VII-13: Structural parameters resulting from the Mo K-edge Fourier-filtered k ³ -weighted EXAFS functions of the in situ sulfided additive-free CoMoP(5d) catalyst.	215
Table VII-14: Structural parameters resulting from the Mo K-edge Fourier-filtered k ³ -weighted EXAFS functions of the in situ sulfided additive-containing CoMoP(5d) catalyst.	215

APPENDIX E: FIGURES INDEX

CHAPTER I: BIBLIOGRAPHIC STUDY

Figure I-1: Refinery scheme.	7
Figure I-2: Simplified reaction scheme of 4,6-DMDBT hydrodesulfurization.	9
Figure I-3: RIM/EDGE model proposed by Daage and Chianelli.	10
Figure I-4: Schematic representation of the different phases present in typical alumina-supported catalysts.	11
Figure I-5: Geometric Model for decorated MoS ₂ proposed by Kasztelan et al.	12
Figure I-6: MoS ₂ crystallites decorated by cobalt - Hexagonally Truncated nanocluster.	12
Figure I-7: Active phase composition influence in toluene HYD activity.	14
Figure I-8: Keggin heteropolyanion.	15
Figure I-9: Dawson heteropolyanion.	15
Figure I-10: Diphosphopentamolybdate heteropolyanion.	15
Figure I-11: Anderson heteropolyanion.	16
Figure I-12: Co ₂ Mo ₁₀ O ₃₈ H ₄ ⁶⁻ heteropolyanion.	16
Figure I-13: Schematic representation of molybdenum and cobalt complexes distribution over an alumina after impregnation with an H ₂ PMo ₁₁ CoO ₄₀ ⁵⁻ solution.	19
Figure I-14: Possible additive impregnation stage locations in the preparation method of CoMo(P) catalysts.	22
Figure I-15: Schematic representation of hydrogen-bonding possibilities for DEGbe adsorption over alumina.	27
Figure I-16: Schematic representation of PEG adsorption mechanisms on alumina..	28
Figure I-17: DRIFT spectra of alumina impregnated with glycol-type additives.	29
Figure I-18: UV-Visible spectra of AHM and cobalt nitrate aqueous solutions in presence of additives.	30
Figure I-19: Laser Raman spectra of CoMoP, CoMoP-TEG and TEG solutions.	19
Figure I-20: HDS activities for additive-containing CoMoP catalysts.	32
Figure I-21: HDS activities for DEG-impregnated CoMoP catalysts.	33
Figure I-22: Liquid State ³¹ P NMR spectra of P ₂ O ₅ dissolved in n-butanol.	35
Figure I-23: Sulfidation degree of additive-free and additive-containing calcined CoMoP catalyst.	36
Figure I-24: Sulfidation degree for additive-free and additive-containing CoMo(P) catalysts.	37

CHAPTER II: EXPERIMENTAL

Figure II-1: CoMo_AHM catalysts preparation.	45
Figure II-2: CoMo(P) catalysts preparation.	46
Figure II-3: Experimental procedure used in the adsorption study.	49
Figure II-4: Experimental procedure used in the adsorption study with an intermediary drying step.	50
Figure II-5: Temperature program used in DRIFT spectroscopy.	54
Figure II-6: Mo K-edge absorption and normalized spectra of the CoMoP(5d) catalyst.	57
Figure II-7: Mo K-edge k ³ -weighted Interference function and FT modulus of the CoMoP(5d) sample.	58
Figure II-8: Main reaction products of toluene hydrogenation and cyclohexane isomerization.	60
Figure II-9: Hydrogenation activity and isomerization conversion of the CoMoP(5d) catalyst.	61
Figure II-10: Sulfur concentration evolution in the HDS test of the CoMoP(5d)+TEG catalyst.	62
Figure II-11: Sulfur content after HDS reaction at different temperatures for the CoMoP(5d)+TEG catalyst.	63

CHAPTER III: THE ROLE OF GLYCOL-TYPE ADDITIVES ON DRIED CoMo(P) CATALYSTS

Figure III-1: Preparation of additive-containing dried CoMoP catalysts.	67
Figure III-2: UV-Visible spectra of the CoMo_AHM and CoMo_HPA impregnation solutions and the cobalt nitrate reference solution.	68
Figure III-3: Raman spectrum of the CoMo_HPA solution.	69
Figure III-4: UV-Visible diffuse reflectance spectra of CoMo_AHM(d), CoMo_HPA(d) and corresponding additive-containing catalysts.	70
Figure III-5: Cobalt K-edge XANES spectra of CoMo_AHM(d), CoMo_HPA(d) and CoMo_HPA(d)+TEG catalysts.	71
Figure III-6: Cobalt K-edge k ³ -weighted EXAFS Fourier transforms of CoMo_AHM(d), CoMo_HPA(d) and corresponding additive-containing catalysts.	72
Figure III-7: Cobalt 2p XPS spectra of the CoMo_HPA(d) and CoMoP(5d) catalysts.	73
Figure III-8: Cobalt 2p XPS spectrum decomposition of the CoMoP(5d) catalyst.	74

Figure III-9: Cobalt 2p XPS spectrum decomposition of the CoMo_HPA(d) catalyst.	74
Figure III-10: Raman spectra of CoMo_AHM(d), CoMo_HPA(d) and additive-containing catalysts.	76
Figure III-11: ^{27}Al MAS NMR spectra and $^{27}\text{Al}/^1\text{H}$ CP MAS NMR spectra of alumina, CoMo_AHM(d) and corresponding additive-containing catalyst.	77
Figure III-12: X-ray Diffraction patterns for CoMo_AHM(d), CoMo_AHM(d)+TEG and CoMo_AHM(d) saturated with TEG.	78
Figure III-13: Mo K-edge XANES and k^3 -weighted EXAFS Fourier Transforms of CoMo_AHM(d), CoMo_HPA(d) and corresponding additive-containing catalysts.	79
Figure III-14: Thermogravimetric analysis, derivative thermogravimetry and mass spectroscopy results of the Mo_AHM(d) sample.	80
Figure III-15: Thermogravimetric analysis, derivative thermogravimetry and mass spectroscopy results of the CoMo_AHM(d) sample.	81
Figure III-16: Mo_AHM(d) and CoMo_AHM(d) samples DTG decompositions.	82
Figure III-17: Thermogravimetric analysis, derivative thermogravimetry and mass spectroscopy results of the CoMo_HPA(d) sample.	83
Figure III-18: DTG decomposition of the CoMo_HPA(d) catalyst.	83
Figure III-19: Thermogravimetric analysis, derivative thermogravimetry and mass spectroscopy results of the Mo_AHM(d) sample.	84
Figure III-20: DTG decomposition of the Mo_AHM(d)+TEG sample.	85
Figure III-21: Thermogravimetric analysis, derivative thermogravimetry and mass spectroscopy results of the CoMo_HPA(d)+TEG sample.	86
Figure III-22: DTG decomposition of the CoMo_HPA(d)+TEG catalyst.	86
Figure III-23: Schematic representations of the redispersion mechanism induced by the additive for the dried CoMo_AHM(d) and CoMo_HPA(d) catalysts.	87
Figure III-24: UV-Visible spectra of CoMo_AHM, CoMo_HPA, CoMoP(1), CoMoP(3) and CoMoP(5) precursor solutions.	88
Figure III-25: UV-Visible spectra of CoP(5), MoP(3), MoP(5), CoMoP(3) and CoMoP(5) solutions.	89
Figure III-26: Raman spectra of the CoMoP precursor solutions.	90
Figure III-27: ^{31}P NMR spectra of MoP(2), MoP(3) and MoP(5) precursor solutions.	91
Figure III-28: Raman spectra of the MoP(5) precursor solution.	92
Figure III-29: UV-Visible DRS of dried CoMoP and corresponding additive-containing catalysts.	93
Figure III-30: Cobalt K-edge k^3 -weighted EXAFS FT of dried CoMoP and corresponding additive-containing catalysts.	94
Figure III-31: Raman spectra of dried CoMoP catalysts.	95
Figure III-32: Raman spectra of additive-containing dried CoMoP catalysts.	96
Figure III-33: Mo K-edge XANES and k^3 -weighted EXAFS FT of dried CoMoP and corresponding additive-containing catalysts.	97
Figure III-34: ^{31}P MAS NMR spectra of dried $\text{P}/\text{Al}_2\text{O}_3$ and corresponding additive-containing samples.	99
Figure III-35: ^{31}P MAS NMR spectra decomposition of dried $\text{P}/\text{Al}_2\text{O}_3$ and corresponding additive-containing samples.	100
Figure III-36: ^{31}P MAS NMR spectrum of the CoMoP(5d) catalyst.	101
Figure III-37: ^{31}P MAS NMR spectra of dried MoP and corresponding additive-containing catalysts.	101
Figure III-38: ^{31}P MAS NMR spectra decomposition of MoP and corresponding additive-containing catalysts.	102
Figure III-39: Raman spectra of the MoP(5d) and corresponding additive-containing catalyst.	103
Figure III-40: Thermogravimetric analysis, derivative thermogravimetry and mass spectroscopy results of the CoMoP(1d) catalyst.	104
Figure III-41: Thermogravimetric analysis, derivative thermogravimetry and mass spectroscopy results of the CoMoP(5d) catalyst.	105
Figure III-42: CoMoP(1d) and CoMoP(5d) catalysts DTG decompositions.	105
Figure III-43: Thermogravimetric analysis, derivative thermogravimetry and mass spectroscopy results of the CoMoP(1d)+TEG catalyst.	106
Figure III-44: Thermogravimetric analysis, derivative thermogravimetry and mass spectroscopy results of the CoMoP(5d)+TEG catalyst.	107
Figure III-45: CoMoP(1d)+TEG and CoMoP(5d)+TEG catalysts DTG decompositions.	107
Figure III-46: Schematic representations of the redispersion mechanism induced by the additive for dried CoMoP catalysts.	109

CHAPTER IV: THE ROLE OF GLYCOL-TYPE ADDITIVES ON CALCINED CoMo(P) CATALYSTS

Figure IV-1: Preparation of additive-containing calcined CoMoP catalysts.	115
Figure IV-2: BJH porous distribution of alumina and calcined CoMo_AHM and CoMo_HPA catalysts.	116
Figure IV-3: UV-visible diffuse reflectance spectra of CoMo_AHM(c), CoMo_HPA(c) and corresponding additive-containing catalysts.	117
Figure IV-4: Cobalt K-edge XANES spectra of the CoMo_AHM(c), CoMo_HPA(c) and corresponding additive-containing catalysts.	118
Figure IV-5: Cobalt K-edge k^3 -weighted EXAFS Fourier Transforms of the CoMo_AHM(c), CoMo_HPA(c) and corresponding additive-containing catalysts.	118
Figure IV-6: Raman spectra of calcined CoMo and corresponding additive-containing catalysts.	119
Figure IV-7: X-Ray Diffraction spectra for CoMo_AHM(c), CoMo_AHM(c)+TEG and CoMo_AHM(c) saturated with TEG.	120
Figure IV-8: Mo K-edge XANES and k^3 -weighted EXAFS Fourier Transforms of CoMo_AHM(c), CoMo_HPA(c) and corresponding additive-containing catalysts.	121
Figure IV-9: Aluminium, molybdenum and cobalt electron probe microanalysis of the CoMo_AHM(c) catalyst.	122
Figure IV-10: Thermogravimetric analysis and derivative thermogravimetry of the CoMo_AHM(c) and CoMo_HPA(c) catalysts.	122
Figure IV-11: Mass spectroscopy follow-up of the CoMo_AHM(c) catalyst.	123
Figure IV-12: DTG decomposition of the calcined CoMo_AHM(c) and CoMo_HPA(c) catalysts.	123
Figure IV-13: Thermogravimetric analysis, derivative thermogravimetry and mass spectroscopy of the CoMo_AHM(c)+TEG sample.	124
Figure IV-14: DTG decomposition of the CoMo_AHM(c)+TEG sample.	124
Figure IV-15: Thermogravimetric analysis, derivative thermogravimetry and mass spectroscopy results of the CoMo_HPA(c)+TEG sample.	125
Figure IV-16: DTG decomposition of the CoMo_HPA(c)+TEG sample.	125
Figure IV-17: Schematic representation of the redispersion mechanism induced by the additive for the alumina-supported calcined CoMo-based catalysts.	126
Figure IV-18: BJH porous distribution of calcined CoMoP catalysts.	127
Figure IV-19: BJH porous distribution of calcined MoP catalysts.	128
Figure IV-20: BJH porous distribution of CoMoP(c), MoP(c), P(c) and alumina solids.	129
Figure IV-21: BET surface area as a function of phosphorus loading and impregnation solution pH.	129
Figure IV-22: UV-visible diffuse reflectance spectra of calcined CoMoP and corresponding additive-containing catalysts.	130
Figure IV-23: Cobalt K-edge spectra of calcined CoMoP and corresponding additive-containing catalysts.	131
Figure IV-24: Cobalt K-edge k^3 -weighted EXAFS Fourier Transforms of calcined CoMoP and corresponding additive-containing catalysts.	131
Figure IV-25: Raman spectra of calcined CoMoP catalysts.	132
Figure IV-26: Raman spectra of additive-containing calcined CoMoP catalysts.	133
Figure IV-27: Mo K-edge XANES and k^3 -weighted EXAFS Fourier Transforms of CoMo_AHM(c), CoMo_HPA(c) and corresponding additive-containing catalysts.	134
Figure IV-28: ^{31}P MAS NMR spectra of calcined $\text{P}/\text{Al}_2\text{O}_3$ and corresponding additive-containing solids.	135
Figure IV-29: ^{31}P MAS NMR spectra decomposition of calcined $\text{P}/\text{Al}_2\text{O}_3$ and corresponding additive-containing solids.	135
Figure IV-30: ^{31}P MAS NMR spectra of the CoMoP(5c) catalyst.	136
Figure IV-31: ^{31}P MAS NMR spectra of calcined MoP and corresponding additive-containing catalysts.	137
Figure IV-32: ^{31}P MAS NMR spectra decomposition of calcined MoP and corresponding additive-containing solids.	138
Figure IV-33: Raman spectra of additive-containing dried and calcined MoP(5) catalysts.	139
Figure IV-34: Aluminium, molybdenum, cobalt and phosphorus Electron Probe Microanalysis of the calcined CoMoP(c) catalysts.	140
Figure IV-35: Electron Probe Microanalysis for phosphorus distribution of the calcined CoMoP catalysts.	141
Figure IV-36: Electron Probe Microanalysis for phosphorus distribution of the calcined MoP catalysts and the calcined $\text{P}/\text{Al}_2\text{O}_3$ solids.	142
Figure IV-37: Schematic representation of the P_2O_5 reaction with DEGbe experimental protocol.	142
Figure IV-38: ^{13}C NMR of liquid DEGbe.	143

Figure IV-39: ^{13}C NMR of a P_2O_5 +DEGbe.	143
Figure IV-40: ^1H NMR of a P_2O_5 +DEGbe.	143
Figure IV-41: ^{31}P NMR of P_2O_5 +DEGbe after 24h at room-temperature and after 20h reflux.	144
Figure IV-42: Thermogravimetric analysis and derivative thermogravimetry of the CoMoP(1c) and CoMoP(5c) catalysts.	145
Figure IV-43: Mass spectroscopy follow-up of the CoMoP(1c) catalysts.	145
Figure IV-44: DTG decomposition of the calcined CoMoP(1c) and CoMoP(5c) catalysts.	146
Figure IV-45: Thermogravimetric analysis, derivative thermogravimetry and mass spectroscopy of the CoMoP(1c) sample.	146
Figure IV-46: DTG decomposition of the CoMoP(1c)+TEG sample.	147
Figure IV-47: Thermogravimetric analysis, derivative thermogravimetry and mass spectroscopy results of the CoMoP(5c) sample.	148
Figure IV-48: DTG decomposition of the CoMoP(5c)+TEG sample.	148
Figure IV-49: Additive-containing CoMoP(5c) catalyst long term stability.	149
Figure IV-50: Schematic representation of the redispersion mechanism induced by the additive for the alumina-supported CoMoP(1c) catalysts.	150
Figure IV-51: Schematic representation of the redispersion mechanism induced by the additive for the alumina-supported CoMoP(5c) catalysts.	150

CHAPTER V: THE ROLE OF GLYCOL-TYPE ADDITIVES ON CoMo(P) CATALYSTS PREPARED FROM AN ADDITIVE-CONTAINING ALUMINA

Figure V-1: Preparation of CoMoP catalysts using a TEG pre-impregnated alumina.	155
Figure V-2: DRIFT spectra in the $2800\text{--}3800\text{ cm}^{-1}$ region of the γ -alumina support from 25 to $550\text{ }^\circ\text{C}$.	156
Figure V-3: Transmission infrared spectrum in the $2800\text{--}3800\text{ cm}^{-1}$ region of the γ -alumina support at $530\text{ }^\circ\text{C}$	156
Figure V-4: Thermogravimetric analysis, derivative thermogravimetry and mass spectroscopy results of the alumina support.	157
Figure V-5: Alumina support DTG decomposition.	158
Figure V-6: Raman spectrum of liquid DEGbe.	158
Figure V-7: Raman spectrum of additive-containing alumina (1.1 DEGbe/nm^2).	159
Figure V-8: DRIFT spectrum of an additive-containing alumina (1.1 DEGbe/nm^2) from 25 to $550\text{ }^\circ\text{C}$.	160
Figure V-9: DRIFT spectra at $200\text{ }^\circ\text{C}$ of additive-free and additive-containing aluminas	160
Figure V-10: DRIFT spectra subtraction of the additive-containing alumina (1.1 DEGbe/nm^2) and the alumina support in the hydroxyl region.	161
Figure V-11: Thermogravimetric analysis, derivative thermogravimetry and mass spectroscopy results of the alumina support.	162
Figure V-12: Thermogravimetric analysis, derivative thermogravimetry and mass spectroscopy results of the alumina support.	162
Figure V-13: TEG- and DEGbe-impregnated aluminas	163
Figure V-14: Chemical adsorption model for DEGbe molecules onto γ -alumina.	164
Figure V-15: Geometrical adsorption model for DEGbe molecules on the alumina support.	164
Figure V-16: DEGbe adsorbed onto alumina by excess impregnation for 96h at room temperature, prior to and after washing.	165
Figure V-17: Additive loading in the mother and washing solutions of the excess impregnations.	165
Figure V-18: Adsorbed DEGbe on the alumina support using incipient wetness impregnations with different ageing conditions, prior to and after the washing stage.	166
Figure V-19: DEGbe loading in the washing solutions of DEGbe/ Al_2O_3	166
Figure V-20: Adsorbed additive on the alumina support using incipient wetness impregnations, prior to and after the washing stage with an intermediary drying step at $70\text{ }^\circ\text{C}$ and 50 mbar.	167
Figure V-21: Additive amount in washing solutions of additive-impregnated aluminas.	167
Figure V-22: Schematic representation of additives adsorption monolayer.	168
Figure V-23: UV-Visible diffuse reflectance spectra of additive-free	169
Figure V-24: Co 2p XPS spectra of the CoMo_HPA(d), CoMo_HPA(d)+TEG and CoMo_HPA+TEG(PI) catalysts.	170
Figure V-25: UV-Visible diffuse reflectance spectra of the CoMoP(5d), CoMoP(5d)+TEG and CoMoP(5)+TEG(PI) catalysts	171
Figure V-26: Cobalt K-edge XANES and k^3 -weighted EXAFS Fourier Transforms of CoMoP(5d), CoMoP(5d)+TEG and CoMoP(5)+TEG(PI) catalysts.	171

Figure V-27: Raman spectra of additive-containing CoMo_HPA catalysts.	172
Figure V-28: Raman spectra of additive-containing CoMoP(5) catalysts.	173
Figure V-29: Molybdenum K-edge XANES and k^3 -weighted EXAFS Fourier Transforms of CoMoP(5d), CoMoP(5d)+TEG and CoMoP(5)+TEG(Pi) catalysts.	174
Figure V-30: EPMA of the CoMo_HPA+TEG(Pi) and CoMoP(5)+TEG(Pi) catalysts.	174
Figure V-31: Thermogravimetric analysis, derivative thermogravimetry and mass spectroscopy results of the CoMoP(5)+TEG(Pi) catalyst.	175
Figure V-32: TEG pre- or sequentially-impregnated CoMoP(5) DTG decomposition curves.	176
Figure V-33: Schematic representation of the surface mechanism for the CoMoP(5)+TEG(Pi) catalyst.	177

CHAPTER VI: THE ROLE OF GLYCOL-TYPES ADDITIVES ON CoMo(P) CATALYSTS PREPARED BY CO-IMPREGNATION

Figure VI-1: Preparation of additive-containing CoMoP catalysts using co-impregnation.	181
Figure VI-2: UV-Visible spectra of additive-free and additive-containing $\text{Co}(\text{NO}_3)_2$ and CoMo solutions.	182
Figure VI-3: UV-Visible spectra of additive-free and additive-containing CoMoP solutions	183
Figure VI-4: Raman spectra of additive-free and additive-containing CoMoP(5) solutions.	184
Figure VI-5: ^{31}P NMR spectra of MoP(2), MoP(3) and MoP(5) precursor solutions.	185
Figure VI-6: UV-Visible diffuse reflectance spectra of CoMoP(5d), CoMoP(5d)+TEG and co-impregnated CoMoP(5)+TEG(Ci) catalysts.	186
Figure VI-7: Raman spectra of additive-containing CoMoP(5) catalysts.	187
Figure VI-8: Electron Probe Microanalysis of the CoMoP(5)+TEG(Ci) catalyst.	187
Figure VI-9: EPMA phosphorus dispersion coefficient as a function of the TEG/Mo molar ratio in CoMoP(5)+TEG(Ci) catalysts.	188
Figure VI-10: Thermogravimetric analysis and derivative termogravimety of the CoMoP(5)+TEG(Ci) catalyst.	189
Figure VI-11: TEG co- or sequentially-impregnated CoMoP(5) DTG decomposition curves.	189
Figure VI-12: Schematic representation of the surface mechanism for the CoMoP(5)+TEG(Ci) catalyst.	190

CHAPTER VII: IMPACT OF THE ADDITIVE ON THE ACTIVATION STAGE AND EVALUATION OF CATALYTIC PERFORMANCES

Figure VII-1: Normalized Co K-edge XANES spectra of the dried CoMo_HPA(d) and corresponding ex situ sulfided catalyst.	196
Figure VII-2: Co K-edge k^3 -weighted EXAFS Fourier Transforms modulus of sulfided dried CoMo(P) and corresponding TEG-containing catalysts.	196
Figure VII-3: Co K-edge k^3 -weighted filtered EXAFS signal and corresponding Fourier Transforms modulus of CoMo_HPA(d) catalyst..	197
Figure VII-4: Cobalt 2p XPS spectrum decomposition of the sulfided CoMoP(5d) catalyst.	198
Figure VII-5: Cobalt 2p XPS spectrum decomposition results for additive-free and additive-containing dried CoMo(P) catalysts.	199
Figure VII-6: Cobalt K-edge k^3 -weighted EXAFS Fourier Transforms of sulfided calcined CoMo(P) catalysts and corresponding TEG-containing catalysts	200
Figure VII-7: Cobalt 2p XPS spectrum decomposition results for additive-free and additive-containing calcined CoMo(P) catalysts	201
Figure VII-8: Normalized Mo K-edge XANES spectra of the dried CoMo_HPA(d) and corresponding ex situ sulfided catalyst.	202
Figure VII-9: Mo K-edge k^3 -weighted EXAFS Fourier Transforms of sulfided dried CoMo(P) and corresponding TEG-containing catalysts.	202
Figure VII-10: Mo K-edge k^3 -weighted filtered EXAFS signal and corresponding Fourier Transforms modulus of CoMo_HPA(d) catalyst.	203
Figure VII-11: Molybdenum 3d XPS spectrum decomposition of the sulfided CoMoP(5d) catalyst.	205
Figure VII-12: Molybdenum 3d XPS spectrum decomposition results for additive-free and additive-containing dried CoMo(P) catalysts.	205
Figure VII-13: Molybdenum K-edge k^3 -weighted EXAFS Fourier Transforms modulus of sulfided calcined CoMo(P) and corresponding TEG-containing catalysts.	206
Figure VII-14: Molybdenum 3d XPS spectrum decomposition results for additive-free and additive-containing calcined CoMo(P) catalysts.	208
Figure VII-15: TEM image of a Co_9S_8 particle	208
Figure VII-16: TEM images of the sulfided CoMo_AHM(d) (left) and CoMo_AHM(d)+TEG catalysts.	209

Figure VII-17: MoS ₂ slab length histogram of the CoMo_AHM(d) and CoMo_AHM(d)+TEG catalysts.	209
Figure VII-18: MoS ₂ slab stacking histogram of the CoMo_AHM(d) and CoMo_AHM(d)+TEG catalysts.	209
Figure VII-19: In situ sulfidation follow-up using the Co K-edge XANES spectra of the additive-free and additive-containing CoMoP(5d) catalysts.	211
Figure VII-20: Cobalt K-edge k ³ -weighted EXAFS Fourier Transforms of the additive-free CoMoP(5d) and additive-containing CoMoP(5d)+TEG catalysts during in situ sulfidations.	212
Figure VII-21: In situ sulfidation follow-up using the Mo K-edge XANES spectra of the additive-free and additive-containing CoMoP(5d) catalysts.	213
Figure VII-22: Molybdenum K-edge k ³ -weighted EXAFS Fourier Transforms of additive-free CoMoP(5d) and additive-containing CoMoP(5d)+TEG catalysts during in situ sulfidations.	214
Figure VII-23: Mo-S coordination number evolution with temperature during the in situ sulfidations.	215
Figure VII-24: Toluene hydrogenation and cyclohexane isomerization reaction rates of the additive-free dried CoMo(P) catalysts.	217
Figure VII-25: Toluene hydrogenation and cyclohexane isomerization reaction rates of the additive-free calcined CoMo(P) catalysts.	218
Figure VII-26: Improvements in toluene hydrogenation and cyclohexane isomerization reactions due to TEG impregnation of dried catalysts.	219
Figure VII-27: Improvements in toluene hydrogenation and cyclohexane isomerization reactions due to TEG impregnation of calcined catalysts.	220
Figure VII-28: Impact of the additive impregnation stage location on toluene hydrogenation and cyclohexane isomerization reaction rates of CoMoP(5) catalysts.	221
Figure VII-29: Impact of the additive impregnation stage location on toluene hydrogenation and cyclohexane isomerization reaction rates of CoMo_HPA catalysts.	221
Figure VII-30: Impact of the additive loading on the toluene hydrogenation and cyclohexane isomerization reaction rates for the dried CoMoP(5d) catalysts.	222
Figure VII-31: Impact of the additive loading on the toluene hydrogenation and cyclohexane isomerization reaction rates for the co-impregnated CoMoP(5) catalysts.	223
Figure VII-32: Diesel sulfur content after HDS reaction at different temperatures using CoMoP(5) catalysts.	224

COMPRÉHENSION DU RÔLE DES ADDITIFS DU TYPE GLYCOL SUR L'AMÉLIORATION DES PERFORMANCES DES CATALYSEURS D'HYDROTRAITEMENT

L'introduction d'additifs de type glycol dans les catalyseurs d'hydrotraitement afin d'avoir une meilleure activité catalytique est une procédure reconnue. Par contre, dans la littérature les avis divergent sur le mécanisme d'augmentation de l'activité. L'objectif de ce travail est donc de rationaliser le rôle des additifs par rapport (i) aux espèces présentes dans la solution d'imprégnation ainsi qu'à la surface du catalyseur et (ii) à l'étape de préparation durant laquelle se fait l'additivation. Des catalyseurs ont été préparés à partir de différentes solutions précurseurs de type CoMo(P) et de triéthylèneglycol (TEG) qui est introduit lors de différentes étapes de préparation. Une relation a été trouvée entre les espèces de surface avant l'étape de sulfuration et les activités catalytiques en hydrogénation du toluène. Plusieurs techniques d'analyse (spectroscopies Raman, UV-Visible, RMN, DRX) ont montré que le TEG joue un rôle de solvant et privilégie la formation et dispersion d'hétéropolycomposés. L'utilisation de cet additif a pour conséquence une meilleure dispersion des précurseurs de la phase active et la formation de la phase "CoMoS" est privilégiée.

UNDERSTANDING THE ROLE OF GLYCOL-TYPE ADDITIVES IN THE IMPROVEMENT OF HYDROTREATMENT CATALYSTS PERFORMANCES

The introduction of a glycol-type additive in hydrotreating catalysts is an efficient procedure to improve catalytic activity. However, controversial explanations about the activity enhancement mechanism exist in the literature. The aim of this work is thus to rationalize the role of the additives with respect to (i) species present in the impregnation solution as well as on the catalyst surface and (ii) the preparation step where the additive impregnation is performed. Catalysts were prepared from different CoMo(P) precursor solutions and triethyleneglycol (TEG) was introduced at different preparation stage locations. A correlation was established between the surface species prior to the sulfidation stage and the catalytic performances tested on toluene hydrogenation. Different characterization techniques (Raman, UV-Visible, NMR, DRX) allowed to evidence that TEG acts as a solvent and favors the formation and dispersion of heteropolycompounds. As a consequence, improved active phase precursor dispersions are achieved and the formation of the "CoMoS" phase is favored.

DISCIPLINE : CATALYSE

MOTS-CLES : Hydrotraitement, Hydrodésulfuration, Additifs, Glycol, TEG

Institut de Recherches sur la Catalyse et
l'Environnement de Lyon - IRCE Lyon
2, Av. A. Einstein
69626 Villeurbanne Cedex

Institut Français du Pétrole
1 & 4, Avenue de Bois-Préau
92852 Rueil-Malmaison Cedex